

AD-A182 459

LARGE-EDDY NUMERICAL SIMULATION OF AN ARRAY OF  
THREE-DIMENSIONAL IMPINGING JETS(U) FLOW RESEARCH CO  
KENT WA M H RIZK ET AL APR 87 FLOW-RR-403

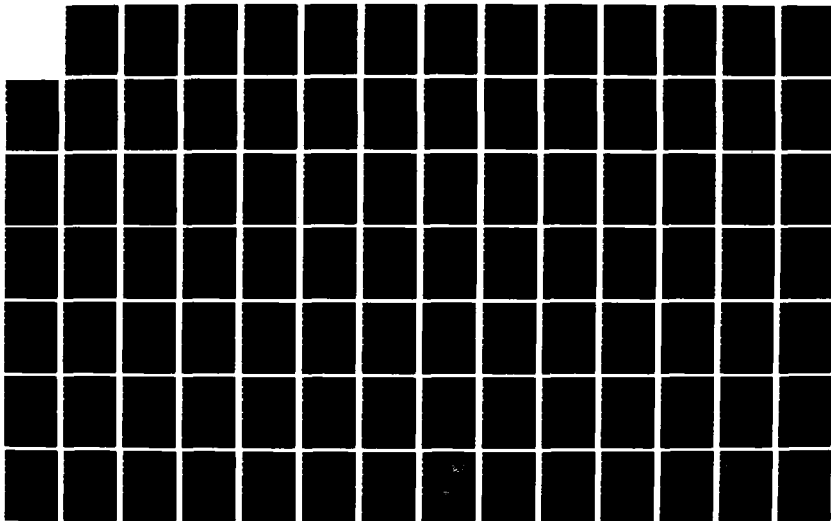
1/2

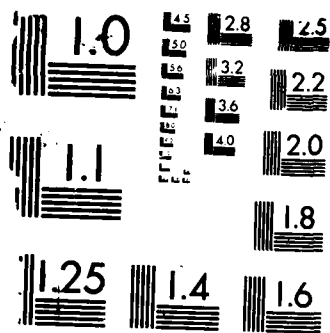
UNCLASSIFIED

AFOSR-TR-87-0900 F49620-85-C-0084

F/G 1/1

NL





MICROCOPY RESOLUTION TEST CHART

DTIC FILE COPY

Flow Research Report No. 403

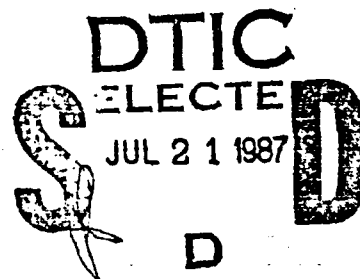
2

AFOSR-TR. 87-0900

AD-A182 459

# LARGE-EDDY NUMERICAL SIMULATION OF AN ARRAY OF THREE-DIMENSIONAL IMPINGING JETS

M. H. Rizk and S. Menon  
Flow Research Company  
21414-68th Avenue South  
Kent, WA 98032



Approved for public release;  
distribution unlimited.

April 1987

AIR FORCE OFFICE OF SCIENTIFIC RESEARCH (AFSC)  
NOTICE OF TRANSMITTAL TO DTIC

This technical report has been reviewed and is  
approved for public release IAW AFR 190-12.  
Distribution is unlimited.

Final Report for Period  
May 1985 - July 1986

MATTHEW J. KERPER  
Chief, Technical Information Division

Contract No. F49620-85-C-0084

APPROVED FOR PUBLIC RELEASE  
DISTRIBUTION UNLIMITED

Prepared for  
Air Force Office of Scientific Research  
Building 410  
Bolling AFB, DC 20332-6448

87 7 17 038

Unclassified

SECURITY CLASSIFICATION OF THIS PAGE

ADA 182459

## REPORT DOCUMENTATION PAGE

1a. REPORT SECURITY CLASSIFICATION <b>UNCLASSIFIED</b>			1b. RESTRICTIVE MARKINGS		
2a. SECURITY CLASSIFICATION AUTHORITY			3. DISTRIBUTION/AVAILABILITY OF REPORT Unlimited		
2b. DECLASSIFICATION/DOWNGRADING SCHEDULE					
4. PERFORMING ORGANIZATION REPORT NUMBER(S) Flow Research Report No. 403			5. MONITORING ORGANIZATION REPORT NUMBER(S) <b>AFOSR-TR-87-0900</b>		
6a. NAME OF PERFORMING ORGANIZATION Flow Research Company		6b. OFFICE SYMBOL (If applicable) <b>AFOSR/NA</b>		7a. NAME OF MONITORING ORGANIZATION <b>Bolling AFB, DC 20332</b>	
6c. ADDRESS (City, State and ZIP Code) 21414 68th Ave. So. Kent, WA 98032			7b. ADDRESS (City, State and ZIP Code) <b>Same as 6c</b>		
8a. NAME OF FUNDING/SPONSORING ORGANIZATION Air Force Office of Scientific Research		8b. OFFICE SYMBOL (If applicable) <b>AFOSR/NA</b>		9. PROCUREMENT INSTRUMENT IDENTIFICATION NUMBER <b>F49620-85-C-0084</b>	
8c. ADDRESS (City, State and ZIP Code) Building 410 Bolling AFB, D.C. 20332-6448			10. SOURCE OF FUNDING NOS.		
			PROGRAM ELEMENT NO. <b>61182F</b>		TASK NO. <b>2307</b>
			PROJECT NO. <b>A-1</b>		WORK UNIT NO.
11. TITLE (Include Security Classification) Large-Eddy Numerical Simulation of an Array of Three-Dimensional Impinging Jets					
12. PERSONAL AUTHOR(S) M. H. Rizk and S. Menon					
13a. TYPE OF REPORT Final Report		13b. TIME COVERED FROM 5-85 TO 7-86		14. DATE OF REPORT (Yr., Mo., Day) April 1987	
15. PAGE COUNT 178					
16. SUPPLEMENTARY NOTATION					
17. COSATI CODES			18. SUBJECT TERMS (Continue on reverse if necessary and identify by block number)		
FIELD	GROUP	SUB. GR.	VTOL, impinging jets, large-eddy simulation, incompressible Navier-Stokes equations		
19. ABSTRACT (Continue on reverse if necessary and identify by block number) Numerical simulations of a row of impinging jets are performed. Both the impinging jets and the fountains caused by the collision of the wall jets are modeled in the simulations. The problem considered contains the essential features of twin jets impinging on the ground, simulating the hovering configuration of a VTOL aircraft. The flow is assumed to be governed by the time-dependent, incompressible Navier-Stokes equations. The large-eddy simulation approach is followed. In this approach all scales resolvable by the grid resolution are computed explicitly, while the small-scale turbulence structures, which are nearly universal in character, are modeled by an eddy viscosity formulation that simulates the energy cascade into the small scales. The Navier-Stokes equations are solved using a staggered computational mesh. Central finite differencing is used to discretize all terms except the convective terms, which are discretized using the QUICK scheme. The Adams-Bashforth scheme is used to advance the solution in time. The pressure Poisson equation is					
20. DISTRIBUTION/AVAILABILITY OF ABSTRACT UNCLASSIFIED/UNLIMITED <input checked="" type="checkbox"/> SAME AS RPT. <input type="checkbox"/> DTIC USERS <input type="checkbox"/>			21. ABSTRACT SECURITY CLASSIFICATION Unclassified		
22a. NAME OF RESPONSIBLE INDIVIDUAL Dr. James Wilson			22b. TELEPHONE NUMBER (Include Area Code) (206) 767-4987		22c. OFFICE SYMBOL <b>AFOSR/NA</b>

DD FORM 1478, 83 APR

EDITION OF 1 JAN 73 IS OBSOLETE.

Unclassified  
SECURITY CLASSIFICATION OF THIS PAGE



## 19. ABSTRACT (Cont.)

used in place of the continuity equation. Efficient direct solutions are obtained for the pressure field, which allows the continuity equation to be satisfied at each time step. ~~The present study~~ focuses on the motion and dynamics of large-scale structures that have been experimentally observed in jet flows. The behavior of the jets and the fountain due to introducing axisymmetric, azimuthal and random disturbances at the jet exits is investigated. The effects of a phase difference in the forcing applied at the jet exits of neighboring jets are also investigated. The results obtained indicate both quantitative and qualitative agreement with some experimental observations.

# ACKNOWLEDGEMENTS

The authors would like to express their appreciation to Dr. James J. Riley for his assistance on this project and to Mr. Morton Cooper, who originally suggested the problem.

Accession For	
NTIS CRA&I	<input checked="" type="checkbox"/>
DTIC TAB	<input type="checkbox"/>
Unannounced	<input type="checkbox"/>
Justification	
By	
Distribution/	
Availability Codes	
Dist	Avail and/or Special
A-1	

# TABLE OF CONTENTS

	<u>Page</u>
ACKNOWLEDGMENTS	iii
LIST OF FIGURES	vii
1. INTRODUCTION	1
2. FORMULATION	3
2.1 Governing Equations	3
2.2 Boundary Conditions	6
2.3 Random Initial Conditions	8
3. METHOD OF SOLUTION	14
4. RESULTS OF SIMULATIONS	17
4.1 Steady Impinging Jets	19
4.2 Axisymmetrically Forced Impinging Jets	24
4.2.1 In-Phase Forcing	26
4.2.2 Out-of-Phase Forcing	41
4.3 Azimuthally Forced Impinging Jets	49
4.3.1 In-Phase Forcing	49
4.3.2 Out-of-Phase Forcing	54
4.4 Randomly Forced Impinging Jets	65
5. CONCLUSIONS	69
REFERENCES	75
FIGURES	77

# LIST OF FIGURES

	<u>Page</u>
Figure 1. Schematic of the Flow Field Below a Hovering VTOL Aircraft	77
Figure 2. v-mesh Computational Cell	78
Figure 3. Top View of Computational Domain for the Double-Jet Configuration	79
Figure 4. Three-Dimensional Perspective of the Absolute Vorticity Surface at a Level $ \omega  = 1.75$ at $t = 11.3$ . View of the Impinging Jet and the Fountain at Steady-State for $H = 1.5D$	80
Figure 5. Steady-State Velocity Profiles at $t = 11.3$ for $H = 1.5D$	81
Figure 6. Steady-State Pressure Variation Along the Boundaries at $t = 11.3$ for $H = 1.5D$	82
Figure 7. Steady-State Spreading of the Impinging Jet and the Fountain at $t = 11.3$ for $H = 1.5D$	83
Figure 8. Three-Dimensional Perspective of the Steady-State Vorticity Surface for $H = 3D$ at $t = 29.5$	85
Figure 9. Steady-State Velocity Vector Diagram in the y-z Plane at $t = 29.3$ for $H = 3D$	89
Figure 10. Steady-State Velocity Vector Diagram in the x-z Plane at $t = 29.5$ for $H = 3D$	87
Figure 11. Steady-State Velocity Profiles at $t = 29.5$ for $H = 3D$	88
Figure 12. Steady-State Pressure Variation and Spreading of the Impinging Jet and the Fountain at $t = 29.5$ for $H = 3D$	89
Figure 13. Time Sequence of the x-Vorticity Contours for a Forcing Cycle at $St = 0.47$ in the y-z plane for $H = 1.5D$ (Contour Interval = 1.0)	91
Figure 14. Time Sequence of the y-Vorticity Contours for a Forcing Cycle at $St = 0.47$ in the x-z plane for $H = 1.5D$ (Contour Interval = 1.0 for a - d; 0.5 for e)	93
Figure 15. z-Vorticity Contours for a Forcing Cycle at $St = 0.47$ in the x-y Plane for $H = 1.5D$ (Contour Interval = 0.25)	94
Figure 16. The Three-Dimensional Perspective of the Vorticity Surface at $t = 37.98$ for Axisymmetric Forcing at $St = 0.47$ for $H = 1.5D$	96

	<u>Page</u>
Figure 17. Distribution of the Velocity, Pressure Gradient and Vorticity Fields at $t = 37.98$ in the $y$ - $z$ Plane at $x = 0$ for Forcing at $St = 0.47$	98
Figure 18. Velocity and Pressure Vector Diagram at $t = 37.98$ in the $x$ - $z$ Plane for Forcing at $St = 0.47$	100
Figure 19. $v$ -Velocity Profiles as a Function of $z$ for Forcing at $St = 0.47$	101
Figure 20. $u$ -Velocity Profiles as a Function of $z$ for Forcing at $St = 0.47$	103
Figure 21. Spreading of the Impinging Jet and the Fountain for a Forcing Cycle at $St = 0.47$	105
Figure 22. Three-Dimensional Perspective of the Vorticity Surface for Combined Forcing at $St = 0.47$ and $St = 0.94$ for $H = 1.5D$	107
Figure 23. Time Sequence of the $x$ -Vorticity Contours in the $y$ - $z$ plane for Combined Forcing at $St = 0.47$ and $0.94$ for $H = 1.5D$ (Contour Interval = 1.0)	108
Figure 24. $y$ -Vorticity Contours in the $x$ - $z$ Plane for Combined Forcing at $St = 0.47$ and $0.94$ . View is of the $y = 0$ Plane at $t = 50.64$ (Contour Interval is 0.8)	109
Figure 25. Three-Dimensional Perspective of the Vorticity Surface for the $H = 3D$ Case at $t = 59.7$ for Forcing at $St = 0.47$	110
Figure 26. Time Sequence of the $x$ -Vorticity Contours in the $y$ - $z$ Plane for Forcing at $St = 0.47$ for $H = 3D$ case (Contour Interval = 1.0)	111
Figure 27. Time Sequence of the $y$ -Vorticity Contours in the $x$ - $z$ Plane for Forcing at $St = 0.47$ for $H = 3D$ Case (Contour Interval = 1.0)	112
Figure 28. Variation of the Velocity Profiles as a Function of $z$ for a Forcing Cycle at $St = 0.47$ for $H = 3D$	114
Figure 29. three-dimensional perspective of the vorticity surface for combined forcing at $St = 0.47$ and $0.94$ for $H = 3D$ case. View of the impinging jet and the outflow at $t = 50.64$ ; $ \omega  = 1.95$	116
Figure 30. Three-Dimensional Perspective of the Vorticity Surface for Combined Forcing at $St = 0.235$ and $0.47$ for $H = 3D$ Case. View of the Impinging Jet and the Outflow at $t = 50.64$ ; $ \omega  = 1.95$	117

	<u>Page</u>
Figure 31. Time Sequence of the x-Vorticity in the y-z Plane for Forcing at $St = 0.235$ and $0.47$ for $H = 3D$ Case (Contour Interval = $0.4$ )	118
Figure 32. y-Vorticity Contours in the x-z Plane for Forcing at $St = 0.235$ and $0.47$ for $H = 3D$ (Contour Interval = $0.4$ )	119
Figure 33. Three-Dimensional Perspective of the Vorticity Surface for Combined Forcing at $St = 0.235$ and $0.47$ . The Forcing Level is $0.2U$	120
Figure 34. x-Vorticity Contours in the y-z Plane for Combined Forcing at $St = 0.235$ and $0.47$ (Contour Interval = $0.5$ )	121
Figure 35. y-Vorticity Contours in the x-z Plane for Combined Forcing at $St = 0.235$ and $0.47$ (Contour Interval = $0.5$ )	122
Figure 36. Variation of the x-Vorticity Contours in the x-y Plane for Combined Forcing at $St = 0.235$ and $0.47$ (Contour Interval = $0.4$ )	123
Figure 37. Variation of the y-vorticity Contours in the x-y Plane for Combined Forcing at $St = 0.235$ and $0.47$ (Contour Interval = $0.4$ )	124
Figure 38. Spread of the Impinging Jet and the Fountain for Combined Forcing at $St = 0.235$ and $0.47$	125
Figure 39. Velocity Profiles in the y-z Plane as a Function of $z$ at $t = 50.64$ for Combined Forcing at $St = 0.235$ and $0.47$	126
Figure 40. Three-Dimensional Perspective of the Vorticity Surface at $t = 22.5$ for Two Jets Forced Axisymmetrically at $St = 0.47$ with a Phase Difference of $\pi$ for $H = 1.5D$ case	127
Figure 41. Three-Dimensional Perspective of the Vorticity Surface at $t = 25.3$ for Two Jets Forced Axisymmetrically at $St = 0.47$ with a Phase Difference of $\pi$ for $H = 3D$	128
Figure 42. x-Vorticity Contours in the y-z Plane for Jets Forced at $St = 0.47$ with a Phase Difference of $\pi$ for $H = 3D$ (contour interval = $0.6$ )	129
Figure 43. y-Vorticity Contours in the x-z Plane for Jets Forced at $St = 0.47$ with a Phase Difference of $\pi$ for $H = 3D$ (Contour Interval = $0.6$ )	130
Figure 44. Time Sequence of y-Vorticity Contours in the x-z Plane at $y = 0$ in the vicinity of the Wall Jet Collision Zone for $H = 3D$ . The Jets are Forced at $St = 0.47$ with a Phase Difference of $\pi$ (Contour Interval = $0.6$ )	131

	<u>Page</u>
Figure 45. z-Vorticity Contours in the x-y Plane for Jets Forced at $St = 0.47$ with a Phase Difference of $\pi$ for $H = 3D$ (contour interval is 0.2)	132
Figure 46. Three-Dimensional Perspective of the Vorticity Surface at $t = 25.3$ for Two Jets Forced Axisymmetrically at $St = 0.47$ with a Phase Difference of $\pi/2$	133
Figure 47. y-Vorticity Contours in the x-z Plane for Jets forced at $St = 0.47$ with a Phase Difference of $\pi/2$ (Contour Interval = 0.6 for a - b; 0.4 for c - e)	134
Figure 48. Vorticity Contours at $t = 25.3$ in the x-y plane for Jets Forced at $St = 0.47$ with a Phase Difference of $\pi/2$ (Contour Interval = 0.4)	135
Figure 49. Three-Dimensional Perspective of the Vorticity Surface at $t = 21.1$ for Only One Jet Forced at $St = 0.47$ at a level $ \omega  = 1.95$	136
Figure 50. y-Vorticity Contours in the x-z Plane at $t = 23.2$ for Only One Jet Forced at $St = 0.47$ (Contour Interval = 0.6 for a - b; 0.3 for c)	137
Figure 51. y-Vorticity Contours in the x-z Plane at $y = 0$ in the Vicinity of the Wall Jet Collision Zone for Only One Jet Forced at $St = 0.47$ (Contour Interval = 0.8)	138
Figure 52. Vorticity Contours in the x-y Plane for Only One Jet Forced at $St = 0.14D$ . View of the $z = 0.14D$ Plane at $t = 21.1$	139
Figure 53. Velocity Vector Diagram in the x-z Plane	140
Figure 54. Three-Dimensional Perspective of the Vorticity Surface for a Jet Forced Azimuthally at $St = 0.47$ for $H = 1.5D$ . The Forcing Level is $0.1U$	141
Figure 55. y-Vorticity Contours in the x-z Plane for a Jet Forced Azimuthally at $St = 0.47$ for $H = 1.5D$ (Contour Interval = 1.0)	142
Figure 56. Three-Dimensional Perspective of the Vorticity Surface for a Jet Forced Azimuthally at $St = 0.47$ for $H = 3D$ at $t = 23.9$ . The forcing level is $0.1U$	143
Figure 57. Time Sequence of the x-Vorticity Contours in the y-z Plane at $x = 0$ for Azimuthal Forcing at $St = 0.47$ (Contour Interval = 0.7)	144
Figure 58. x-Vorticity Contours in the y-z Plane for Azimuthal Forcing at $St = 0.47$ (Contour Interval = 0.7)	145

	<u>Page</u>
Figure 59. Time Sequence of the y-Vorticity Contours in the x-z Plane at $y = 0$ for Azimuthal Forcing at $St = 0.47$ (Contour Interval = 0.7)	146
Figure 60. Time Sequence of the y-Vorticity Contours in the x-z Plane at $y = -1.5D$ for Azimuthal Forcing at $St = 0.47$ (contour Interval = 0.3)	147
Figure 61. Time Sequence of the y-Vorticity Contours in the x-z Plane at $y = 1.5D$ for Azimuthal Forcing at $St = 0.47$ (Contour Interval = 0.3)	148
Figure 62. Time Sequence of the y-Vorticity Contours in the x-z Plane at $y = -0.51D$ for Azimuthal Forcing at $St = 0.47$ (Contour Interval = 0.6)	149
Figure 63. Time Sequence of the y-Vorticity Contours in the x-z Plane at $y = 0.5D$ for Azimuthal Forcing at $St = 0.47$ (Contour Interval = 0.6)	150
Figure 64. Variation of the Centerline Velocity as a Function of $z$ for an Azimuthally Forced Cycle at $St = 0.47$ for $H = 3D$	151
Figure 65. Velocity Vector Field in the y-z Plane at $t = 23.91$ for Azimuthal Forcing at $St = 0.47$	152
Figure 66. Velocity Vector Field in the x-z Plane at $t = 23.91$ for Azimuthal Forcing at $St = 0.47$	153
Figure 67. Pressure Gradient Vector Field in the Centerline Planes at $t = 32.91$ for Azimuthal Forcing at $St = 0.47$	154
Figure 68. Velocity Contours in the x-y Plane at $t = 23.91$ for Azimuthal Forcing at $St = 0.47$	155
Figure 69. Azimuthal Disturbance at Jet Exits for the Double-Jet Configuration	156
Figure 70. Three-Dimensional Perspective of the Absolute Vorticity Surface at a Level $ \omega  = 2.1$ for the Unperturbed Double-Jet Computation	157
Figure 71. Three-Dimensional Perspective of the Vorticity Surface $\omega_\theta = -3.1$ for Forced Double-Jet Computations	158
Figure 72. y-Vorticity Contours in the $y = 0$ Plane for Forced Double-Jet Computations (Contour Interval = 0.8)	159
Figure 73. y-Vorticity Contours in the $y = -1.5D$ plane for Forced Double-Jet Computations (Contour Interval = 0.4)	161



	<u>Page</u>
Figure 74. y-Vorticity Contours in the $y = 1.5D$ Plane for Forced Double-Jet Computations (Contour Interval = 0.4)	163
Figure 75. y-Vorticity Contours in the $y = 0$ Plane for a Complete Forcing Cycle, CW-CW, $\phi = 0$ (Contour Interval = 0.8)	165
Figure 76. y-Vorticity Contours in the $y = -1.5D$ Plane for a Complete Forcing Cycle, CW-CW, $\phi = 0$ (Contour Interval = 0.4)	166
Figure 77. y-Vorticity Contours in the $z = 1D$ Plane for Forced Double-Jet Computations (Contour Interval = 0.6)	167
Figure 78. y-Vorticity Contours in the $z = 1.5D$ Plane for Forced Double-Jet Computations (Contour Interval = 0.6)	168
Figure 79. Velocity Vector Plots in the $x = x_F$ Plane for Forced Double-Jet Computations	169
Figure 80. Velocity Vector Plots in the $y = 0$ Plane for Forced Double-Jet Computations	170
Figure 81. Velocity Vector Plots in the $y = -1.5D$ Plane for Forced Double-Jet Computations	171
Figure 82. Velocity Vector Plots in the $y = 1.5D$ Plane for Forced Double-Jet Computations	172
Figure 83. Relative Positions of Vortex Tubes at Fountain Base	173
Figure 84. Relative Positions of Vortex Tubes in Fountain	174
Figure 85. Three-Dimensional Perspective of the Absolute Vorticity Surface at a level $ \omega  = 2.1$ for Forced Double-Jet Computations	175
Figure 86. x-Vorticity Contours in the y-z Plane Due to Random Excitation for $H = 3D$	176
Figure 87. y-Vorticity Contours in the x-z Plane at $t = 50.62$ Due to Random Excitation for $H = 3D$	177
Figure 88. Spanwise Variation of x- and y-Vorticity Contours in the $z = 0$ , x-y Plane at $t = 50.62$ Due to Random Excitation for $H = 3D$	178

## 1. INTRODUCTION

The fluid dynamics of impinging jets of vertical takeoff and landing (VTOL) aircraft is of great complexity. The ability to optimize the design of these aircraft and to predict their performance requires a good understanding of the jet-induced phenomena associated with them. VTOL aircraft have different operating modes (hovering and transition in and out of ground effect). The flow fields associated with these modes of operation are substantially different. Many of the complex flow phenomena are poorly understood. The main flow regions associated with a hovering VTOL aircraft are shown in Figure 1. The impinging jets entrain air, which leads to induced suction pressure on the lower surface of the aircraft. When the aircraft is hovering near the ground, further entrainment is caused by the wall jets, increasing the suckdown force on the aircraft. The wall jets associated with multiple impinging jets collide and form a fountain that impinges on the lower surface of the aircraft. This causes an increase in pressure on the lower surface, resulting in a lift-off effect that partially offsets the suckdown force on the aircraft.

The majority of the research into VTOL flows to date has been experimental. A list of references for the experimental work is given in Reference 1. However, experimental studies of VTOL flows are extremely cumbersome, and measurements are inaccurate owing to the flow being turbulent, globally unsteady, and three-dimensional. Experimental studies of the jet flows indicate that the jet is susceptible to instabilities that cause the shear layer to roll up into vortex rings. During their spatial evolution, these rings pair and then merge into larger structures that are initially spatially coherent but eventually break down into turbulence. The characteristics of large-scale structures in turbulent flows have been a focus of research due to their importance in turbulent transport and noise production. There is also evidence of the presence of large-scale structures in impinging jet flows. Due to their deterministic nature, these large-scale structures have been studied both analytically and, more recently, numerically. Only within the past few years have sufficient advances in computer capabilities made it feasible to attempt numerical simulation of the three-dimensional viscous VTOL flow fields. While numerical simulations are not expected to replace experimental investigations, they are expected to complement experimental efforts in resolving many of the complex problems associated with VTOL flows.

Computational efforts for investigating impinging jets were initially limited to solving two-dimensional problems. Using an incompressible inviscid rotational flow model, Rubel<sup>2</sup> investigated the normal impingement of axisymmetric jets and the oblique impingement of two-dimensional jets upon a flat surface. This model was then extended to allow three-dimensional computations.<sup>3</sup> Kotansky and Bower<sup>4</sup> investigated planar turbulent jet impingement by solving the time-averaged Navier-Stokes equations using a one-equation turbulence model. In this approach, it was necessary to specify the turbulence length scale distributions. To avoid this disadvantage, Agarwal and Bower<sup>5</sup> replaced the one-equation turbulence model with the two-equation (k- $\epsilon$ ) turbulence model. The work of Kotansky and Bower<sup>4</sup> was extended to solve the problem of three-dimensional lift jets in ground effect by Bower et al.<sup>6</sup> This work was the first attempt to calculate both interacting jets and the subsequent fountain formation. Computer limitations restricted the computations to a relatively coarse computational mesh and to low Reynolds numbers.

More recent studies include the unsteady simulations of Childs and Nixon<sup>7,8</sup> and Rizk and Menon.<sup>9</sup> In their investigations, Childs and Nixon used the compressible Navier-Stokes equations to investigate fluid/acoustic interactions in two different regions of the VTOL flow field. An isolated, single impinging jet was investigated by assuming an axisymmetric configuration, and the upwash fountain, which results from the collision of two planar wall jets, was studied for three-dimensional flows. The incompressible Navier-Stokes equations were used by Rizk and Menon to simulate both planar single impinging jets and an array of three-dimensional impinging jets. Both the impinging jet and the fountain caused by the collision of the wall jets were modeled in these three-dimensional simulations. The simulations were directed toward studying the effect of controlled excitation on the development of large structures in the impinging jets. The results presented by Rizk and Menon<sup>9</sup> are preliminary results that were obtained at the early stages of the present investigation.

The three-dimensional, time-dependent Navier-Stokes equations are used here to investigate the characteristics of jets impinging on the ground and of the fountain generated due to the collision of the wall jets that are formed by the impinging jets. Both steady-state and unsteady computations are performed. In the unsteady computations, the behavior of the jets and the fountain due to forcing introduced at the jet exit is investigated. The disturbances introduced at the jet exit are axisymmetric, azimuthal, and random disturbances.

## 2. FORMULATION

The problem under investigation here is that of an infinite row of jets impinging on the ground. This problem contains the essential features of twin jets impinging on the ground, simulating the hovering configuration. The jets are assumed to exit from a horizontal plate parallel to the ground. The x-z plane is assumed to be the plane of the jet axes, with the x-axis in the horizontal direction and the z-axis in the vertical direction upwards. The y-axis is normal to the plane of jets. The velocity components in the x-, y-, z-directions are u, v, w, respectively. The governing equations and the boundary conditions used are described below.

### 2.1 Governing Equations

In turbulent flows, a wide range of length and time scales exist. The separation between the largest scales of motion and the smallest scales of motion widens as the Reynolds number increases. For VTOL flows, the numerical resolution of all relevant scales of motion is impossible. Modeling of some aspects of the flow is therefore necessary. In the classical approach, based on Reynold's ideas for solving turbulent flow problems, the Navier-Stokes equations are averaged. All fluctuations are modeled, and only mean flow variables are calculated. Only steady-state solutions are possible. In the VTOL problem, the flow field is usually both unsteady and turbulent. Furthermore, different flow regions exist in which the scales of motion vary greatly from one to another. It is, therefore, difficult to resolve all the relevant scales using the current computing capability. Here, the large-eddy simulation (LES) approach is followed. In this approach, all scales resolvable by the grid resolution are computed explicitly using the time-dependent equations, while the small-scale turbulence structures, which are nearly universal in character, are modeled by an eddy viscosity formulation that simulates the energy cascade into the small scales. The use of the time-dependent equations in this manner provides the ability to investigate the temporal development of the flow field. A broad range of problems may, therefore, be investigated, e.g., the unsteady separation in boundary layers,<sup>10</sup> the evolution of large, spatially coherent structures in jets,<sup>11</sup> and the different stability modes in jets.<sup>12</sup>

In the large-eddy simulation approach, a flow variable  $f$  is decomposed as follows:

$$f = \bar{f} + f'$$

where  $\bar{f}$  is the large-scale, resolvable part and  $f'$  is the subgrid-scale, unresolvable part of the variable  $f$ . The large-scale component  $\bar{f}$  is defined by

$$\bar{f}(\underline{x}) = \int G(\underline{x} - \underline{x}') f(\underline{x}') d\underline{x}' \quad (1)$$

where  $G(\underline{x} - \underline{x}')$  is a filter function. Applying operation (1) to the incompressible Navier-Stokes equation

$$\underline{q}_t + \nabla \cdot (\underline{q} \underline{q}^T) = -\nabla p + \nu \nabla^2 \underline{q} \quad (2)$$

and to the continuity equation

$$\nabla \cdot \underline{q} = 0 \quad (3)$$

leads to the following equations:

$$\bar{\underline{q}}_t + \nabla \cdot (\overline{\underline{q} \underline{q}^T}) = -\nabla \bar{p} + \nu \nabla^2 \bar{\underline{q}} \quad (4)$$

$$\nabla \cdot \bar{\underline{q}} = 0 \quad (5)$$

where  $\underline{q}$  is the velocity vector,  $p$  is the pressure and  $\nu$  is the kinematic viscosity. The term  $\underline{q} \underline{q}^T$  includes unresolvable variables and therefore is not explicitly calculated. This term is given by

$$\overline{\underline{q} \underline{q}^T} = \overline{\bar{\underline{q}} \bar{\underline{q}}^T} + \overline{\bar{\underline{q}} \underline{q}'^T} + \overline{\underline{q}' \bar{\underline{q}}^T} + \overline{\underline{q}' \underline{q}'^T}. \quad (6)$$

The Fourier transform method used by Mansour et al.<sup>13</sup> allows the first term on the right-hand side of Equation (6) to be easily calculated. Otherwise this term may be written as

$$\overline{\bar{\underline{q}} \bar{\underline{q}}^T} = \bar{\underline{q}} \bar{\underline{q}}^T + \left( \overline{\bar{\underline{q}} \bar{\underline{q}}^T} - \bar{\underline{q}} \bar{\underline{q}}^T \right) \quad (7)$$

where the term within parentheses is the Leonard term. Leonard<sup>14</sup> shows that this term may be expanded in a Taylor series in terms of the resolvable variables. The last three terms in Equation (6) are usually modeled in terms of the resolvable variables; however, part of their effects can be captured by a Taylor series expansion of the resolved variables.<sup>15</sup> Here we follow Deardorff<sup>16</sup> in lumping the Leonard term with the subgrid terms and modeling  $R$ , where

$$R = \overline{\tilde{q} \tilde{q}^T} - \tilde{\bar{q}} \tilde{\bar{q}}^T.$$

In this case, Equation (4) becomes

$$\frac{\partial \tilde{q}}{\partial t} + \nabla \cdot (\tilde{q} \tilde{q}^T + \tau) = -\nabla P + \nu \nabla^2 \tilde{q} \quad (8)$$

where the elements  $\tau_{ij}$  of the tensor  $\tau$  are given by

$$\tau_{ij} = R_{ij} - \frac{1}{3} R_{kk} \delta_{ij}$$

and

$$P = \bar{p} + \frac{1}{3} R_{kk}.$$

The elements of  $\tau$ , responsible for the energy drain to the subgrid scales, are represented by an eddy viscosity model:

$$\tau_{ij} = -2 \nu_s S_{ij}$$

where the element  $S_{ij}$  of the rate-of-strain tensor  $S$  is given by

$$S_{ij} = \frac{1}{2} \left( \frac{\partial \bar{u}_i}{\partial x_j} + \frac{\partial \bar{u}_j}{\partial x_i} \right).$$

Here

$$(\bar{u}_1, \bar{u}_2, \bar{u}_3) = (\bar{u}, \bar{v}, \bar{w})$$

$$(x_1, x_2, x_3) = (x, y, z).$$

Smagorinsky's<sup>17</sup> model for the eddy viscosity, also used by Deardorff, is given by

$$\nu_s = (C_1 \Delta)^2 (2 S_{ij} S_{ij})^{1/2}$$

where  $C_1$  is a constant and  $\Delta$  is the characteristic length scale of the smallest resolved eddies. In the present simulations, we use  $C_1 = 0.1$  similar to Deardoff.

The equations governing the resolvable variables are written as

$$\underline{q}_t + \nabla \cdot [\underline{q} \underline{q}^T - 2(\nu + \nu_g)S] = -\nabla P \quad (9)$$

and

$$\nabla \cdot \underline{q} = 0 \quad (10)$$

where the bars have been dropped for simplicity. By taking the divergence of Equation (9), the following equation governing  $P$  is obtained:

$$\nabla^2 P = -\nabla \cdot \underline{q}_t - \nabla \cdot \underline{Q} \quad (11)$$

where

$$\underline{Q} = \nabla \cdot [\underline{q} \underline{q}^T - 2(\nu + \nu_g)S]$$

and

$$\nabla \cdot \underline{q}_t = 0$$

The system of Equations (9) and (11) is equivalent to the original system, Equations (9) and (10), and is used here in place of it.

## 2.2 Boundary Conditions

The vector equation (9) is solved subject to the periodicity condition in the  $x$ -direction, thereby simulating an infinite array of jets. The condition

$$\frac{\partial u}{\partial y} = \frac{\partial w}{\partial y} = 0 \quad (12)$$

with  $\partial v / \partial y$  being determined from the continuity equation, is applied at the side boundaries of the computational domain parallel to the row of jets. The computational mesh in the present calculations is not fine enough to resolve the viscous sublayer. Therefore, it is not proper to apply the no-slip condition at the upper and lower boundaries. The solution in the near wall region is therefore patched to the solution at the first computational mesh point away from the wall through the use of Spalding's<sup>18</sup> expression in this region.

The vertical velocity component is specified to be zero at the lower boundary and the upper boundary, except at the jet exit where it is specified as a function of space and time. The other two velocity components are specified to be zero at the jet exit.

Equation (11) is solved subject to the periodicity condition in the x-direction and the following Neumann boundary conditions determined from Equation (9) at the top and bottom boundaries:

$$\frac{\partial P}{\partial z} = -\underline{k} \cdot (\underline{q}_x + \underline{q}) \quad (13)$$

where  $\underline{k}$  is a unit vector in the vertical direction. Unlike the solid-wall boundaries, the side boundaries of the computational domain, which will also be referred to as outflow boundaries, are not physical boundaries. They are artificial boundaries created to limit the computational domain to a finite region. The boundary conditions are therefore not known at these boundaries. In cases where experimental measurements are available at these boundaries, it is possible to use them as boundary conditions. However, in general, such measurements are not available. Without experimental data, it is necessary to choose a set of boundary conditions at the side boundaries. In general, these conditions will create local disturbances near the boundaries. However, since the side boundaries are mainly outflow boundaries, it is expected that the local disturbances at the boundaries will have a negligible effect on the inner computational region of interest, provided reasonable conditions are applied and the boundaries are placed far enough away from the jets. A set of "approximate" boundary conditions at the side boundaries was chosen for Equation (9) and is given by Equation (12). For the pressure equation, the condition

$$\frac{\partial P}{\partial y} = 0 \quad (14)$$

is applied, with two modifications. The modifications are necessary due to the approximate nature of the conditions applied at the side boundaries. At the side boundaries there does occur some inflow due to the entrainment caused by the impinging jets, the wall jets, and the fountains. However, since the solution outside the computational domain is not known, it is not possible to specify the correct velocity distribution at the boundary. The weak



boundary conditions applied here were found in certain calculations to allow a continuous, nonphysical buildup in the inflow velocity in certain regions of the boundary, resulting in numerical instability. To avoid this problem, a restriction is imposed on the inflow velocity. At boundary points where the inflow velocity exceeds a certain specified limit, the value of  $\partial P/\partial y$  is modified so that the inflow velocity does not exceed this limit. Secondly, the existence of a solution to Equation (11) with Neumann boundary conditions applied at the horizontal and the side boundaries requires that

$$\int_V s \, dV = \int_S \frac{\partial P}{\partial n} \, dS \quad (15)$$

where  $s$  is the source term appearing on the right-hand side of Equation (11),  $V$  is the volume of the computational domain,  $S$  is the boundary of the computational domain, and  $n$  is the outward normal to that boundary. Since the value of  $\partial P/\partial n$  is specified on the upper and lower boundaries by Equation (13), condition (15) is satisfied through the proper modification of  $\partial P/\partial n$  on the side boundaries. Assuming that the first modification to the pressure boundary condition, limiting the inflow velocity, leads to the following boundary condition along the boundary  $S$ :

$$\frac{\partial P}{\partial n} = g \quad ,$$

in order to satisfy Eq. (15),  $\partial P/\partial n$  is modified at the side boundaries so that

$$\frac{\partial P}{\partial n} = g + \frac{\int_V s \, dV - \int_S g \, dS}{2A}$$

where  $A$  is the area of one of the side boundaries.

### 2.3 Random Initial Conditions

Here we present the rationale behind the model used to generate the random turbulent field that is imposed at the jet exit. We generate a random turbulent field, subject to particular constraints (to be discussed below) and impose this field at the jet exit. Numerical simulation of the subsequent development of the flow field is then carried out. By imposing such a random field at the jet inflow boundary condition, during the spatial development of

the jet, the unstable frequencies will amplify in a realistic manner. This approach is a more accurate way of forcing the jet compared to forcing at a single frequency. Furthermore, this approach does not require the a priori identification of the most unstable frequency, and the stability of the jet flow can be studied in a more general way. Due to the presence of the solid surfaces, the characteristic unstable frequency may depend on the location of the ground wall, and identification of the most unstable frequency is quite difficult. By imposing a random field at the jet exit containing all the possible frequencies (limited, of course, by the grid resolution), the most unstable frequency (or mode) may evolve naturally. Such an approach is expected to give a better understanding of the instability mechanism involved during the impingement of a jet on a ground plane.

The instantaneous velocity  $q_j(\underline{x}, t)$  at the jet exit is defined by

$$q_j(\underline{x}, t) = q_{ja}(\underline{x}) + q_j'(\underline{x}, t), \quad \underline{x} = (x, y) \quad (16)$$

where  $q_{ja}$  and  $q_j'$  are the ensemble average and the random turbulent jet velocity at the jet exit, respectively. We define the turbulent field  $q_j'(\underline{x}, t)$  at the jet exit as

$$q_j'(\underline{x}, t) = \sigma(\underline{x}) \sum_{|\underline{k}| \leq \underline{K}} \sum_{|\omega| \leq \Omega} \hat{q}_j(\underline{k}, \omega) e^{i(\underline{k} \cdot \underline{x} + \omega t)}. \quad (17)$$

In general, the turbulent field is three-dimensional. However, this field is specified at a given  $z$ -location and, therefore, the field is assumed to be a function of  $x$  and  $y$  only. Here,  $\underline{k} = (k_x, k_y)$ , is the wave-number vector and  $\omega$  is the frequency. Also,  $\underline{K} = (K_x, K_y)$ , is the wave-number cutoff and  $\Omega$  is the frequency cutoff, which are determined by the grid resolution and computation time, and  $\hat{q}_j(\underline{k}, \omega)$  are the Fourier modes of  $q_j'(\underline{x}, t)$ . Equation (17) is assumed to satisfy

$$\overline{q_j'} = 0 \quad (18a)$$

$$\overline{q_j'^2} = \sigma^2(\underline{x}) \quad (18b)$$

Here, the bar indicates ensemble averaging and  $\sigma(\underline{x})$  is the root-mean-square value. The random field is then generated such that Equation (18) is satisfied. In the subsequent formulation, the subscript  $j$  is omitted for simplicity. On averaging Equation (17), we obtain

$$\overline{\underline{q}'(\underline{x}, t)} = \sigma(\underline{x}) \sum_{\underline{k}, \omega} \overline{\hat{\underline{q}}(\underline{k}, \omega) e^{i(\underline{k} \cdot \underline{x} + \omega t)}} , \quad (19)$$

which implies that for Equation (18a) to be satisfied,

$$\overline{\hat{\underline{q}}(\underline{k}, \omega)} = 0 \quad \text{for each } (\underline{k}, \omega) . \quad (20)$$

Also,

$$\begin{aligned} \overline{q'^2(\underline{x}, t)} &= \sigma^2(\underline{x}) \overline{\sum_{\underline{k}, \omega} \hat{\underline{q}}(\underline{k}, \omega) e^{i(\underline{k} \cdot \underline{x} + \omega t)} \sum_{\underline{l}, \nu} \hat{\underline{q}}^*(\underline{l}, \nu) e^{-i(\underline{l} \cdot \underline{x} + \nu t)}} \\ &= \sigma^2(\underline{x}) \sum_{\underline{k}, \omega; \underline{l}, \nu} \overline{\hat{\underline{q}}(\underline{k}, \omega) \hat{\underline{q}}^*(\underline{l}, \nu) e^{i[(\underline{k} - \underline{l}) \cdot \underline{x} + (\omega - \nu)t]}} . \end{aligned} \quad (21)$$

We then choose  $\hat{\underline{q}}(\underline{k}, \omega)$  such that

$$\begin{aligned} \overline{\hat{\underline{q}}(\underline{k}, \omega) \hat{\underline{q}}^*(\underline{l}, \nu)} &= \overline{\hat{\underline{q}}(\underline{k}, \omega) \hat{\underline{q}}^*(\underline{k}, \omega) \delta(\underline{k} - \underline{l}, \omega - \nu)} \\ &= \overline{|\hat{\underline{q}}(\underline{k}, \omega)|^2} \delta(\underline{k} - \underline{l}, \omega - \nu) \end{aligned} \quad (22)$$

where  $\delta$  is the Dirac delta function and  $\hat{\underline{q}}^*$  is the complex conjugate of  $\hat{\underline{q}}$ . The delta function is defined as

$$\delta(\underline{k} - \underline{l}, \omega - \nu) = \begin{cases} 1, & \underline{k} = \underline{l}, \omega = \nu \\ 0, & \underline{k} \neq \underline{l}, \omega \neq \nu \end{cases} \quad (23)$$

Then, Equation (22) becomes

$$\overline{q'^2(\underline{x}, t)} = \sigma^2(\underline{x}) \sum_{\underline{k}, \omega} \overline{|\hat{\underline{q}}(\underline{k}, \omega)|^2} . \quad (24)$$

Note here that, by virtue of this equation, we are assuming that the Fourier modes  $\hat{q}(\underline{k}, \omega)$  are chosen such that there is no correlation between the various wave-number and frequency modes, that is, the wave numbers  $\underline{k}$  and  $\omega$  are uncorrelated. This is a reasonable first approximation.

We now choose

$$\sum_{\underline{k}, \omega} \overline{|\hat{q}(\underline{k}, \omega)|^2} = 1 \quad (25)$$

so that Equation (24) satisfies the requirement given by Equation (18b). Now,  $|\hat{q}(\underline{k}, \omega)|^2$  is the turbulence kinetic energy present in each  $(\underline{k}, \omega)$ . Therefore, the total turbulence energy is

$$\sum_{\underline{k}, \omega \in S} \overline{|\hat{q}(\underline{k}, \omega)|^2} = \iint_S E(\underline{k}, \omega) d\underline{k} d\omega \approx E(\underline{k}, \omega) \Delta\underline{k} \Delta\omega \quad (26)$$

where  $\Delta\underline{k} \Delta\omega$  is the volume contained within the surface S. Also  $E(\underline{k}, \omega)$  is the turbulence kinetic energy spectrum in the  $(\underline{k}, \omega)$  space. If we assume that there are  $N_s$  cells within the surface S and also assume  $|\hat{q}(\underline{k}, \omega)|^2$  is constant within each cell, then we may write

$$\sum_{\underline{k}, \omega \in S} \overline{|\hat{q}(\underline{k}, \omega)|^2} \approx N_s \overline{|\hat{q}(\underline{k}, \omega)|^2} \quad (27)$$

On combining Equations (26) and (27), we get

$$\overline{|\hat{q}(\underline{k}, \omega)|^2} = \frac{\Delta\underline{k} \Delta\omega}{N_s} E(\underline{k}, \omega) \quad (28)$$

The Fourier modes  $\hat{q}(\underline{k}, \omega)$  can then be determined provided that the energy spectrum  $E(\underline{k}, \omega)$  is known. It is possible to specify the energy spectrum from experimental data. For example, we may write

$$E(\underline{k}, \omega) = E_1(\underline{k}) E_2(\omega) \quad (29)$$

where  $E_1(\underline{k}) [= E_1(k_x, k_y)]$  is the two-dimensional energy spectrum in the wave-number space and  $E_2(\omega)$  is the one-dimensional energy spectrum in the frequency

space. We may then choose  $E_1(\underline{k})$  and  $E_2(\omega)$  from experimental data and normalize the energy spectrum such that

$$\int_{-\infty}^{\infty} \int_{-\infty}^{\infty} \int_{-\infty}^{\infty} E(k_x, k_y, \omega) dk_x dk_y d\omega = 1 \quad (30)$$

Then the Fourier modes  $\hat{q}(\underline{k}, \omega)$  would have the following properties:

- (i)  $\hat{q}(\underline{k}, \omega) = 0$  for each  $(\underline{k}, \omega)$  .
- (ii)  $\hat{q}(\underline{k}, \omega)$  is statistically independent of  $\hat{q}(\underline{l}, \nu)$  for  $\underline{k} \neq \underline{l}, \omega \neq \nu$  .
- (iii)  $\overline{|\hat{q}(\underline{k}, \omega)|^2} = \frac{\Delta k \Delta \omega}{N_s} E_1(\underline{k}) E_2(\omega) = F(\underline{k}, \omega)$  . (31)

So the Fourier modes  $\hat{q}(\underline{k}, \omega)$  are then determined subject to constraints (i) through (iii). The modes so defined are also chosen such that Equation (18) is implicitly satisfied. Once these modes are known, the random turbulent field  $q(\underline{x}, t)$  can be immediately determined by taking a fast Fourier transform by virtue of Equation (17). The steps necessary to determine the random field can then be summarized as follows:

- (1) Choose an energy spectrum  $E(\underline{k}, \omega)$  from experimental data and normalize according to Equation (30). Also determine  $\underline{K}$  and  $\Omega$ , the wave-number and frequency cutoffs.
- (2) Choose an elemental volume ( $\Delta k_x \Delta k_y \Delta \omega$ ) and determine the number of cells ( $N_s$ ) within that volume.
- (3) Use Equation (28) to determine  $\overline{|\hat{q}(\underline{k}, \omega)|^2}$  for each  $(\underline{k}, \omega)$ .

Note that

$$\overline{|\hat{q}(\underline{k}, \omega)|^2} = \overline{|\hat{q}_R|^2} + \overline{|\hat{q}_I|^2} = F(\underline{k}, \omega)$$

where the subscripts R and I denote the real and imaginary parts of  $\hat{q}$ . We assume

$$\overline{|\hat{q}_R|^2} = \overline{|\hat{q}_I|^2} = \frac{1}{2} F(\underline{k}, \omega) = q^{*2} \quad .$$

Then

$$q^* = \sqrt{\frac{1}{2} F(\underline{k}, \omega)} \quad .$$

- (4) For  $|\underline{k}| \leq K$  and  $|\omega| \leq \Omega$ , generate random numbers  $(R_1, R_2)$  such that  $\overline{R_1} = \overline{R_2} = 0$  and  $\overline{R_1^2} = \overline{R_2^2} = 1$  for each  $(\underline{k}, \omega)$ . The vector  $R_1$  indicates that the random field is generated for all  $\hat{q}$ ,  $\hat{q} = (\hat{u}, \hat{v}, \hat{w})$ .

- (5) For all  $(\underline{k}, \omega)$ , compute the Fourier modes

$$\hat{q}(\underline{k}, \omega) = (\hat{q}_R, \hat{q}_I) = (q^* R_1, q^* R_2)$$

where  $( , )$  indicates the real and imaginary parts.

- (6) Obtain  $q(\underline{x}, t)$  by taking a fast Fourier transform of  $\hat{q}(\underline{k}, \omega)$ .

### 3. METHOD OF SOLUTION

To solve the flow governing equations, we use a staggered computational mesh.<sup>19</sup> This resolves many of the difficulties associated with incompressible Navier-Stokes computations on a regular mesh.<sup>20</sup> The main computational mesh is the P-mesh. The pressure  $P$  is defined at the nodal points  $(x_i, y_j, z_k) = (i\Delta x, j\Delta y, k\Delta z)$  of this mesh, where  $\Delta x$ ,  $\Delta y$ ,  $\Delta z$  are the mesh spacings in the  $x$ -,  $y$ -,  $z$ -directions, respectively. The  $u$ -,  $v$ -,  $w$ -velocity components are defined at the nodal points  $(x_{i+\frac{1}{2}}, y_j, z_k)$ ,  $(x_i, y_{j+\frac{1}{2}}, z_k)$ ,  $(x_i, y_j, z_{k+\frac{1}{2}})$  of the  $u$ -,  $v$ -,  $w$ -meshes, respectively. These meshes are displaced from the P-mesh by half a mesh spacing in the  $x$ -,  $y$ -,  $z$ -directions, respectively. The  $x$ -,  $y$ -,  $z$ -momentum equations are discretized at the nodal points of the  $u$ -,  $v$ -,  $w$ -meshes, respectively, while the discretized Poisson equation for pressure is obtained at the nodal points of the P-mesh by central differencing of the discretized momentum equations at the neighboring points. The pressure gradient terms and the diffusive terms of the momentum equations are approximated by central differencing. The use of central differencing to approximate the convective terms leads to unphysical oscillatory behavior at relatively low Reynolds numbers and to divergence of the solution as the Reynolds number is increased. Classical alternatives of upstream differencing avoid the problems associated with central differencing by introducing numerical diffusion terms. However, they often suffer from severe inaccuracies due to truncation errors<sup>21</sup> or streamline-to-grid skewness.<sup>22</sup> The problems associated with central differencing and upstream differencing of the convective terms are avoided by using quadratic upstream interpolation for convective kinematics (QUICK) to approximate the convective terms. The original one-dimensional QUICK scheme developed by Leonard<sup>23</sup> was extended to two dimensions by Davis and Moore.<sup>24</sup> A three-dimensional extension of the scheme is used here.

While the QUICK scheme is used to discretize all the convective terms of the momentum equations, only the discretization of the term  $(uv)_x$  of the  $y$ -momentum equation is presented here. Discretization of the rest of the convective terms may be obtained in a similar manner. At the mesh node  $(x_i, y_{j+\frac{1}{2}}, z_k)$  (see Figure 2) the convective term  $(uv)_x$  is approximated by the finite difference expression

$$\frac{u^{i+\frac{1}{2}, j+\frac{1}{2}, k} v^{i+\frac{1}{2}, j+\frac{1}{2}, k} - u^{i-\frac{1}{2}, j+\frac{1}{2}, k} v^{i-\frac{1}{2}, j+\frac{1}{2}, k}}{\Delta x} \quad (32)$$

where

$$u_{i+\frac{1}{2}, j+\frac{1}{2}, k} = \frac{1}{2} (u_{i+\frac{1}{2}, j, k} + u_{i+\frac{1}{2}, j+1, k})$$

and  $v_{i+\frac{1}{2}, j+\frac{1}{2}, k}$  is an approximation for  $v$  at the point  $(x_{i+\frac{1}{2}}, y_{j+\frac{1}{2}}, z_k)$ . It is obtained by averaging a truncated Taylor series expansion for  $v$  over the cell side centered at the point  $(x_{i+\frac{1}{2}}, y_{j+\frac{1}{2}}, z_k)$ . The Taylor series is taken about the point  $(x_{i+\frac{1}{2}-\frac{1}{2}}, y, z)$  if  $u_{i+\frac{1}{2}, j+\frac{1}{2}, k} > 0$  or about the neighboring point  $(x_{i+\frac{1}{2}+\frac{1}{2}}, y, z)$  if  $u_{i+\frac{1}{2}, j+\frac{1}{2}, k} < 0$ . Assuming that  $u_{i+\frac{1}{2}, j+\frac{1}{2}, k} > 0$ , set

$$v(x_{i+\frac{1}{2}}, y, z) = \left[ 1 + \left( \frac{\Delta x}{2} \frac{\partial}{\partial x} + \eta \frac{\partial}{\partial y} + \zeta \frac{\partial}{\partial z} \right) + \frac{1}{2} \left( \frac{\Delta x}{2} \frac{\partial}{\partial x} + \eta \frac{\partial}{\partial y} + \zeta \frac{\partial}{\partial z} \right)^2 \right] v(x_{i+\frac{1}{2}-\frac{1}{2}}, y_{j+\frac{1}{2}}, z_k) \quad (33)$$

where

$$\eta = y - y_{j+\frac{1}{2}}$$

$$\zeta = z - z_k$$

The expression for  $v_{i+\frac{1}{2}, j+\frac{1}{2}, k}$  is obtained by taking the average

$$v_{i+\frac{1}{2}, j+\frac{1}{2}, k} = \frac{1}{\Delta y \Delta z} \int_{-\frac{\Delta z}{2}}^{\frac{\Delta z}{2}} \int_{-\frac{\Delta y}{2}}^{\frac{\Delta y}{2}} v(x_{i+\frac{1}{2}-\frac{1}{2}}, y_{j+\frac{1}{2}} + \eta, z_k + \zeta) d\eta d\zeta$$

and approximating the derivatives by central finite differences. Therefore

$$\begin{aligned} v_{i+\frac{1}{2}, j+\frac{1}{2}, k} = \frac{1}{24} & \left( 9v_{i+\frac{1}{2}+\frac{1}{2}, j+\frac{1}{2}, k} + 14v_{i+\frac{1}{2}-\frac{1}{2}, j+\frac{1}{2}, k} \right. \\ & - 3v_{i+\frac{1}{2}-\frac{3}{2}, j+\frac{1}{2}, k} \\ & + v_{i+\frac{1}{2}-\frac{1}{2}, j-\frac{1}{2}, k} + v_{i+\frac{1}{2}-\frac{1}{2}, j+\frac{3}{2}, k} \\ & \left. + v_{i+\frac{1}{2}-\frac{1}{2}, j+\frac{1}{2}, k-1} + v_{i+\frac{1}{2}-\frac{1}{2}, j+\frac{1}{2}, k+1} \right) \end{aligned} \quad (34)$$

For advancing the solution from time  $t^n$  to time  $t^{n+1}$ , where  $t^n = n \Delta t$ , the Poisson equation for pressure

$$\bar{\nabla}^2 p^{n+\frac{1}{2}} = - \frac{\bar{\nabla} \cdot \tilde{q}^{n+1}}{\Delta t} + \bar{\nabla} \cdot \left( \frac{\tilde{q}^n}{\Delta t} - \tilde{q}^{n+\frac{1}{2}} \right) \quad (35)$$



is first solved to determine the pressure distribution that will allow the continuity equation to be satisfied at time  $t^{n+1}$ . In Equation (35)

$$Q^{n+\frac{1}{2}} = \frac{3}{2} Q^n - \frac{1}{2} Q^{n-1}$$

and  $\bar{\nabla}$  indicates the central finite difference approximation of the operator  $\nabla$ . For the continuity equation to be satisfied at time  $t^{n+1}$ , it is necessary to set the first term on the right-hand side of Equation (35) equal to zero. An efficient method for the direct solution of the discrete Poisson equation is used.<sup>25</sup> Following the determination of the pressure field, the Adams-Bashforth scheme is used to calculate the velocity at the new time step. Therefore,

$$\tilde{q}^{n+1} = \tilde{q}^n - \Delta t \left( \tilde{Q}^{n+\frac{1}{2}} + \bar{\nabla} p^{n+\frac{1}{2}} \right). \quad (36)$$

The finite difference scheme used here is second-order accurate in both space and time.

#### 4. RESULTS OF THE SIMULATIONS

The study of impinging jets brings into focus a combination of different types of flows that are interrelated in a very complicated manner. For example, an impinging jet flow field is a combination of free jet flows, vortices in the curved shear layer, stagnation point flow and wall jet flow. During the operation of VTOL aircraft near the ground, this flow field is further complicated by the presence of the fountain due to collision between two wall jets (see Figure 1). Understanding the large-scale motion in such a geometry is essential to determining the characteristics of the flow field associated with VTOL aircraft operating near the ground. The approach taken here involves the simulation of forced impinging jets to study the complex vortex dynamics that occur when the VTOL aircraft is operating in the vicinity of the ground plane.

The basic configuration considered in this study is that of an infinite row of jets. In the following computations, the distance between the axes of neighboring jets is taken to be equal to  $3D$ , where  $D$  is the jet diameter. Two values of  $H$  are considered:  $H = 1.5D$  and  $H = 3D$ , where  $H$  is the distance between the upper and lower horizontal plates. The side boundaries are assumed to be two vertical planes parallel to the plane of jet axes and at a distance of  $3D$  on either side of it. Periodic boundary conditions are assumed in the  $x$ -direction. The periodic boundaries are assumed to be the vertical planes normal to the row of jets and positioned at the mid-distance between two neighboring jets.

Computations were performed in which a single period in the  $x$ -direction includes a single jet and two neighboring jets. Symmetry conditions are applied whenever possible to reduce the cost of computation. The top view of the computational domain for computing two neighboring jets is shown in Figure 3. A fraction of this domain is required for several of the computations that follow. Figure 3 will be referred to below to define the different computational domains used in the calculations.

In the following computations, a basic axisymmetric velocity profile given by

$$w_o = - \left[ 1 - \left( \frac{r}{r_j} \right)^6 \right] w \quad (37)$$

is assumed at the jet exit, where  $r_j$  is the jet exit radius,  $r$  is the radial coordinate, and  $W$  is the axial velocity magnitude at the jet exit. In the following discussion, all velocities are normalized by a reference velocity  $U$ ,  $U = W$ . The velocity components in the  $x$ - and  $y$ -directions are assumed to be zero at the jet exit. The basic steady state solution is perturbed by adding a time-dependent perturbation velocity  $[0, 0, w'(x,y,t)]$  at the jet exit. In the following computations, the jet diameter  $D$  and the jet axial velocity  $W (= U)$  are specified to be 1.0. A Reynolds number of 1000 is assumed, based on the jet diameter and the unperturbed exit velocity at the jet axis. The time step  $\Delta t$  used in the computations is given by  $\Delta t = 0.3 \min(\Delta x, \Delta y, \Delta z)$  where  $\Delta x$ ,  $\Delta y$  and  $\Delta z$  are the uniform mesh spacings in the three coordinate directions. The Cartesian coordinate system is chosen so that  $x_L = y_J = 0$  in Figure 3, while  $z = 0$  is the ground plane.

In all the following computations, a steady-state solution is obtained initially and is used as an initial solution for the simulations in which the jet is disturbed. The initial solution for the steady-state computations was that of a flow at rest. The velocity profile given by Equation (37) was gradually introduced at the jet exit. The velocity was linearly increased in time from zero to the velocity indicated by Equation (37) within 10 time steps. The computation was then continued in time until all initial transients disappear and a steady-state solution is obtained.

To reduce the cost of obtaining the steady-state solutions, they were obtained initially on a coarse computational mesh. This coarse-mesh solution is then interpolated onto the fine mesh and used as an initial solution for the fine mesh computation. These computations assume symmetry conditions in both the  $x$ - and  $y$ -directions. They are therefore obtained on the computational domain bounded by the planes  $x = x_L$ ,  $x = x_F$ ,  $y = y_J$  and  $y = y_2$ , which composes one-eighth of the domain depicted in Figure 3. The solution is then reflected as many times as necessary to obtain the steady-state solution in the computational domain of interest.

The computations were performed on the NASA Ames Cray X-MP/48 computer. So that computer memory capabilities are not exceeded, computational data were buffered in and out of core using the Solid State Storage Device (SSD), which functions as a very high-speed disk with transfer rates of 1000 MB/second.

Since the present computations are incompressible computations, it was necessary to keep the pressure array in core. However, all other large arrays were divided into eight horizontal slabs that were buffered in and out of core.

The present computer code has been optimized for vector operations wherever possible and performs at a computational speed of  $1.45 \times 10^{-5}$  cpu seconds per time step per grid point. The actual computational time for a simulation depends upon the grid used and the total time period of forcing being simulated.

#### 4.1 Steady Impinging Jets

Steady-state solutions for the impinging jets for both a short height case ( $H = 1.5D$ ) and a longer height case ( $H = 3D$ ) were first obtained. For these steady-state calculations, the planes  $x = x_L$ ,  $x = x_F$ , and  $y = y_J$  are assumed to be planes of symmetry. This reduces the computational time required to obtain the steady-state flow field. The computational domains for the short and long height cases were, respectively,  $1.5D \times 3D \times 1.5D$  and  $1.5D \times 3D \times 3D$ . The computational domain is bounded by the planes  $x = x_L$  and  $x = x_F$  in the  $x$ -direction and by the planes  $y = y_J$  and  $y = y_2$  in the  $y$ -direction (see Figure 3). A  $32 \times 64 \times 32$  grid was employed for all the steady-state calculations.

The computations are begun with the fluid in the domain initially at rest. At time zero, a velocity jet profile [Equation (37)] is introduced at the circular jet exit plane on the top wall to simulate the incoming jet. The jet shear layer sheds a vortex ring, often called the starting vortex, that impinges on the ground plane and then propagates along the surface. The propagation of this starting vortex ring was discussed in Rizk and Menon.<sup>26</sup> This vortex ring eventually leaves the computational domain. The flow field reaches a steady-state situation when there are no further changes in the flow field. Figure 4 shows the three-dimensional view of the total vorticity magnitude, defined as  $|\omega| = \sqrt{\omega_1^2}$ ,  $i = 1, 3$ , in a view that shows the jet and the fountain region for the  $H = 1.5D$  case. This figure shows the three-dimensional perspective of the vorticity surface at the level  $|\omega| = 1.75$ , which implies that all vorticity levels higher than this value are enclosed inside this surface. Visualization at a lower vorticity level would show more regions of vorticity but would hide the regions of higher vortical motion that are of major interest. This figure shows the characteristic shear flow at steady state. The vorticity surface in the impinging jet shear layer is

smooth in general, indicating a uniform shear flow that grows as the jet spreads before impacting on the ground. The vorticity in the fountain is also smooth, and the recirculation of the flow due to the impact and spreading of the fountain on the top wall is also visible. There is an indication that this recirculation of the flow causes the fluid to be entrained into the jet, thereby contributing to the spreading of the jet. This is a consequence of the presence of the second jet in the  $x$ -direction. The close proximity of the top wall to the ground causes the fountain's spreading on the top wall to be quite distinct.

Figure 5a shows the steady-state  $v$ -velocity profile in the  $x = 0$  plane, normal to the plane of jets, as a function of  $z$  at various  $y$ -locations. In this figure, and all subsequent figures showing velocity profiles, the abscissa shows the scale for the velocity. The impinging jet and the fountain regions are excluded from this figure due to the rapid changes in the flow direction in those regions. This figure shows the wall jet propagating towards the outflow. The wall jet is strong and narrow in the initial regions where the wall shear layer thickness is small and the impinging jet shear layer is accelerating due to the curvature effects. Further downstream, the wall boundary layer grows and the jet peak velocity decreases as the flow spreads on the ground and weakens. Some regions of reverse flow are seen around  $y = 2.25D$ , indicating that there is some entrainment from the outflow region near the top wall. The  $u$ -velocity profile in the  $y = 0$  plane, which coincides with the plane of the jet axes, is shown in Figure 5b as a function of  $z$  at various  $x$ -locations. The wall jet on the ground grows towards the fountain and then slows down as the collision zone is approached. There is a reverse wall jet on the top wall due to the spreading and recirculation of the fluid in the fountain. This reverse shear flow spreads over the top wall and weakens as the impinging jet region is approached. There is evidence that some of the fluid in the recirculation flow is entrained into the impinging jet, thereby modifying the spreading of the jet.

Figure 6a shows the steady-state pressure in the  $y$ - $z$  plane at  $x = 0$  as a function of  $S$ , where  $S$  is the distance from the jet exit plane (see inset). The pressure rises to its stagnation value at the impingement point (I) on the ground and then decreases towards the outflow (O). Pressure is nearly uniform as the outflow is approached. The slight increase in the pressure towards the outflow is probably related to the slowing down of the vortex ring as it

propagates to the outflow. On the outflow boundary, the pressure is not uniform but shows a slight decrease as the top wall is approached (W). On the top wall, the pressure is uniform. The pressure variation in the  $x$ - $z$  plane at  $y = 0$  as a function of  $S$  (see inset) is shown in Figure 6b. The pressure decreases from the maximum at the impingement point (I) as the fountain is approached and then increases in the wall jet collision zone. The rise in pressure at the fountain axis (F) is lower than the stagnation pressure at the jet impingement point. The peak pressure in the wall jet collision zone occurs slightly above the ground, after which it starts to decrease as the fountain spreads. The pressure then again increases to another local maximum at the location where the fountain impinges on the top wall (W'). This local maximum is about the same as the peak near the wall jet collision.

The growth of the impinging jet is shown in Figure 7a in terms of the jet half velocity width,  $J_{x1/2}/D$ , in the  $x$ - $z$  plane at  $y = 0$  as a function of  $z/D$ . This jet width is calculated based on the location at which the velocity is half the local maximum velocity. The jet width is nearly constant until about  $z = 0.5D$ , where it starts to spread rapidly as the shear layer curves outwards near the impingement region. The growth of the fountain due to wall jet collisions is shown in Figure 7b, which indicates a slow spreading of the fountain as the top wall is approached. This is partly due to the presence of the jet exit plane close to the ground, resulting in a smaller distance for the fountain to have for spreading. The calculated fountain width for  $z < 0.3D$  may not be reliable due to the rapid changes in the flow direction in the wall jet collision zone.

Figure 7c shows the variation of the centerline velocity,  $w_c/U$ , as a function of distance from the jet exit plane to the ground,  $z/D$ . The velocity is scaled by the jet-to-ground distance,  $H/D$ . The jet is nearly uniform until about  $z = 0.5H$ , after which it rapidly slows down as the ground is approached. As it slows, the jet also spreads outwards causing the observed jet spreading.

Steady-state simulations for the  $H = 3D$  case were also performed. Figure 8a shows the three-dimensional perspective of the vorticity surface for the impinging jet flow in this case. The vorticity surface is at the same absolute vorticity level as in Figure 4. Comparison with Figure 4 indicates that increasing the jet-to-ground distance increases the dissipation and diffusion of the vorticity and weakens the shear regions in the flow field.

At the level shown, there is insignificant vorticity on the top wall, unlike the  $H = 1.5D$  case, and the reverse flow on the top wall is also indistinct. Visualization of the vorticity at a lower level would show that there is vorticity in those regions but at a much lower level. Figure 8b shows the view of the outflow for the  $H = 3D$  case. The steady-state vorticity in the shear layer of the jet is smooth, and the shear region in the wall region is also smooth. The fountain is weaker, however, than for the  $H = 1.5D$  case. This would reduce the pressure increase on the top wall, thereby reducing the liftoff effect of the fountain. In general, the flow field is similar to the  $H = 1.5D$  case; however, due to the increase in the jet-to-ground distance, there are only local regions of high vorticity present in the domain.

Figure 9a shows the steady-state velocity vector diagram in the  $y-z$  plane at  $x = 0$ . This figure shows the flow field in the incoming jet and in the outflow direction. There is some indication of entrainment of the fluid near the outflow boundary at the top wall. This is possibly due to the finite extent of the computational domain and the implementation of the outflow boundary conditions. Figure 9b shows the velocity vector field in the  $y-z$  plane at  $x = 1.5D$ , which is the fountain flow region. The characteristic fanlike behavior of the fountain as it spreads up and outwards is clearly visible. This is due to the collision of two wall jets, which results in the fluid rising into the fountain and spreading up and out towards the outflow. Figure 10a shows the velocity vector diagram in the  $x-z$  plane at  $y = 0$ , and Figure 10b shows the corresponding velocity field at the  $x-z$  plane at  $y = 1.5D$ . These views show the impingement of the jet on the ground and the fountain due to wall jet collisions. The formation of a recirculatory region on the top wall is observed in Figure 10b, which shows the  $x-z$  plane halfway to the outflow. This is due to the impact of the fluid in the fountain on the top wall.

The steady-state  $v$ -velocity profiles are shown in Figure 11a as a function of  $z$  in the  $x = 0$  plane. The behavior of the wall jet on the ground towards the outflow is similar to that in the  $H = 1.5D$  case. There are more regions of reverse flow on the top wall due to the entrainment near the outflow, as seen in Figure 9a. Figure 11b shows the corresponding  $u$ -velocity profiles in the  $y = 0$  plane. The wall jet on the ground towards the fountain and the reverse jet flow on the top wall are observed. This reverse jet flow is weaker than in the  $H = 1.5D$  case. It is evident from these figures that the resolution in the

z-direction for the  $H = 3D$  case is very poor, with the wall region resolved within two grid points. The only solution to this lack of resolution is to increase the number of points in the z-direction, which would also increase the computational effort required. However, the coarser resolution simulations did reproduce the large-scale motion reasonably well. For this reason, and also for computational ease, we have restricted ourselves to the coarser mesh in these simulations.

The variation of pressure in the y-z plane at  $x = 0$  is similar to that in the  $H = 1.5D$  case. The variation of pressure in the x-z plane at  $y = 0$  is shown in Figure 12a. The pressure increases to its stagnation value at the jet impingement point and then decreases in the x-direction. As the fountain axis is approached, the pressure rises again due to the collision between the wall jets. The pressure reaches another local maximum at the fountain axis. This pressure peak is lower than the stagnation value at the jet impingement point. The pressure then decreases along the fountain axis but then increases to another local maximum at the location where the fountain impinges on the top wall. However, unlike in the  $H = 1.5D$  case, this local peak is much lower than the peak at the wall jet collision zone. This again shows that increasing the jet-to-ground distance decreases the liftoff capability of the fountain. These results also suggest that, in VTOL-type flow fields, there are three stagnation regions. The impingement point is the primary stagnation point, and secondary stagnation regions occur in the wall jet collision zone and the fountain impingement zone on the top wall.

The variation of the jet half-velocity width as a function of height, as shown in Figure 12b, indicates that the jet starts to spread at around  $0.75D$  from the jet exit plane, which is about the same location for the  $H = 1.5D$  case. This jet spread is much more than in the short height case due to the longer distance the jet has to travel before impinging on the ground. The spread of the fountain is also large and quite rapid above  $z = 1.2D$ , as shown in Figure 12c. The increase in spreading seen below  $z = 0.75D$  is probably not very reliable, since near the wall jet collision zone the flow changes direction rapidly and the width calculations may not be accurate.

These results show the characteristic steady-state flow field obtained due to impinging jets. The general flow patterns observed in these calculations are in agreement with the experimental data. However, in actual VTOL operations near the ground, the exhaust from the engines is usually highly



turbulent and unsteady. This causes the jet shear layer to go unstable due to the growth of the shear layer instability mechanism. The shear layer rolls up into vortices that undergo a pairing/merging process to form large-scale coherent structures. The motion of these large-scale structures is the area of main interest. To simulate the large-scale motion, we have simulated impinging jets that are forced at a specified frequency. To initialize the flow field for the forcing studies, we use the steady-state solution shown above as an initial condition. The results of the forced impinging jet simulations are described in the following sections.

#### 4.2 Axisymmetrically Forced Impinging Jets

The study of turbulent shear flow has undergone considerable changes in the recent past, brought about by the discovery of large, spatially coherent structures in various types of shear flows. These structures have been shown to be an intrinsic part of the shear layer growth and its mixing processes. In experiments by Brown and Roshko<sup>27</sup> and Crow and Champagne,<sup>11</sup> these large-scale structures were observed as spatially coherent and predominantly two-dimensional in the earlier part of the shear layer development. In jet flows, for example, the shear layer instability plays a pivotal role in the transition of the initially laminar shear layer to turbulent flow. The shear layer becomes unstable due to the growth of linear instability waves and rolls up into axisymmetric vortex rings that undergo a pairing/merging process, resulting in a large coherent structure downstream. These structures eventually break down due to three-dimensional effects into small-scale turbulent flow. It has been observed that the formation of these large-scale structures has a predominant preferred frequency called the jet-preferred mode. This preferred mode has been shown to fall in the Strouhal number ( $St = fD/U$ ) range of 0.2 to 0.6 (Gutmark and Ho<sup>28</sup>). This wide variation in the jet-preferred mode has been linked to the differences in experimental facilities and in background turbulence levels. It is generally agreed, however, that this preferred mode is almost independent of the initial shear layer thickness. It was also observed that the motion and growth of these structures are highly sensitive to harmonic forcing. This indicates that a study of forced jets can provide a detailed understanding of the evolution and dynamics of large-scale coherent structures in the flow field.

In this section we present results obtained for the case when the jet is forced axisymmetrically. Both single- and two-frequency forcing were simulated. Essentially, to perturb the incoming jet profile at a specified frequency, a sinusoidal waveform was superimposed on the jet mean velocity profile. Thus, the ring vortices that are generated due to forcing were embedded in the mean flow. The frequency of forcing was chosen to correspond to a Strouhal number based on the jet diameter of around 0.47 for the single-frequency forcing. This Strouhal number falls within the so-called jet-preferred mode range and is used here as a characteristic forcing situation. No attempts were made to vary the forcing frequency. For the two-frequency forcing cases, forcing simultaneously at  $St = 0.235$  and  $St = 0.47$  and at  $St = 0.47$  and  $St = 0.94$  was investigated. The forcing levels were varied from 10 percent to 20 percent of the mean velocity. Although these are relatively high forcing levels, they are similar to the experimental study by Didden and Ho,<sup>10</sup> who used  $0.18U$  forcing levels to study isolated impinging jets. Furthermore, an advantage of using such high levels of excitation is that the imposed disturbance suppresses the natural jet instability and the background small-scale fluctuations so that the response of the jet and the flow field is controlled by the forcing. Thus we can study the development of the coherent vortices in the impinging jet flow field.

All simulations were first computed to steady state as discussed in Section 4.1, and then the disturbance at a prescribed frequency was added to the jet velocity profile at the jet exit plane. The results presented here are after approximately 10 to 12 cycles of forcing so that the flow field has reached a quasi-stationary state. Detailed data were then obtained for one to two cycles of forcing. Although a large amount of data has been obtained, only characteristic results are presented here. To understand the dynamics of the large-scale coherent motion, the main focus has been to look at the detailed vorticity patterns in the flow field. The vorticity contour fields provide a visualization of the motion and structure of the vortex rings that are shed by the jet during a forcing cycle. The three-dimensional vorticity surface plots provide a means for studying the stretching, tearing, and breakdown of the vortex rings in three-dimensional flow fields. Additional information of the flow field has also been obtained in terms of the velocity fields and pressure field in the computational domain. These data are presented wherever appropriate.

The results presented in this section fall into the following two general categories:

- (1) Impinging jets forced in phase
- (2) Impinging jets forced out of phase

For the in-phase forcing studies, a single-jet geometry is modeled. The periodic boundary condition at the fountain axis forces the wall jets to collide at the fountain plane,  $x = x_F$ , in phase. For the out-of-phase forcing simulations, we use a double-jet configuration. The forcing is imposed on both jets independently so that the effect of the phase difference between the forcing of the two jets can be studied and its effect on the fountain spreading can be evaluated.

The effect of forcing on impinging jets at two different heights above the ground was studied. However, both the short height ( $H = 1.5D$ ) and the long height ( $H = 3D$ ) jets studied here are located quite close to the impinging plane. This implies that the simulations performed here are studying the situation when the forced jet is located in close proximity to the ground plane, which is characteristic of the initial stages of takeoff or the final stages of landing of a VTOL aircraft (Kuhn<sup>1</sup>). In actual VTOL operations, in the vicinity of the ground the jet-to-ground distance will vary considerably.

For the single jet, since all the forcing studies presented in this section employ axisymmetric forcing, the planes  $x = x_L$ ,  $x = x_F$ , and  $y = y_J$  are assumed to be planes of symmetry. The computational domain in this case is bounded by the planes  $x = x_L$  and  $x = x_F$  in the  $x$ -direction and by the planes  $y = y_J$  and  $y = y_2$  in the  $y$ -direction (see Figure 3). A grid of  $32 \times 64 \times 32$  is used for these single-jet configurations. For the double-jet configuration for axisymmetric forcing, the planes  $x = x_L$ ,  $x = x_R$ , and  $y = y_J$  are assumed to be planes of symmetry. The computational domain in this case is bounded by the planes  $x = x_L$  and  $x = x_R$  in the  $x$ -direction and by the planes  $y = y_J$  and  $y = y_2$  in the  $y$ -direction. A grid of  $64 \times 64 \times 32$  is used for the double-jet configuration.

#### 4.2.1 In-Phase Forcing

For the in-phase forcing, the velocity perturbation at the jet exit is defined by

$$w'(x,y,t) = -A w_0(r) \sin(2\pi/t_p)$$

where  $r$  is the radial coordinate relative to the jet axis and  $A$  is the amplitude of the forcing, which is varied between 10 and 20 percent of the mean flow. Also,  $w_0(r)$  is the unperturbed mean jet profile defined by Equation (37). Two different heights of the jet exit location with respect to the ground were studied in these simulations. Due to the enormous amount of data obtained, to simplify the presentation of the results we discuss each class of simulation separately. Wherever possible the plots presented for these simulations are shown, for example, using identical contour intervals to allow ease in comparison. We first discuss the results of the simulation of the forced impinging jet for the jet-to-ground distance of  $1.5D$ . The simulation of the case with a jet-to-ground distance of  $3D$  is then discussed.

#### Short Height Case ( $H = 1.5D$ )

Figures 13a through 13c show the  $x$ -vorticity contours in the  $y$ - $z$  plane at the centerline ( $x = 0$ ) plane for a cycle of forcing at a Strouhal number of 0.47. This plane shows the outflow direction, and the figures are shown one half cycle apart. As can be seen, during a forcing cycle, a large vortex ring is shed by the jet. In these calculations,  $D = 1$  and  $U = 1$ , and thus  $f = St = 0.47$ . The phase speed of this shed vortex ring in the jet before impingement, based on the forcing frequency, is approximately  $0.65U$ , which is consistent with experimental observations in both the impinging jet and the free jet. Didden and Ho<sup>10</sup> measured a value of  $0.61U$  for the phase speed of the vortex ring in an isolated impinging jet. The shed vortex is convected downstream towards the ground plane and is stretched as the impingement region is approached. Near the impingement region, the jet shear layer deflects outwards and is under a stabilizing curvature effect. Upon impinging the wall, the vortex ring shape starts to distort as it continues to propagate along the ground wall. Unlike in an isolated impinging jet where the vortex propagation on the ground plane is uniform in all directions, in the present case the presence of the fountain modifies the vortex dynamics considerably. In these calculations, the fountain plane is located at  $1.5D$  and the outflow is located at  $3D$  from the jet centerline (see Figure 3 for the geometry). Thus, the flow field is not the same in these two directions. The ring vortex reaches the fountain region and collides with the other wall jet before it reaches the outflow. Therefore, although the initial propagation on the ground plane is uniform in all directions, due to the fountain effect, the vortex ring starts

to twist by around  $y/D = 1.5$ . As the impingement region is approached, the centerline velocity of the jet goes to zero as the flow approaches the stagnation point. However, this does not seem to affect the propagation speed of the vortex ring in the jet significantly because of the balance between the deceleration due to the plate and the acceleration due to the shear layer curvature. This is again in agreement with the experimental observations. On the wall, the vortex ring propagates towards the outflow at a convective speed that is much slower than the value of  $0.65U$  in the impinging jet. The value obtained in these calculations indicates a phase speed of around  $0.2U$  to  $0.3U$  in the outflow direction. This is slower than the value measured ( $0.45U$ ) for the isolated wall jet flow in the experiments.<sup>10</sup> This slower speed is due to the presence of the fountain, which entrains the vortex ring into it and thereby slows down the convective speed of the ring in the outflow direction.

As the vortex ring propagates along the wall, it induces a secondary vorticity on the ground as can be seen in the figures. This region of secondary vorticity also moves downstream with the primary vortex and evolves into a ring vortex of opposite vorticity. During propagation on the ground, the primary vortex ring diameter increases and the vorticity in the ring increases. However, further downstream the rings start to break down due to three-dimensional effects and they start to lose their coherence. This breakdown was also observed in the experiments and was attributed to possible growth of azimuthal instability. However, the present simulation imposes symmetry on the flow field, so only symmetric instability waves can grow. Thus, it is possible that the observed breakdown may be caused by the excitation of higher axisymmetric modes. The observed breakdown is possibly due to a combination of the effects of the vortex diffusion, the liftoff of the vortex ring into the fountain, and the growth of axisymmetric instability.

The appearance of the secondary vorticity on the ground is observed around  $y/D = 0.6$ . Although the presence of secondary vorticity on the wall boundary layer does not imply separation, separation is always accompanied by secondary vorticity. The appearance of the secondary vorticity is in agreement with the experiments of Didden and Ho,<sup>10</sup> and the general behavior observed in their experiments was also reproduced in these calculations. For example, as the primary vortex ring propagates downstream, the secondary vortex region also moves with it, and the counterrotating vortex rings show an indication of lifting off the ground as the outflow boundary is reached. This can be seen more

clearly in Figure 13d, which shows the wall region in more detail corresponding to Figure 13a, and in Figure 13e, which shows the x-vorticity in the y-z plane at  $x = 0.51D$  which is just outside the impinging jet region. The observed liftoff phenomenon is due to their mutually induced velocity fields. This liftoff of the counterrotating vortex rings was also observed in the experiments. However, the secondary vortex lifting off the ground and wrapping around the primary vortex was not fully observed perhaps due to the proximity of the outflow boundary.

In the direction of the fountain axis, the primary vortices reach the collision axis before the vortex reaches the outflow and starts to climb up the fountain axis. Figures 14a through 14c show the y-vorticity component in the x-z plane at  $y = 0$  for a forcing cycle corresponding to Figure 13. The vortex in the fountain after reaching the top wall continues to move along the upper wall until it reaches the impinging jet region, where a part of it is entrained into the primary jet. This contributes to the spread of the jet by entraining fluid into the jet. The presence of secondary vorticity can be seen on both the top and ground walls in these figures. However, the secondary region on the ground plane is relatively steady compared to the secondary regions observed in the outflow direction. This is due to the collision of the wall jet with an equal and opposite wall jet. Just outside the jet region, the vorticity pattern shown in Figure 14d shows that the structures in the fountain are still coherent, but by  $y/D = 1.5$  (Figure 14e) the fountain has broken down to much weaker structures. Therefore, the fountain maintains its identity only in the region  $y/D < 1.5$ . Hence, the extra lift effect of the fountain probably will come from the increase in pressure in a limited region on the top wall.

In Figures 15a and 15b we present, one-half cycle apart, the z-vorticity contours in the x-y plane just above the ground plane. These z-vorticity contours show the vorticity due to motion in the x-y plane. This is a top view of the vortex pattern on the ground. Figure 15a shows the curved vortex rings on the ground, and comparison with Figures 13 and 14 indicates that the observed counterrotating pairs correspond to the primary-secondary vortex ring pairs. As the fountain axis is approached, the coherency of the z-vorticity is lost. At an x-y plane  $1D$  above the ground, the z-vorticity contours are quite different, as shown in Figures 15c and 15d. The vortex rings are more skewed towards the outflow in this plane, and regions of small-scale structures are observed. The flow field region in the fountain axis is made

of isolated structures each of which corresponds to a vortex ring that has lifted off the ground and become entrained into the fountain. On the top wall, the z-vorticity contours (not shown here) indicate breakdown into small-scale structures.

To visualize the flow field in a more realistic manner, we show in Figure 16a the three-dimensional vorticity field. In this figure we have plotted the total vorticity magnitude as defined before and view it in a direction that shows the outflow region. Both the primary and the secondary vorticity are shown as surfaces of the specified vorticity level, which indicates that all vorticity higher than that shown is inside the surface. To show the liftoff of the vortex rings into the fountain more clearly, we show in Figure 16b the same view as in Figure 16a but at a much higher vorticity level. Only structures containing vorticity higher than the level shown are visible in this figure. The liftoff of the primary vortex ring into the fountain is clearly shown. Although the adjacent counterrotating secondary vortex ring attempts to follow the primary ring up the fountain, it does not completely achieve this and remains attached on the ground. Figure 16c shows the total vorticity surface from a view that shows the fountain region. The liftoff of the primary vortex ring into the fountain and the secondary vortex ring on the ground plane can be seen. Using these three-dimensional vorticity field surfaces, we can now understand Figures 13 and 14 more clearly. It can be immediately seen that the primary vortex ring on the wall moves on the wall in the outflow direction but is lifted off the plate as the ring climbs in the fountain axis. As this happens, the vortex ring is stretched and twisted, and further downstream it breaks down due to three-dimensional effects. The secondary vortex ring generated by the primary vorticity on the wall, however, does not follow the primary ring up the fountain and seems to lose coherence as the primary ring lifts off the ground.

Additional data in terms of the velocity vector and pressure gradient fields were also obtained in these calculations. Figure 17a shows the instantaneous velocity vector field at  $x = 0$  in the  $y$ - $z$  plane corresponding to Figure 13a. The vector field indicates that regions of recirculating flow are associated with each of the vortex rings and that the fluid is being entrained into the wall jet. This has also been observed in the experiments. Figure 17b shows the pressure gradient vector field in the vicinity of the impingement point. In this figure, the vector length indicates the magnitude of the

pressure gradient, and the direction of the vector indicates the region of high pressure. The pressure reaches a maximum at the impingement point. The regions of entrainment and recirculation are shown more clearly in Figure 17c, which shows the velocity vector field near the wall. Figures 17d and 17e show, respectively, the corresponding vorticity contour and pressure gradient fields. Comparison of Figures 17c and 17d indicates that the region of vortical motion is not the same as the region of rotating fluid. This is important because in interpreting the velocity vector field to identify vortices is not correct and would produce erroneous conclusions. In experimental visualization, particle tracing coupled with time-lapse photography is usually employed to obtain the instantaneous pathlines. The velocity vector field can be determined from these data. However, to determine the vorticity, the gradient of the velocity vector field must be calculated from the vector field. It is quite difficult to observe the vortical motion directly in experiments. To visualize vortical motion it is necessary to look at the vorticity contours. The velocity vector field, however, provides an understanding of the flow motion caused by the coherent vortices and shows entrainment of the potential flow region into the wall jet very clearly. Figure 17e indicates that the region of adverse pressure gradient is associated with the formation of secondary vorticity. Therefore, it seems from these calculations that the contention by Didden and Ho,<sup>10</sup> that the formation of secondary vorticity is due to the unsteady separation of the wall boundary layer induced by an adverse pressure gradient, seems justified. The adverse pressure gradient is associated with each of the secondary vortex rings shown in these figures and indicates low-pressure zones in the recirculation regions.

Figure 18a shows the velocity vector field in the  $x$ - $z$  plane at  $y = 0$ , which is the plane at the jet axis. The impinging jet and the fountain regions are visible in these figures. Comparison with Figure 14a, which shows the corresponding vorticity contours, again indicates the inability of the velocity vector field to resolve the vortical motion. The corresponding pressure gradient field is shown in Figure 18b. This figure again shows the relationship between an adverse pressure gradient and the formation of secondary vorticity. Figure 18c shows the velocity vector field in the  $x$ - $z$  plane at  $y = 1.5D$ , which is halfway to the outflow. Figure 14e shows the corresponding vorticity contour field. Comparison again shows the different



types of flow fields observed by viewing the velocity field and the vorticity contour field. The velocity vector field indicates a large region of recirculation caused by the impingement and the spreading of the fountain on the top wall.

Additional data of the flow field were also obtained in terms of the velocity profiles on the ground plane. Detailed velocity field data were obtained. Here we present some characteristic results. Figures 19a and 19b show at  $x = 0$  and  $x = 0.51D$ , respectively, the instantaneous  $v$ -velocity profile between the two walls as a function of  $y$ -locations. The wall jet is quite strong just after impingement but then slows down as the outflow is approached. On the ground plane, a small region of reverse flow is seen throughout the forcing cycle. This implies that the wall boundary layer may have undergone separation at this location. These velocity profiles also show that there are local regions of reverse flow just outside the wall region. This is due to the recirculation and entrainment of the fluid as seen in Figure 17. Figures 19c and 19d show at  $x = 0$  and  $x = 0.51D$ , respectively, the velocity profiles for a period of forcing plotted one-half cycle apart. These profiles are plotted at  $y = 1.5D$ , which is halfway to the outflow. The wall boundary layer thickness does not vary significantly with forcing at this location. Regions of reverse flow on the top wall are observed, which is indicative of entrainment from the outflow region.

Figures 20a and 20b show at  $y = 0$  and  $y = 0.51D$ , respectively, the  $u$ -velocity profiles as a function of  $x$ -locations. The region of the impinging jet and the fountain was excluded from these figures. The wall jet speeds up first and then starts to slow as the fountain is approached. The reverse wall jet on the top wall due to the spread of the fountain is clearly visible. Figures 20c and 20d show at  $y = 0$  and  $y = 0.51D$ , respectively, the  $u$ -velocity profiles for the forcing cycle. These profiles are at  $x = 0.75D$ , which is halfway to the fountain. Forcing causes the wall jet on the ground to accelerate and decelerate, but the wall jet on the top wall is affected only weakly. The flow reverses above the wall jet on the ground as seen in Figure 20c due to recirculation from the fountain. However, towards the outflow, the recirculation effect is weaker and, hence, the reverse flow region is observed only near the top wall.

Figures 21a and 21b show, respectively, the jet width at the  $x = 0$  plane and the  $y = 0$  plane. These figures show the width of the impinging jet viewed

in the outflow and in the fountain directions. There is some ambiguity near the ground plane where the shear layer is highly curved and the jet spreads rapidly. Therefore, the jet width calculated for  $z < 0.2D$  may be meaningless and should be disregarded. In any case, these figures show that the jet grows with the shedding of the vortex ring and shrinks in the region where there are no vortices present. This variation is more observable in the outflow direction than in the direction of the fountain. The jet spreading is limited in the  $x$ - $z$  plane (Figure 21b), which may be due to the effect of recirculation from the spread of the fountain on the top wall as seen in the earlier figures. The recirculation results in the fluid getting entrained into the jet region resulting in a more uniform spread of the jet in this plane. This entrainment may be the reason why the jet spread at the beginning and the end of a forcing cycle does not repeat itself. The pattern of alternating increase and decrease of the jet width with the passage of a large vortex ring is also observed in the fountain as shown in Figure 21c. Again, in this figure, the fountain width near the wall jet collision zone ( $z < 0.2D$ ) is unreliable. The variation of the centerline velocity for a forcing cycle is shown in Figure 21d. The effect of forcing is predominantly strong in a region ( $z > 0.25H$ ) above the ground and is weak near the impingement region. This is due to the wall acting like a filter and damping out the disturbances.

In the above set of figures we have presented in detail the results of the simulation of the forced impinging jet for a jet-to-ground distance of  $1.5D$ . This extensive set of data was shown to indicate the details of the flow field that was obtained. The result of this simulation shows remarkable agreement with the experiments of Didden and Ho and reproduces many of the experimentally observed features. The formation of secondary vortex rings due to the impingement of the primary vortex is observed, along with the downstream propagation of the counterrotating vortex ring pair. The formation of the secondary region on the ground plane seems to be associated with the unsteady separation of the wall boundary layer just downstream of the primary vortex ring. There is evidence that this is caused by the adverse pressure gradient downstream of the core of the primary vortex ring. This result agrees with the experimental observations of Didden and Ho. The convective speed of the vortex ring in the jet is about the same as that observed in the experiments. However, the convective speed in the wall jet is slower than the experimental value, which

is due to the formation of the fountain in these calculations. Due to the collision and the formation of the fountain, the vortex rings do not propagate outwards uniformly in all directions but are skewed and lift off the ground plane as they are entrained into the fountain. This results in the vortex rings being twisted and eventually breaking down into isolated small-scale structures. There is evidence of entrainment into the wall jet caused by the propagation of the vortex rings.

We have presented a detailed data analysis of this simulation to indicate the characteristic flow field dynamics associated with forcing of impinging jets. In the following, we present only characteristic results obtained with two-frequency forcing. In the experiments with free jets, it was observed that the large-scale structure formed at the so-called jet-preferred frequency is usually the end product and does not undergo any further pairing. No experimental data are available for the corresponding impinging jet situation. Therefore, we have studied numerically the effect of forcing at two frequencies that are both in the jet-preferred frequency range. Some characteristic results of these simulations are presented in the following sections. The general conclusions discussed above are still valid for the rest of the simulations.

We performed simulations in which two frequencies of forcing were imposed on the jet profile. For this case we forced the jet simultaneously at Strouhal numbers of 0.47 and 0.94. A forcing level of  $0.1U$  was used for both the frequencies. Figure 22a shows the three-dimensional perspective of the absolute total vorticity at the same level and orientation as in Figure 16a. The jet shear layer does not show any clear indication of the vortical structures, and the primary vortex rings on the ground show two kinds of structures. Merged vortex rings and isolated rings can be seen in this figure. There is an indication of pairing of the vortex rings near the outflow, which is not completed since the rings are lifted off into the fountain. Figure 22b shows the view of the fountain for this forcing case. This figure indicates the liftoff and merging of the primary vortex rings in the fountain. No pairing is observed in the impinging jet itself.

With these three-dimensional views in mind, we now look at the x-vorticity contours in Figures 23a through 23c for a period corresponding to a Strouhal number of 0.47. The figures are half a cycle apart, which in this case is the period of the second forcing frequency. Figure 23a corresponds to the view shown in Figure 22. These figures show that the primary vortices that are

shed are stretched in the jet shear layer but becomes more coherent before impingement. On the ground, complex vortex merging process is observed unlike the single frequency forcing where the shed axisymmetric rings were all isolated. In Figures 23b and 23c we see that the smaller vortex C begins a merging event with vortex D near the outflow, and vortex B is left on its own. From the periodic behavior it is evident that vortex B will probably pair in the next forcing cycle with vortex A, the vortex that is following it. It also appears that the effect of multiple forcing frequencies delays the formation of the secondary vortex rings on the ground and the liftoff of the counterrotational pair is not observed until around  $y = 2.5D$ . The  $y$ -vorticity contours in the  $x$ - $z$  plane at  $y = 0$ , shown in Figure 24, show the vortical motion in the fountain. No major differences are observed between the single- and double-frequency forcing studies in this plane except that a larger vortex ring climbs up the fountain axis for the latter case and the structure entrained into the impinging jet due to recirculation is also larger. This may, of course, cause an increase in the spread of the impinging jet.

#### Long Height Case ( $H = 3D$ )

The above calculations of the forced impinging jet were for the jet location at  $H = 1.5D$ . Similar forcing studies were repeated for the  $H = 3D$  case. For these calculations, the same number of grid points was used in the  $z$ -direction. Therefore, there was a reduction in resolution in the  $z$ -direction for the  $H = 3D$  case. Although it was possible to double the grid points in the  $z$ -direction, this would have increased the computational time considerably. The calculations using 32 grid points provide only a limited resolution of flow in the wall boundary layer but in general resolves the large-scale motion in the flow field.

Figure 25a shows the three-dimensional view of the total vorticity surface at a level  $|\omega| = 1.95$ , which is the same level as in Figure 16a. The forcing at  $St = 0.47$  using a level of  $0.2U$  causes in the shedding of a large coherent vortex ring. This ring impinges on the plate and propagates in a manner similar to the  $H = 1.5D$  case. However, at the level shown, the vorticity is less pronounced and the spacing between the vortex rings on the ground is larger than in the short height case. This is expected because of the larger distance the vortex ring has to travel before impinging on the plate. Upon impingement, these vortex rings propagate on the wall towards the outflow and

are lifted off the ground and carried into the fountain. There is a secondary vorticity region on the ground, but it is not distinct until near the outflow where it rolls into a counterrotating structure and shows an indication of lifting off. Due to the increase in the jet-to-ground distance, the vorticity on the top wall is weaker and does not show up on this figure. This indicates a much weaker effect of the fountain as compared to the short height case. Figure 25b shows the view of the fountain region. The vortex rings in the fountain are much smaller and less coherent than in the short height case.

Figures 26a and 26b show the  $x$ -vorticity contours half a cycle apart for this forcing case. The large vortex shed by the jet is clearly seen, and the contours are plotted at the same interval to correspond to Figures 13 and 14 for the short height case. The vortex ring shed by the jet is much larger than in the short height case. The formation of the secondary vorticity on the ground plane is not observed until around  $y = 1.6D$ . The appearance of secondary vorticity around  $y = 1.6D$  for this case seems to agree with Didden and Ho's observation of a distance of  $r/D = 1.6$ . However, this delay in the appearance of the secondary vorticity could be attributed to a lack in grid resolution in the wall region. As the primary vortex ring climbs up into the fountain, the vortex ring in the outflow region starts to lift off the ground plane, and the secondary region also lifts off. In the fountain axis, the flow pattern is quite similar to the short height case except that the vortex has to climb a longer distance, which causes it to diffuse and lose coherence. Figures 27a through 27c show the  $y$ -vorticity contours in the  $x$ - $z$  plane at  $y = 0$  half a cycle apart. The characteristic pattern described above is clearly observed. The entrainment into the jet due to recirculation on the top wall may be causing the increase in the jet spread more than in the  $H = 1.5D$ . Figures 27d and 27e show the  $y$ -vorticity contours in the  $y = 1.5D$  plane which is just outside the jet region and halfway to the outflow. The fountain again loses its identity beyond  $y = 1.5D$ .

The variation of the  $v$ -velocity in the  $y$ - $z$  plane at  $x = 0$  for the forcing cycle is shown in Figure 28a halfway to the outflow ( $y = 1.5D$ ). No major effect is observed except near the wall jet region. There is reverse flow on the top wall near the outflow possibly due to local entrainment. Figure 28b shows the corresponding  $u$ -velocity variation for the forcing cycle in the  $x$ - $z$  plane halfway to the fountain ( $x = 0.75D$ ). The wall jet regions on the bottom and the top wall are not significantly affected, but the flow in the middle

shows local reverse flow. The sinusoidal variation in the velocity profile is caused by the motion of the vortex ring. Figure 28c shows the variation of the jet width for the forcing cycle indicating the spreading of the jet with the passage of the vortex ring. The forcing effect is more pronounced in the fountain as can be seen in Figure 28d, which shows the variation of fountain width as a function of height above ground.

Simulations with two frequencies at  $St = 0.47$  and  $0.94$  imposed at the jet exit planes similar to the short height case were also carried out. Figure 29 shows the three-dimensional vorticity surface at the same level as in the previous cases. The basic pattern of the primary vortex structures on the ground right after impingement is similar to the short height case. The vortex ring becomes more coherent further downstream and is lifted into the fountain. However, unlike the short height case, the ring structure stays on the ground as it approaches the outflow. The formation of a secondary vortex tube occurs as the primary vortex ring moves downstream. Breakdown of the vortex ring near the outflow and in the fountain axis is also observed. The vorticity surface at a lower vorticity level shows that there are other weaker vortical structures in the flow field that are the remnants of the vortices shed by the jet.

To understand the effect of the second frequency on the vortex dynamics, we repeated the previous case with excitation at frequencies corresponding to Strouhal numbers of  $0.47$  and  $0.235$ . In this case, the second frequency is the subharmonic of the primary forcing frequency. A forcing level of  $0.1U$  is used for both the frequencies. The computations were carried out from identical initial conditions as for the case shown in Figure 29. Figure 30 shows the three-dimensional vorticity field after the same elapsed time as in Figure 29. Comparison of these two figures indicates similar flow features on the ground plane. However, the vortex structure in the impinging jet is not as distinct as in the previous case. This is possibly due to the effect of the subharmonic in the forcing. However, there was again no real indication of any pairing in the jet. This seems to indicate that in impinging jets the presence of two frequencies in the jet-preferred range does not produce any enhancement of the pairing process. Of course, the effect of jet-to-ground distance is an important variable that can possibly cause the observed effect. Simulations at various jet heights will have to be performed to understand the effect of forcing at multiple frequencies in the preferred mode range.

In Figures 31a through 31c we present the  $x$ -vorticity in the  $y$ - $z$  plane at  $x = 0$  for the case shown in Figure 30. The appearance of the secondary structure is delayed until  $y = 1.6D$ , but near the outflow as the primary structure starts to pair and lift off the secondary region again becomes quite distinct and coherent. Pairing is completed between the two structures near the outflow in Figure 31a as shown in Figure 31b. The vortex ring immediately behind these two rings attempts to pair with the previously paired structure near the outflow. However, this process is not completed before the paired structure lifts off and weakens due to diffusion and vortex stretching. The phase speed of the vortex ring in the outflow direction is around  $0.2U$ . This is again slower than the phase speed observed in isolated impinging jets.

Although it is not clearly visible in these figures, a closer view indicates that there are actually two vortex cores in the structure seen at the impinging region in Figure 31c. This can be seen more clearly in Figure 31d, which shows the vorticity at  $x = 0.51D$  which is just outside the jet shear layer. This may indicate that the effect of two-frequency forcing in the impinging jet is to cause a pairing/merging process to occur while impinging on the ground. The pairing observed near the outflow is probably due to higher axisymmetric modes generated in the flow field. Further comparison of Figures 31c and 31d indicates that although the pairing has been completed at  $x = 0$ , it is still incomplete at  $x = 0.5D$ . Figure 32a shows the  $y$ -vorticity in the  $y = 0$  plane showing the fountain region at the end of the cycle. Close examination of the vorticity indicates that there are two vortex cores in the structure impinging on the ground. Figures 32b and 32c show the  $y$ -vorticity in the  $y = 0.5D$  and  $y = 1.5D$  planes, respectively. The vortex pattern in the fountain is still distinct at  $y = 1.5D$  and is more complicated with multiple cores.

To determine whether the forcing level had anything to do with the dynamics of vortex cores in the impinging jet, we repeated the previous calculation with 20 percent forcing levels. Figure 33a shows the three-dimensional vorticity at the same level as in Figures 29 and 30. At this level of forcing, the structure in the impinging jet is more distinct, as is expected. The vortex ring on the ground plane is also more distinct. The vorticity pattern two cycles later in time is shown in Figure 33b. The primary vortex ring in the jet is still the same. There is no vortex ring impinging on the

plate at this instant, and therefore there is a region where there are no vortex rings present. A complicated pairing phenomenon is observed in the outflow region, and there is an indication of breakdown of the vortex rings into isolated vortical tubes. Comparison with the simulation at the lower forcing level indicates that similar vortical structures are present but have lower vorticity in the cores of the structure.

Figure 34a shows the x-vorticity contours in the y-z plane at  $x = 0$  corresponding to Figure 33b. The liftoff of the counterrotating vortex rings is observed around  $y = 2D$ . The appearance of the secondary vorticity region is delayed until the primary vortex core starts to lift off the ground. The pairing/merging between the three vortex rings in Figure 33b is seen in this figure. However, in a y-z plane at  $x = 0.51D$ , the x-vorticity contours shown in Figure 34b indicates that the vortex rings are still independently coherent. This indicates that the pairing between large vortex rings on the ground plane may be more of a local phenomenon than a global one in these impinging jet flows. In these figures, no multiple core in the impinging vortex rings is seen. However, Figure 35a, which shows the y-vorticity contours in the x-z plane at  $y = 0$  corresponding to Figure 34a, indicates the presence of multiple vortex cores in the impinging jet region. The y-vorticity contours in the x-z plane at  $y = 1.5D$  half a cycle apart are shown in Figures 35b and 35c. The merging of different vortex rings is occurring, which results in spreading of the shear flow region in the fountain. This in turn causes the fountain width to increase.

To determine whether the structures observed on the ground maintain their coherence in the spanwise direction during propagation, we looked at the x- and y-vorticity contours in the x-y planes. Figures 36a and 36b show the x-vorticity contours in the x-y plane at  $z = 0.14D$  and  $z = 0.8D$ , respectively. Figures 37a and 37b show the corresponding y-vorticity contours in the same two z-locations. The spanwise coherence of the primary and secondary vortex rings propagating towards the outflow is evident in Figure 36a almost to the fountain axis. Near the outflow, the structures lose their coherence. The lack of coherence of the x-vorticity near the fountain is due to the change of flow direction causing the vorticity to shift to the y-component. Figure 37 shows that the coherence of the y-vorticity in the fountain is distinct more at  $z = 0.8D$  than near the ground.



The effect of forcing on the spread of the jet is shown in Figure 38a. This figure shows that the rapid sinusoidal variation observed in the single-frequency forcing case is absent when two frequencies are imposed on the jet. This figure shows the jet width in the  $y = 0$  plane. The corresponding jet width in the  $x = 0$  plane is shown in Figure 38b. Evidently the jet spread is not the same in the two directions. This is due to the presence of the fountain, which modifies the jet spread in the  $x$ - $z$  plane. The jet width variation actually shows a pinching effect due to the passage of the vortex. Similar effects are observed in the spread of the fountain in the  $x$ - $z$  plane at  $y = 0$  as shown in Figure 38c. Comparison of Figures 38b and 38c, which presents the jet width and the fountain width in the same  $x$ - $z$  plane, shows that there is an in-phase variation near the ground but above it, the fountain shows more oscillatory motion. This is due to the presence of more vortices in the fountain.

It was mentioned in the preceding discussion that the formation of the counterrotating vortex rings is observed in the flow on the ground. It was also shown using the vorticity contour plots that this primary secondary vortex pair rolls downstream and shows signs of lifting off the ground due to the mutually induced velocity field. This liftoff phenomenon is similar to the experimental observation, and it is interesting to see if this fact can be further verified. To do this we need to look at the variation of the  $z$ -component of the velocity as a function of height. Figures 39a and 39b show, respectively, the  $w$ -velocity profile in the  $y$ - $z$  plane at  $x = 0$  and  $x = 0.5D$ . The profiles are plotted from the jet centerline ( $y = 0$ ) to the outflow ( $y = 3D$ ). Figures 39c and 39d show for comparison purposes the corresponding  $v$ -velocity profiles at the same locations. Figures 39a and 39b both show a negative  $w$ -velocity in the jet region. No positive  $w$ -velocity (indicating liftoff from the ground) is seen until around  $y = 2.25D$ , when significant positive  $w$ -velocity is observed. This corresponds to the liftoff observed in the vorticity contour figures. The variation of the  $w$ -velocity in the  $x$ - $z$  plane at  $y = 0$  and  $y = 0.5D$  in the fountain showed no significant lift-off from the ground until the fountain axis is approached. In the fountain there is mostly an upwash, and therefore there was significant positive  $w$ -velocity. It seems from this calculation that the primary-secondary vortex ring pairs do indeed lift off the ground as they propagate to the outflow. This is consistent with the experimental observation.

These calculations indicate that the  $H = 3D$  flow field is different from the  $H = 1.5D$  case in many ways. The vortex rings are much larger and the jet and fountain spreads more than in the short height case. However, the general dynamics of the vortex rings are similar. The liftoff of the vortex ring into the fountain is again observed. However, the vorticity diffuses more for the longer height and, therefore, the vortex structures lose their coherence more rapidly. The appearance of the secondary vorticity region on the wall seems to be delayed until around  $y = 1.6D$ , unlike in the  $H = 1.5D$  case, where the secondary region was observed much earlier. Although this is in agreement with experimental data, the lack of grid resolution in the wall region may be contributing to this observance. Increased resolution in the vertical direction should clarify the validity of the observed features in the wall region.

The effect of forcing at two frequencies in the jet-preferred mode range was also investigated. No significant effects were observed in the impinging jet region. This seems to agree with the free jet studies, which indicates that the coherent structure formed at the jet-preferred frequency is the terminal structure of the shear layer pairing process and does not undergo any further pairing. There are more complicated effects near the outflow as the vortex rings start to show a complex pairing/merging process, possibly due to the excitation of higher axisymmetric modes. The liftoff of the primary secondary vortex pair during propagation to the outflow is also observed in almost all the simulations performed here. This agrees with the experimental visualization of impinging jets.

#### 4.2.2 Out-of-Phase Forcing

To investigate the dynamics of large-scale motion in the fountain formed by the collision of two wall jets, we have simulated two jets impinging on the ground. This is one step further towards the more realistic flow fields associated with VTOL aircraft. In actual flight configurations, the two jets correspond to the exhaust of the engines. There is no reason to assume that the engine exhaust will be in phase. Therefore, the effect of a phase difference between the large vortex rings shed by each jet can possibly effect the spread and stability of the fountain and hence contribute to the liftoff caused by the fountain. In the previous section, we simulated the computational domain of a single impinging jet, which assumed by virtue of the

periodic boundary condition that the jets in an infinite array in the  $x$ -direction are forced in phase. In this section, we discuss the results of the simulations when the two jets are forced out of phase. Periodic boundary conditions are still applied at the boundaries in the  $x$ -direction. Thus, an infinite array of jets in the  $x$ -direction now consists of sets of two jets forced out of phase. Axisymmetric forcing of the two jets is again studied in this section. In this case the flow field is symmetric about the plane  $y = 0$  and, therefore, only half the domain needs to be modeled.

To initialize the flow, the steady-state flow field obtained in the quarter plane is reflected about the plane  $x = x_p$ . This results in a symmetric flow field as a starting solution. To study the effect of phase difference, the two jets are forced independently. The effect of phase difference between the two jets of  $\pi/2$  and  $\pi$  were studied for both of the height cases. The jet exit velocity profiles were perturbed at 10 percent forcing levels at the same frequency corresponding to a Strouhal number of 0.47. No attempts to force the two jets at different frequencies were carried out due to lack of time. However, such simulations could easily be carried out and will be of interest and must be considered to understand the complex vortex dynamics in the fountain. Detailed data of the flow field were obtained as for the single jet simulations. However, we present only characteristic results that show the influence of different phase effects.

For these out-of-phase forcing simulations, the velocity perturbations at the jet exit are defined by

$$\begin{aligned}w_L'(x,y,t) &= -A w_o(r_L) \sin(2\pi t/t_p) \\w_R'(x,y,t) &= -A w_o(r_R) \sin(2\pi t/t_p - \phi)\end{aligned}$$

where  $w_L'$  and  $w_R'$  are the velocity perturbations experienced by the jets located at stations  $x = x_L$  and  $x = x_R$ , respectively. Also,  $r_L$  and  $r_R$  are the radial coordinates relative to the left and right jet axes, respectively, and  $\phi$  is the phase angle difference between the two jets.

Figure 40a and 40b show the three-dimensional vorticity surface at two different levels and views. These figures correspond to the  $H = 1.5D$  case and show the characteristic flow field associated with forced impinging double jets. The large vortex rings that are shed by the forced jets roll along the

ground towards the outflow and are lifted into the fountain region. The large structure observed near the outflow closer to the top wall is again similar to the structure seen in the single-jet case. This structure is seen only in the  $H = 1.5D$  case and may be a consequence of entrainment from the outflow boundary near the top wall. There are secondary vortex rings formed just ahead of the primary vortex rings on the ground. The liftoff of the vortex rings into the fountain can be observed. Although in this simulation the two impinging jets were forced at a phase difference of  $\pi$ , there was no profound effect on the fountain development. The vortex rings from the jets reach the wall jet collision zone at different times, essentially phase lagging/leading each other. The centerline of the fountain is no longer steady due to the asymmetric orientation of the vortex rings in the fountain. Due to the close proximity of the two walls to each other, the effect of varying the phase of one jet with respect to the other did not result in any major changes as compared to the in-phase forcing studies shown in the previous section. The effects were more pronounced for the  $H = 3D$  case, and therefore we concentrate on the results obtained for that height case.

Figure 41a shows the three-dimensional perspective of the vorticity surface at the same level as in Figure 40a but for the  $H = 3D$  case. This view shows the outflow direction and the characteristic pattern due to the propagation of the vortex rings on the ground and the liftoff of the vortex rings into the fountain. The breakdown of the vortex rings due to liftoff can also be seen. In the outflow direction, no major changes were observed. Due to the forcing of the jets at a phase difference of  $\pi$ , the vortex rings from each jet on the ground plane are offset from each other. Figure 41b shows the view of the fountain for this simulation. The offset of the vortex rings in the fountain from the two jets is clearly apparent. The offset is almost half the distance between the vortex rings in the fountain. This in effect results in the vortex rings from each jet to mesh together in a uniform manner. When the vortex rings are in phase, they form discrete pairs, as was observed in the in-phase forcing study described in the previous section. The perspective view of the flow field at lower vorticity levels did show the characteristic recirculation of the fluid in the fountain due to impact on the top wall. The level of  $|\omega| = 1.95$  used in these three-dimensional simulations provided an optimum view of the regions of strong coherent vorticity and is the same level used to visualize the impinging jets forced in phase. Therefore, these figures can also be directly compared with Figure 25.

Figures 42a and 42b show, respectively, the x-vorticity contours in the y-z plane at  $x = 0$  and  $x = 3D$ . These two figures are at the same time and correspond to the centerline view of the two jets showing the outflow direction. The effect of a different phase of forcing results in the two jets shedding vortex rings at half a wavelength apart. The phase speed in the impinging jets is unaffected by the phase difference. Figure 42a shows a large vortex ring impinging on the ground in the left jet, whereas the vortex ring in the right jet is still approaching the ground. The propagation of the primary vortex rings in both jets in the outflow direction is basically similar, and the appearance of the secondary vorticity is observed at nearly the same location. The liftoff of the primary and secondary vortex rings is observed near the outflow. The speed of propagation of the vortices in both the wall jets is around  $0.2U$ .

Figures 43a through 43c show, respectively, at  $y = 0$ ,  $0.51D$  and  $1.5D$  the y-vorticity contours in the x-z plane at the same time as in Figures 40 through 42. These views show the vorticity in the fountain regions looking in the outflow direction. In Figure 43a, which shows the centerline ( $y = 0$ ) plane, the impingement of the vortex rings on each other at the wall jet collision zone is seen. Due to the phase difference, the vortex rings do not reach the collision zone at the same time. For a phase difference of  $\pi$ , the vortex ring from the left jet is already entrained into the fountain before the vortex ring from the right jet is lifted off into the fountain. The phase difference causes the core of the vortex rings from the two jets to be offset by exactly half a wavelength. The vorticity thickness of the fountain is then more uniform than for the case when the jets are in phase, in which case the vorticity thickness grows and shrinks with the passage of two in-phase vortex rings. As the vortex rings climb up into the fountain, they are also stretched, thereby decreasing the strength and size of their cores. However, they are still distinct in this plane when impinging on the top wall. The reverse flow and the entrainment of the wall jet on the top wall into the impinging jet is also apparent. There is some evidence of the increase in the jet shear layer due to this entrainment. The structures seen in the center plane weaken by  $y = 0.5D$ , as shown in Figure 43b. The effect of a phase difference is more apparent in Figures 43b and 43c, which are just outside the impinging jet region and halfway to the outflow. The spread of the fountain

seems to be increased as compared to the in-phase forcing result. The time sequence of the vorticity for a forcing cycle shows that the fountain is flapping near the top wall at a region around  $y = 1.5D$ . This is due to the the arrival of vortex rings near the top wall from the jets half a wavelength apart. This causes the upwash of the fountain to bend whenever a vortex ring reaches the top wall. There is an indication of a complicated merging process occurring near the top wall. The observed motion of the fountain on the top wall indicates that the out-of-phase forcing can modify the spread of the upwash and, hence, significantly affect its liftoff qualities.

To understand the effect of a phase differences on the collision of wall jets, we show in Figure 44 a sequence of  $y$ -vorticity contours in the  $x$ - $z$  plane showing the region of collision in more detail. These figure are at quarter cycle apart and are plotted using the same contour intervals. The solid and dotted lines indicate direction of rotation out and into the paper, respectively. Thus, the primary vortex rings in the left jet are negative, and the primary rings in the right jet are positive. Figure 44a shows the collision region corresponding to Figures 42 and 43. The vortex ring in the left jet is already entrained into the fountain, while the ring in the right jet is still being lifted off. As the primary vortex ring is lifted off into the fountain, the secondary vorticity associated with that ring dissolves. This secondary vorticity is due to the formation of the wall boundary layer as the primary vortex rings propagate above the wall. Near the collision zone, there is a saddle point behavior that is quite complicated. It appears that the secondary region associated with the right jet is entrained into the left jet shear zone as can be observed in Figures 44a and 44b. This sequence is reversed in the next two figures due to entrainment of the secondary region of the left jet into the right jet. This is due to the phase shift between the two vortex rings arriving at the collision zone. This behavior is quite different from the in-phase forcing studies, which showed a symmetric and nearly steady secondary region near the collision zone. The observed entrainment may modify the strength of the vortex rings in the fountain. Further analysis indicated that this entrainment weakens as the outflow is reached due to the breakdown of the primary rings.

Figure 45 shows the  $z$ -vorticity contours in the  $x$ - $y$  plane as a function of height. Near the ground ( $z = 0.14D$ , Figure 45a), the vortex rings form the

curved counterrotating pattern similar to the in-phase single jet case. In these figures, the impinging jet is located in the lower left- and right-hand corners of the figures but at  $z = 3D$ . At a distance of  $0.8D$  above the ground (Figure 45b), the structure shows the characteristic offset between the left and the right jet in the fountain in the middle of the figure. The spread of the fountain and the formation of small-scale eddies is more apparent in Figure 45c at a distance  $1.45D$  from the ground. On the top wall there is no significant motion in the  $x$ - $y$  plane, and there is also a loss in symmetry about the fountain axis.

A simulation of the two jets forced at a phase difference of  $\pi/2$  was also performed under otherwise identical initial conditions. There were some differences between the two phase difference cases. A forcing at the same Strouhal number and the same level of  $0.1U$  was performed. Figure 46a shows the three-dimensional perspective of the view of the fountain region at the same elapsed time as in Figure 44. For this visualization, we used a higher vorticity level to show the vortex rings lifting into the fountain. The vortex rings from the two wall jets are not offset as for the  $\pi$  phase forcing study. There is some indication of merging in the fountain. The liftoff of the primary vortex rings into the fountain can be seen clearly in Figure 46b, which shows the three-dimensional perspective of  $\omega_\theta$ . During axisymmetric forcing, the dominant vorticity in the jet is in the theta component. Therefore, this figure clearly shows the characteristic axisymmetric puffs shed by the jet due to forcing. The vortex rings stretch and the core sizes decrease during propagation. Eventually, these structures break down into small-scale structures.

Figures 47a and 47b show the  $y$ -vorticity contours in the  $x$ - $z$  plane at  $y = 0$  and  $y = 0.5D$ , respectively. These figures are at the same time as the results shown for the  $\pi$ -phase forcing. In these figures, there is an indication of some type of merging process occurring in the shear layer in the fountain. For example, in Figure 47a the right fountain shows a merged structure at around  $1D$  above ground, whereas the left fountain shows a merged structure at around  $z = 2D$ . Due to the phase difference of  $\pi/2$ , the vortices in the two wall jets arrive at the fountain a short time apart. This offset may cause the vortex in one side of the fountain to slow the corresponding vortex in the other side, thereby allowing it to merge with the ring following it. The merging is still obvious in the plane  $y = 0.5D$  shown

in Figure 47b. Figures 47c through 47e show the y-vorticity in the x-z plane at  $y = 1.5D$  for three different times of the forcing. The complex patterns discussed above are again seen. Both merging and splitting of the vortex structures near the top wall is seen in this sequence. The tendency of the fountain to undergo a slow flapping can be discerned in these figures.

The spanwise coherency of the vortex rings on the ground plane can be seen in Figure 48a, which shows the x-vorticity contours in the x-y plane. These structures lose their coherence near the fountain axis where the flow changes direction. The secondary vortex ring ahead of the primary ring near the outflow is also visible. The coherency of the y-vorticity is dominant in the fountain region as shown in Figure 48b, which presents the x-y plane view at  $z = 0.8D$ .

To understand the dynamics of the fountain further, a simulation was carried out with only one jet forced. In this case, the left jet at  $x = 0$  was forced at a Strouhal number of 0.47 and a  $0.2U$  forcing level, whereas the right jet was maintained at steady-state flow conditions. Figure 49a shows the three-dimensional perspective view of the fountain region for this simulation. The characteristic shedding of the vortex rings by the left jet is clearly visible, and the steady flow in the right jet is also shown. However, the flow in the fountain is quite different. There is an indication of structures forming in the right jet as it climbs up the fountain. Breakdown of the rings in the fountain occurs much earlier than in the previous simulations. Figure 49b shows another perspective view of this simulation showing the forced jet region. No vortex rings on the ground for the steady jet are visible. The breakdown of the vortex rings in the fountain is again visible in this figure.

Figures 50a through 50c show at  $y = 0$ ,  $0.5D$  and  $1.5D$ , respectively, the y-vorticity contours in the x-z plane. It is clear from these figures that the forced jet sheds vortex rings whereas the unforced jet shear layer shows the steady flow features. The vortex rings from the forced jet propagate along the wall towards the fountain axis, where they collide with the steady wall jet from the right impinging unforced jet. The periodic appearance of the vortex ring in the fountain from the left wall jet perturbs the right wall jet at the collision zone. This causes the right part of the fountain to also start breaking down into discrete vortices that are generally in phase with the vortices in the forced part of the fountain. The structures shed at the collision zone are as strong as the vortex rings that initiate the shedding.



However, the fountain does not climb up to the top wall smoothly but indicates a significant flapping motion. This is also quite obvious in the planes  $y = 0$  (Figure 50b) and  $y = 1.5D$  (Figure 50c).

The interaction between the two wall jets in the collision zone is similar to that discussed for the  $\pi$ -phase simulation. This can be seen in Figures 51a and 51b, which show the collision zone in more detail. As a vortex ring reaches the collision zone from the left, it seems to perturb the right jet to generate a weak structure. As the vortex ring in the left part of the fountain rises into the upwash, it induces the same motion to the structure generated in the right part of the fountain. Due to the lack of coherence in the right fountain, the fountain first bends to the left; but further into the upwash, the fountain bends back due to the growth of the structure in the right fountain. There is again evidence in these figures of the merging of the secondary vorticity of one wall jet into the fountain caused by the other wall jet.

The coherency of the vortex rings in the spanwise direction above the ground plane is quite distinct. Figure 52a shows the x-vorticity contours in the x-y plane at  $z = 0.14D$  for the case of one jet forced at a Strouhal number of 0.47. Figures 52b and 52c show, respectively, the y- and z-vorticity in the same z plane. The vortex rings in the left jet are quite coherent, whereas the x-vorticity in the right jet is spread out as in the situation for steady flow. The y-vorticity contours show coherency in the fountain region and also show that a region of coherent y-vorticity in the right jet is created due to the forcing effect of the left jet. The z-vorticity contours show only local regions of rotation.

The effect of forcing on the flow field can also be visualized in terms of the velocity vector field to show the large-scale recirculation motion. Figures 53a and 53b compare the velocity vector field for the cases with the jets forced at a  $\pi/2$  phase and a single forced jet. The bending of the fountain when only one jet is forced is evident in Figure 53b. Comparison also indicates no significant differences near the wall jet collision zone. Since we have already seen quite a complicated motion of the vortical rings in the collision zone, it is again clear that the velocity vector field cannot show the regions of vortical motion. The spread of the fountain is quite dramatic in Figures 53c and 53d, which show the velocity vector field in the x-z plane at  $y = 1.5D$ . The  $\pi/2$ -phase forced jets case (Figure 53c) shows a much more complicated pattern of recirculation than the single forced jet case (Figure 53d).

### 4.3 Azimuthally Forced Impinging Jets

In the previous section we discussed the effect of forcing the jets axisymmetrically. Both in-phase and out-of-phase forcing of the jets were studied in detail, and the characteristic shedding of the axisymmetric vortex rings was simulated. For those simulations, we assumed symmetry wherever possible to reduce the computational effort. By this assumption, the generation and growth of nonaxisymmetric modes of disturbances were excluded. However, this is not possible in reality. In fact, experiments indicate that the axisymmetric rings shed by the jet propagate along the ground and eventually break down possibly due to the growth of azimuthal disturbances. The simulations discussed in the previous sections did not allow the growth of azimuthal disturbances by virtue of the symmetry condition. However, the growth of azimuthal instabilities is of great interest in the case of impinging jets because so little of the vortex dynamics is understood. Therefore, in the present section we present the results of studies of the case where the jets are forced in the azimuthal direction. For these simulations, no symmetry in the computational domain is assumed, and thus the whole domain is computed. Unfortunately, this causes a fourfold increase in the computational effort as compared to the axisymmetric forcing discussed in Section 4.2. Therefore, only characteristic forcing studies have been carried out.

Two different configurations consistent with the axisymmetric forcing studies have been simulated. The first configuration assumes that the jets in the infinite array in the  $x$ -direction are all forced in-phase in the same azimuthal direction. The second configuration assumes that every other jet in the infinite array is forced in the opposite azimuthal direction. For the former case, only a single impinging jet needs to be modeled by virtue of the periodic boundary condition at the fountain plane. For the latter case, two jets have to be numerically modeled.

#### 4.3.1 In-Phase Forcing

In these azimuthal simulations, the computational domain for a single jet simulation was a  $64 \times 128 \times 32$  computational mesh. The computational domain is bounded by the planes  $x = x_1$  and  $x = x_F$  in the  $x$ -direction and by the planes  $y = y_1$  and  $y = y_2$  in the  $y$ -direction (see Figure 3). To be consistent with the previous axisymmetric forcing studies, we investigated azimuthal forcing at the same Strouhal number of 0.47. A forcing level of  $0.1U$  was used, and both

the  $H = 1.5D$  and  $H = 3D$  cases were simulated. The azimuthal forcing function is defined as

$$w'(x, y, t) = -A w_0(r) \sin \psi$$

where  $A = 0.1$  and  $\psi = (2\pi/t_p + \theta)$ . Here,  $(r, \theta)$  are the polar coordinates relative to the jet axis. The forcing function defined above causes the perturbation velocity distribution at the jet exit to rotate at the characteristic frequency of forcing. Although simulations with axisymmetric forcing would be necessary to study the possible growth of azimuthal instabilities on axisymmetric vortex rings, such simulations have not yet been performed. Here, we shall concentrate on the effect of pure azimuthal forcing on the dynamics of impinging jets. Although azimuthal forcing studies of both of the jet-to-ground distance cases have been performed, in this section we discuss only characteristic solutions that show the effects of such forcing very clearly.

Figure 54a shows the three-dimensional perspective of the total vorticity surface for the  $H = 1.5D$  case. Here, the jet is forced at  $St = 0.47$  in the azimuthal direction. The jet is seen in the middle of the figure, and some structures can be seen in the fountain plane. The azimuthal forcing causes the velocity perturbation at the jet exit to spin in the clockwise direction. This causes the impinging jet shear layer to shed in a helical structure. This helical shear layer impinges on the ground and propagates to the outflow and the fountain. The lifting of the helical vortex tube into the fountain is seen in this figure. To visualize the helical nature of the jet shear layer, we show in Figure 54b the three-dimensional perspective of the  $\omega_\theta$  for this simulation. The helical vortex sheet impinging on the ground can be seen, and the spiral vortex structure formed on the ground is also seen.

In general, the effect of this azimuthal forcing is not very evident for the  $H = 1.5D$  case due to the close proximity of the two wall planes. The jet shear layer does not complete more than one helical turn before impinging on the ground. This causes the vortex structure on the ground to be more diffused. Due to azimuthal forcing, there is no symmetry in the flow field. This is evident in Figure 55, which shows the  $y$ -vorticity in the  $x$ - $z$  plane at various  $y$ -locations. Figure 55a shows the  $y$ -vorticity in the  $y = 0$  plane. In this centerline plane we observe no vortex ring shedding from the jet as was observed in the symmetric forcing case. Vortical structures are observed in the wall jet and the fountain. These structures are associated with the helical vortex tubes shed from the jet. Due to the helical nature of the

vortex tube as it impinges on the ground, the vortex imprint is a spiral, and, therefore, the vortex structure is not symmetric. The fountains at  $x = -1.5D$  and  $x = 1.5D$  are not the same at any given instant. The recirculation of the vortex into the jet is visible in this figure. The y-vorticity contours in the x-z plane at  $y = 0.51D$  and  $y = -0.51D$  are shown in Figures 55b and 55c, respectively. These views are just outside the jet shear layer. The asymmetry of the vortex pattern is again evident. Figure 55d shows the y-vorticity contours in the x-z plane at  $y = -1.5D$ . The merging of the structures is visible in this figure.

Although a large amount of data was collected for the  $H = 1.5D$  case, the effect of the proximity of the ground plane to the jet exit plane caused the details to be smeared. The  $H = 3D$  case showed the structures more clearly, so we will concentrate on that simulation. Figure 56a shows the three-dimensional vorticity surface for the helical forcing of the jet at  $H = 3D$ . The forcing was again at  $St = 0.47$  and at a forcing level of  $0.1U$ . This figure clearly shows the helical shape of the impinging jet shear layer as it propagates towards the ground. The lifting of the helical vortex into the fountain is again evident. To visualize the spiral nature of the structure on the ground plane, we show in Figure 56b the three-dimensional perspective of the  $\omega_\theta$  at a level of  $3.0$ . This view shows the spiral shape of the vortex tube and indicates how the vortex tube rises into the fountain.

The helical nature of the jet shear layer can be seen in Figure 57, which shows the time sequence of the x-vorticity in the y-z plane at  $x = 0$  for forcing at  $St = 0.47$ . The jet shear layer shows the undulation due to rotation. No vortex rings as in the axisymmetric forcing case were observed. The jet shear layer impinges on the ground and spreads to the outflow. No significant coherent structure is seen near the impingement point in this y-z plane. However, further downstream the vortex tubes can be seen. The size of these tubes is not similar to the axisymmetric case. Since all the figures shown in this report are plotted in the physical domain, the full mesh simulation results are shown smaller. This is due to the  $6D \times 3D$  dimension in the y-z plane for the azimuthal forcing study as compared to the  $3D \times 3D$  domain for the axisymmetric studies. Regions of secondary vorticity are also observed in the outflow direction forming just ahead of the primary structures, as was seen in the axisymmetric cases. Both the primary and the associated secondary regions show an indication of lifting off as the outflow is approached. This

is again similar to the observations for the symmetric forcing case. The  $x$ -vorticity contours in the  $x = -0.51D$  and  $x = 0.51D$  planes are shown in Figures 58a and 58b. These figures show the characteristic asymmetry of the flow field in the planes just outside the jet shear flow region.

The time sequence of the  $y$ -vorticity contours in the  $x$ - $z$  plane at  $y = 0$  is shown in Figure 59. The physical domain in the  $x$ - $z$  plane is  $3D \times 3D$ . The shedding of the helical vortex tube is observed in this sequence. The structures in the two parts of the jet shear layer show the characteristic tilt of the vorticity in the shear layer. The structures seen in these figures are not independent but related to each other since the shear layer is a continuously twisting helical structure. The lifting of the vortex tube into the fountain is observed around the  $x = 0$  and  $x = 3D$  boundaries. The pattern is not symmetric and shows some evidence of merging of the vortices.

Figure 60 shows the time sequence of the  $y$ -vorticity contours in the  $x$ - $z$  plane at  $y = -1.5D$ , and Figure 61 shows the corresponding time sequence in the  $x$ - $z$  plane at  $y = 1.5D$ . The two planes are halfway to the outflow, and the flapping type of behavior of the fountain shown. Complicated structures are observed, and also a definite indication of the merging process. This is possible because the vortices in the fountain slow down as they climb into the upwash and can therefore pair with the structures following them. Comparison of the sequences in these two figures also shows the asymmetry of the flow field in the fountain.

Figure 62 shows the time sequence of the  $y$ -vorticity in the  $x$ - $z$  plane at  $y = -0.51D$ , and Figure 63 shows the time sequence of the  $y$ -vorticity contours in the  $x$ - $z$  plane at  $y = 0.51D$ . These two planes are just outside the jet shear flow region, so the jet shear region is missing. These sequences show the bending of the fountain with the arrival of vortex structures. These figures also show the characteristic asymmetry of the fountain. As the vortex rings climb into the fountain, they start to pair and increase its size. There is even an indication of multiple merging occurring in the fountain. Comparison with figures for the corresponding axisymmetric forcing studies also shows the difference due to azimuthal forcing.

The variation of the centerline velocity as a function of  $z$  is shown in Figure 64 for the forcing cycle at  $St = 0.47$ . Unlike the case with axisymmetric forcing, no sinusoidal variation is observed. The centerline velocity of the jet begins to decrease from the value in the jet exit plane but then

increases in the region of  $z = 0.75H$ . The velocity then rapidly decays as the impingement point on the ground is reached.

Figure 65a shows the velocity vector field in the  $y$ - $z$  plane at  $x = 0$ . The impinging jet region shown in this figure corresponds to the  $x$ -vorticity contours shown in Figure 57a. The velocity vector field in the  $y$ - $z$  plane at  $x = 1.5D$  is shown in Figure 65b. This view shows the characteristic fanlike behavior of the fountain as it spreads up in the fountain axis. There is an asymmetry in the flow field due to the helical forcing.

Figure 66a shows the velocity vector field in the  $x$ - $z$  plane at  $y = 0$  for the same time shown in Figure 65. The corresponding  $y$ -vorticity contours in this plane are shown in Figure 59a. The impinging jet and the fountain regions are shown in this figure. Due to the entrainment observed in this plane the jet appears to spread more as compared to the axisymmetric case. Figure 66b shows the velocity vector field in the  $x$ - $z$  plane at  $y = 1.5D$ , which is halfway to the outflow. Figure 61a shows the corresponding  $y$ -vorticity contours in this plane. The characteristic large-scale recirculation associated with the vortex motion is also seen.

Although a secondary vorticity region was observed on the ground just ahead of the primary vortex spiral, it is not as distinct as in the axisymmetric case. To determine if the wall boundary layer is undergoing any unsteady separation, we show in Figure 67a the pressure gradient vector field in the  $x$ - $z$  plane at  $y = 0$ . This view corresponds to the view shown in Figure 66a. The secondary region is nearly steady in this case, and the pressure gradient field shows a region of change in the gradient direction around  $x = \pm 0.75D$ . The rise in pressure at the impingement point and the wall jet collision regions is also observed in this figure. Figure 67b shows the pressure gradient vector field in the  $y$ - $z$  plane at  $x = 0$  corresponding to Figure 67a. This view shows the region  $z < 0.5H$  and shows the outflow direction. The rise in pressure at the impingement point is seen in the middle of the figure. There are regions of change in the pressure gradient direction indicating the possibility of separation of the wall shear layer. Figure 67c shows the pressure gradient in the region close to the ground. The change in the pressure gradient direction is clearly observable in this figure.

Figure 68 shows the velocity contours in the  $x$ - $y$  plane at various  $z$ -locations for this simulation. These figures show the velocity contour in the jet region quite clearly. In the  $z = 0.75D$  plane, the spread of the jet

as it approaches the ground is observed. The negative contours indicate flow into the paper, and the positive contours in the fountain axis show spread of the fountain. In the  $z = 1.5D$  plane, the jet is more circular, and the asymmetric spreading of the fountain due to helical forcing is also seen. The  $z = 2.25D$  and the  $z = 2.98D$  planes show the velocity contours in the jet region as mostly circular. The upwash of the fountain is much weaker in these two planes. A closer observation of the contours in this figure shows that the peak in the jet is not in the same plane but is offset in each figure. This is indicative of the helical nature of the forcing, which causes the jet to spin and the jet core to become offset from the center.

#### 4.3.2 Out-of-Phase Forcing

In these simulations the computational domain includes two jets. This allows simulating flows in which neighboring jets are forced independently. A  $64 \times 64 \times 32$  computational mesh is used. The computational domain extends six jet diameters in each of the  $x$  and  $y$  directions, and three jet diameters in the  $z$  direction. A plan view of the domain is depicted in Figure 3. The forced solutions are computed from an initial steady state solution. The results presented here are obtained at the end of twelve cycles of forcing at a frequency corresponding to a Strouhal number of 0.47.

Computations for jets subjected to azimuthal forcing are performed for various forcing configurations. In these computations, the jet located at the station  $x = x_L$  (see Figure 3) experiences a perturbation velocity given by

$$w_L'(x, y, t) = -A w_o(r_L) \sin \psi_L$$

where

$$A = 0.2$$

$$\psi_L = \frac{2\pi t}{\tau_p} + \theta_L$$

and  $(r_L, \theta_L)$  are the polar coordinates relative to the jet axis. The jet located at the station  $x = x_R$  (see Figure 3) experiences a perturbation velocity given by

$$w_R'(x, y, t) = -A w_o(r_R) \sin \psi_R \quad (38)$$

where

$$\psi_R = \frac{2\pi}{t_p} - \phi \pm \theta_R \quad (39)$$

and  $(r_R, \theta_R)$  are the polar coordinates relative to the jet axis while  $\phi$  is the phase angle shift between the two jets. The sign of  $\theta_R$  is taken to be positive for the case of clockwise (CW) forcing and is taken to be negative for the case of counterclockwise (CCW) forcing. Figure 69 is a top view indicating different configurations for the azimuthal disturbances applied at the jet exits of the two neighboring jets centered at the positions  $x = x_L$  and  $x = x_R$ . Each number in this figure indicates a specific disturbance velocity, or a specific  $\psi$  value. In addition to the set of solutions obtained by imposing azimuthal forcing at the jet exits, two solutions have been obtained as reference solutions. They are an unperturbed flow solution and a solution obtained by imposing axisymmetric forcing at the jet exits.

The fountain created by the two neighboring jets is located close to the plane  $x = x_F$  (see Figure 3) in the middle of the computational domain. This fountain will be referred to as the central fountain. A second fountain is generated at the periodic boundaries ( $x = x_1, x = x_2$ ) of the computational domain. This fountain will be referred to as the side fountain. In general, these two fountains will not have the same properties since the disturbances experienced by the two neighboring jets to each of them are not the same. The vortical structures in the undisturbed jets are shown in Figure 70 where the surfaces shown have a vorticity level  $|\omega|$  of 2.1. The vorticity levels in the volumes enclosed within these surfaces are greater (higher magnitude) than that of the surface. The figure shows the vortical cylinders composed of the jet shear layers. In the case of a single impinging jet, the vortical cylinder expands on the ground plane into a circular disc. However, in the present case of a row of impinging jets, the circular discs expand until they collide. Then they expand upwards as vortical sheets in the fountain. The vortical structures at the top plane above the fountains are due to the impingement of the fountain on the upper plane.

The effects of perturbing the jet exit conditions are investigated below. Imposing axisymmetric velocity perturbations at the jet exits given by



$$w'_L(x, y, t) = -A w_0(r_L) \sin \frac{2\pi t}{t_p}$$

$$w'_R(x, y, t) = -A w_0(r_R) \sin \frac{2\pi t}{t_p}$$

results in vorticity rings, propagating from each of the jet exits, which alternate in the sign of the azimuthal vorticity  $\omega_\theta$  associated with them. As the vortical rings impinge on the ground plane, they propagate outwardly away from the jet axis which leads to an increased radius and a reduced strength. In the fountain region, the rings expand upward. Figure 71a shows the vortical rings with azimuthal vorticity levels of -3.1 at their surface. The vorticity levels in the volumes enclosed within the surfaces shown are lower (higher magnitude) than that at the surface. This vorticity level is chosen here to be relatively low to suppress the main unperturbed vortical structures. The vortical rings shown in the figure coincide with the cores of the vortical rings which have negative azimuthal vorticity. Vortical rings which have positive azimuthal vorticity are not shown. Vorticity rings in the ground plane with large radii and those in the fountain are not apparent in the figure since vorticity levels in these rings are higher than the value specified here.

Imposing azimuthal velocity perturbations at the jet exits given by Equations (38) and (39) with  $\phi = 0$ , corresponding to a clockwise-clockwise disturbance and a zero phase shift, results in two helical vorticity tubes propagating from each of the jet exits to the ground plane. The azimuthal vorticity in one of these helical vortical tubes is positive while it is negative in the other one. As the helical tubes impinge on the ground plane, they propagate away from the jet axis. In the fountain region, the tubes expand upward. Figure 71b shows the helical vortical tubes with azimuthal vorticity levels of -3.1 at their surface. The vortical tubes shown in the figure coincide with the cores of the vortical tubes which have negative azimuthal vorticity only. The corresponding vortical tubes for imposed azimuthal velocity perturbations at the jet exits given by Equations (38) and (39) with  $\phi = 0$ , corresponding to a clockwise-counterclockwise disturbance and a zero phase shift, are shown in Figure 71c.

Figure 72 presents y-vorticity contours in the plane of the jets ( $y = y_j = 0$ ) for the undisturbed jets, the axisymmetrically forced jets and the six

azimuthally forced jet configurations indicated in Figure 69. The dashed lines indicate negative vorticity levels, while the solid lines indicate positive vorticity levels. For the two azimuthally forced cases in which  $\phi = 0$ , the forcings applied in the plane  $y = 0$  at the two jet exits are identical. Figures 72c and 72d indicate that the disturbances remain identical within the jets in this plane. For the two cases in which  $\phi = \pi/2$  the forcing applied at the exit of the right jet lags that applied at the jet exit of the left jet by a quarter of a cycle. A comparison between Figures 72e and 72f indicates a similar phase shift in the positions of the vortical structures generated within the jets by these forcings. For the two cases in which  $\phi = \pi$ , the forcings applied in the plane  $y = 0$  at the two jet exits are symmetric relative to the plane  $x = x_F$ . Figures 72g and 72h indicate that the disturbance remains symmetric within the jets in this plane. Although the initial development of the left jets is the same in all these cases, deviations become apparent as the jets approach the ground plane. These deviations are due to the influence of the right-hand jet, through the fountain created by the collision of the wall jets. Figures 72a through 72h indicate that the general characteristics of the fountain in the unperturbed flow and the axisymmetrically perturbed jets are shared with those of the CW-CCW azimuthally perturbed flows. In these cases, we note that the fountain is confined to the region midway between the jets. The lateral interaction between the jets and the fountain seems to be weak. The main influence of the fountain on the jets occurs through the influence of the wall jet on the upper wall, generated by the fountain impingement. There is an indication of entrainment of this wall jet into the impinging jet. This can modify the jet spreading characteristics. On the other hand, the CW-CW azimuthally perturbed flows develop fountains that tend to extend farther in the  $x$  direction towards the neighboring jets. This is an indication that the spreading rate for the case of the CW-CW forcing is larger than that for the CW-CCW forcing. The main influence of the fountain on the impinging jets is due to lateral interaction and not to the influence of the wall jet at the upper plane. The plane  $y = 0$  for the CW-CW forcing case with  $\phi = \pi$ , shown in Figure 72g, is a special plane in which the flow is symmetric about the line  $x = x_F$ . In this particular plane, some of the features observed are not typical of CW-CW forcing. The CW-CCW forcing case with  $\phi = \pi$  is a special case since it is the only case in which the plane  $x = x_F$  is a

plane of symmetry. This case shares the symmetry about this plane with the unperturbed flow and the axisymmetrically forced flow. This symmetry has a very strong influence on the fountain characteristics. The figures indicate that, among all the azimuthally forced flows, fountain characteristics for the CW-CCW forcing with  $\phi = \pi$  (Figure 72h) are the closest to those of the two reference cases (Figures 72a and 72b).

Figures 73a through 73h and 74a through 74h present  $y$ -vorticity contours in the planes  $y = -1.5D$  and  $y = 1.5D$ , respectively, for the same cases presented in Figure 72. While the central and side fountain characteristics in Figure 72 were in general agreement, Figures 73 and 74 indicate some dissimilarity in these characteristics in certain cases. The discussions presented here will be limited to the central fountain characteristics unless otherwise specified. The individual vortical structures apparent in Figures 73 and 74 are cross-sections of vortical tubes moving upward into the fountain. The figures indicate that the individual structures tend to merge. Distinct features are observed among solutions resulting from CW-CW forcing and among solutions resulting from CW-CCW forcing. In the case of CW-CW forcing the vortical structures move upward in a direction inclined to the plane  $x = x_F$ , towards the left, in the negative  $x$  direction at the plane  $y = -1.5D$ . At this plane, the vortical tubes originally shed by the left jet, with negative vorticity, move toward this jet resulting in a reduction of vortex "ring" radius and an increased vorticity strength. The individual vortex structures merge into a larger structure nearly circular in its cross sectional shape extending to the left. The vortical tubes originally shed by the right jet, with positive vorticity, move away from this jet resulting in an increase of vortex "ring" radius and a reduced vorticity strength. The positive vorticity region tends to branch to the right towards the jet at which it originated and to the left above the negative vorticity region. At the plane  $y = 1.5D$ , the vortical structures move upward in a direction inclined to the plane  $x = x_F$ , towards the right, in the positive  $x$  direction. At the plane  $y = 1.5D$ , a similar picture develops to that observed in plane  $y = -1.5D$ , however, with the positive and negative vortical tubes reversing their role. Vortical tubes with negative vorticity tend to move away from the jet at which they originated, while vortical tubes with positive vorticity tend to move toward the jet at

which they originated. This role reversal indicates that significant changes occur in the vortical tubes along their length in the fountain. Figures 73 and 74 indicate that the vortical structures spread in a relatively wide region sideways in the  $x$ -direction, however, they extend to relatively low levels upward. The symmetry observed in the plane  $y = 0$  about the plane  $x = x_F$  for the fountain developing in the case of CW-CW forcing with  $\phi = \pi$  is no longer observed in the planes  $y = -1.5D$  and  $y = 1.5D$ .

In the case of CW-CCW forcing, the vortical structures move upward in the general direction defined by the plane  $x = x_F$ . They spread in a relatively narrow region sideways in the  $x$  direction. In the vertical direction the vortical structures extend upward to levels in the plane  $y = 1.5D$  higher than those in the plane  $y = -1.5D$ . The strong similarity observed in the plane  $y = 0$  between the fountain developing in the case of CW-CCW forcing with  $\phi = \pi$  and the two reference solutions continues to be apparent in the planes  $y = -1.5D$  and  $y = 1.5D$ .

The results presented here for the azimuthal forcing are limited to a single time, i.e., they correspond to a particular  $\beta$  value which we denote as  $\beta_0$ , where  $2\pi t/t_p = \text{constant} + \beta$ . A second set of solutions half a cycle later at  $\beta = \beta_0 + \pi$  for the central fountain may be constructed from a knowledge of the side fountain solution at  $\beta = \beta_0$ . This solution for the central fountain at  $\beta = \beta_0 + \pi$  is obtained at  $y = \pm Y$  by applying the transformation

$$(x - x_F) \rightarrow -(x - x_F)$$

to the side fountain solution obtained at  $y = \mp Y$  for  $\beta = \beta_0$ . Moreover, the side fountain provides solutions for several additional cases. For example, in the case of CW-CW forcing with  $\phi = \pi/2$ , the side fountain is equivalent to a central fountain resulting from CW-CW forcing with  $\phi = -\pi/2$ , at  $\beta = \beta_0 - \pi/2$ . Similarly in the case of CW-CW forcing with  $\phi = \pi$  the side fountain is equivalent to a central fountain resulting from CW-CW forcing with  $\phi = -\pi$ , at  $\beta = \beta_0 - \pi$ . In view of the new information obtained from the side fountain, it is appropriate to review Figures 72 through 74 and to identify two solutions for each forcing cycle. It is apparent that the general shape of the fountain structure remains nearly fixed. Within a forcing cycle the inner details of the fountain structure will slowly vary due to the movement of the vortex tubes. However, it is noted that the individual sizes of the cross section of these tubes are

smaller than the corresponding tubes in the jet, due to the stretching that takes place. Secondly, the flow velocity in the fountain is smaller than that in the jet. This indicates that changes in vortical structures in the fountain occur at a much slower rate than in the jets. These observations are also confirmed by Figures 75 and 76 where vorticity contours are presented at different times for a complete forcing cycle. The figures are presented for the two planes  $y = 0$ , and  $y = -1.5D$  for the case of CW-CW forcing with  $\phi = 0$ .

The  $y$ -vorticity contours presented for different  $x$ - $z$  planes have indicated that common features are shared among the members of each of the two sets investigated (clockwise-clockwise disturbance and clockwise-counterclockwise disturbances). An investigation of the  $y$ -vorticity contours in the  $x$ - $y$  planes leads to a similar conclusion. These contours for a single case ( $\phi = 0$ ) from each of the two sets are presented in Figures 77 and 78 with the corresponding contours for the two reference solutions. The contours are given at the two planes  $z = 1D$  and  $z = 1.5D$ . A comparison between the case of axisymmetric forcing and the undisturbed case indicates relatively high vorticity levels of  $|\omega_y|$  within the jets for the axisymmetric forcing case at  $z = 1D$  and lower levels at  $z = 1.5D$ . This simply indicates the presence of a vortex ring with negative azimuthal vorticity at the plane  $z = 1D$  and the presence of a vortex ring with positive azimuthal vorticity at the plane  $z = 1.5D$ . As a result, the basic vorticity levels in the jet are augmented at the first plane and weakened at the second plane. The vorticity distribution in both the clockwise-clockwise and the clockwise-counterclockwise cases differ from the previous two reference cases. However, the similarity between the reference cases and that of the clockwise-counterclockwise disturbance is greater than that between the reference cases and that of the clockwise-clockwise disturbance. In Figures 77d and 78d, showing the effect of a clockwise-counterclockwise disturbance, the fountain is nearly symmetric. Its direction only deviates slightly from the direction of the undisturbed fountain. That is, the  $y$ - $z$  plane midway between the jets is basically the plane going through the middle of the fountain. There does not seem to be strong interaction between the fountain and the jets. The jets are well defined at the upper plane ( $z = 1.5D$ ) and as they reach the lower plane ( $z = 1D$ ) they are still well defined. In Figures 77c and 78c showing the effect of clockwise-clockwise disturbance, the fountain is no longer symmetric about the  $y$ - $z$  plane

at mid-distance between the jets. It is, however, inclined to that plane. There seems to be interaction between the fountain and the jets as indicated by the vortex structures connecting them. The effect of the fountain on the jets is relatively strong. The well-defined jet vortical structure at the level  $z = 1.5D$  near the jet exit becomes illdefined as the jet reaches the plane  $z = 1D$ .

The main features for the different forcing conditions were concluded from vorticity contour plots. The same features are apparent in velocity vector plots. For the two reference solutions, the CW-CW solution with  $\phi = 0$  and the CW-CCW solution with  $\phi = 0$  velocity vector plots are shown in the plane  $x = x_F$  (see Figure 79), the planes  $y = 0$  (see Figure 80),  $y = -1.5D$  (see Figure 81), and  $y = 1.5D$  (see Figure 82). Figure 79c indicates that the fountain deviates from the plane  $x = x_F$  except near  $y = 0$  for CW-CW forcing. Figure 79d indicates that some deviation from the plane  $x = x_F$  is also present for CW-CCW forcing, however, to a much lesser extent. Figures 80 through 82 indicate features similar to those observed from the vorticity plots. These figures indicate that the impingement of the fountain on the upper wall is relatively weak for the case of CW-CW forcing and that it is relatively weak for the case of CW-CCW forcing at  $y = -1.5D$  while it is relatively strong for the same case at  $y = 1.5D$ .

The results presented up to this point present a clear picture of the fountain characteristics. Three main categories may be identified:

(1) Undisturbed Flow and Axisymmetric Forcing

Here the fountain is symmetric about the plane  $x = x_F$  and about the plane  $y = y_J$ . The fountain occupies a relatively narrow region near the plane  $x = x_F$ , indicating relatively weak lateral spreading. There is relatively little lateral interaction between the fountain and jets. However, the impingement of the fountain on the upper plane is relatively strong. The wall jets which develop on the upper wall due to this impingement are entrained into the impinging jets near the jet exit. The main influence of the fountain on the jet occurs through this entrainment.

(2) Clockwise-Counterclockwise Azimuthal Forcing

Here the fountain is nearly symmetric about the plane  $x = x_F$ . However, it is not symmetric about the plane  $y = y_J$ . The fountain occupies a relatively narrow region near the plane  $x = x_F$ , indicating relatively weak lateral spreading. There is relatively little lateral interaction

between the fountain and the jets. The impingement of the fountain on the upper plane is relatively strong for positive  $y$ -values where the directions of the azimuthal forcing at the jet exits is such that they both are directed towards the plane  $x = x_F$ . The impingement of the fountain on the upper plane is relatively weak for negative  $y$ -values where the directions of the azimuthal forcing at the jet exits is such that they both are directed away from the plane  $x = x_F$ . The wall jets that develop on the upper wall due to the fountain impingement are entrained into the impinging jets near the jet exit. The main influence of the fountain on the jet is due to this entrainment.

(3) Clockwise-Clockwise Azimuthal Forcing

Here the fountain is inclined to the plane  $x = x_F$ . For negative  $y$ -values, the fountain is directed towards the negative  $x$ -axis that coincides with the clockwise direction there. For positive  $y$ -values, the fountain is directed towards the positive  $x$ -axis that coincides with the clockwise direction there. The fountain spreads in a relatively wide region in the direction of the neighboring jets. The impingement of the fountain on the upper wall is relatively weak. The main influence of the fountain on the jets is due to their lateral interactions. The fountain generated in this case has the strongest influence on the jets among the three categories. This is due to the strong lateral spreading of the fountain.

Based on kinematic considerations explanations may be found for the results observed. Figure 83 shows the vortex tubes in the wall jets as they approach the fountain base. For the case of axisymmetric forcing, these tubes are in the form of rings that are nearly circular. The spiral shape of the vortex tubes in the cases of azimuthal forcing results in the relative positions shown in Figure 83a for the tubes as they approach the fountain base for the case of CW-CW forcing and the corresponding relative positions shown in Figure 83b for the case of CW-CCW forcing. The figure is shown for the case  $\phi = \pi$ . While the midplane between the tubes at the base of the fountain in both the axisymmetric forcing case and in the case of CW-CCW forcing is the plane  $x = x_F$ , the midplane in the case of CW-CW forcing is a plane inclined to the plane  $x = x_F$  to the right for positive  $y$  values and to the left for negative  $y$  values. As the vortex tubes shown in Figure 83 at the base of the fountain expand upward

into the fountain, the configurations indicated in Figure 84 result. The circular vortex tubes resulting from axisymmetric forcing touch the fountain base initially at the plane  $y = 0$ . As these tubes are convected upward into the fountain, they take the shape of arcs symmetric in the  $y$ -direction about the plane  $y = 0$ , while the plane  $x = x_F$  becomes a plane of symmetry between the two tubes. In the case of CW-CW forcing, Figure 83a indicates that the end c of the right vortex tube segment and the end b of the left vortex tube segment reach the plane  $x = x_F$  first, then the end d of the right vortex tube segment and the end a of the left vortex tube segment reach the plane  $x = x_F$ . The plane  $x = x_F$  is the plane of symmetry for the fountain generated by the basic undisturbed flow. The inclined vortex tubes shown in Figure 83a will tend to modify the fountain plane. The final plane will be somewhere between that defined by the unperturbed flow and that in the direction defined by the perturbation vortex tubes. Therefore, the plane  $x = x_F$  should no longer be the reference plane, strictly speaking, however, it is used here for the purpose of showing some qualitative characteristics. Assuming that the vortex tubes generated by CW-CW forcing expand upward at the plane  $x = x_F$ , then the relative positions of the tubes will be as shown in Figure 84b. We note that the average height of the structure composed of both tubes remain fixed along the  $y$  direction. Finally, the vortex tube segments resulting from CW-CCW forcing will collide at the base of the fountain, as shown in Figure 83b. The ends b and d will reach the fountain base before the ends a and c. The resulting configuration as the tubes expand into the fountain is shown in Figure 84c. Figures 84a through 84c show, in a simple manner, the relative positions of the vortex tubes resulting from different forcing configurations. The results presented earlier indicated that the vortex tube interactions are more complex than presented here, including recombination of vortex structures and deformation of the vortex tube shapes. Nevertheless, the simplified sketches of Figure 84 do allow us to explain some of the results associated with the different types of forcing.

The main characteristic shared by Figures 84a and 84c is the fact that the plane  $x = x_F$  is a plane of symmetry. Consequently, the flow is restricted in the  $x$  direction. This common factor explains the great similarity between the axisymmetric forcing results and the CW-CCW forcing results with  $\phi = \pi$ , previously presented. As shown in Figure 84b, the symmetry about the plane  $x = x_F$  is nonexistent except locally at the plane  $y = 0$ . In the plane  $y = 0$ ,



Figure 72 indicates a great deal of similarity between the case of CW-CW forcing with  $\phi = \pi$  and the case of axisymmetric forcing. In the planes  $y = -1.5D$  and  $y = 1.5D$ , however, where no symmetry exists, the differences between the two cases are apparent in Figures 73 and 74.

For values of  $\phi$  other than  $\pi$ , the relative vertical positions of the two tubes shown in Figures 84b and 84c slightly changes. The main effect in Figures 84b would be to displace the local plane  $y = y_j$ , at which symmetry exists about the plane  $x = x_p$ , to another near by plane. The role reversal observed at stations  $y = -1.5D$  and  $y = 1.5D$  for the vortical tubes generated at the left and right jets for the case of CW-CW forcing can be explained by Figure 84b where the relative positions of the tubes are reversed at these two planes. In the case of  $\phi = \pi$ , the plane  $y = 0$  is the plane about which an antisymmetry exists in the relative positions of the vortex tubes. A comparison between Figures 73g and 74g indicates that this antisymmetry in the shapes of vortex structures does exist in planes  $y = -1.5D$  and  $y = 1.5D$ . For the cases  $\phi = 0$  and  $\phi = \pi/2$ , however, the point at which the two tubes of Figure 84b coincide is no longer at the position  $y = 0$ . Therefore, the planes  $y = -1.5D$  and  $y = 1.5D$  are not the planes at which the relative positions of the tubes are exactly reversed. Therefore, a general reversal in the roles of the vortical structures associated with the tubes is observed at the planes  $y = -1.5D$  and  $y = 1.5D$ , however, a complete antisymmetry is not observed. This is indicated by a comparison of Figures 73c and 74c for  $\phi = 0$  and 73e and 74e for  $\phi = \pi/2$ . The main effect in Figure 84c of specifying  $\phi$  values other than  $\pi$  is to destroy the symmetry about the plane  $x = x_p$ . However, the two vortex tubes do remain parallel even though a relative shift in their vertical positions occurs. Therefore, the vortical tubes originating from two neighboring jets mesh together in an organized fashion in the fountain generated between the jets. This organized meshing of the vortex tubes in the case of the CW-CCW forcing is the common feature shared by all members of this group regardless of the phase shift. In the case of CW-CW forcing, the vortex tubes generated at the two neighboring jets are inclined in different directions as indicated in Figure 84b. This relative position does not allow the organized meshing of the vortex tubes, resulting in the relatively unorganized fountain characteristics observed in the different CW-CW forcing cases. The inclination of the vortex tubes shown in Figure 84c coincides with the observed results, which indicates that for CW-CCW forcing, vortical structures reach a relatively high

level at the plane  $y = 1.5D$  while they reach a relatively low level at the plane  $y = -1.5D$ . For the axisymmetric forcing, we have assumed in our computations a zero phase shift. The effect of using a phase shift value other than zero would be to vertically displace the relative positions of the two vortex tubes shown in Figure 84a. The main difference between this case and the CW-CCW forcing with  $\phi \neq 0$  would be the symmetry across the  $y = 0$  plane in the axisymmetric case and the nonsymmetry for the CW-CCW forcing. Other than this difference, both flows are expected to be similar with no symmetry across the  $x_F$  plane, however, with an organized meshing of the vortex tubes in the fountain.

Three-dimensional views of the vortical structures resulting from axisymmetric, clockwise-clockwise and clockwise-counterclockwise forcings with  $\phi = 0$  are presented in Figures 85a-85c. As in Figure 70, the surfaces shown in these figures are those with a vorticity level given by  $|\omega| = 2.1$ . In Figure 85a, it is apparent that the vortical rings resulting from axisymmetric forcing deviate from their initial axisymmetry, as they move downwards in the jets, due to the influence of the fountain. This is particularly apparent in the rings with positive  $\omega_\theta$  vorticity. The vorticity in these rings tends to cancel the negative  $\omega_\theta$  vorticity associated with the unperturbed flow. The figure indicates that the levels for  $|\omega|$  are higher in the jet "sides" facing the fountain than in those "sides" facing the outflow boundaries. The near planar vorticity sheets in the fountain are a common feature between Figures 70 and 85a. The vortical structures in Figure 85b (CW-CW forcing) appear to be no longer planar in the fountain region. A three-dimensional branching of the vortical tubes is observed in the fountain region, with some branches extending to the jets. The vortical structures in Figure 85c (CW-CCW forcing) are intermediate in nature between those of Figures 85a and 85b. They are no longer planar, and some vortical tubes are seen to be breaking away from the main fountain structure, however, the structures are still confined to the region mid-distance between the jets and the strong branching and three-dimensional character of Figure 85b is not observed here.

#### 4.4 Randomly Forced Impinging Jets

In the previous three sections we investigated the effects of coherent forcing in the development of the impinging jets. In all the previous calculations, we assumed that the flow field is laminar initially and is then perturbed at the prescribed frequency. Although complicated vortex ring

propagation and merging processes were observed, they were all controlled by the forcing frequency(ies). No attempt was made to model the turbulent flow field. Since the present numerical approach utilizes large-eddy simulations with subgrid-scale modeling, it is expected that all scales within the grid resolution can be resolved. Thus, the observation of small-scale structures in the flow field during axisymmetric and azimuthal forcing is realistic. However, the origin of all the structures observed in the previous coherent forcing studies is dependent on the initial conditions. Therefore, if the initial condition is random in origin, the development of the flow field will be random in general, and any formation of large-scale structures in the domain will be the result of natural growth of the instability imbedded in the random initial field. Such turbulent simulations have been the main avenue of research into turbulent flows in mixing layers and jets. A recent study by Childs et al.<sup>8</sup> investigated the collision of turbulent wall jets by introducing random disturbances into the mean profile at the inflow. In the present study we shall discuss some results obtained when the impinging jets in the present case were forced in a random manner.

In Section 2.3 we presented the rationale behind the random field generation. The random velocity field so generated can be imposed in the inflow and the computations continued. For realistic simulations, the full computational domain used for the azimuthal forcing needs to be used for realistic random field development. However, this would require an extensive computational effort and, therefore, has not been studied in great detail. Some simulations have been performed using random forcing initial conditions under some simplifying assumptions. The random field is generated according to the formulation discussed in Section 2.3. We then assume symmetry in the x- and y-directions for the computational domain in a manner similar to the axisymmetric forcing study. The random field is then imposed on the quarter plane of the jet exit such that only the lowest Fourier modes are present. The symmetry assumption was used to reduce the computational effort required to understand the effects of forcing at random frequencies. This assumption essentially reduces the problem to simulating the flow with multiple frequencies that are generated randomly according to the rules discussed in Section 2.3. Therefore, the simulation using symmetry in the domain is strictly not random. But the jet flow can be studied under such assumptions to understand the dynamics of vortex formation resulting from random excitation.

A simulation was performed using the symmetry assumption for  $Re = 1000$  and the  $H = 3D$  case. The random field in a  $32 \times 32$  domain was generated for a simulation time of length  $T$  under the assumption of symmetry in the  $x$ - and  $y$ -directions. This random field is then imposed in the quarter plane of the jet at its exit location such that at each time step a new random field is added to the jet exit velocity profile. The computations shown in this simulation assumed a relatively high turbulence level of 10 percent. This was required to overcome the inbuilt dissipation of the numerical scheme and the damping effects of the ground plane that would suppress the natural growth of the random modes. It was determined that, for low-level forcing, a very long period of time integration has to be performed to obtain any significant statistical information. To avoid the large computational time required for such simulations, we have utilized a high forcing level of 10 percent. This is, of course, consistent with the study of coherent forcing studied in the previous sections. It must also be mentioned that the results presented in this section are still somewhat preliminary, since there are various variables that need to be looked at for simulating the random field as discussed in Section 2.3.

Figures 86a through 86c show the characteristic  $x$ -vorticity contours in the  $y$ - $z$  plane at three different times. This view shows the  $x = 0$  plane, which is the centerline plane. The figures correspond to the instantaneous vorticity field after random forcing was initiated from steady-state initial conditions. There is no clear indication of the shedding of a large-scale structure in the jet shear layer. This is expected, since the forcing at random does not necessarily excite the jet at the jet-preferred mode. However, there is an indication of a vortical structure in the jet shear layer forming just before impinging on the ground plane. As the jet shear layer curves outwards and propagates towards the outflow, there is the formation of a structure in the wall jet region. This vortex seems quite coherent further downstream and then shows signs of lifting off from the ground. Figure 86b shows on careful study that there are possibly two vortex cores in the structure impinging on the ground. Evidently, random forcing does cause the formation of large scale structures on the ground. This observation is in agreement with experimental observations of random excitation of jets. In the experiments, the jet when forced randomly causes the most unstable mode to

grow naturally from the random background. This growth of the most unstable waves causes the jet shear layer to undergo rollup and then pairing until the large-scale structure is formed at the jet-preferred frequency. In free jets, this large coherent structure is usually formed within four jet diameters downstream. Since, in the present simulation, the jet height is three jet diameters, it is possible that the jet-preferred mode is not reached before the jet impinges on the ground.

The appearance of secondary vorticity is similar to the coherent forcing case and is observed around  $y = 2D$ . The downstream propagation and the lifting of the primary-secondary vorticity is again observed. These vortices maintain their coherency even at  $x = 0.51D$ , as shown in Figure 86c, indicating that these are vortex rings. The distribution of the  $y$ -vorticity in the  $x$ - $z$  plane is shown in Figure 87. Figure 87a shows the  $y = 0$  plane showing the jet and the fountain region in the center plane. There is evidence of the vortex cores in this figure, and the recirculation of the fountain on the top wall is also observed. Vortical motion in the fountain is visible, indicating that quite a few structures have been entrained into the fountain. Figures 87b and 87c show the  $y$ -vorticity contours in the  $x$ - $z$  plane at  $y = 0.51D$  and  $y = 1.5D$ , respectively. In these planes we see the characteristic upwash of the fountain and the impingement on the top wall. In general, the view in these figures is quite similar to the axisymmetric simulations.

To show that the observed structures in Figures 86 and 87 have any spanwise coherency, we present in Figures 88a and 88b, respectively, the  $x$ - and  $y$ -vorticity contours in the  $x$ - $y$  plane at  $z = 0.14D$ . This plane is just above the ground and shows the characteristic vortex rings on the ground, indicating that the structures formed in these simulations are also quite coherent.

A simulation was also performed in which a coherent mode at the frequency corresponding to  $St = 0.235$  was added to the random initial field. The results indicate that the coherent mode organizes the randomly excited vortices into larger and more coherent structures. The fountain is also more coherent indicating that perhaps coherent forcing can be utilized to control the behavior of the fountain.

It seems from this calculation that the forcing studied using axisymmetric forcing is quite reliable for understanding the dynamics of the large vortex rings on the ground and the formation of the fountain. The limitations imposed by assuming symmetry in the  $x$ - and  $y$ -directions can be relaxed without any problem except the increase in computational effort.

## 5. CONCLUSIONS

The results presented in this report catalog the findings of the study of impinging jets under both coherent and random excitation. These results have been obtained using a three-dimensional, incompressible Navier-Stokes solver that was developed to simulate the problem of an infinite row of jets impinging on the ground. This problem contains the essential physics of the case of a VTOL aircraft hovering near the ground. The characteristic flow field of the exhaust of the engines near the ground is very complex containing motion in a wide variety of scales. The approach used here applies the large-eddy simulation techniques to resolve scales above the grid resolution and uses a subgrid model to simulate the cascade of energy into the unresolvable scales. The grid resolution used in these simulations is the largest possible using state-of-the-art computers such as the CRAY XMP without causing a significant increase in cpu time. Although the present grid resolution is insufficient to resolve the finer details of the small-scale motion, especially in the wall-bounded shear layer regions, it is quite adequate to resolve the large-scale motion. Therefore, the present study focuses on the motion and dynamics of large-scale structures that have been experimentally observed in jet flows. To investigate this complex physical process, we perturb the mean jet exit velocity profile by superposing a prescribed disturbance. The resulting motion of the impinging jet is simulated using a time- and space-accurate numerical scheme. To characterize the motion due to different families of possible disturbances, we have studied separately the effect of forcing the impinging jet using axisymmetric, azimuthal and random disturbances. The principal advantage of studying the motion of forced jets is that the forcing suppresses the natural instability of the jet, and the motion of the large structures in the jet is governed by the imposed excitation. Therefore, the effect of external excitation can be studied in detail.

Since the primary interest in this study was to investigate the motion of large-scale structures in the flow, we force the jet at frequencies corresponding to a Strouhal number range of 0.23 to 0.47. This range falls in the range of the jet-preferred mode instability observed in a wide variety of experiments. It has been pointed out that, in jet flows, the formation of the large-scale structures occurs at the so-called jet-preferred frequency that corresponds to a Strouhal number range of 0.24 to 0.64.<sup>28</sup> Therefore, to

simulate the motion of these large-scale structures, we force the jet in the above-mentioned range.

An enormous amount of data has been collected on the three-dimensional flow field for various forcing conditions during the course of the present investigation. Due to lack of time and resources, all the data has not yet been analyzed in detail. However, the results presented in this report provide sufficient information to characterize the large-scale motion caused by coherent excitation. To visualize the formation, motion, and breakdown of the large-scale structures, extensive use has been made of the spatial and temporal variation of the three components of the vorticity vector. Both two-dimensional and three-dimensional representations have been used to study the structures in the flow.

The results obtained from the study of axisymmetrically forced impinging jets indicate both quantitative and qualitative agreement with some experimental observations. A large axisymmetric vortex ring is shed by the jet at the frequency of forcing that impinges on the ground and propagates above the ground. The calculated phase speed of the impinging vortex ring is similar to the experimental value. During propagation on the ground, a region of secondary vorticity appears just ahead of the primary vortex core, again in agreement with the experimental observation. Further downstream this secondary vorticity rolls up into a vortex ring of opposite rotation, and there is some indication that the counterrotating vortex rings start to lift off the ground due to their mutually induced velocity fields. This has also been observed experimentally. The formation of the secondary vorticity has been attributed to the unsteady separation of the wall boundary layer caused by an adverse pressure gradient on the ground. The numerical results appear to agree with this hypothesis. The calculated phase speed of the vortex rings on the ground is lower than the experimental value obtained with an isolated impinging jet. Since, in the present case, an infinite row of impinging jets has been simulated, the presence of the adjacent jet causes the formation of a fountain at the midplane between two jets. This fountain forms due to the collision of two opposite wall jets on the ground and then climbs up and impinges on the top plane. During vortex propagation on the ground, the vortex ring is entrained into the fountain, resulting in the lifting of the vortex ring from the ground. Thus, as the vortex ring continues to propagate to the

outflow boundary, it is also lifted into the fountain causing it to twist and finally break up. Due to the close proximity of the ground to the jet exit plane, the spread of the fountain on the top plane recirculates and shows signs of reentrainment into the impinging jet. This results in an increase in the spread of the jet.

The formation of the fountain is a unique characteristic of multiple impinging jets. A consequence of the impingement of the fountain on the top wall is an increase of pressure on the plane resulting in an increased liftoff effect for a VTOL aircraft. Since this is an important factor in the operation of VTOL aircraft in ground effect, the dynamics of the formation and spreading of the fountain were studied in more detail. Two impinging jets were simulated such that the forcing frequency and phase of each can be varied independently. At present, the effect of phase difference has been studied in detail. The two jets were forced at the same frequency but with a phase difference of  $\pi$  and  $\pi/2$ , respectively. The results indicate that the effect of the phase difference is to stagger the vortex rings on the ground from the two jets. This causes the fountain to entrain vortex rings from each jet at a different time. A detailed study of the wall jet collision zone indicates a complex flow pattern caused by the phase difference. The fountain spread is more uniform for the  $\pi$  phase difference case, and these simulations also showed a complex merging pattern near the top wall. Another simulation with only one jet forced was also carried out that indicates a complex pattern near the wall jet collision zone. Due to the forcing of one jet, the vortices in it and hence in its wall jet perturbs the steady wall jet of the other jet. This causes the steady wall jet to undergo a disturbance at the same frequency of the appearance of the vortex ring in the wall jet collision zone. The resulting fountain thus again shows vortical motion from both the wall jets. However, the fountain is no longer uniformly spreading up and shows a significant flapping behavior. These simulations show quite clearly that the effect of a phase difference between two impinging jets can significantly modify the motion and structures in the fountain. It is expected that the effect of varying the forcing frequency will also result in significant changes in the dynamics of the fountain. A complete parametric analysis can be easily be carried out provided enough resources are available to determine the effect of frequency and phase differences on the spread of the fountain. This in turn will provide



information on the effectiveness of the fountain to provide the liftoff effect. For example, since realistic flow fields are usually highly turbulent, the formation of large coherent structures due to the natural excitation of the impinging jet may not be a highly periodic or energetic event. In this case, the fountain spreads much more rapidly and has been observed in some experiments to result in a weak liftoff effect. Thus, a possible solution to increasing the liftoff effect will be to perturb the jet exit velocity profile in a coherent manner so that large coherent structures are shed. This would result in a more coherent fountain and hence an increase in the liftoff effect. However, to determine an optimum situation would require further study as discussed above.

The characteristics of the impinging jet flow due to azimuthal excitation were also studied. The jet was again forced at the same frequency at  $St = 0.47$ . The results indicate the characteristic formation of the helical structures due to azimuthal excitation. The asymmetry in the fountain due to azimuthal forcing is also clearly indicated in the results. The vortical structures in the wall jet are less coherent as compared to the axisymmetric forcing studies. The response of the fountain to various azimuthal excitations applied at the exits of its neighboring jets was investigated. The disturbances at the jet exits were applied with phase shifts of  $0$ ,  $\pi/2$ , and  $\pi$ . Fountain characteristics were shared among the different cases in which the disturbances were applied in the clockwise direction in both jets. A different set of characteristics was shared by the cases in which the disturbances were applied in the clockwise direction at one of the jet exits and in the counterclockwise direction at the other jet exit. In the case of clockwise-clockwise forcing, the fountain spreading towards the neighboring jets and its interaction with them is relatively strong. The fountain plane in this case is inclined to the plane that is normal to the plane of jet axes. The impinging effect on the aircraft's undersurface in this case is relatively weak, indicating a weak fountain liftoff effect. In the case of clockwise-counterclockwise forcing, the fountain is confined to a relatively narrow region near the midplane between the jet axes. Its interaction with the neighboring jets is weak. The impinging effect on the aircraft's undersurface is relatively strong. However, it is not uniform in the direction normal to the plane of jet axes. The liftoff effect is relatively strong in the half of the fountain in which

the disturbances in both jet exits are directed towards the fountain plane, while they are relatively weak in the half in which these disturbances are directed away from the fountain plane. The observed weak lateral spreading of the fountain is due to lateral flow restrictions, imposed by the existence of a plane of symmetry through the fountain for the case of a  $\pi$  phase difference. For the general case with  $\phi \neq \pi$ , the weak lateral spreading is due to the well-organized meshing of the vortical tubes in the fountain. These two effects are also present in the case of axisymmetric forcing. Consequently, strong similarities exist between the fountain characteristics in the cases of axisymmetric forcing and azimuthal clockwise-counterclockwise forcing. These effects, however, are not shared by the case of clockwise-clockwise forcing.

Some study of the impinging jet under random excitation has also been performed. The random field was determined by prescribing the energy spectrum and the rms value of the fluctuation and is imposed on the jet profile as a function of time. The results indicate that there is no clear formation of vortex rings in the jet as in the coherent forcing studies. However, as the jet impinges and spreads on the ground, there is a definite indication of coherent vortical motion in the wall shear layer that is also coherent in the spanwise direction. Simulations using both random forcing and a coherent forcing frequency were also performed, and the results indicate that the effect of the coherent frequency is to organize the motion in the impinging jet and also to form a more coherent vortex ring on the ground. This again clearly indicates that coherent excitation of randomly forced impinging jets can possibly modify and organize the motion. This could result in a more coherent fountain, thereby increasing the liftoff effect of the fountain.

## REFERENCES

1. Kuhn, R. E., "V/STOL and STOL Ground Effects and Testing Techniques," Task I Report Prepared under Contract No. NAS2-11912 for Ames Research Center, NASA, December 1984.
2. Rubel, A., "Computations of Jet Impingement on a Flat Surface," AIAA Paper 78-207, January 1978.
3. Rubel, A., "Computations of the Oblique Impingement of Round Jets Upon a Plane Wall," AIAA J., Vol. 19, pp. 863-871, July 1981.
4. Kotansky, D. B., and Bower, W. W., "A Basic Study of the V/STOL Ground Effect Problem for Planar Flow," J. Aircraft, Vol. 15, pp. 214-221, April 1978.
5. Agarwal, R. K., and Bower, W. W., "Navier-Stokes Computations of Turbulent Compressible Two-Dimensional Impinging Jet Flowfields," AIAA J., Vol. 20, pp. 577-584, May 1982.
6. Bower, W. W., Agarwal, R. K., Peters, G. R., and Kotansky, D. R., "Viscous Flowfields Induced by Two- and Three-Dimensional Lift Jets in Ground Effect," Report ONR-CR215-246-3F, March 1979.
7. Childs, R. E., and Nixon, D., "Unsteady Three-Dimensional Simulations of a VTOL Upwash Fountain," AIAA Paper 86-0212, January 1986.
8. Childs, R. E., and Nixon, D., "Further Studies of Impinging Jet Phenomena," AIAA Paper 87-0017, January 1987.
9. Rizk, M. H., and Menon, S., "Numerical Simulation of Impinging Jets," AIAA Paper 86-0279, January 1986.
10. Didden, N., and Ho, C.-M., "Unsteady Separation in a Boundary Layer Produced by an Impinging Jet," J. Fluid Mech., Vol. 160, pp. 235-256, November 1985.
11. Crow, S. C., and Champagne, F. H., "Orderly Structure in Jet Turbulence," J. Fluid Mech., Vol. 48, pp. 547-591, August 1971.
12. Strange, P. J. R., and Crighton, D. G., "Spinning Modes on Axisymmetric Jets, Part 1," J. Fluid Mech., Vol. 134, pp. 231-245, September 1983.
13. Mansour, N. N., Moin, P., Reynolds, W. C., and Ferziger, J. H., "Improved Methods for Large Eddy Simulations of Turbulence," Turbulent Shear Flows I, Berlin: Springer, pp. 386-401, 1979.
14. Leonard, A., "Energy Cascade in Large Eddy Simulations of Turbulent Fluid Flows," Advances in Geophysics, Vol. 18A, New York: Academic, pp. 237-248, 1974.

15. Rogallo, R. S., and Moin, P., "Numerical Simulation of Turbulent Flows," Ann. Rev. Fluid Mech., Vol. 16, pp. 99-137, 1984.
16. Deardorff, J. W., "A Numerical Study of Three-Dimensional Turbulent Channel Flow at Large Reynolds Numbers," J. Fluid Mech., Vol. 41, pp. 453-480, 1970.
17. Smagorinsky, J., "General Circulation Experiments with the Primitive Equations," Mon. Weather Rev., Vol. 91, pp. 99-164, 1963.
18. Spalding, D. B., "A Single Formula for the Law of the Wall," J. Appl. Mech., Vol. 28, pp. 455-458, 1961.
19. Harlow, F. H., and Welch, J. E., "Numerical Calculation of Time-Dependent Viscous Incompressible Flow of Fluid with Free Surface," Phys. Fluids, Vol. 8, pp. 2182-2189, 1965.
20. Patankar, S. V., Numerical Heat Transfer and Fluid Flow, Hemisphere, 1980, pp. 115-120.
21. Roache, P. J., Computational Fluid Dynamics, Hermosa, Albuquerque, NM, 1972.
22. Raithby, G. D., "A Critical Evaluation of Upstream Differencing Applied to Problems Involving Fluid Flow," Computer Methods in Appl. Mech. and Eng., Vol. 9, pp. 75-103, 1976.
23. Leonard, B. P., "A Stable and Accurate Convective Modelling Procedure Based on Quadratic Upstream Interpolation," Computer Methods in Appl. Mech. and Eng., Vol. 19, pp. 59-98, 1979.
24. Davis, R. W., and Moore, E. F., "A Numerical Study of Vortex Shedding from Rectangles," J. Fluid Mech., Vol. 116, pp. 475-506, 1982.
25. Adams, J., Swarztrauber, P., and Sweet, R., Subroutine HW3CRT of the FISHPAK package of FORTRAN subprograms for the solution of seperable, elliptic, partial differential equations developed at the National Center for Atmospheric Research, 1979.
26. Rizk, M. H., and Menon, S., "A Numerical Investigation of Three-Dimensional Impinging Jets," Report No. 326, Flow Research Company, April 1985.
27. Brown, G. L., and Roshko, A., "On Density Effects and Large Structure in Turbulent Mixing Layers," J. Fluid Mech., Vol. 64, pp. 775-816, 1974.
28. Gutmark, E., and Ho, C.-M., "Preferred Modes and the Spreading Rates of Jets," Phys. Fluids, Vol. 26, pp. 2932-2938, 1983.

5438R

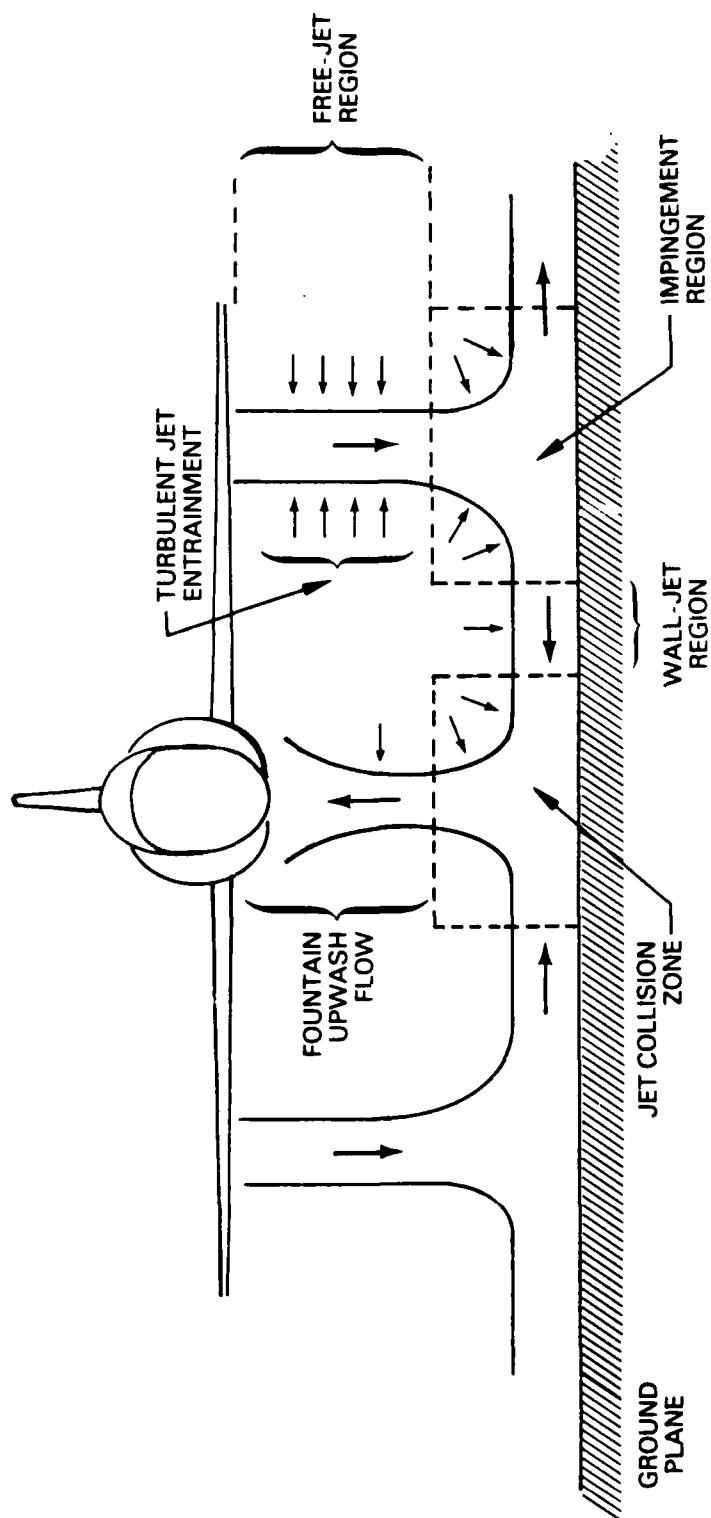


Figure 1. Schematic of the flow field below a hovering VTOL aircraft.

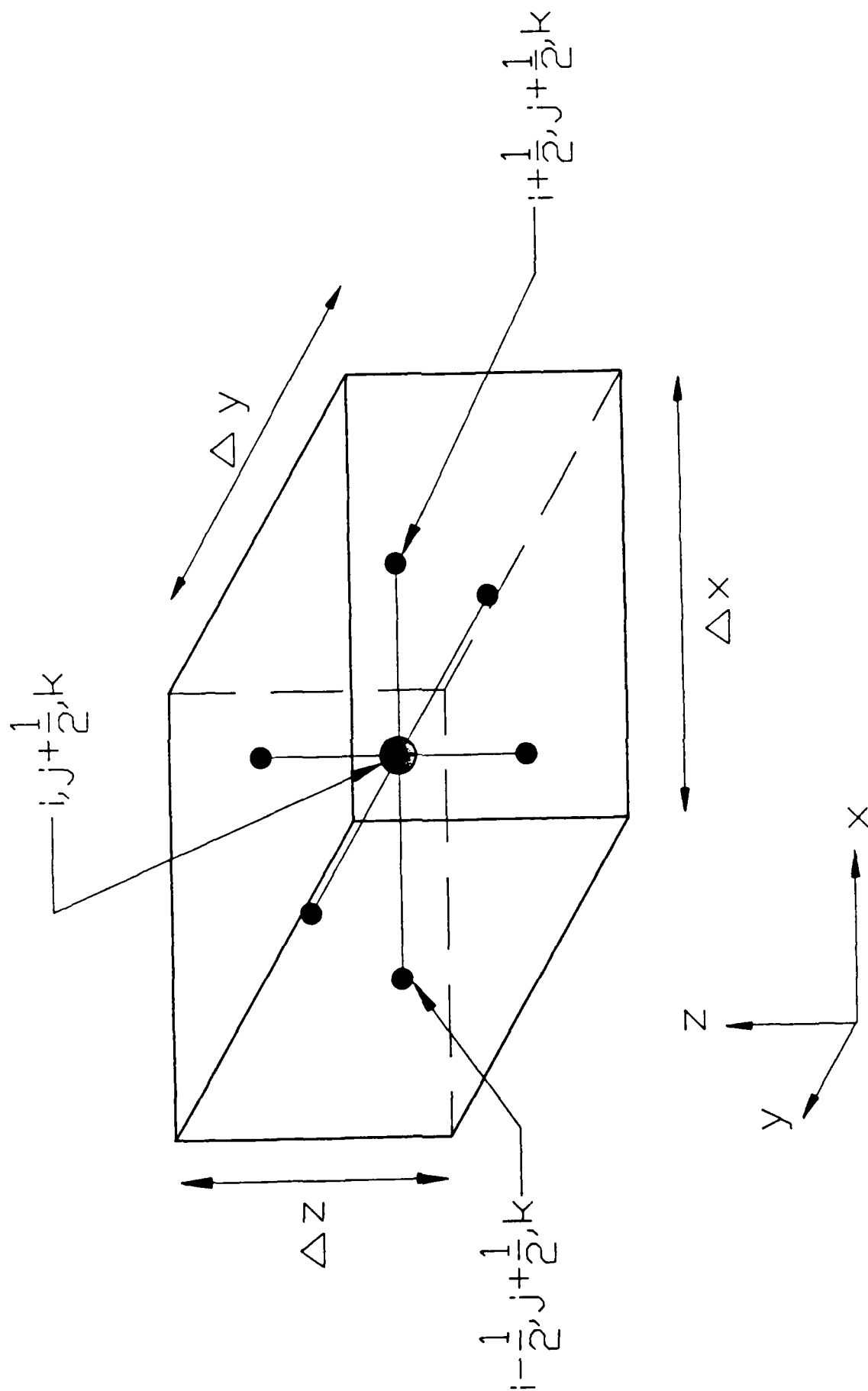


Figure 2. v-mesh computational cell.

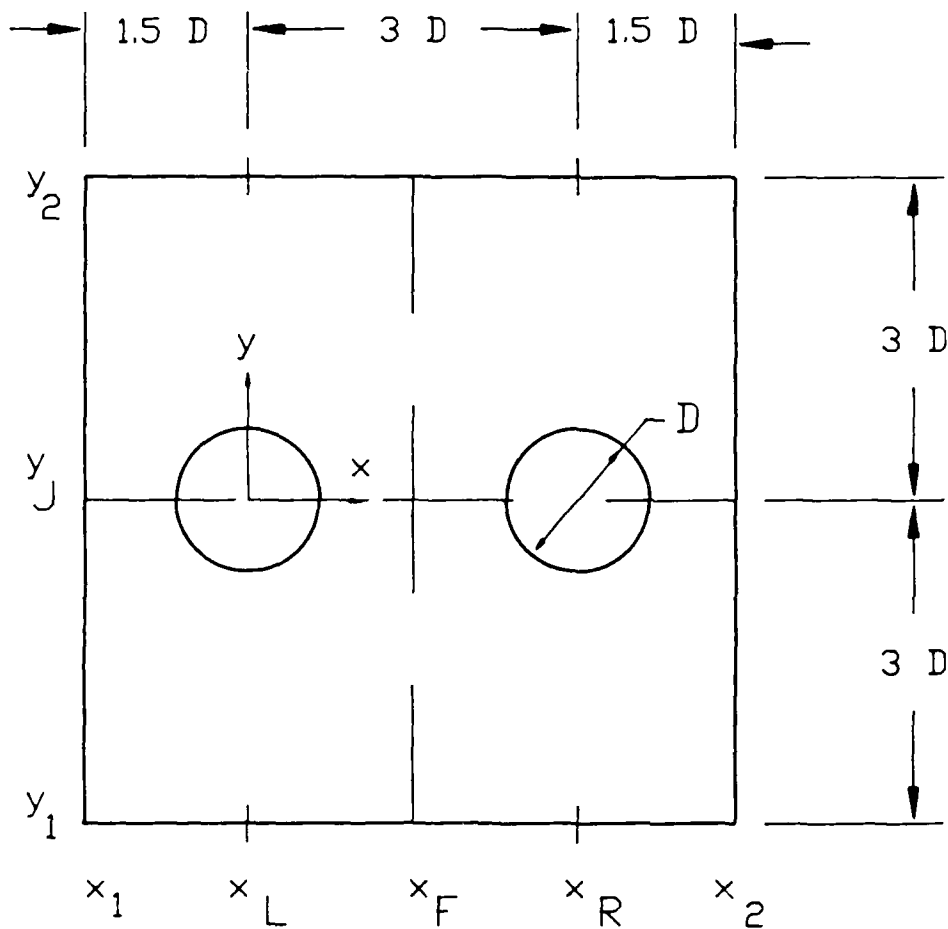


Figure 3. Top view of computational domain for the double-jet configuration.

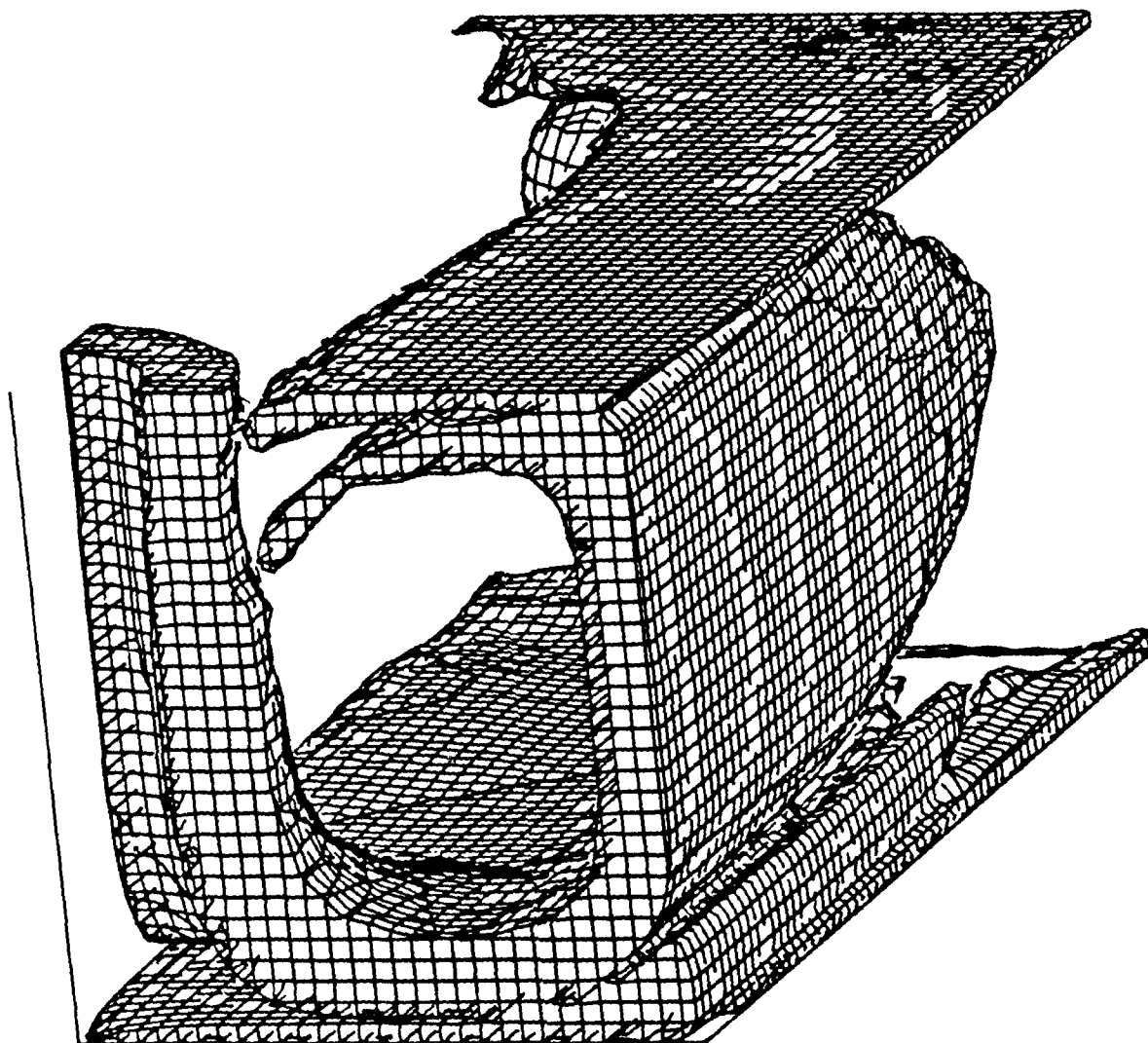
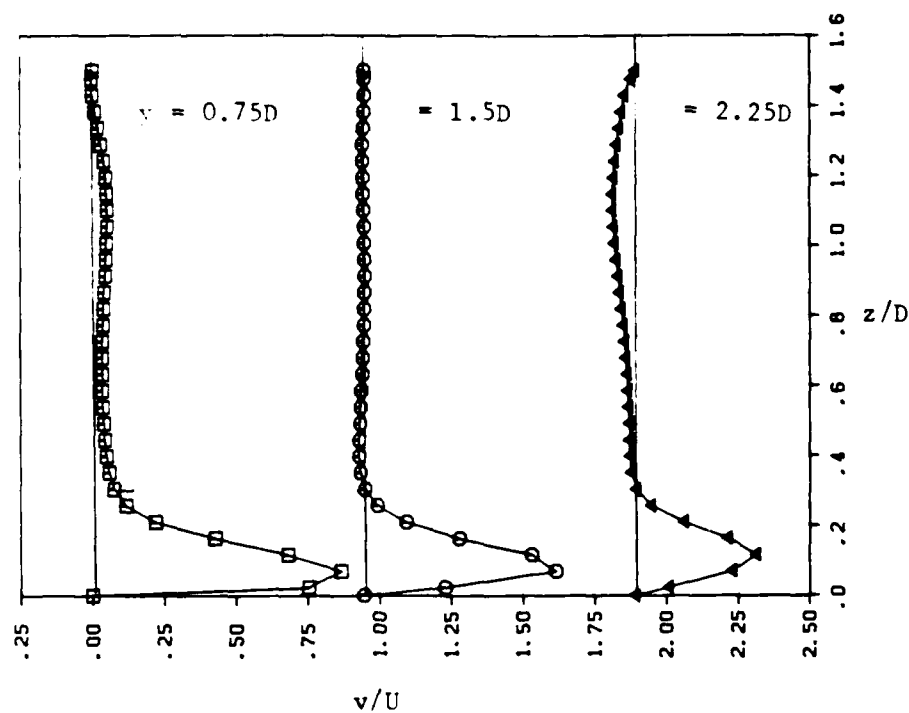
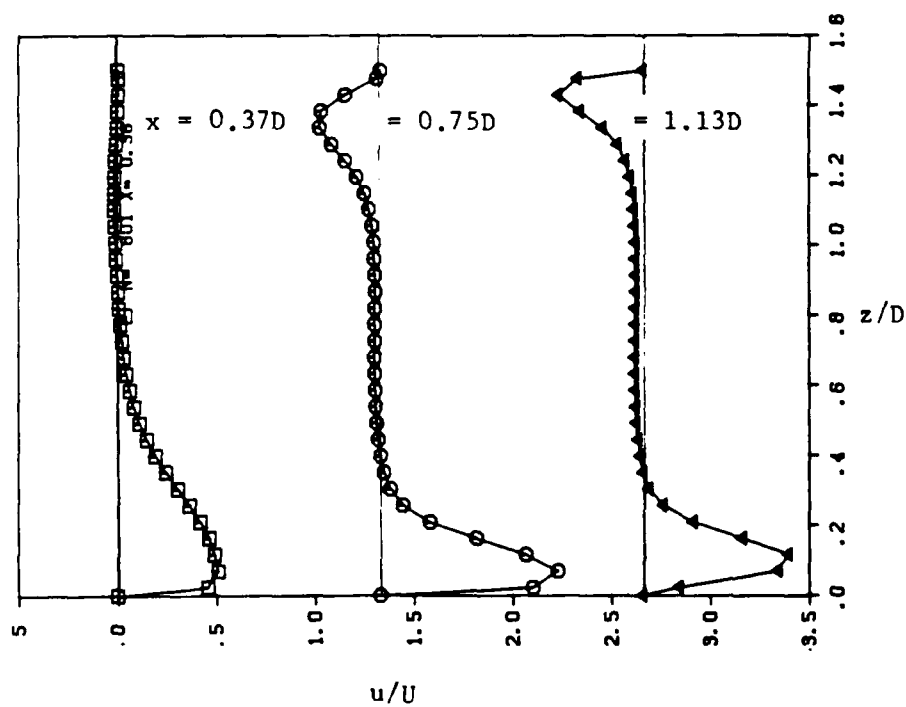


Figure 4. Three-dimensional perspective of the absolute vorticity surface at a level  $|\psi| = 1.75$  at  $t = 11.3$ . View of the impinging jet and the fountain at steady state for  $H = 1.5D$ .



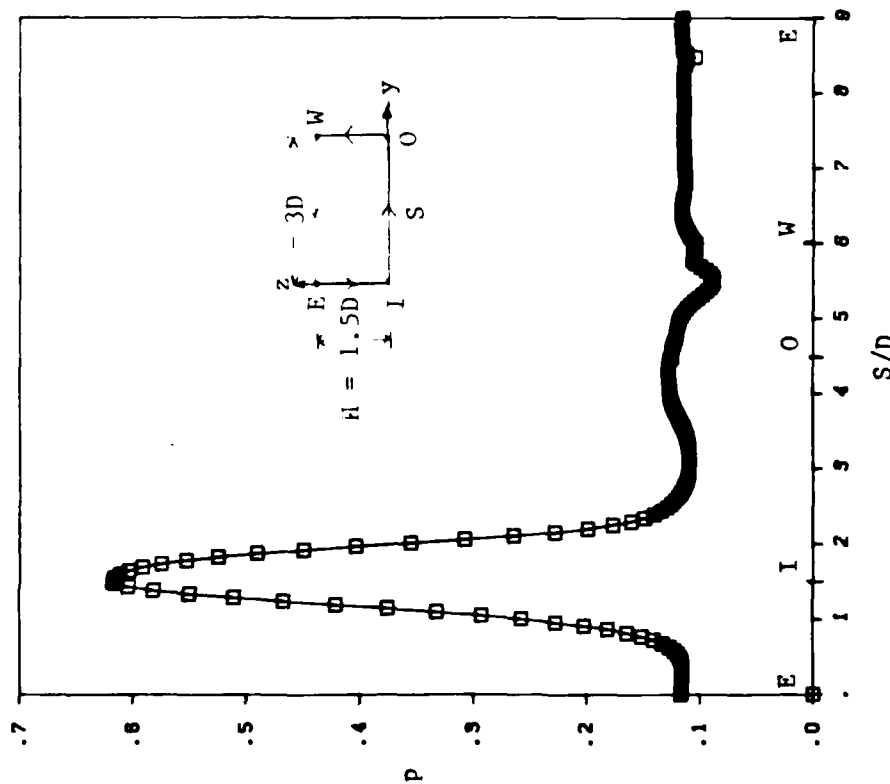


a.  $v$ -velocity in the  $y$ - $z$  plane at  $x = 0$  as a function of  $z$  at various  $y$ -locations

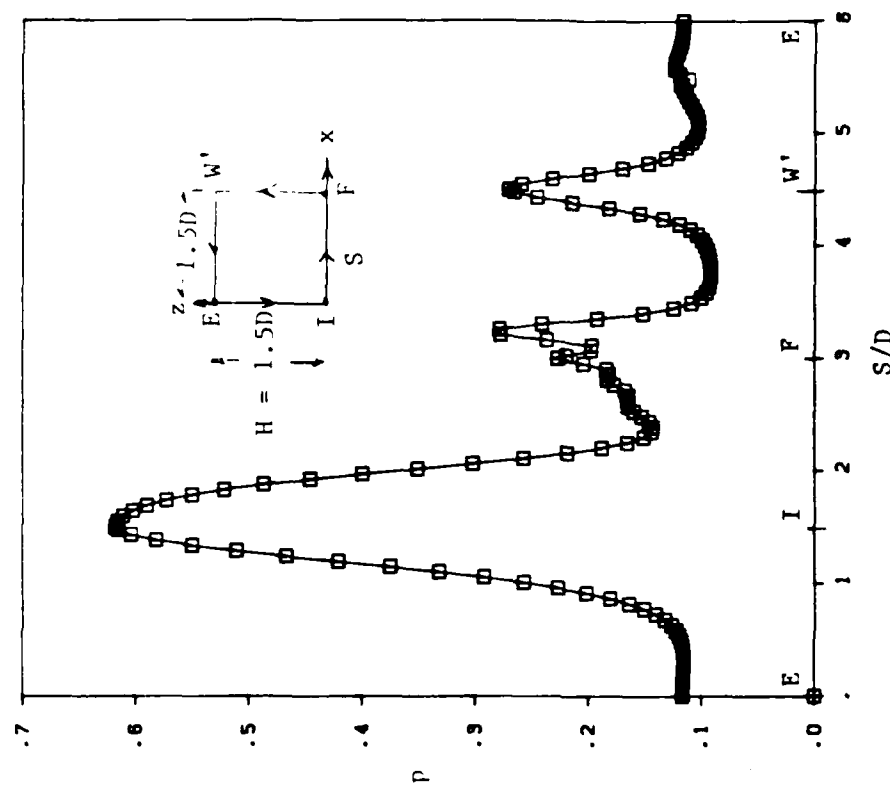


b.  $u$ -velocity in the  $x$ - $z$  plane at  $y = 0$  as a function of  $z$  at various  $x$ -locations

Figure 5. Steady-state velocity profiles at  $t = 11.3$  for  $H = 1.5D$ .

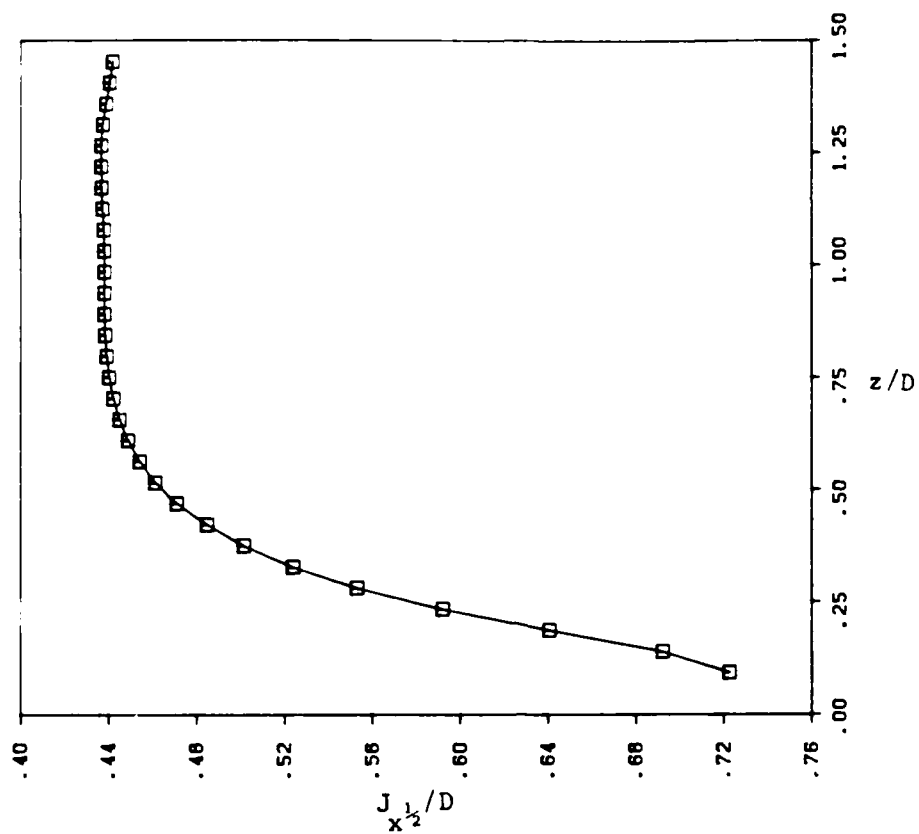


a. pressure in the y-z plane at  $x = 0$

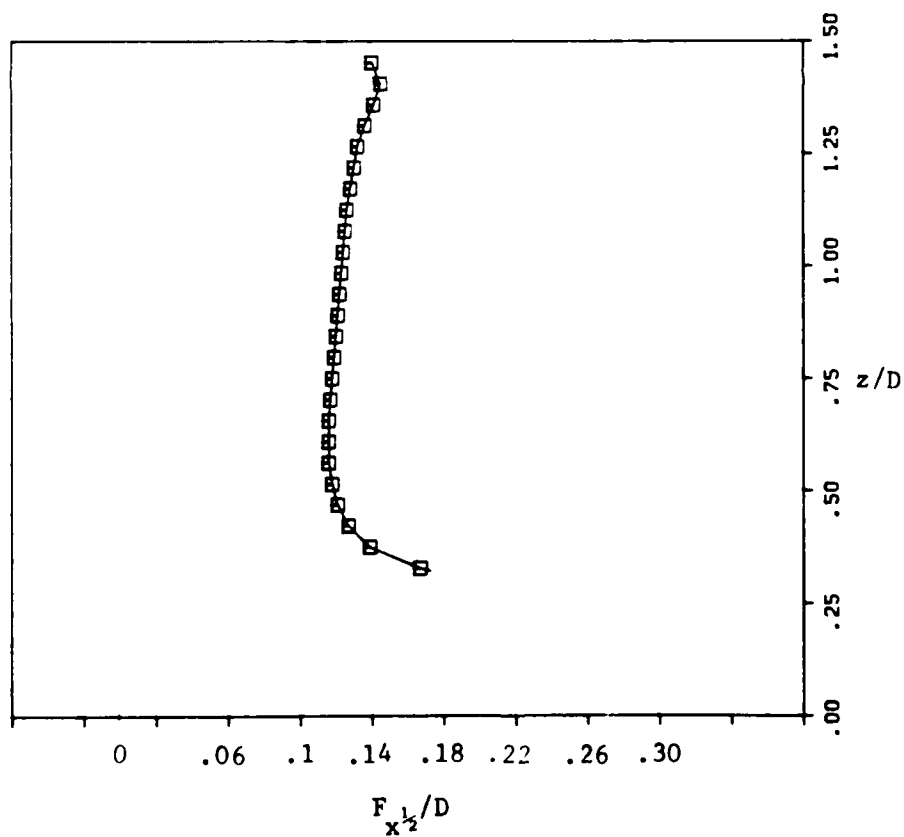


b. pressure in the x-z plane at  $y = 0$

Figure 6. Steady-state pressure variation along the boundaries at  $t = 11.3$  for  $H = 1.5D$ .

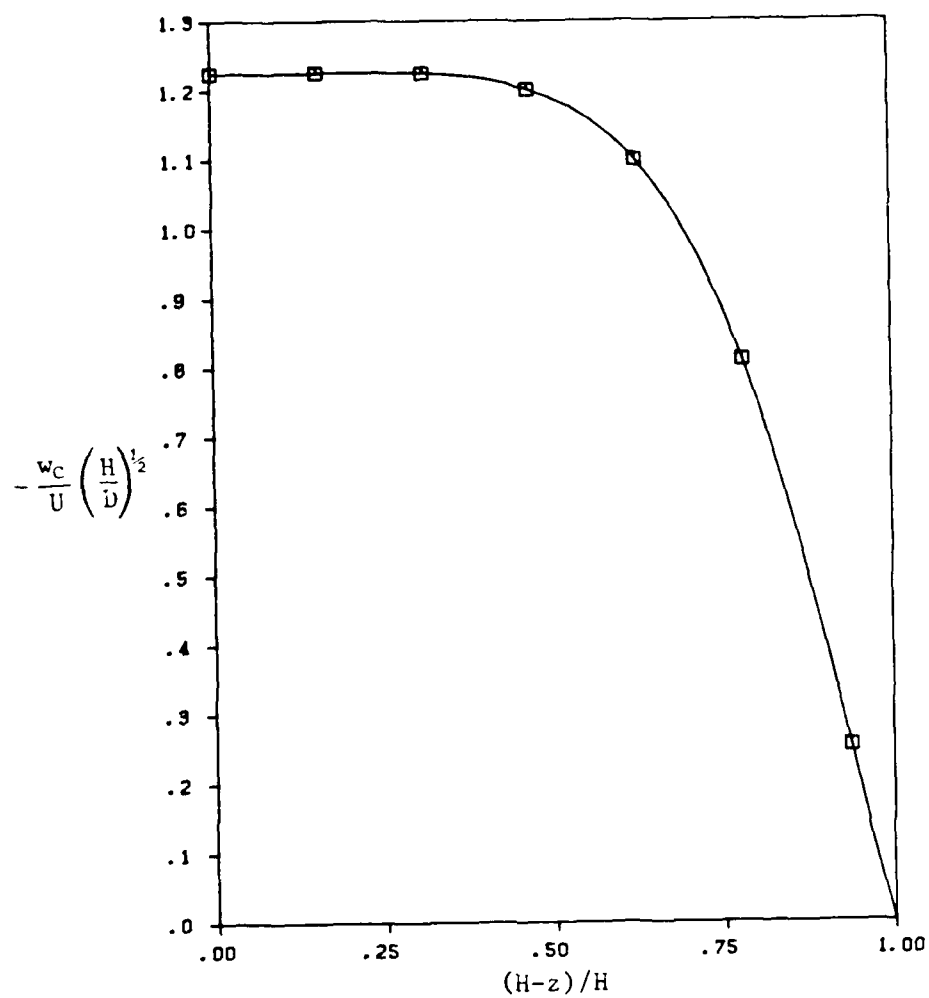


a. jet half-velocity width as a function of  $z/D$



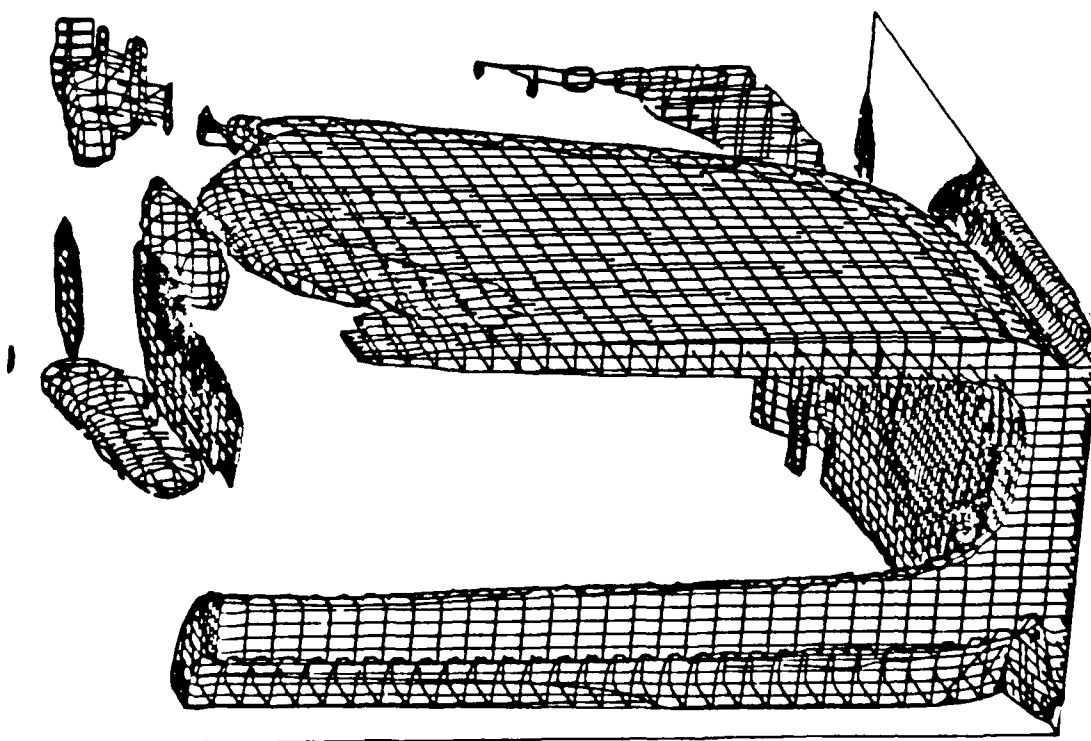
b. fountain half-velocity width as a function of  $z/D$

Figure 7. Steady-state spreading of the impinging jet and the fountain at  $t = 11.3$  for  $H = 1.5D$ .

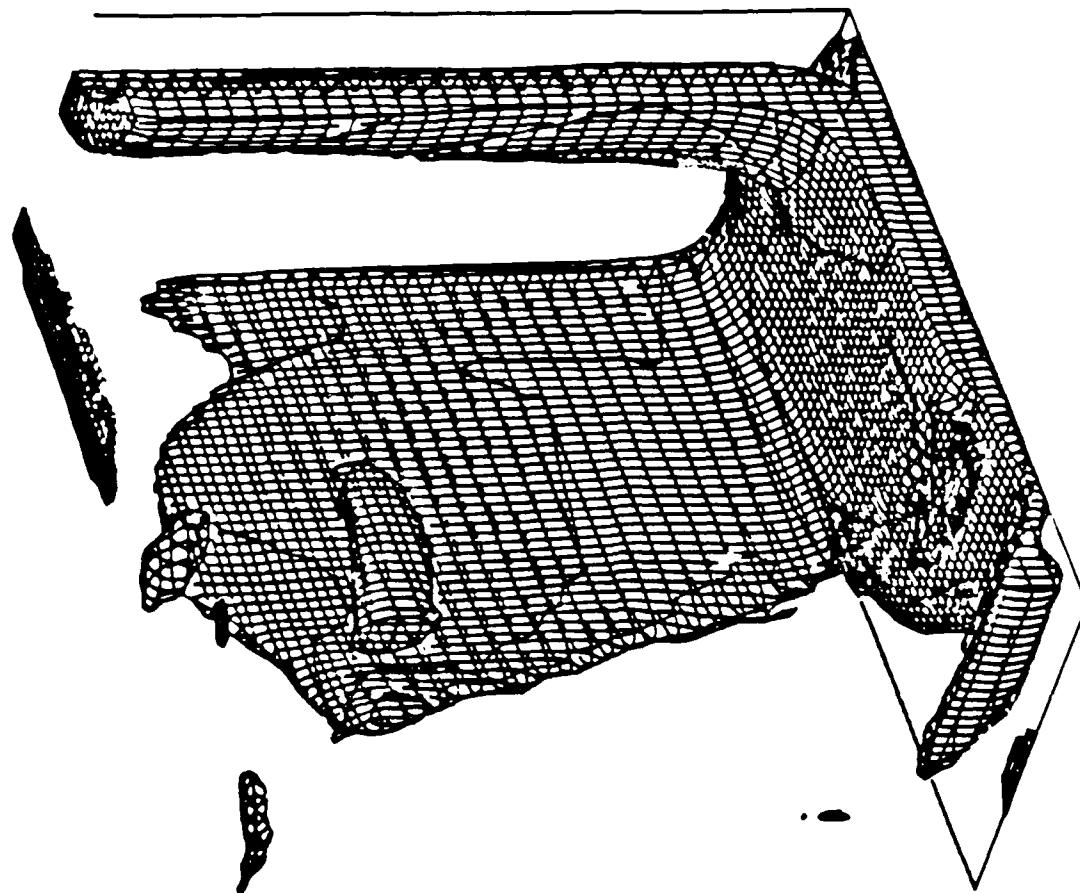


c. variation of the centerline velocity as a function of height

Figure 7. Steady-state spreading of the impinging jet and the fountain at  $t = 11.3$  for  $H = 1.5D$ . (Cont.)

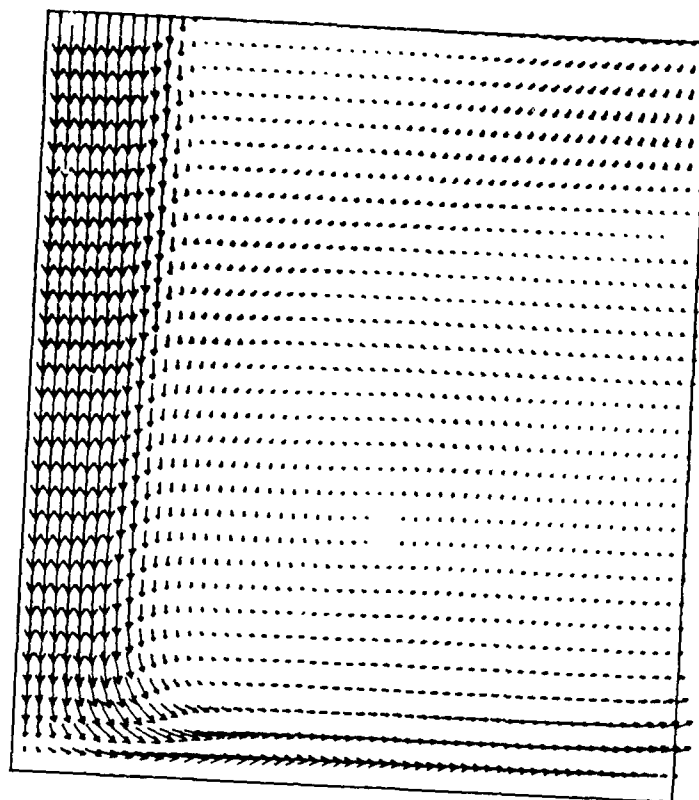


a. view of the impinging jet and the fountain at a level  $|\omega| = 1.75$

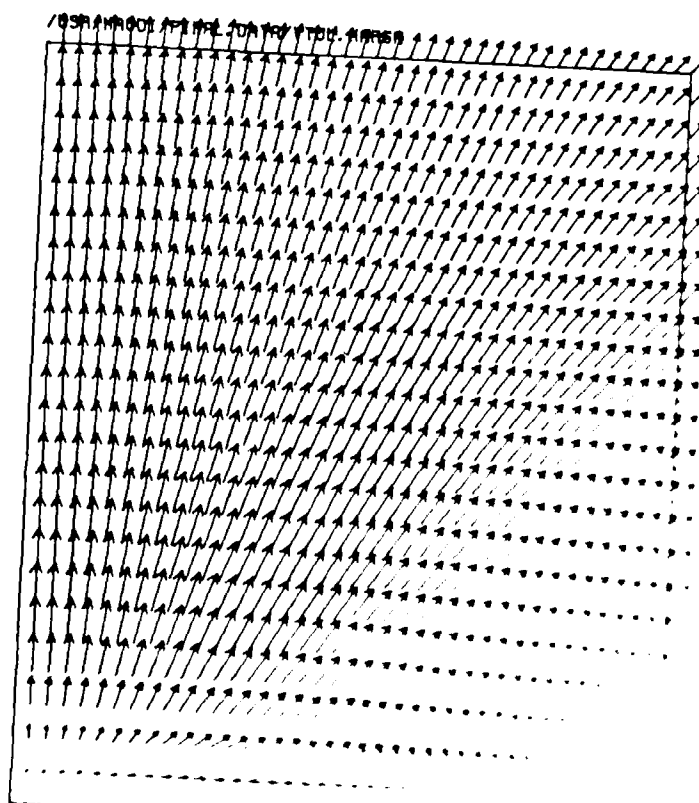


b. view of the impinging jet and the outflow at a level  $|\omega| = 1.95$

Figure 8. Three-dimensional perspective of the steady-state vorticity surface for  $H = 3D$  at  $t = 29.5$ .



a. velocity vector field in the  $x = 0$  plane



b. velocity vector field

Figure 9. Steady-state velocity vector field for  $H = 3D$ .

TR-403/4-87

AD-A182 459

LARGE-EDDY NUMERICAL SIMULATION OF AN ARRAY OF  
THREE-DIMENSIONAL IMPINGING JETS(U) FLOW RESEARCH CO  
KENT WA M H RIZK ET AL APR 87 FLOW-RR-483

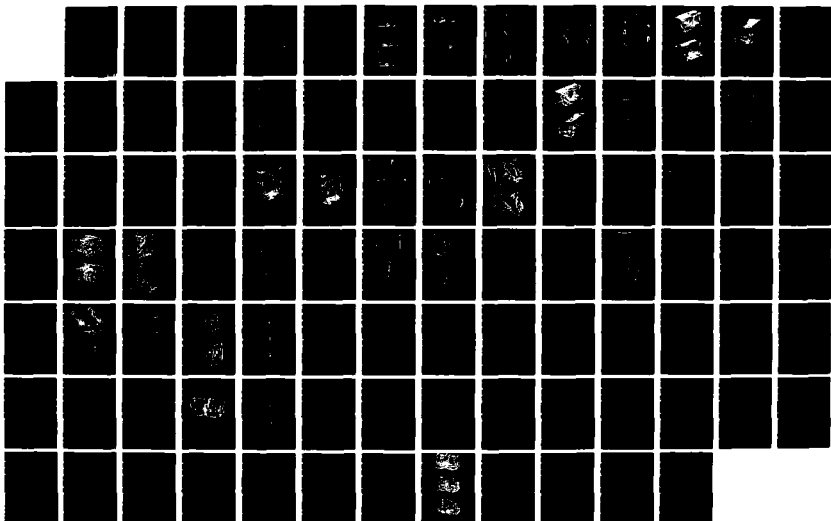
2/2

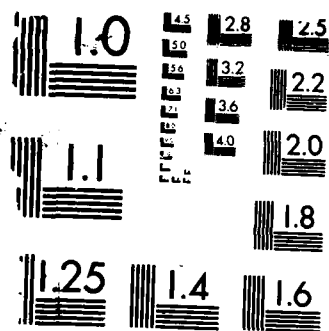
UNCLASSIFIED

AFOSR-TR-87-0908 F49620-85-C-0084

F/G 1/1

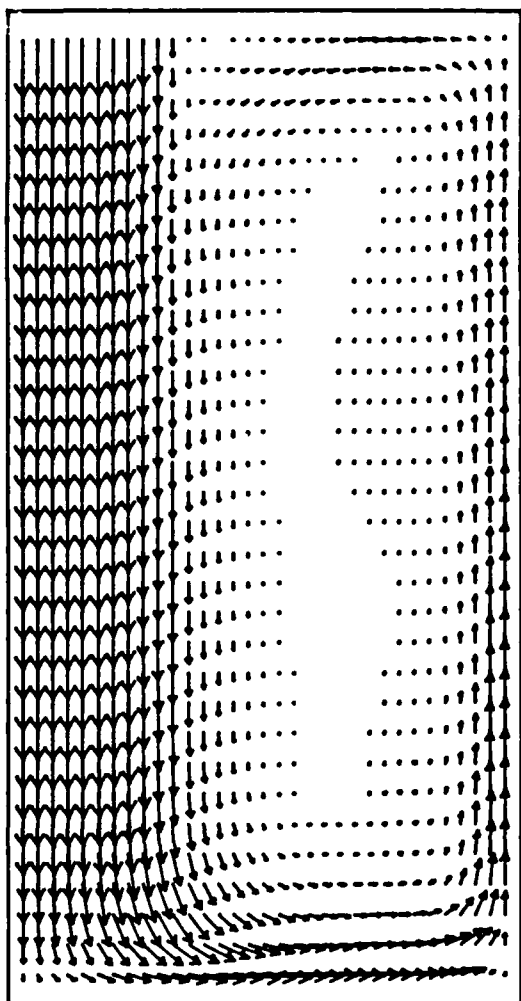
NL



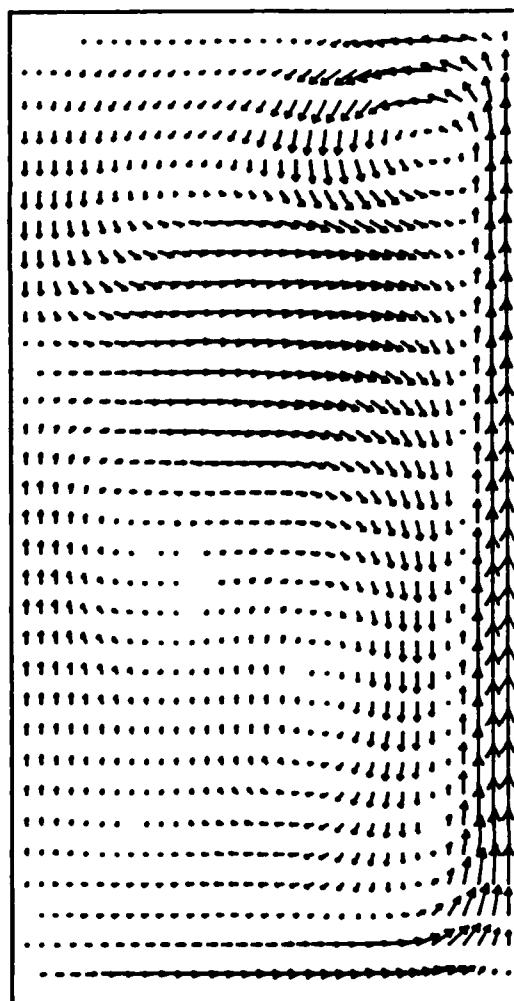


MICROCOPY RESOLUTION TEST CHART



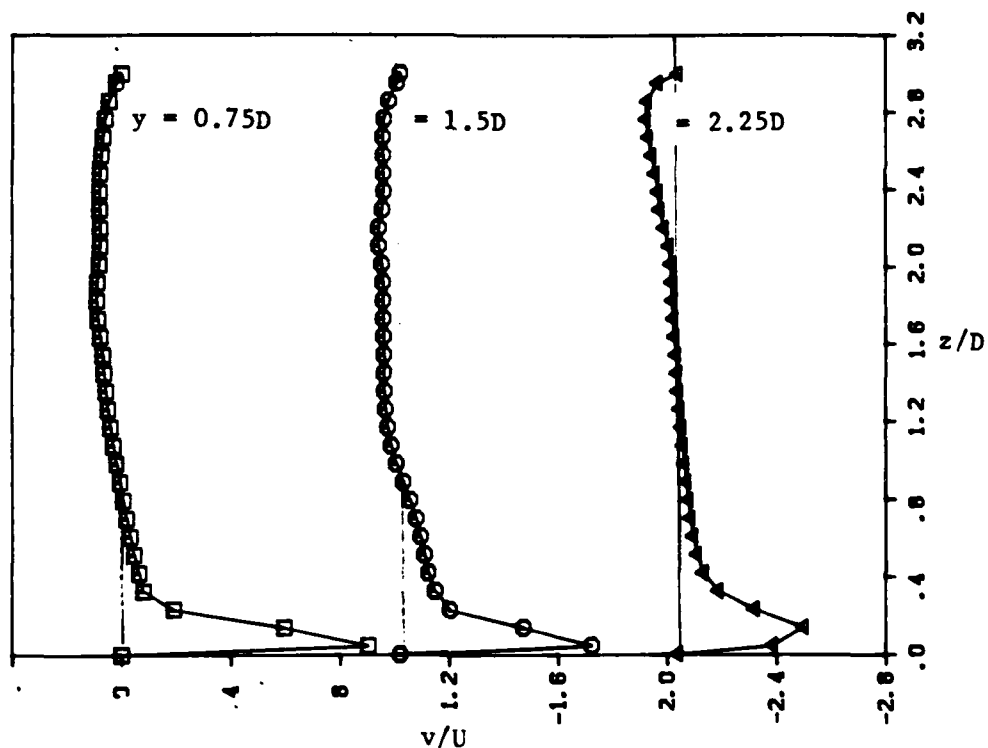


a. velocity vector field in the  $y = 0$  plane

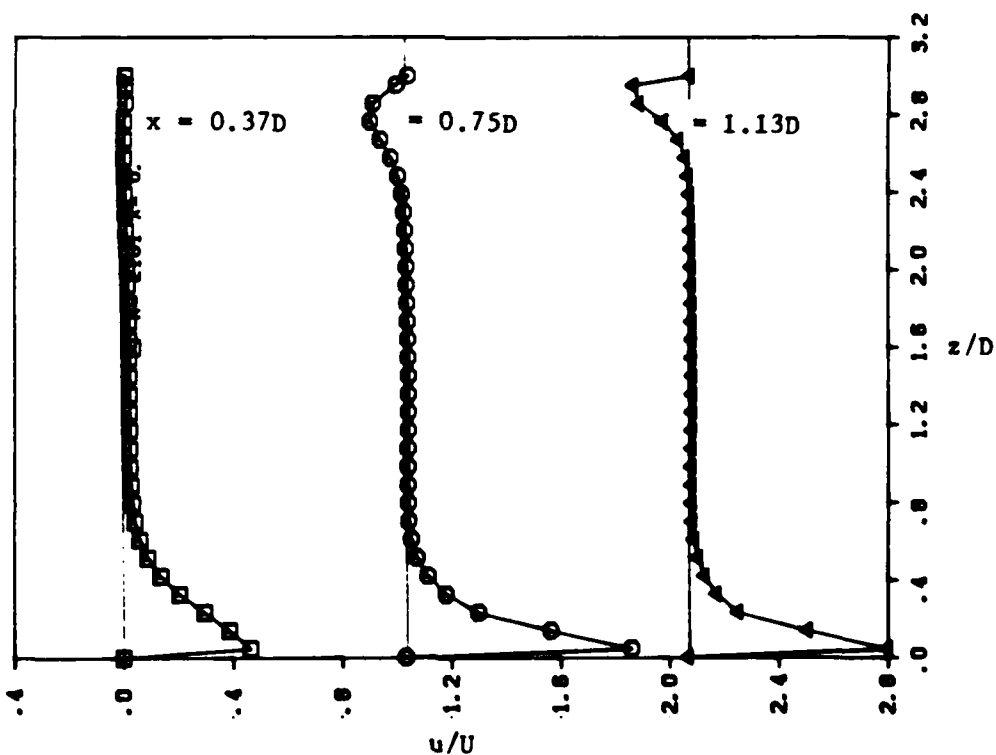


b. velocity vector field in the  $y = 1.5D$  plane

Figure 10. Steady-state velocity vector diagram in the  $x$ - $z$  plane at  $t = 29.5$  for  $H = 3D$ .

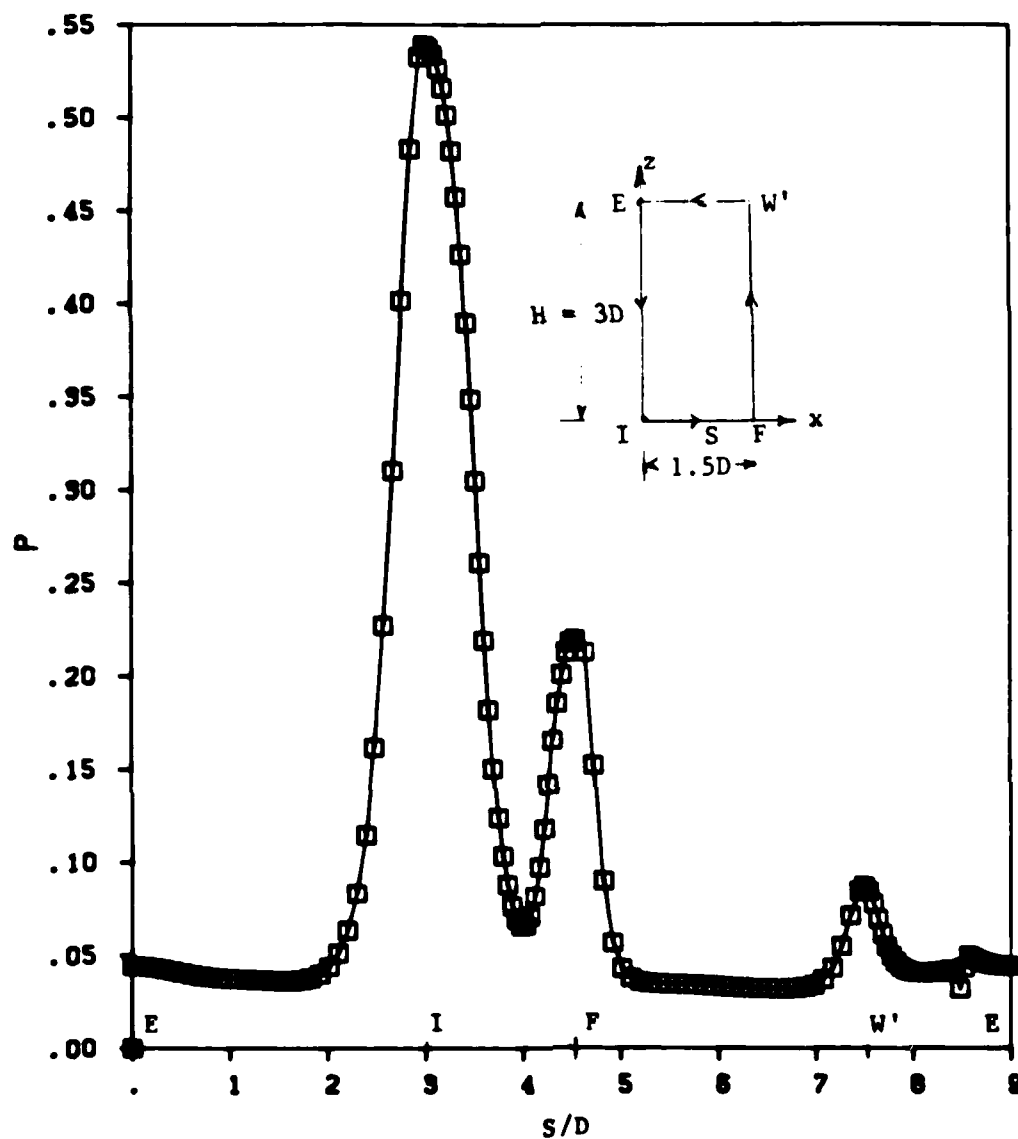


a. v-velocity profiles in the y-z plane at  $x = 0$   
as a function of  $z$  at various y-locations



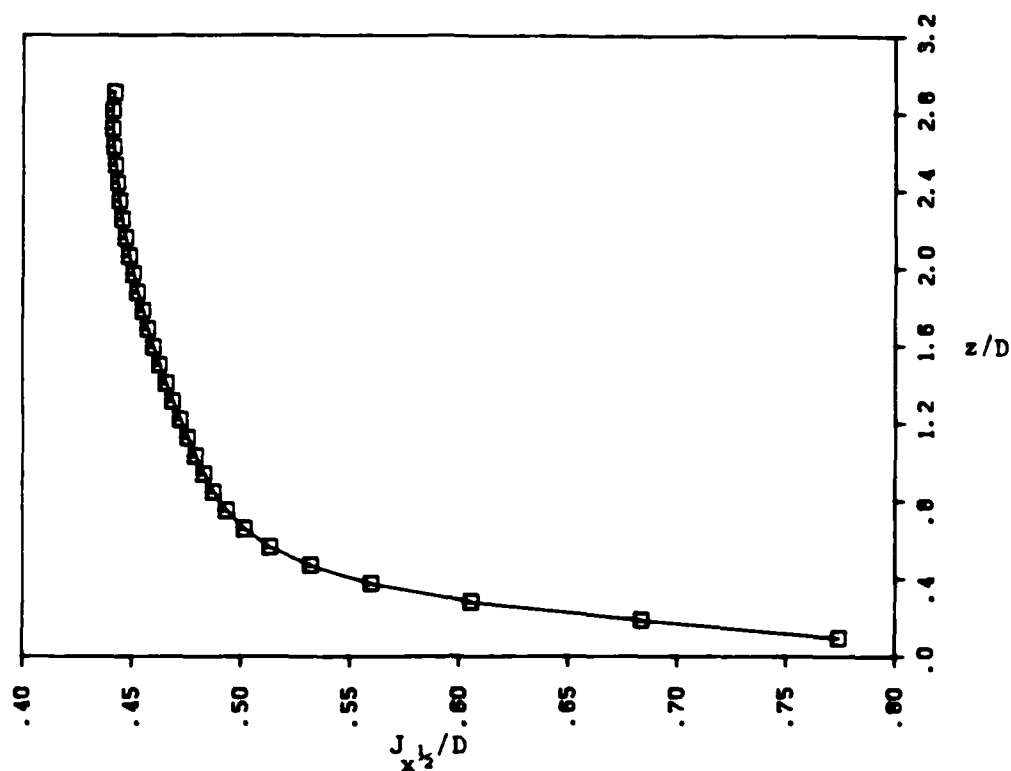
b. u-velocity profiles in the x-z plane at  $y = 0$   
as a function of  $z$  at various x-locations

Figure 11. Steady-state velocity profiles at  $t = 29.5$  for  $H = 3D$ .

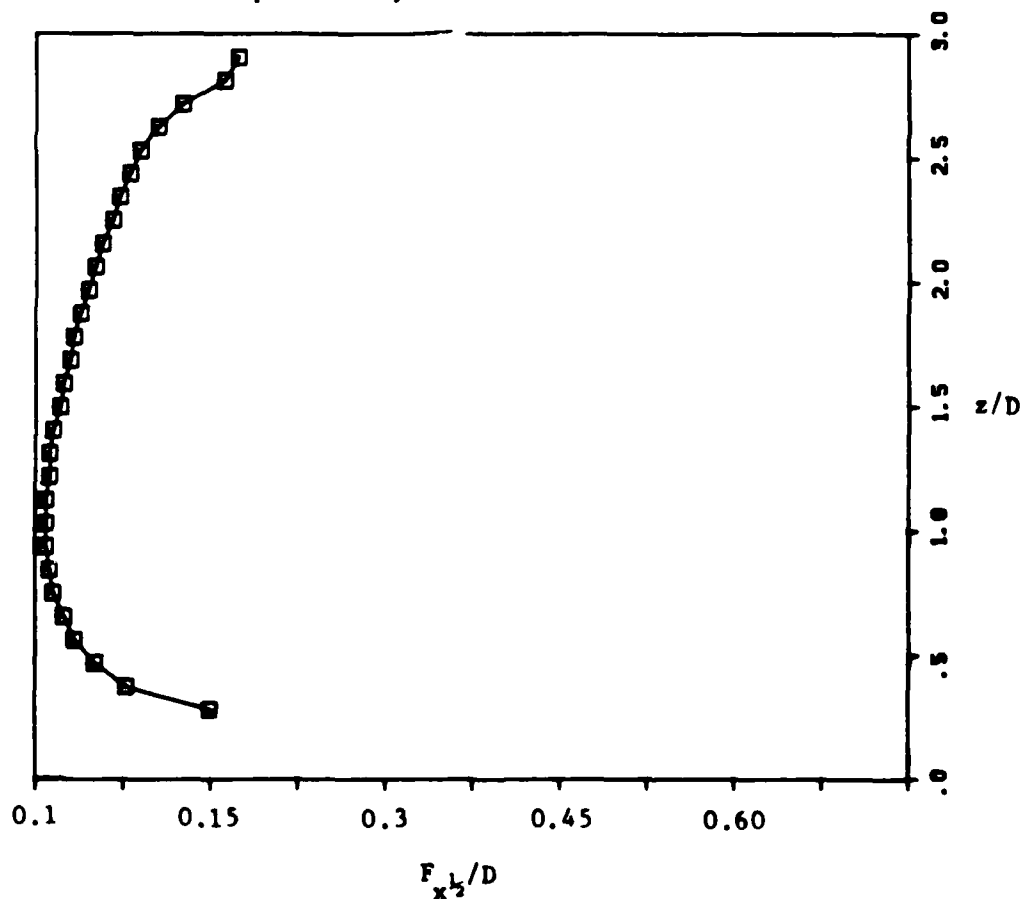


a. steady-state pressure variation along the boundaries

Figure 12. Steady-state pressure variation and spreading of the impinging jet and the fountain at  $t = 29.5$  for  $H = 3D$ .

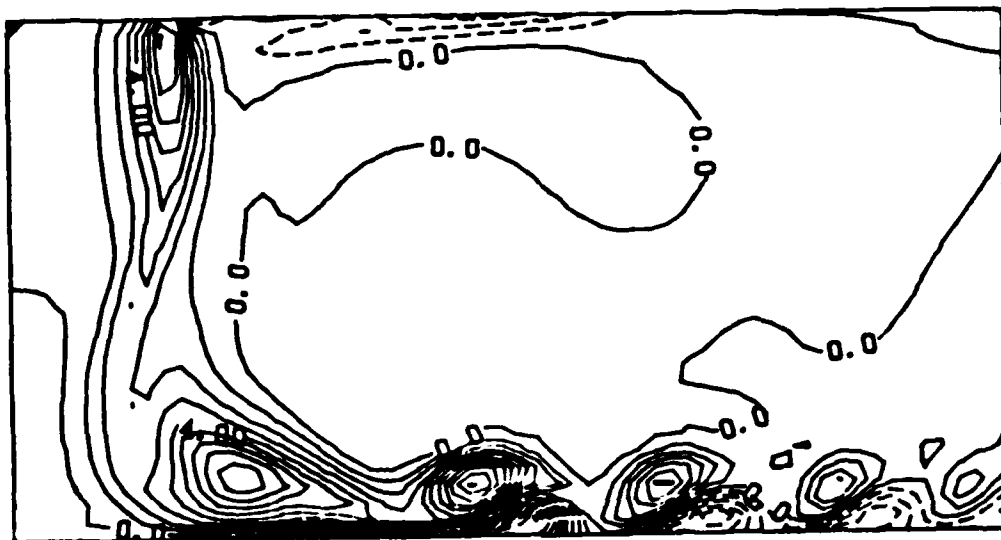


b. steady-state jet half-velocity width as a function of  $z$  in the  $x$ - $z$  plane at  $y = 0$

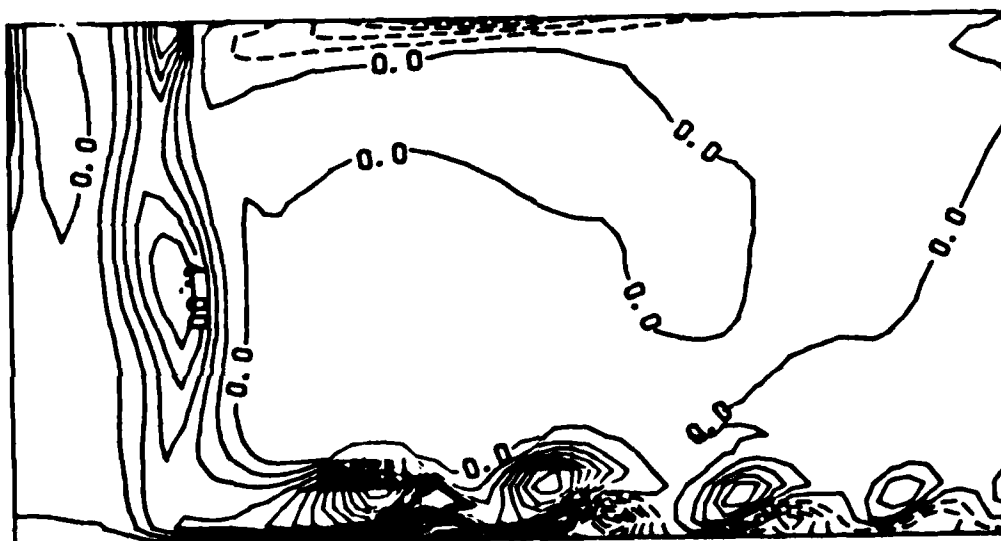


c. steady-state fountain half-velocity width as a function of  $z$  in the  $x$ - $z$  plane at  $y = 0$

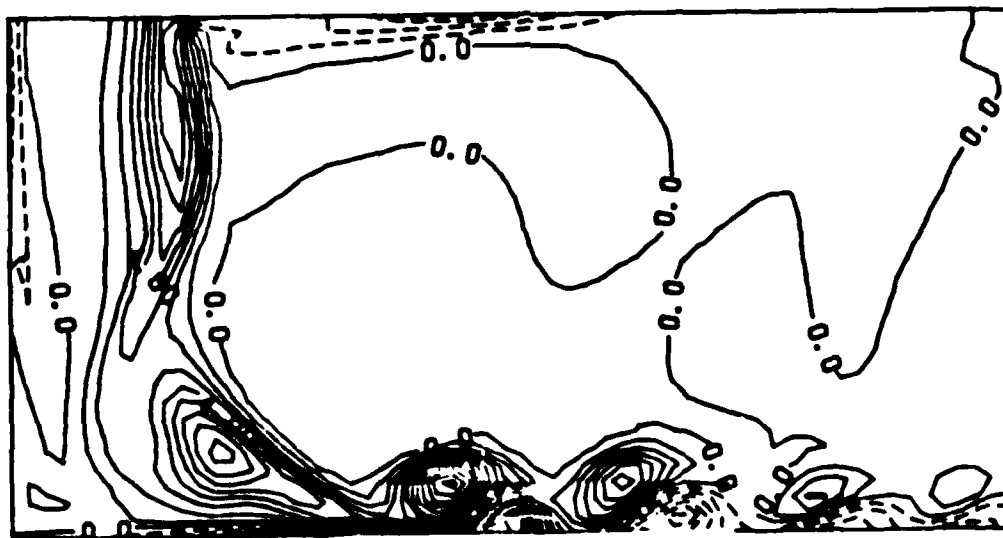
Figure 12. Steady-state pressure variation and spreading of the impinging jet and the fountain at  $t = 29.5$  for  $H = 3D$ . (Cont.)



a.  $x = 0$  plane at  $t = 37.98$

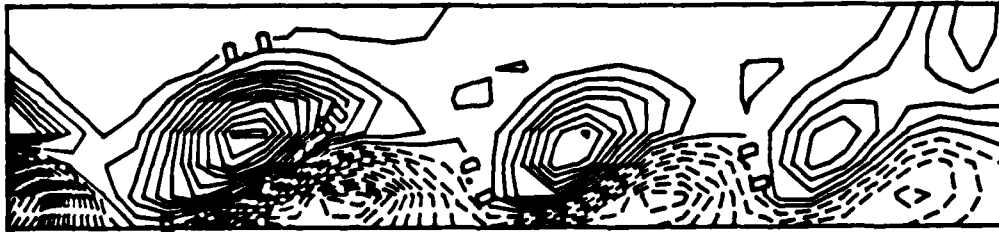


b.  $x = 0$  plane at  $t = 39.02$

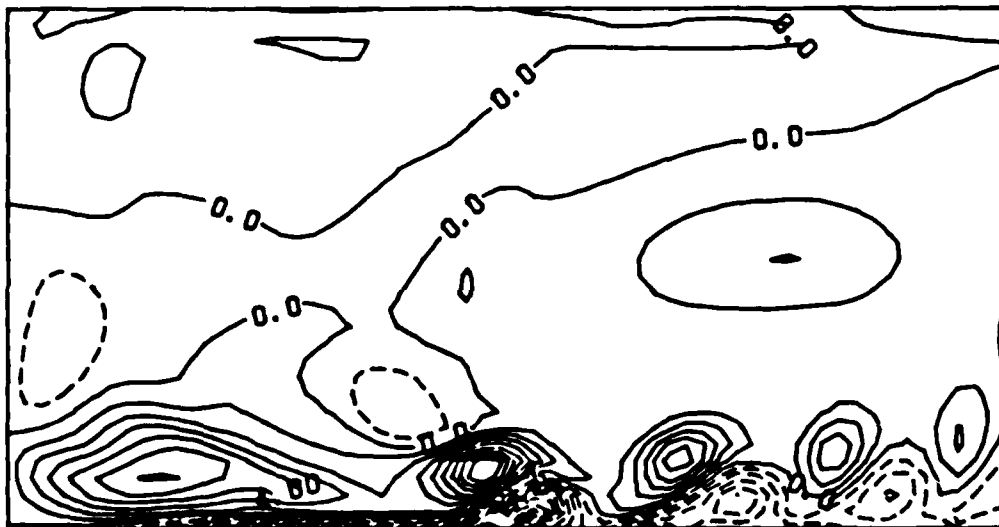


c.  $x = 0$  plane at  $t = 40.08$

Figure 13. Time sequence of the  $x$ -vorticity contours for a forcing cycle at  $St = 0.47$  in the  $y$ - $z$  plane for  $H = 1.5D$  (contour interval = 1.0).

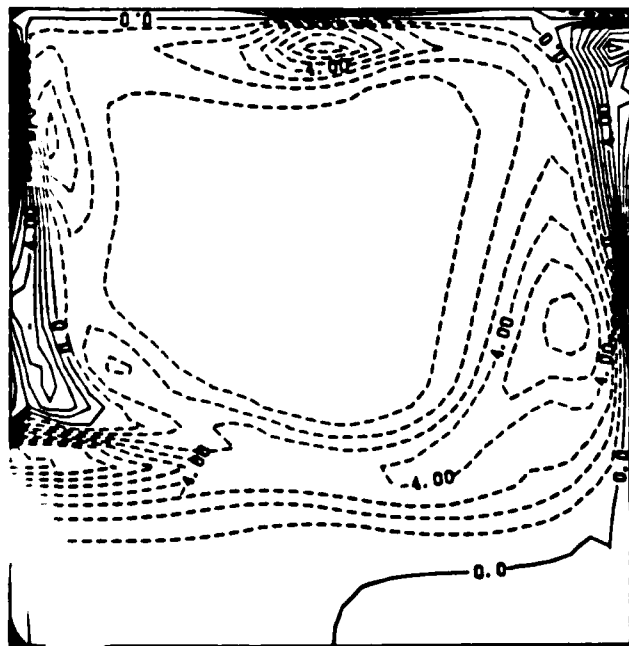


d. x-vorticity contours in the vicinity of the ground plane in the y-z plane at  $x = 0$  and  $t = 37.98$  (contour interval = 0.5)

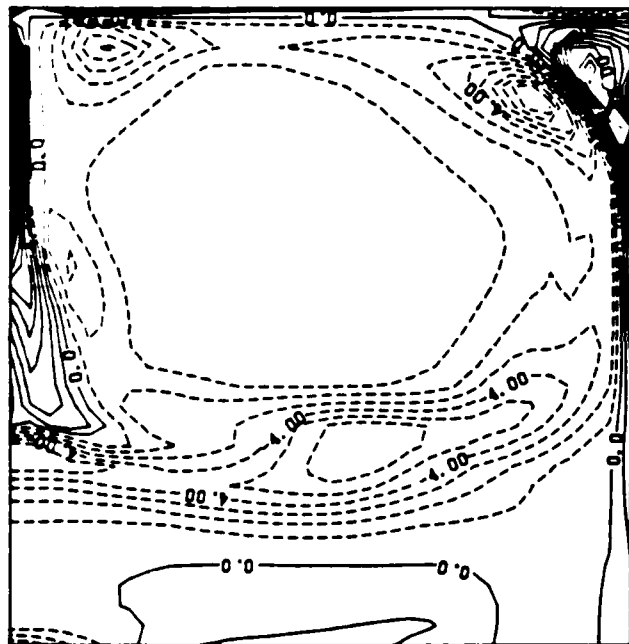


e.  $x = 0.51D$  plane at  $t = 37.98$

Figure 13. Time sequence of the x-vorticity contours for a forcing cycle at  $St = 0.47$  in the y-z plane for  $H = 1.5D$  (contour interval = 1.0). (Cont.)



a.  $y = 0$  plane at  $t = 37.98$



b.  $y = 0$  plane at  $t = 39.02$



c.  $y = 0$  plane at  $t = 40.08$



d.  $y = 0.51D$  plane at  $t = 37.98$

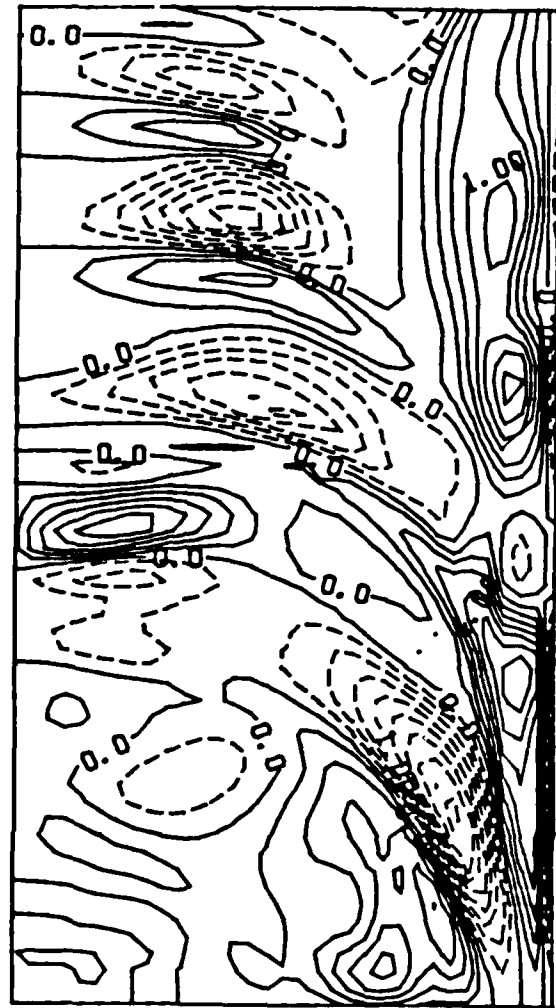


e.  $y = 1.5D$  plane at  $t = 37.98$

Figure 14. Time sequence of the y-vorticity contours for a forcing cycle at  $St = 0.47$  in the x-z plane for  $H = 1.5D$  (contour interval = 1.0 for  $a - d$ ; 0.5 for  $e$ ).



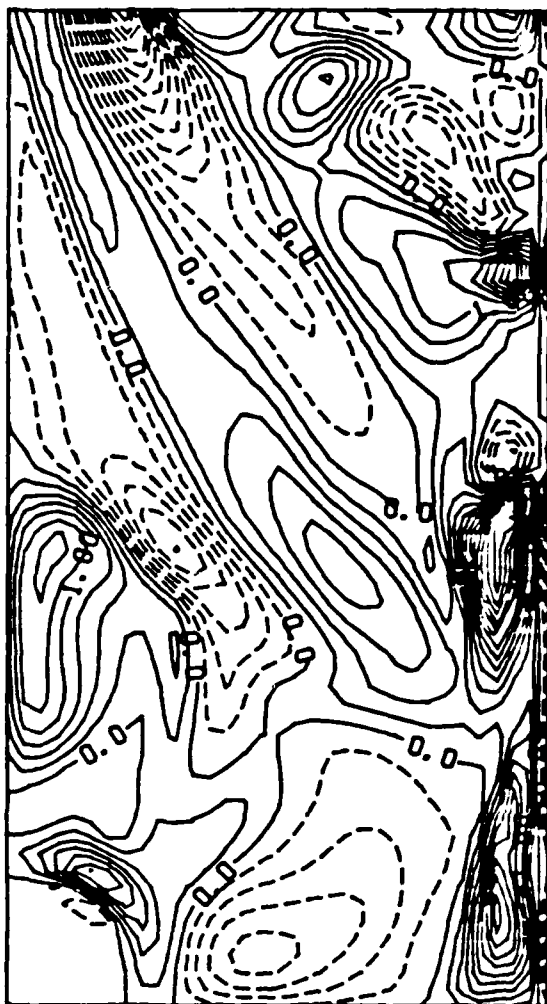
a.  $z = 0.14D$  plane at  $t = 37.98$



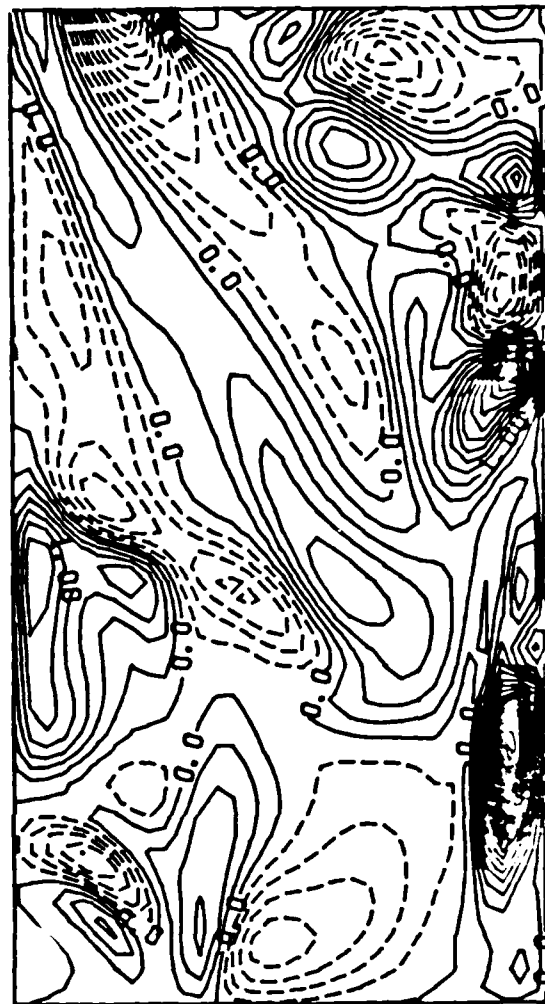
b.  $z = 0.14D$  plane at  $t = 39.02$

Figure 15.  $z$ -vorticity contours for a forcing cycle at  $St = 0.47$  in the  $x$ - $y$  plane for  $H = 1.5D$  (contour interval = 0.25).



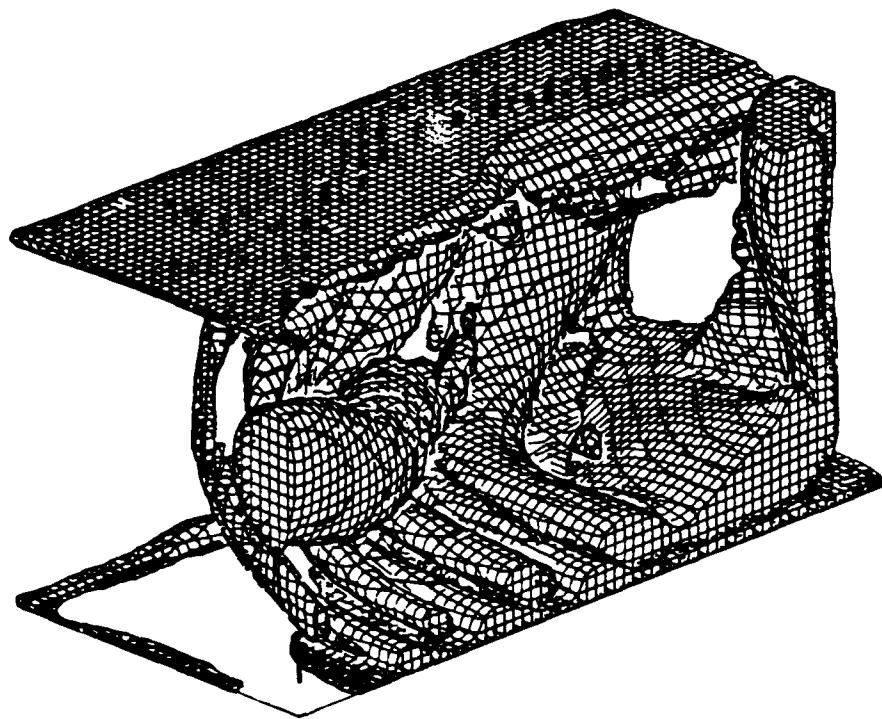


c.  $z = 0.8D$  plane at  $t = 37.98$

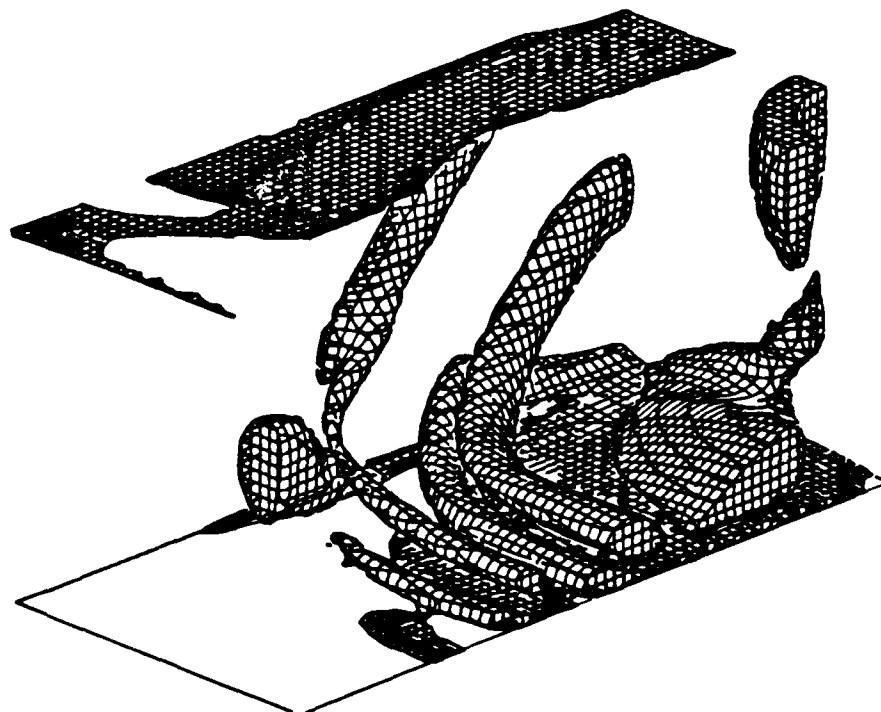


d.  $z = 0.8D$  plane at  $t = 39.02$

Figure 15.  $z$ -vorticity contours for a forcing cycle at  $St = 0.47$  in the  $x$ - $y$  plane for  $H = 1.5D$  (contour interval = 0.25). (Cont.)

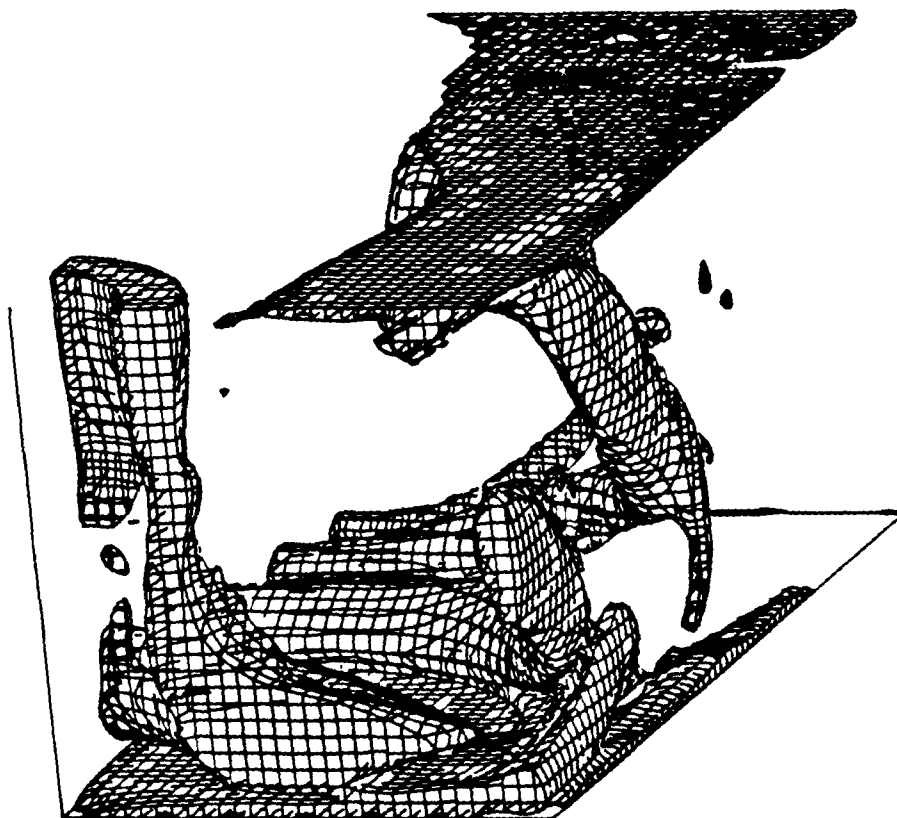


a. view of the impinging jet and the outflow at a level  $|\omega| = 1.95$



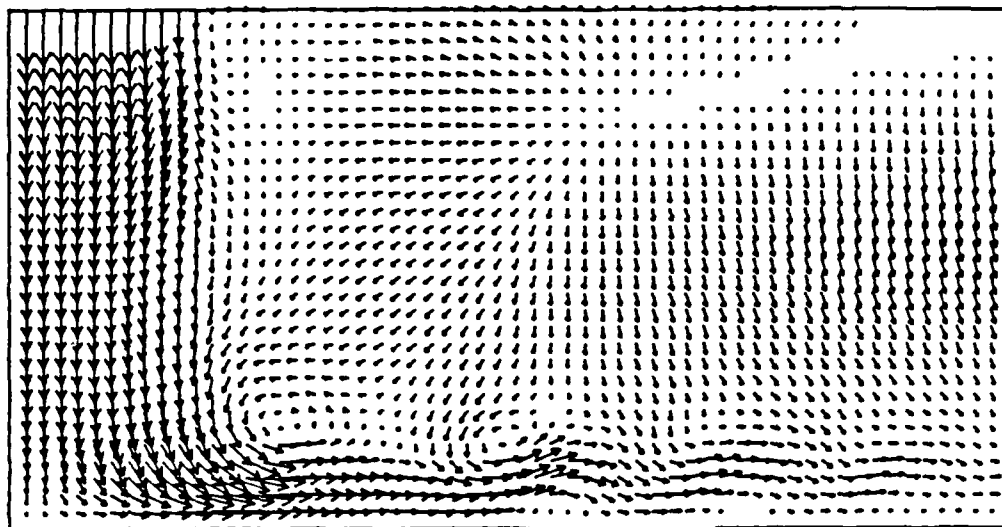
b. view of the impinging jet and the outflow at a level  $|\omega| = 3.72$

Figure 16. Three-dimensional perspective of the vorticity surface at  $t = 37.98$  for axisymmetric forcing at  $St = 0.47$  for  $H = 1.5D$ .

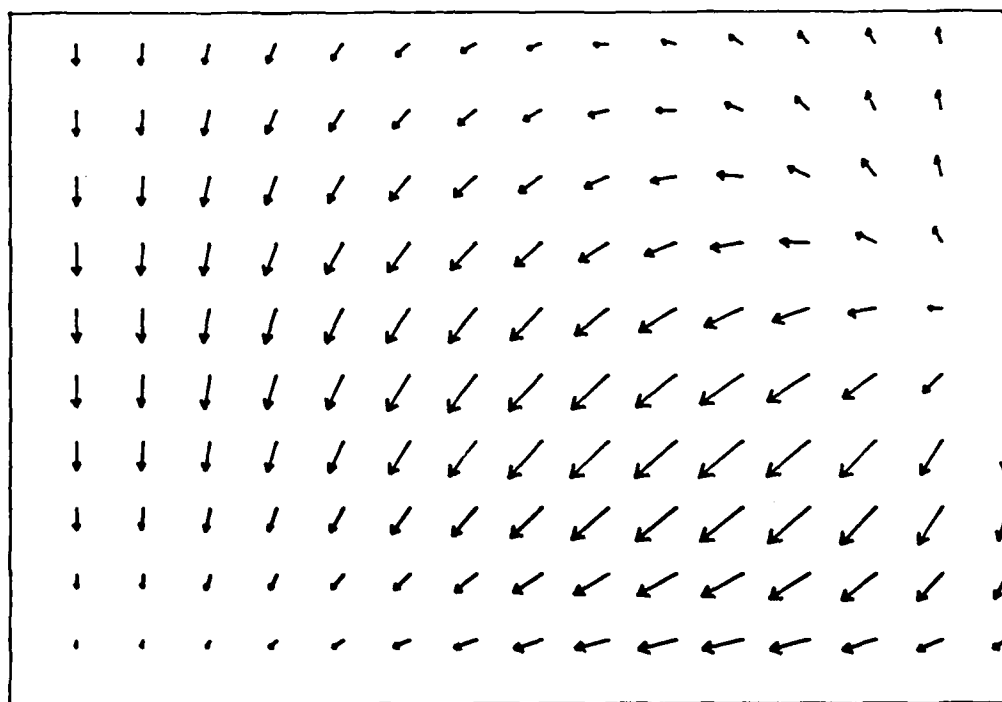


c. view of the impinging jet and the fountain at a level  $|\omega| = 2.90$

Figure 16. Three-dimensional perspective of the vorticity surface at  $t = 37.98$  for axisymmetric forcing at  $St = 0.47$  for  $H = 1.5D$ . (Cont.)

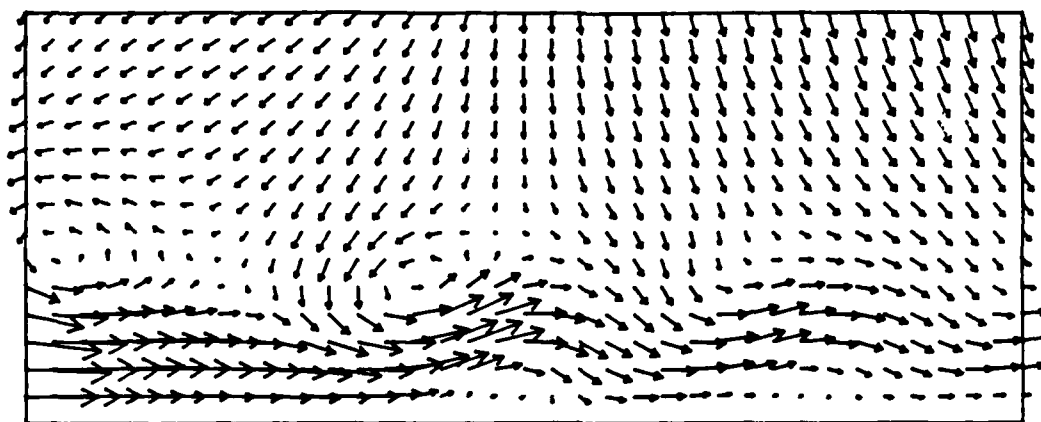


a. velocity vector field



b. pressure gradient vector field near the impingement zone

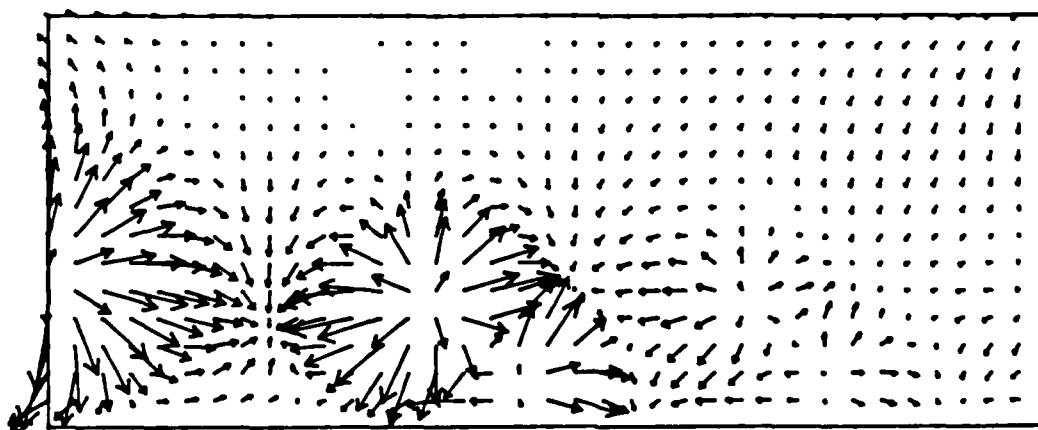
Figure 17. Distribution of the velocity, pressure gradient and vorticity fields at  $t = 37.98$  in the  $y$ - $z$  plane at  $x = 0$  for forcing at  $St = 0.47$ .



c. velocity vector field near the ground

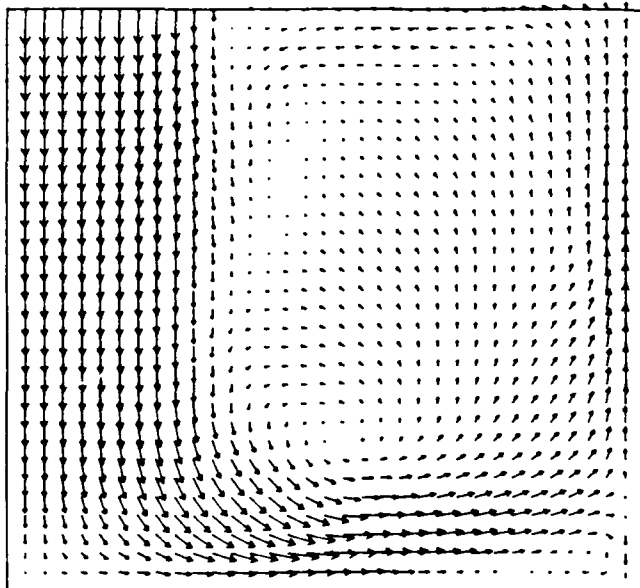


d. x-vorticity contours near the ground  
(contour interval = 1.0)

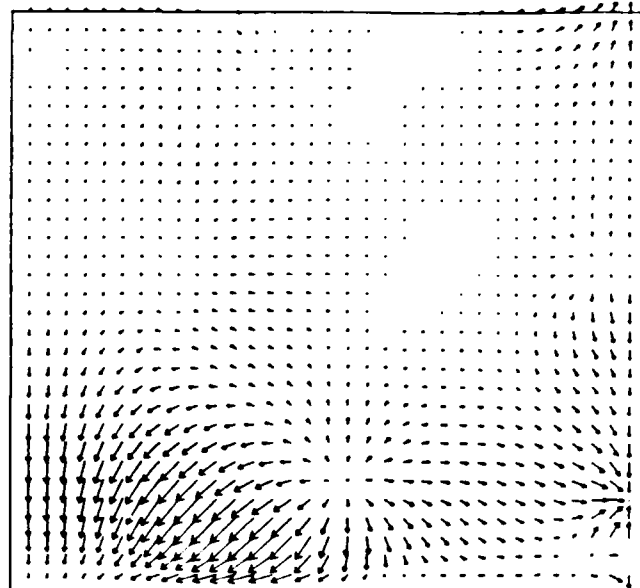


e. pressure gradient field near the ground

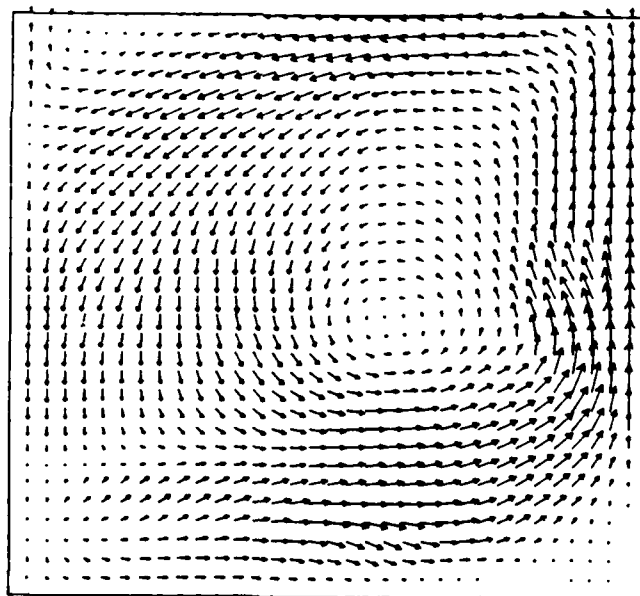
Figure 17. Distribution of the velocity, pressure gradient and vorticity fields at  $t = 37.98$  in the  $y-z$  plane at  $x = 0$  for forcing at  $St = 0.47$ . (Cont.)



a. velocity vector field in the  $y = 0$  plane

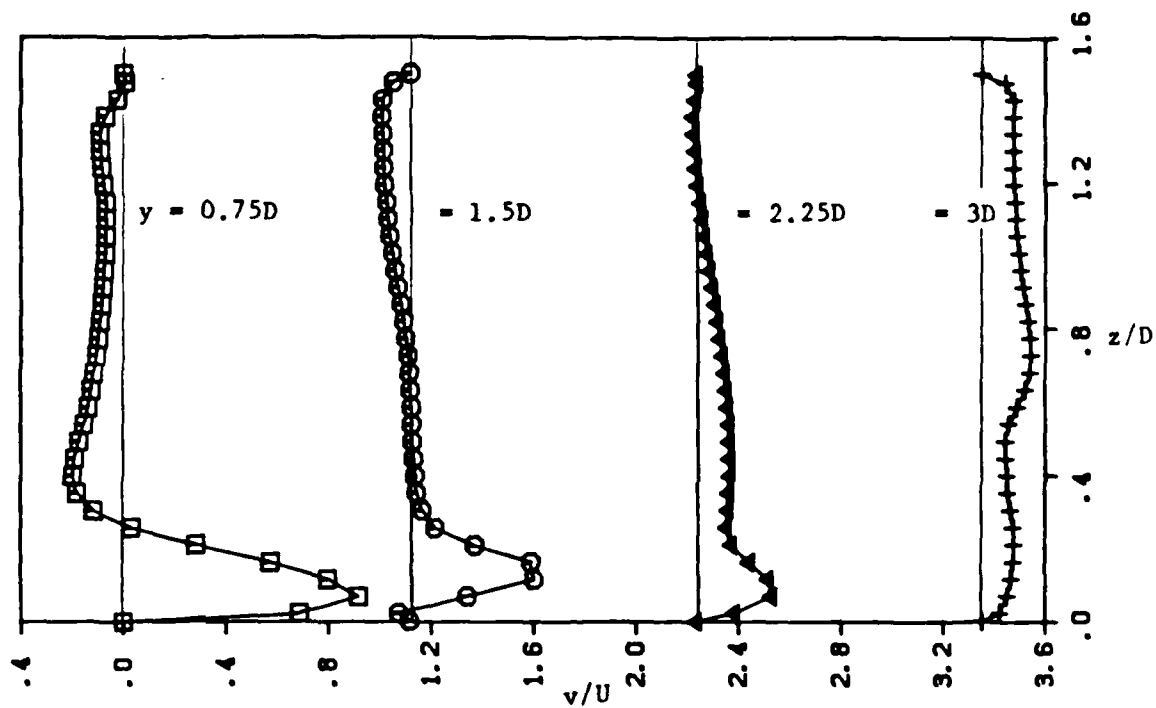


b. pressure gradient field in the  $y = 0$  plane

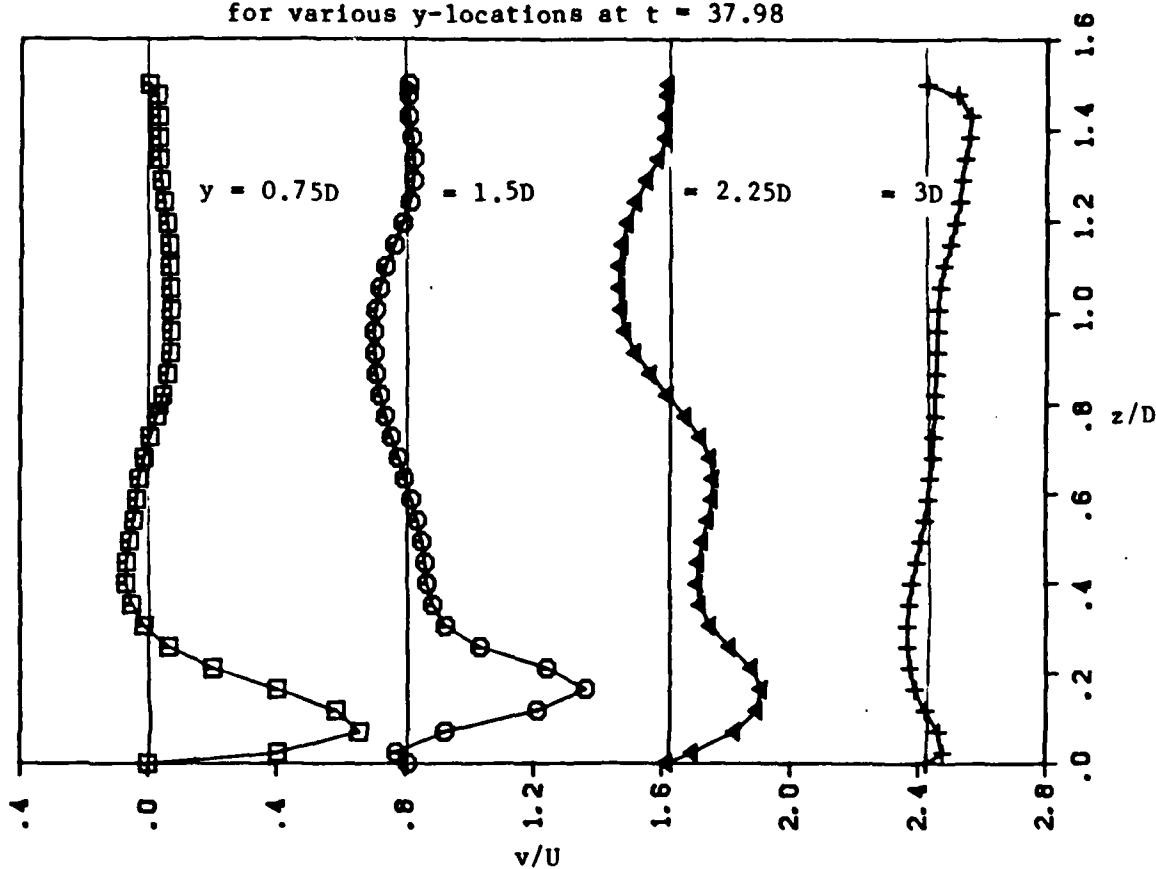


c. velocity vector field in the  $y = 1.5D$  plane

Figure 18. Velocity and pressure vector diagram at  $t = 37.98$  in the  $x$ - $z$  plane for forcing at  $St = 0.47$ .

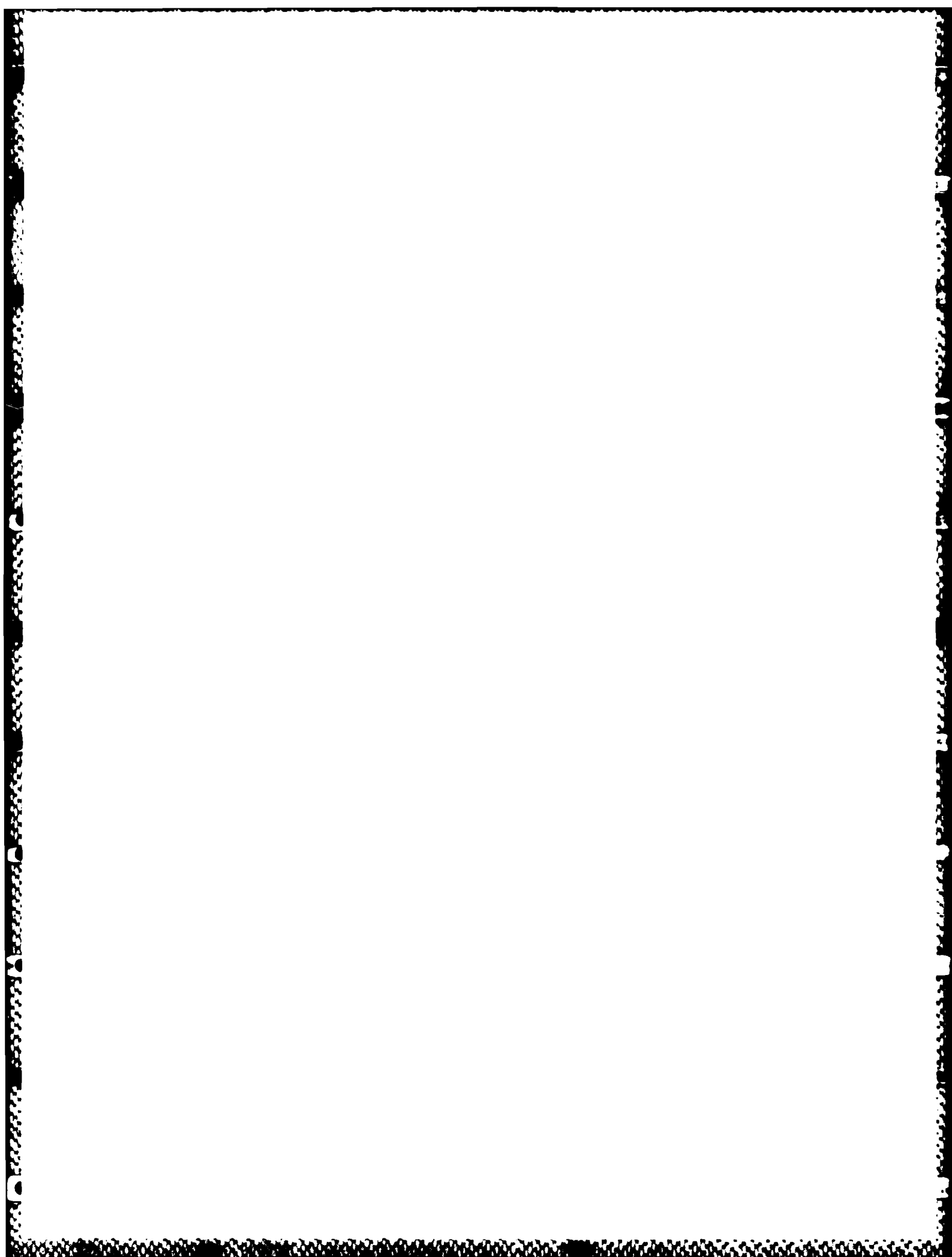


a. v-velocity profiles in the y-z plane at  $x = 0$   
for various y-locations at  $t = 37.98$

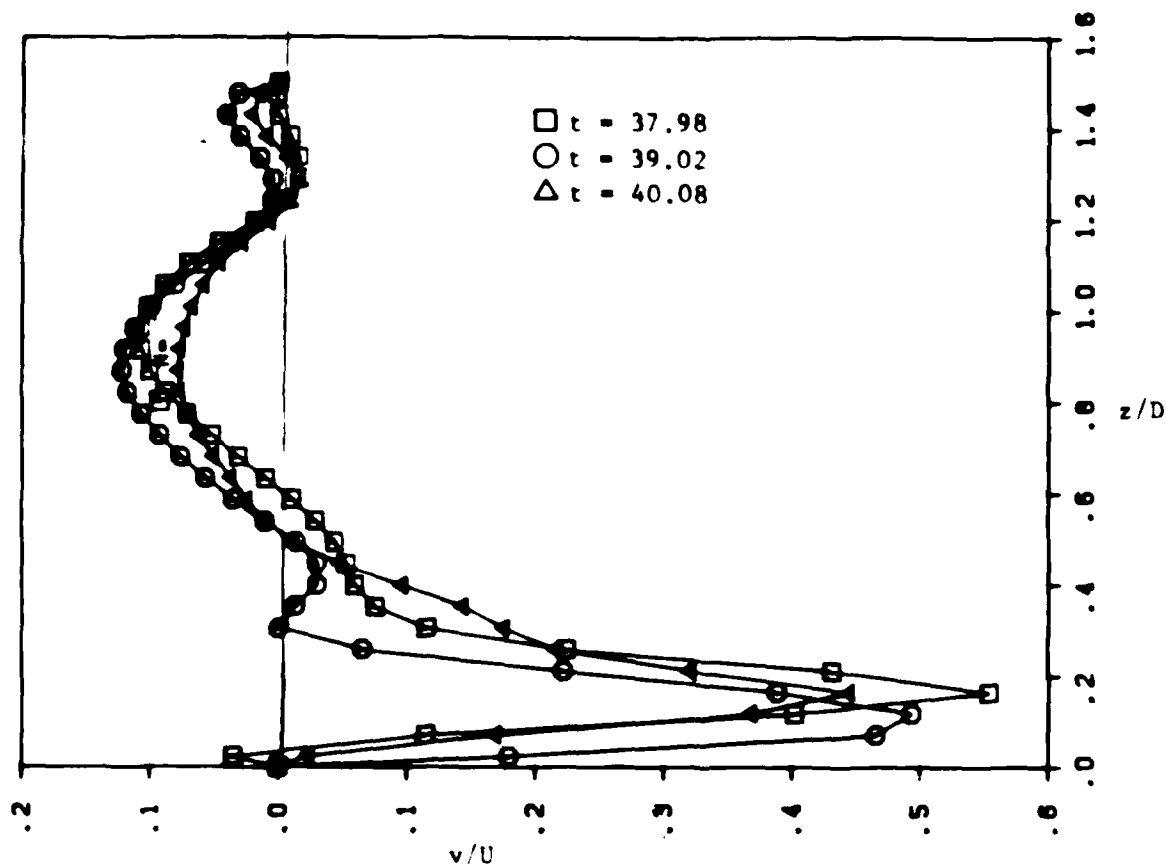


b. v-velocity profiles in the y-z plane at  $x = 0.5D$   
for various y-locations at  $t = 37.98$

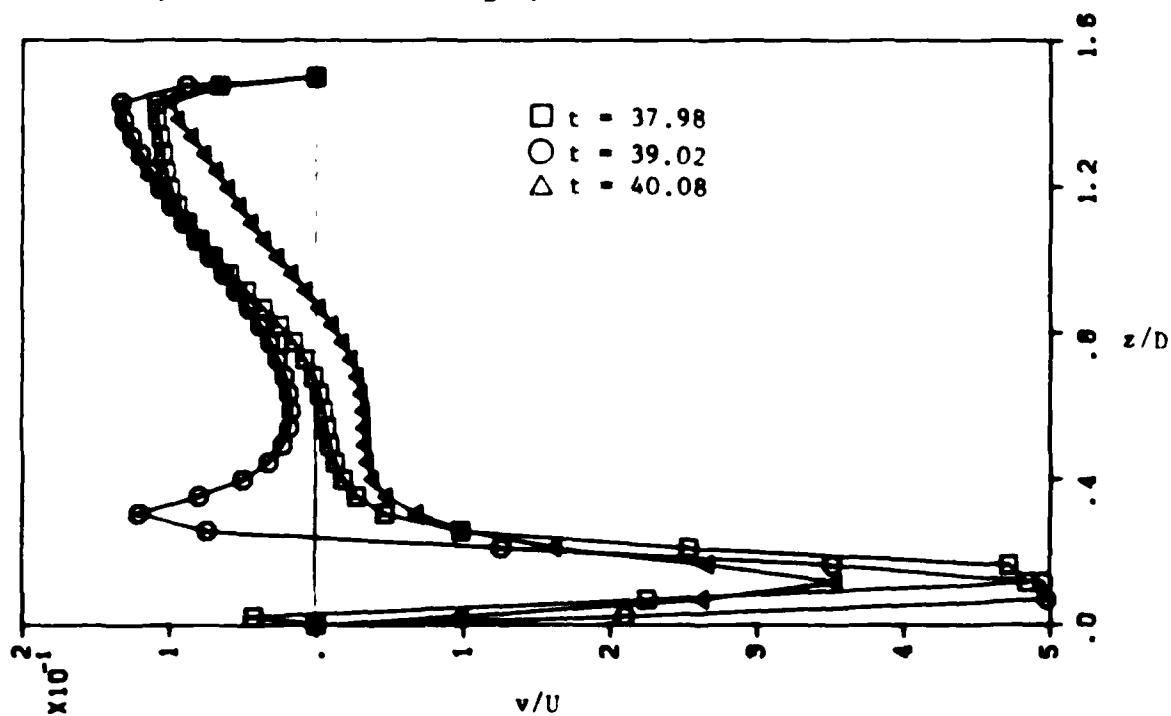
Figure 19. v-velocity profiles as a function of  $z$  for forcing at  $St = 0.47$ .





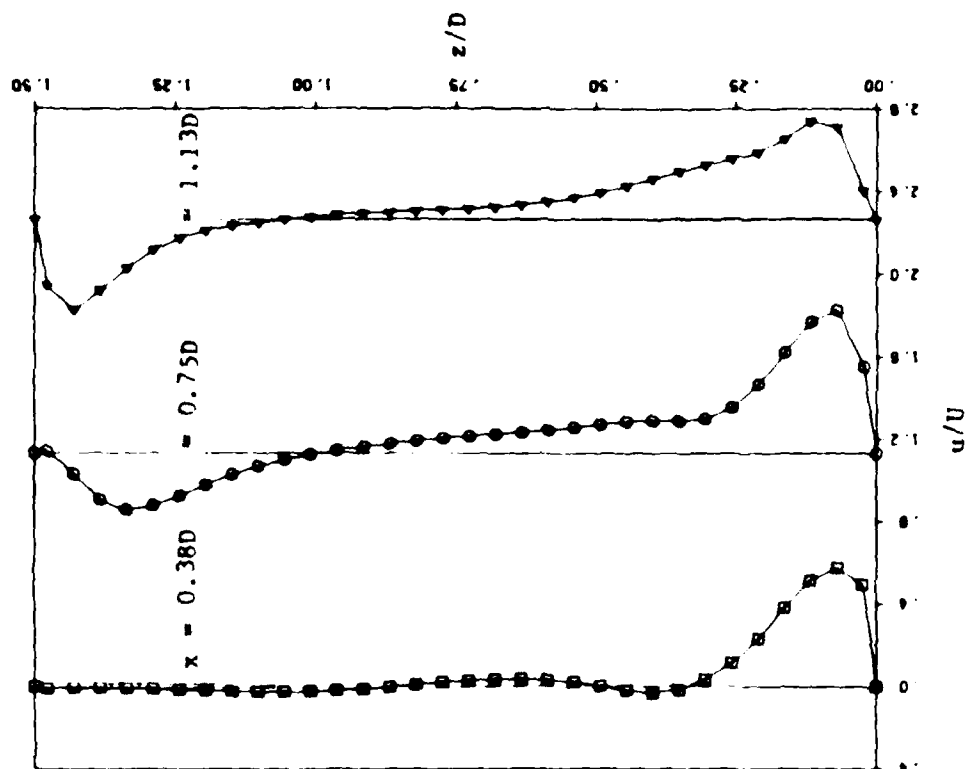


c. v-velocity profiles in the y-z plane at  $x = 0$  and  $y = 1.5D$  for a forcing cycle

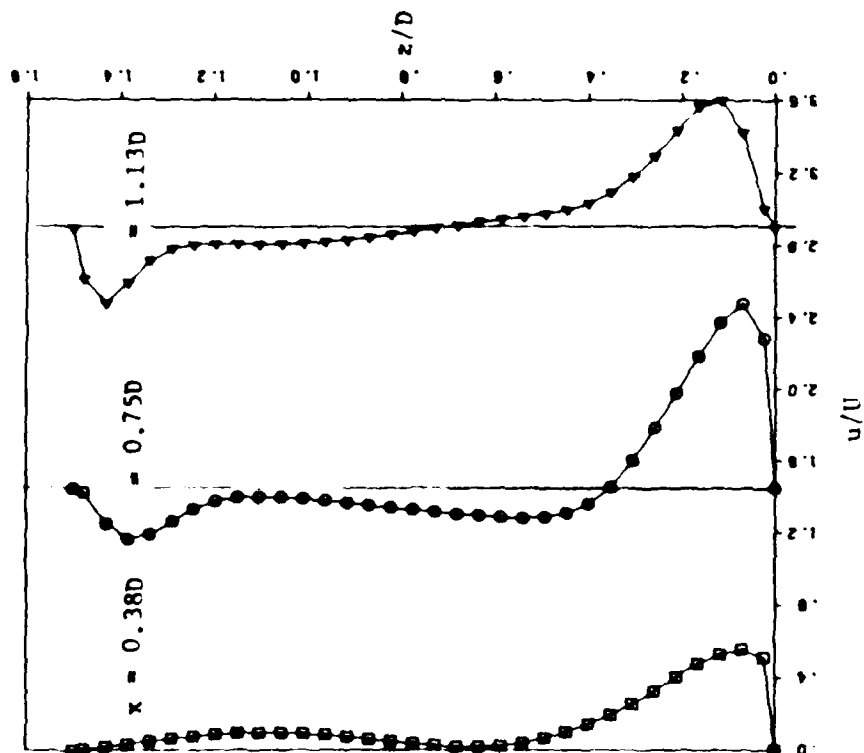


d. v-velocity profiles in the y-z plane at  $x = 0.5D$  and  $y = 1.5D$  for a forcing cycle

Figure 19. v-velocity profiles as a function of  $z$  for forcing at  $St = 0.47$ . (Cont.)

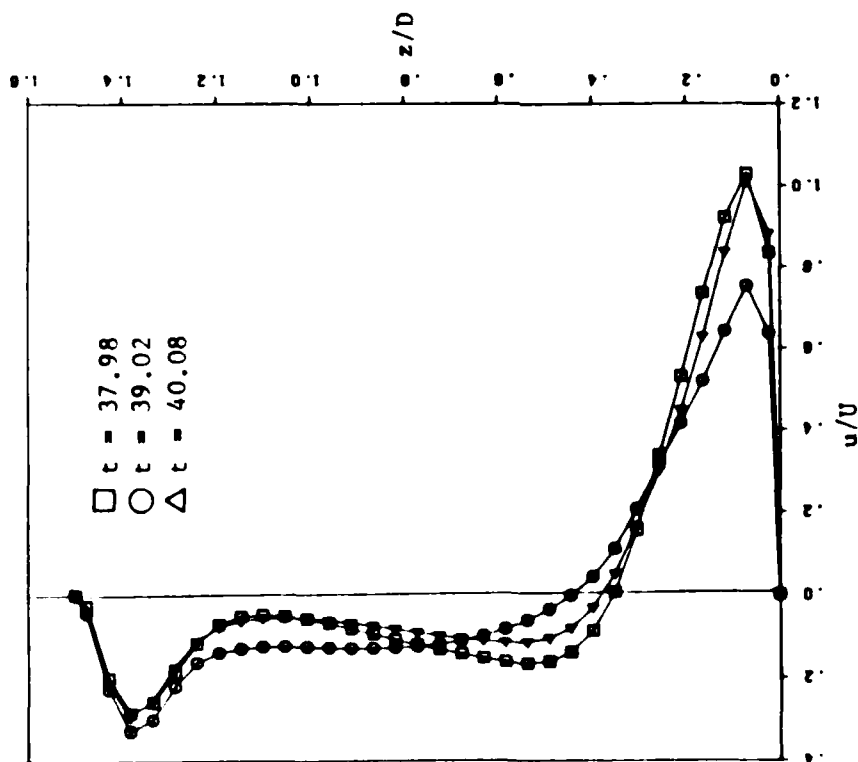


b. u-velocity profiles in the x-z plane at  $y = 0.50$  for various x-locations at  $t = 37.98$

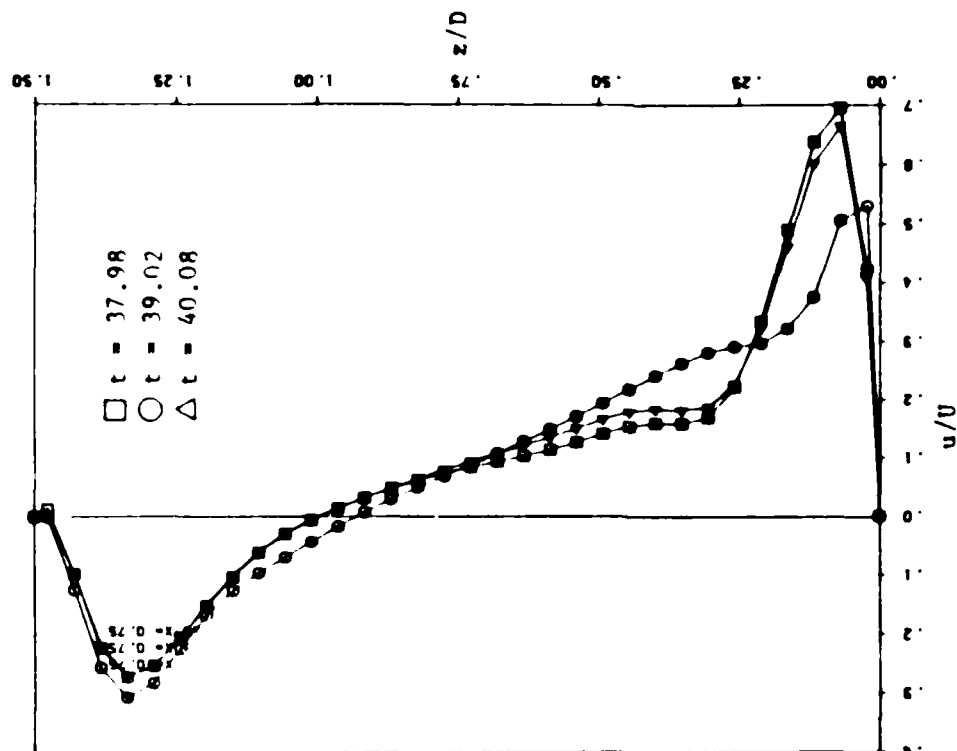


a. u-velocity profiles in the x-z plane at  $y = 0$  for various x-locations at  $t = 37.98$

Figure 20. u-velocity profiles as a function of  $z$  for forcing at  $St = 0.47$ .

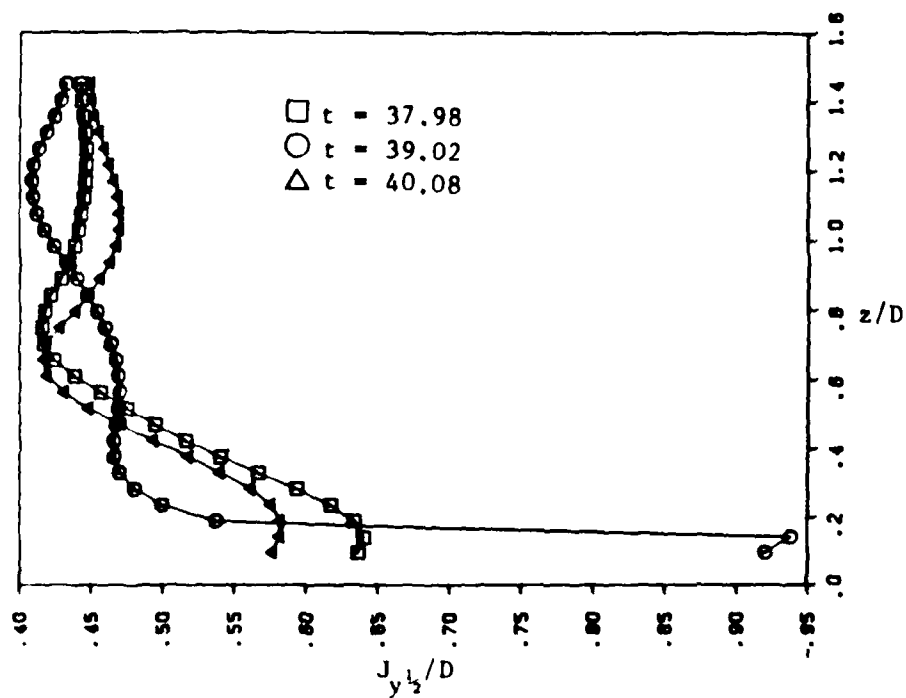


c. u-velocity profiles in the x-z plane at  $y = 0$  and  $x = 0.75D$  for a forcing cycle

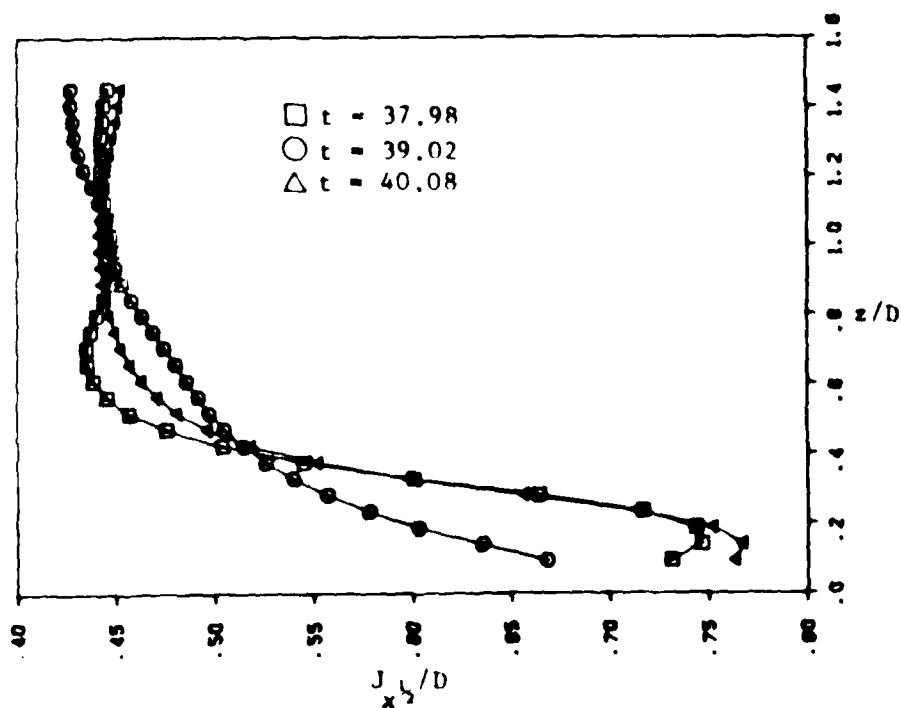


d. u-velocity profiles in the x-z plane at  $y = 0.5D$  and  $x = 0.75D$  for a forcing cycle

Figure 20. u-velocity profiles as a function of  $z$  for forcing at  $St = 0.47$ . (Cont.)

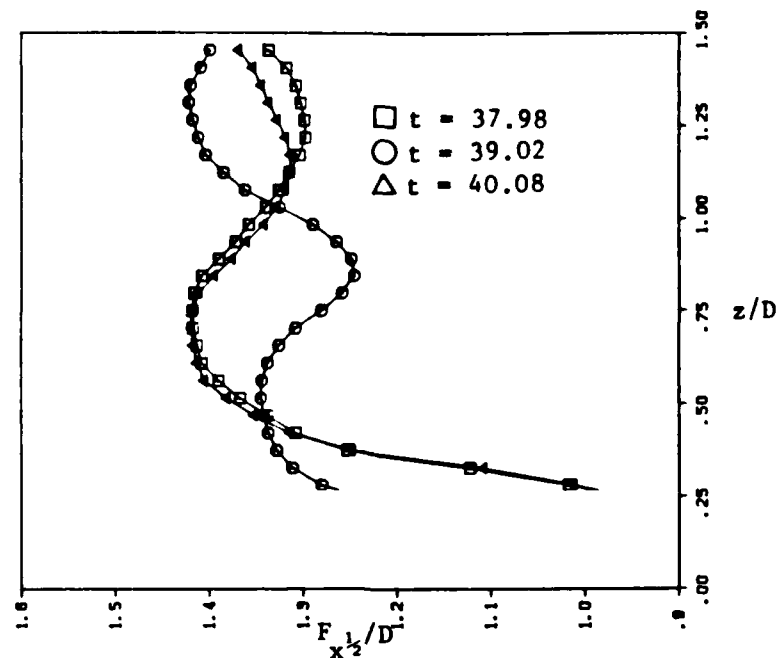


a. variation of the jet half-velocity width in the y-z plane at  $x = 0$  as a function of  $z$

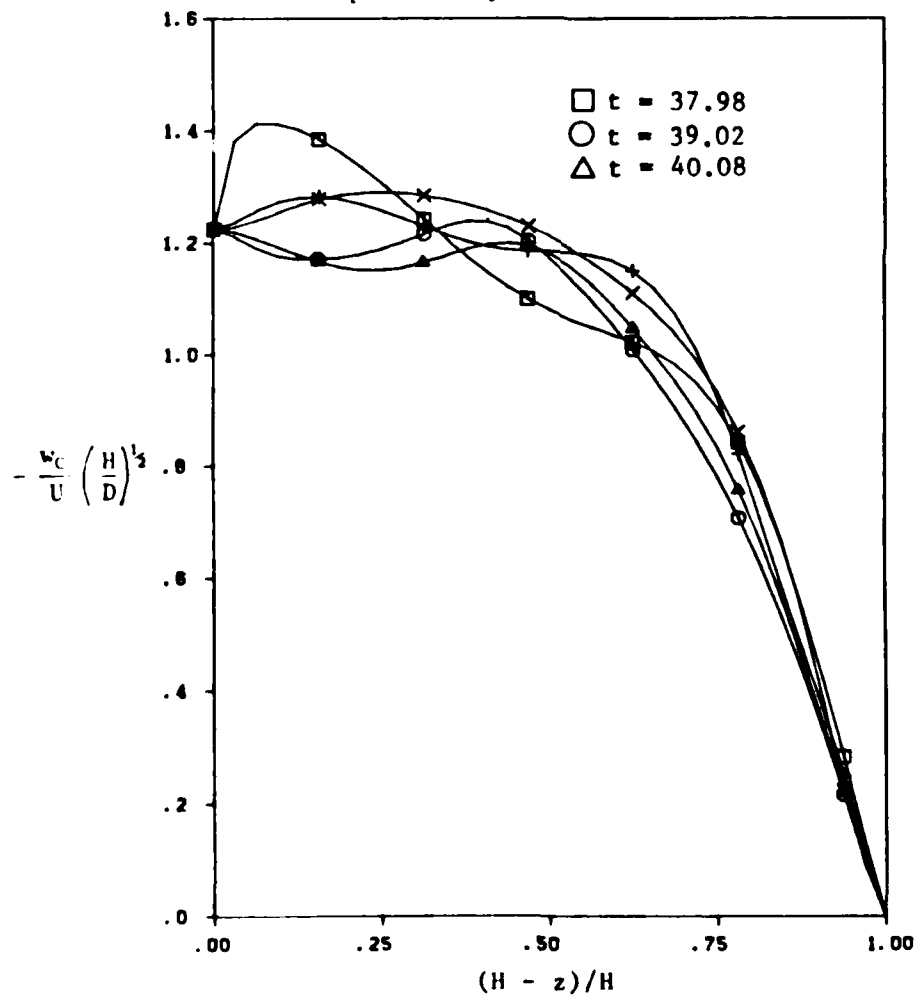


b. variation of the jet half-velocity width in the x-z plane at  $y = 0$  as a function of  $z$

Figure 21. Spreading of the impinging jet and the fountain for a forcing cycle at  $St = 0.47$ .

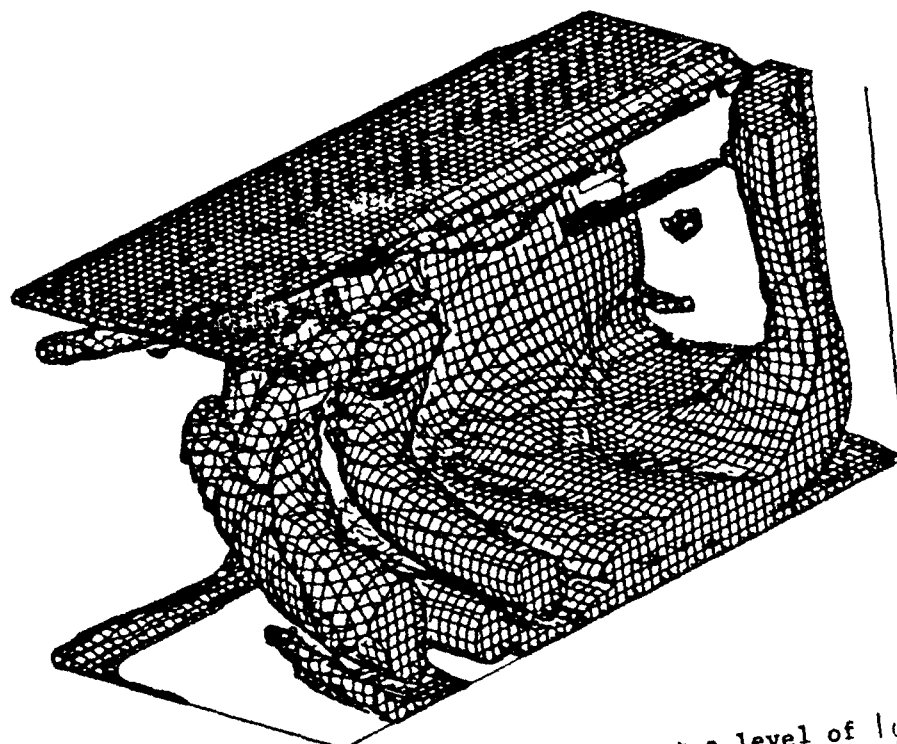


c. variation of the fountain half-velocity width in the x-z plane at  $y = 0$  as a function of  $z$

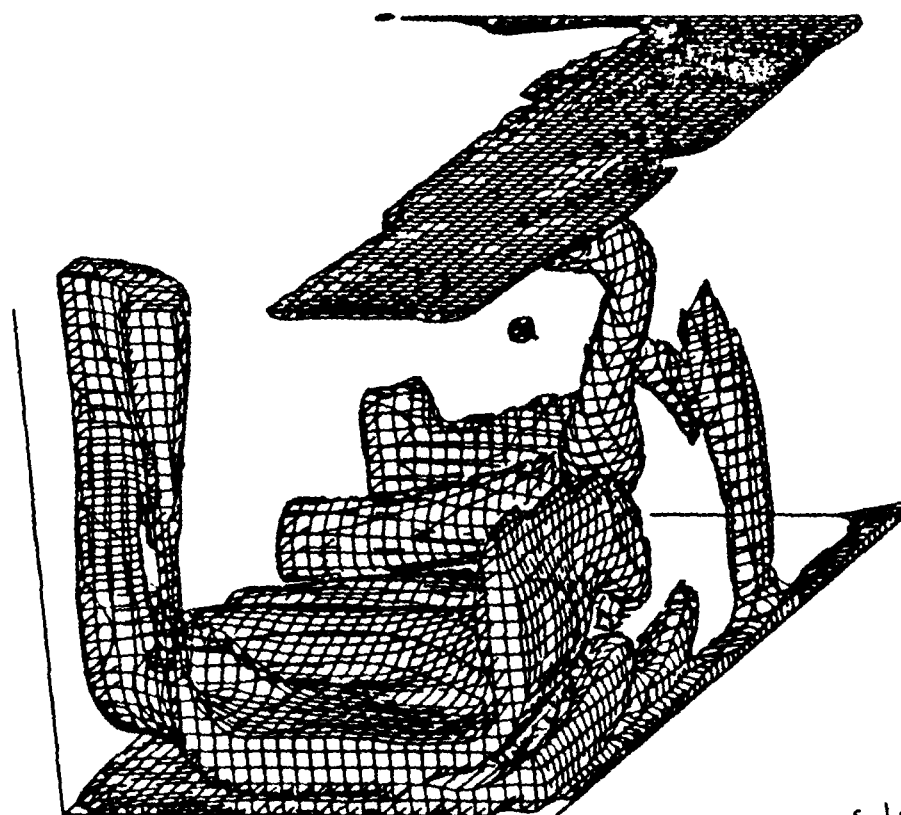


d. variation of the centerline velocity of the jet as a function of height

Figure 21. Spreading of the impinging jet and the fountain for a forcing cycle at  $St = 0.47$ . (Cont.)

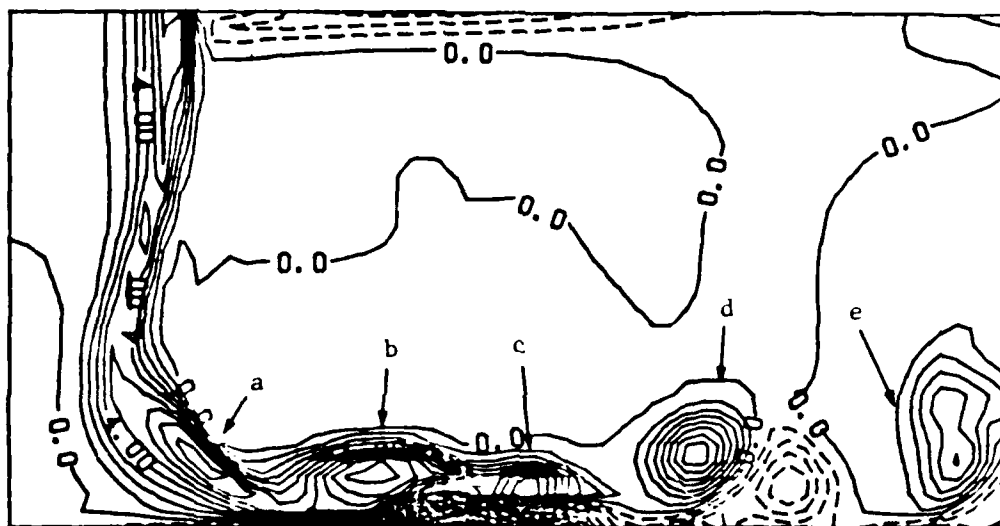


a. view of the impinging jet and the outflow at a level of  $|\omega| = 1.95$

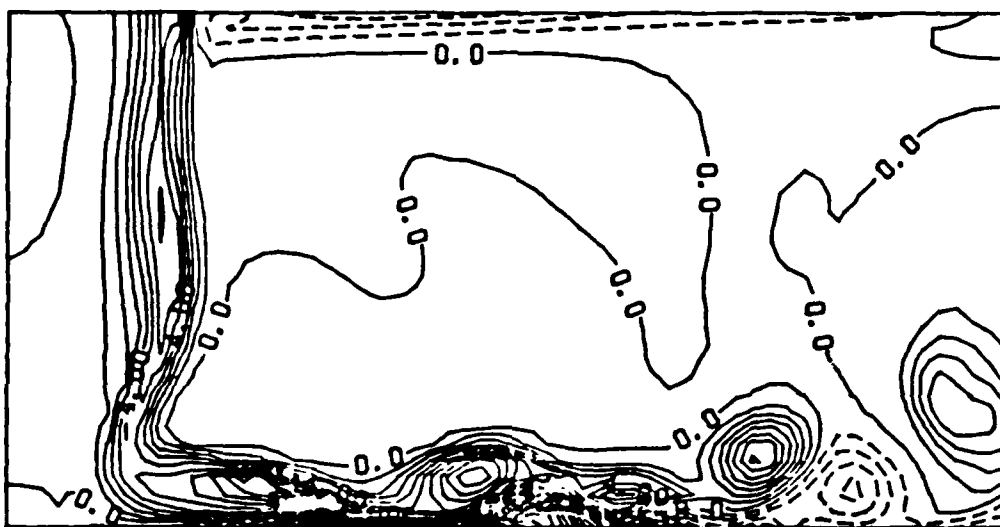


b. view of the impinging jet and the fountain at a level of  $|\omega| = 2.90$

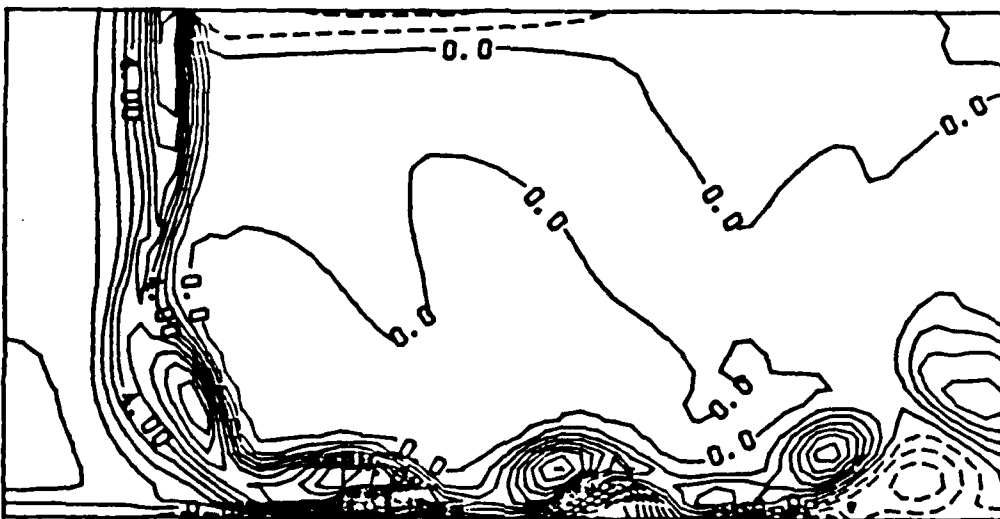
Figure 22. Three-dimensional perspective of the vorticity surface for combined forcing at  $St = 0.47$  and  $0.94$  for  $H = 1.5D$ .



a.  $x = 0$  plane at  $t = 50.64$



b.  $x = 0$  plane at  $t = 51.68$



c.  $x = 0$  plane at  $t = 52.73$

Figure 23. Time sequence of the x-vorticity contours in the y-z plane for combined forcing at  $St = 0.47$  and  $0.94$  for  $H = 1.5D$  (contour interval =  $1.0$ ).

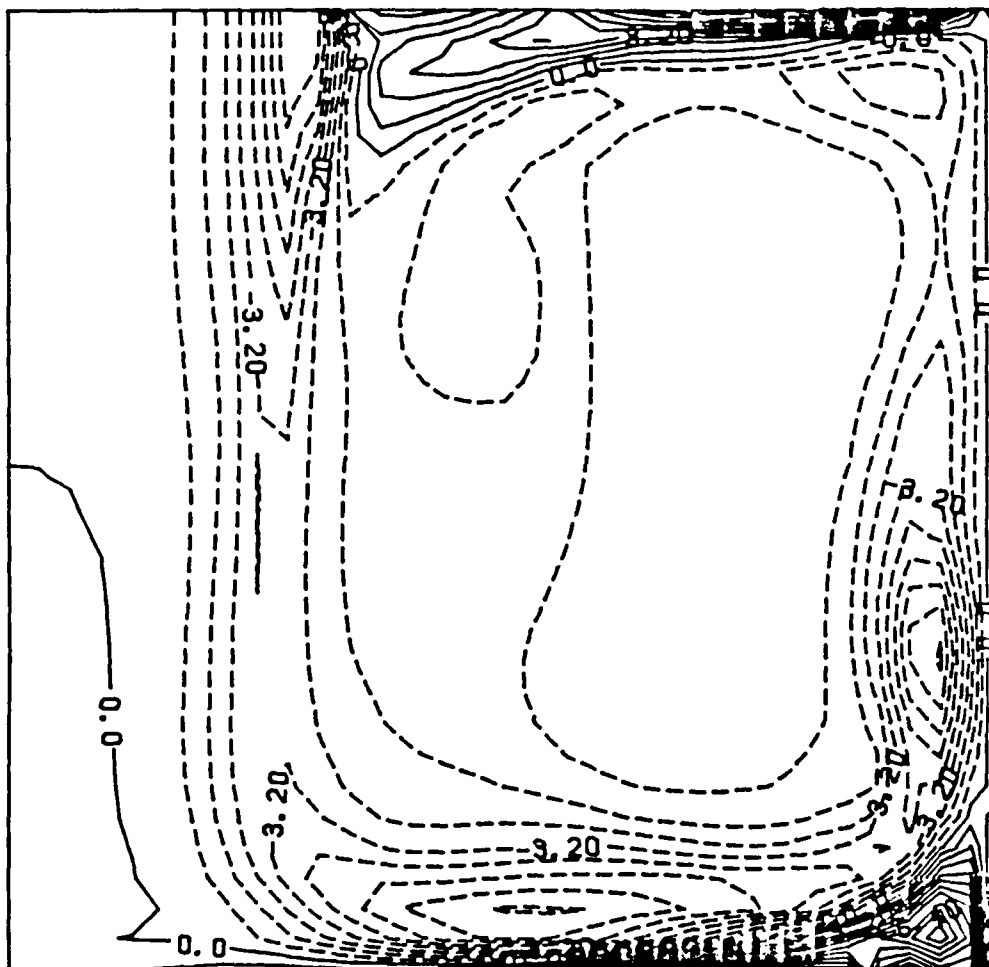
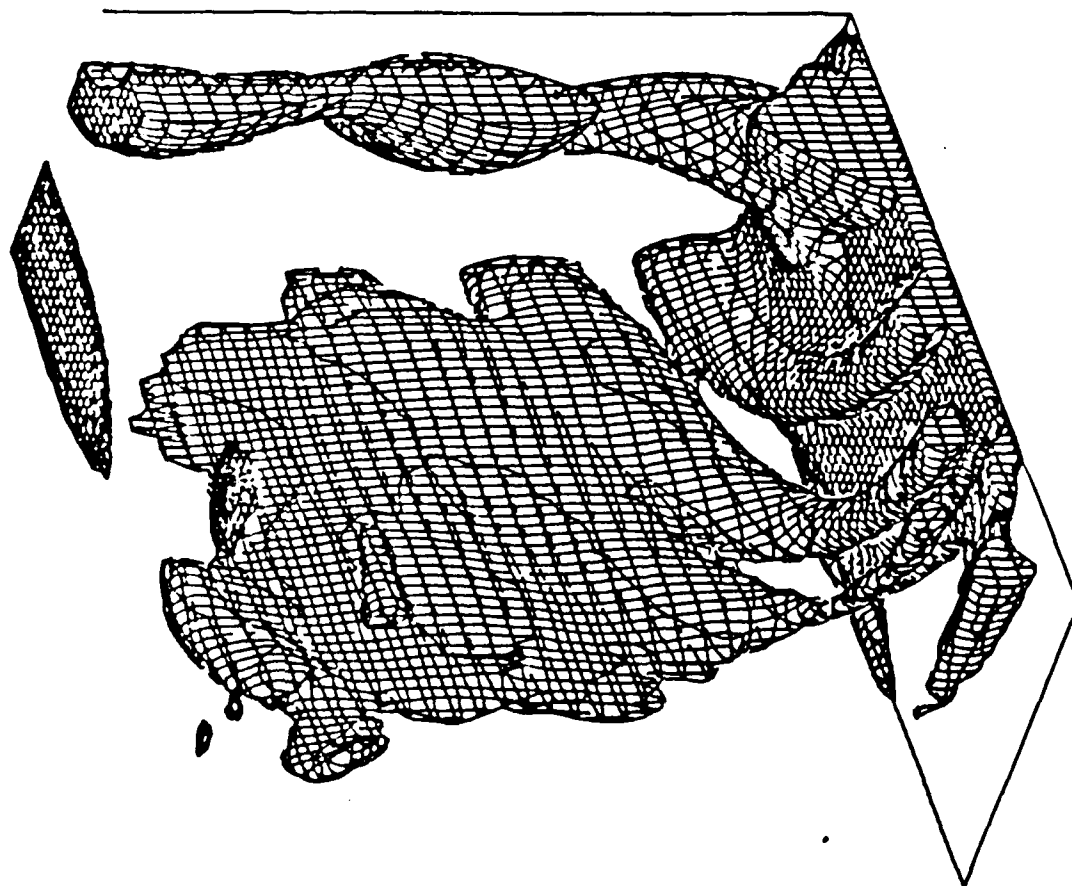
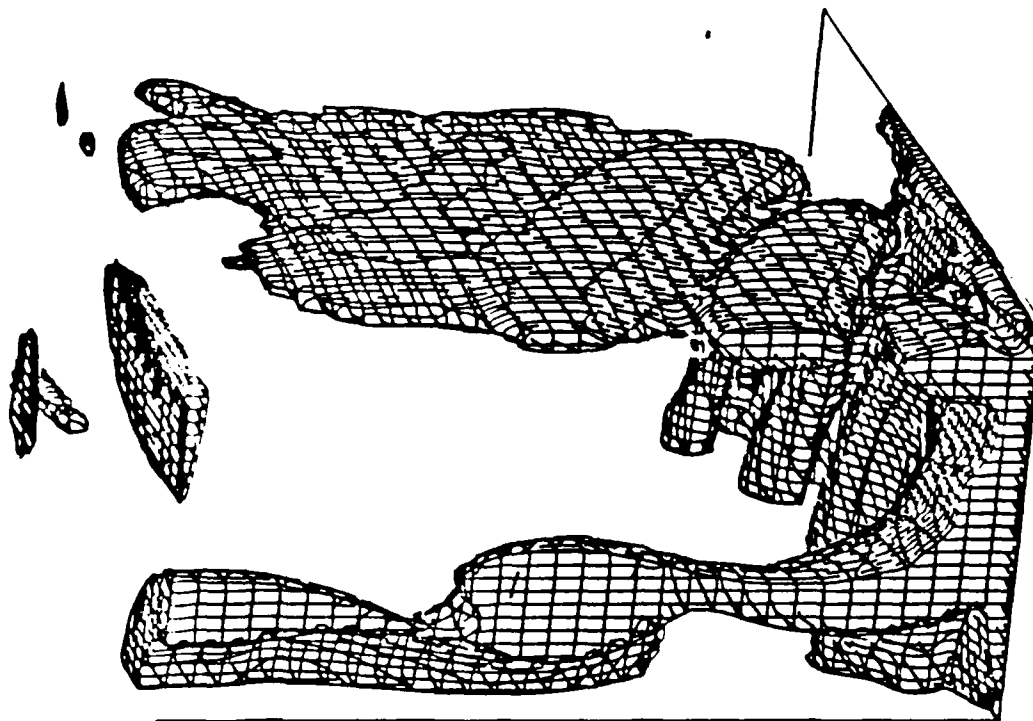


Figure 24.  $y$ -vorticity contours in the  $x$ - $z$  plane for combined forcing at  $St = 0.47$  and  $0.94$ . View of the  $y = 0$  plane at  $t = 50.64$  (contour interval =  $0.8$ ).



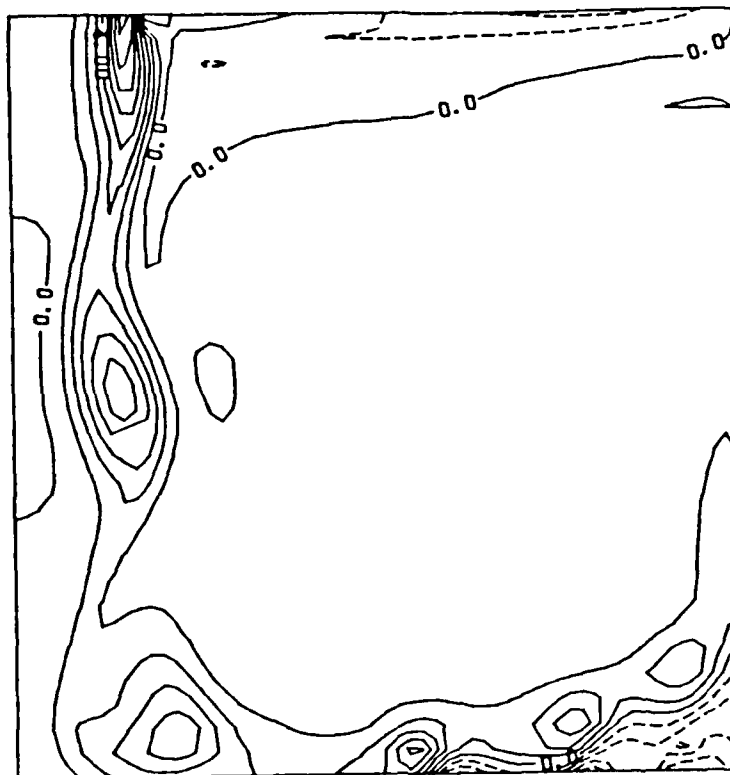


a. view of the impinging jet and the outflow  
at a level  $|\omega| = 1.95$

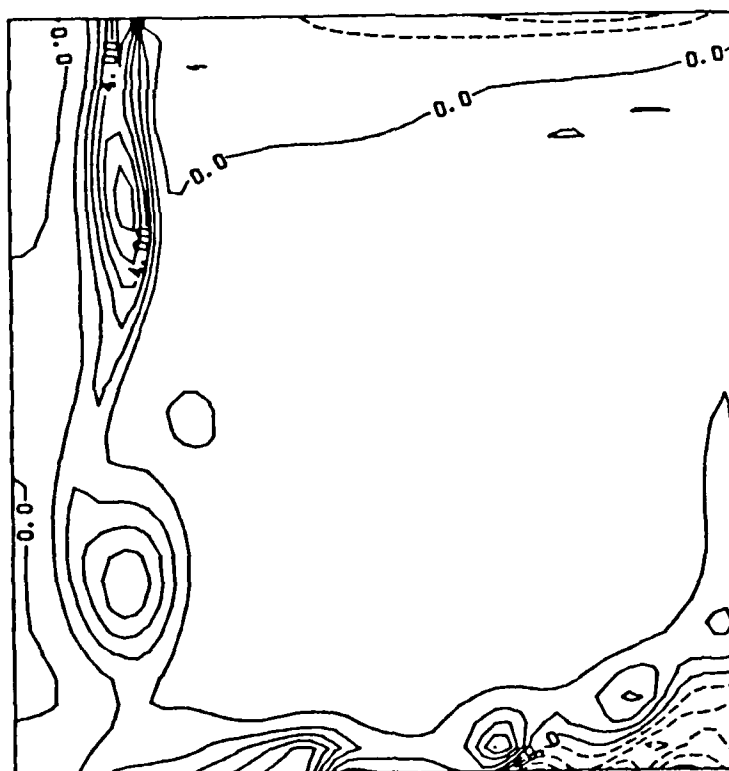


b. view of the impinging jet and the fountain  
at a level  $|\omega| = 1.95$

Figure 25. Three-dimensional perspective of the vorticity surface for the  
 $H = 3D$  case at  $t = 59.07$  for forcing at  $St = 0.47$ .

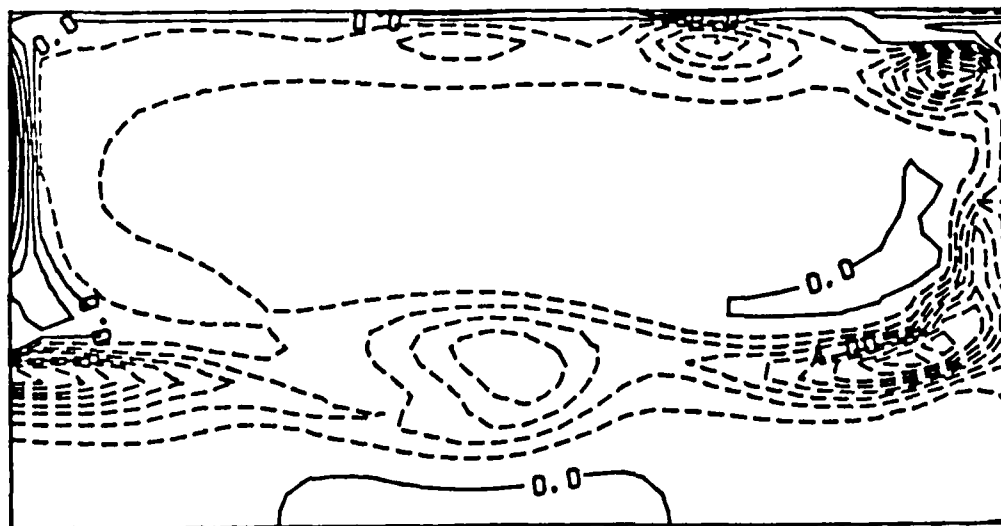


a.  $x = 0$  plane at  $t = 59.07$

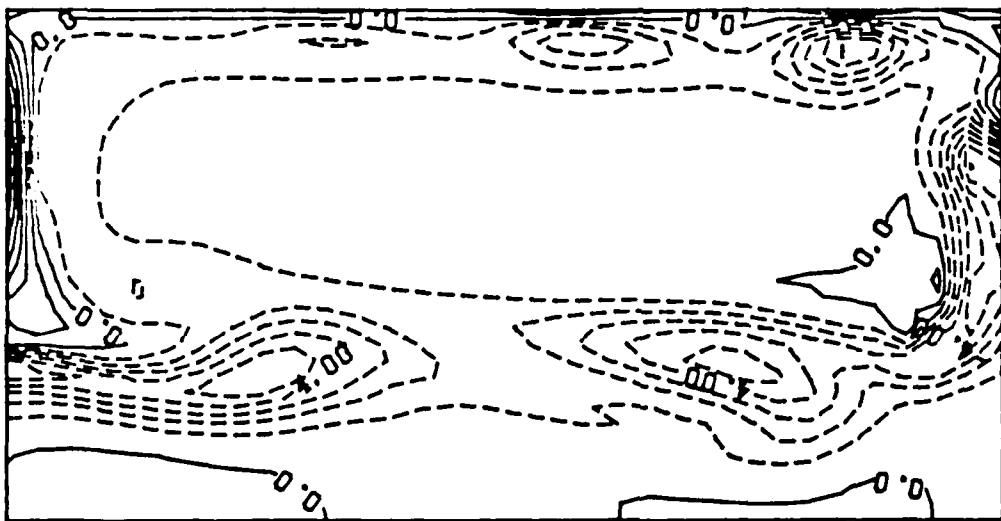


b.  $x = 0$  plane at  $t = 60.10$

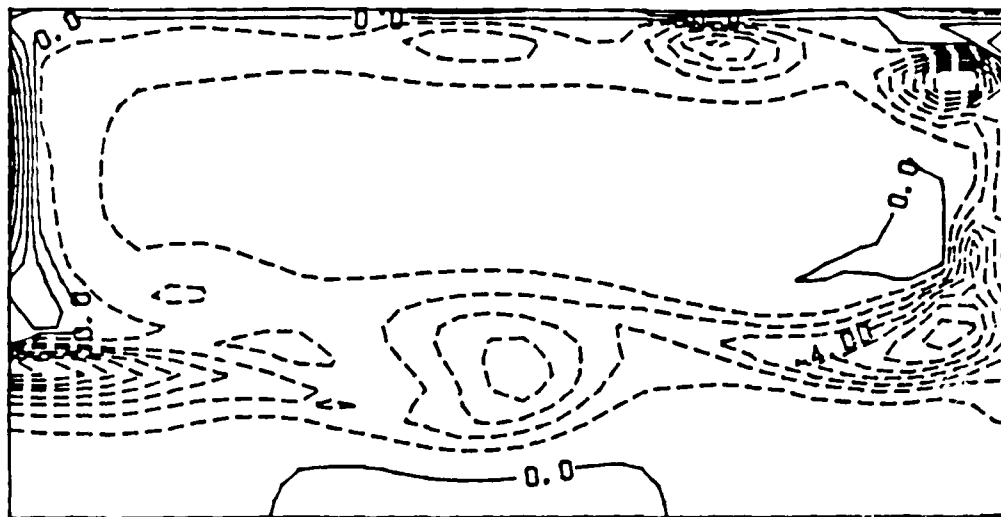
Figure 26. Time sequence of the x-vorticity contours in the y-z plane for forcing at  $St = 0.47$  for  $H = 3D$  (contour interval = 1.0).



a.  $y = 0$  plane at  $t = 59.07$

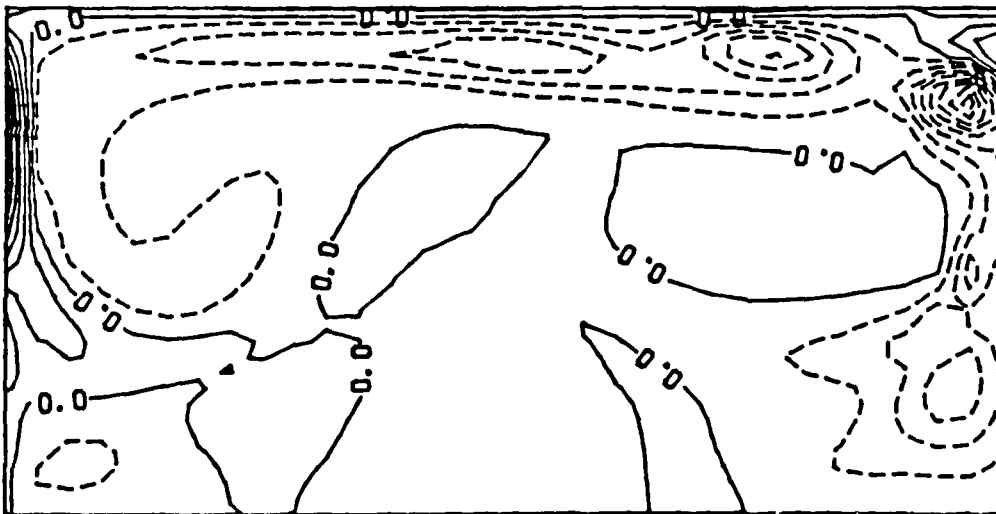


b.  $y = 0$  plane at  $t = 60.10$

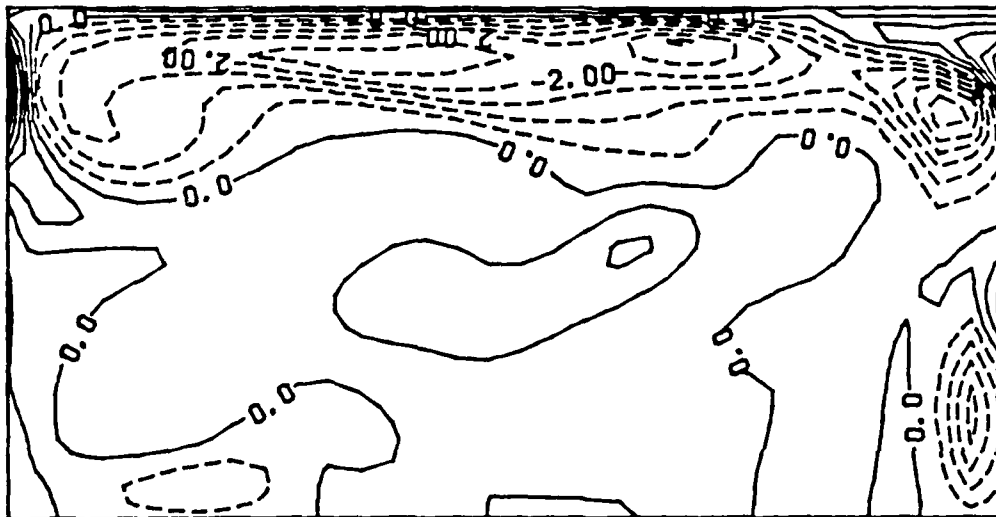


c.  $y = 0$  plane at  $t = 61.17$

Figure 27. Time sequence of the  $y$ -vorticity contours in the  $x$ - $z$  plane for forcing at  $St = 0.47$  for  $H = 3D$  (contour interval = 1.0 for a - d; 0.5 for e).

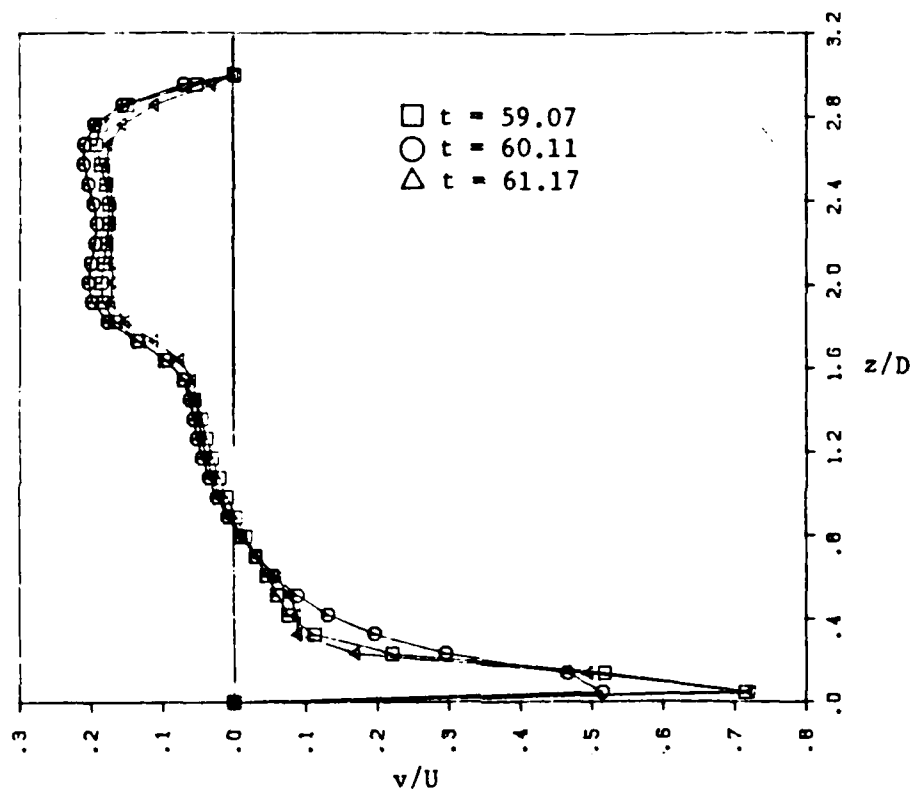


d.  $y = 0.5D$  plane at  $t = 61.17$

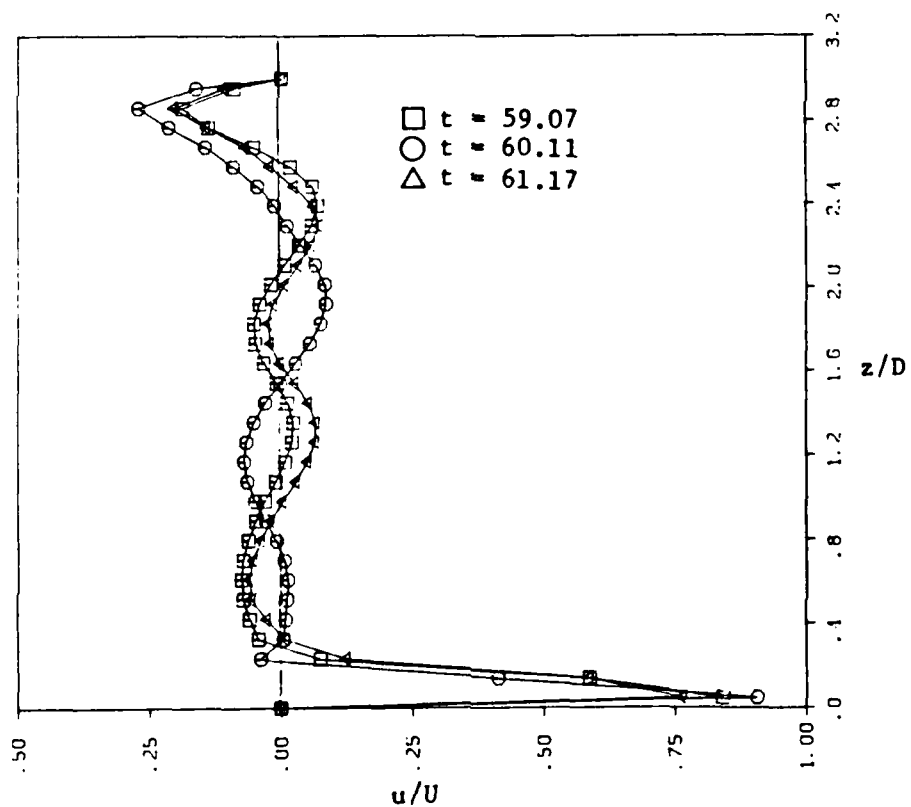


e.  $y = 1.5D$  plane at  $t = 61.17$

Figure 27. Time sequence of the y-vorticity contours in the x-z plane for forcing at  $St = 0.47$  for  $H = 3D$  (contour interval = 1.0 for a - d; 0.5 for e). (Cont.)

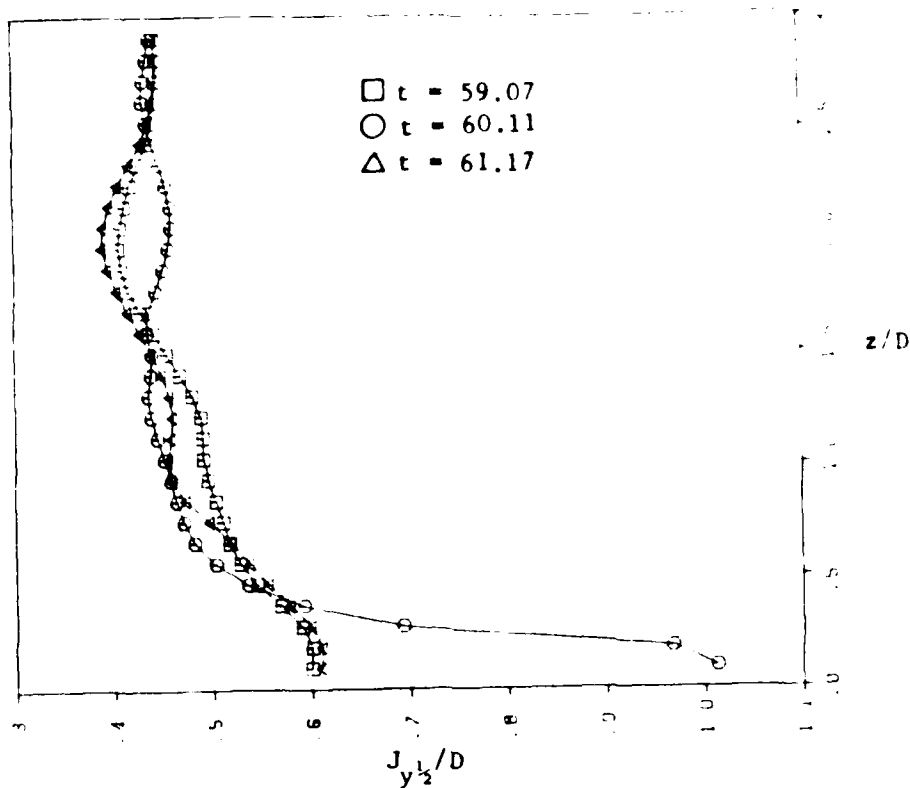


a. v-velocity profiles in the  $x = 0$  plane at  $y = 1.5D$

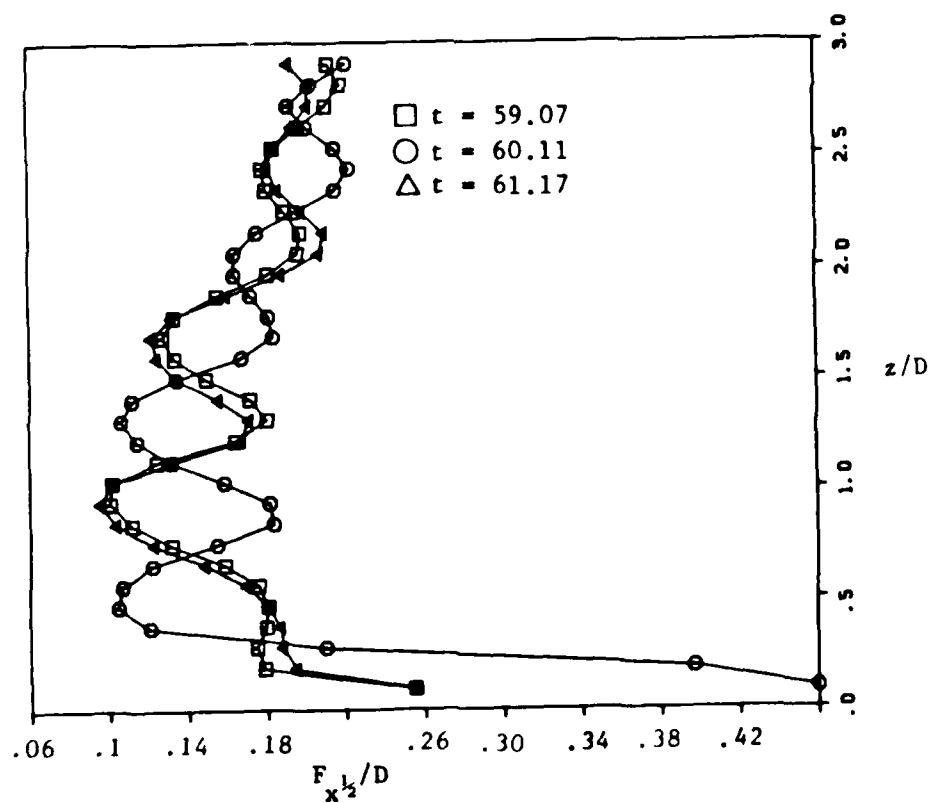


b. u-velocity profiles in the  $y = 0$  plane at  $x = 0.75D$

Figure 28. Variation of the velocity profiles as a function of  $z$  for a forcing cycle at  $St = 0.47$  for  $H = 3D$ .



c. jet half-velocity width as a function of  $z$  in the  $y$ - $z$  plane at  $x = 0$



d. fountain width variation as a function of  $z$  in the  $x$ - $z$  plane at  $y = 0$

Figure 28. Variation of the velocity profiles as a function of  $z$  for a forcing cycle at  $St = 0.47$  for  $H = 3D$ . (Cont.)

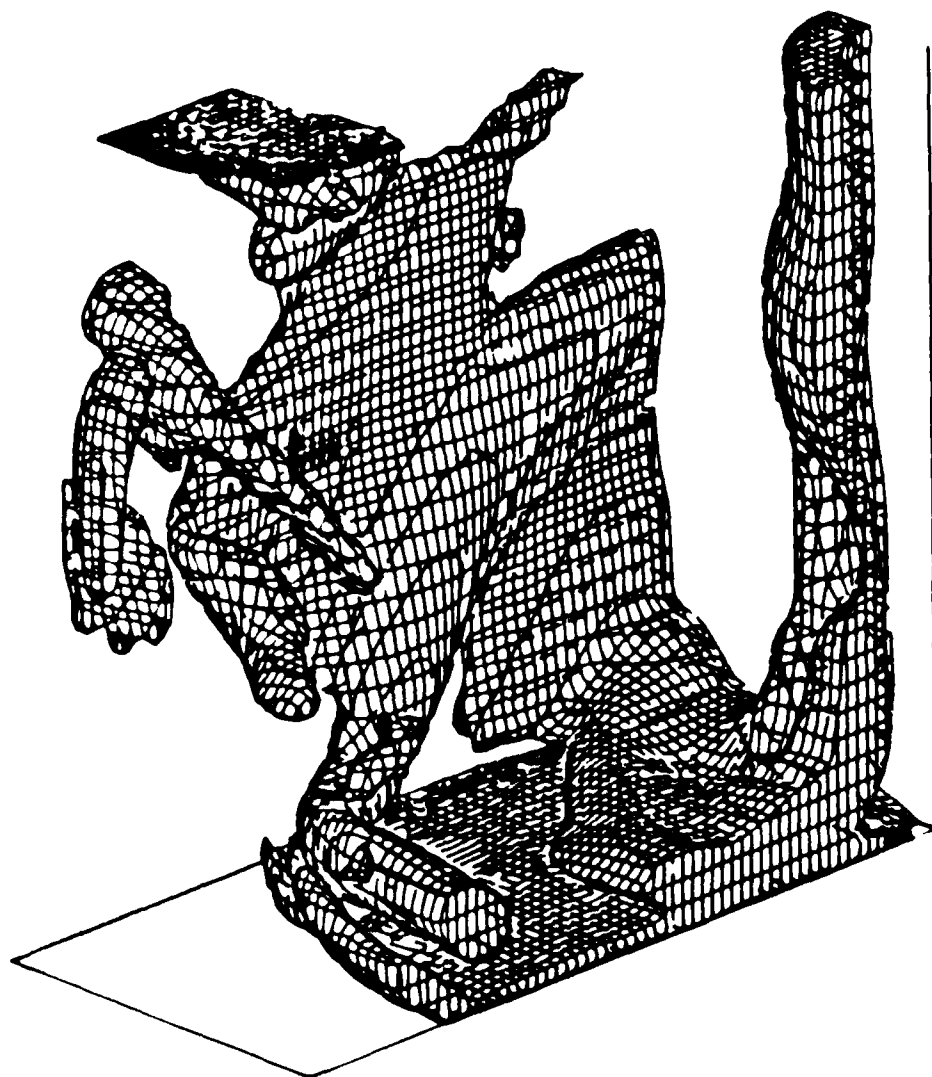


Figure 29. Three-dimensional perspective of the vorticity surface for combined forcing at  $St = 0.47$  and  $0.94$  for  $H = 3D$ . View of the impinging jet and the outflow at  $t = 50.64$ ;  $|\omega| = 1.95$ .

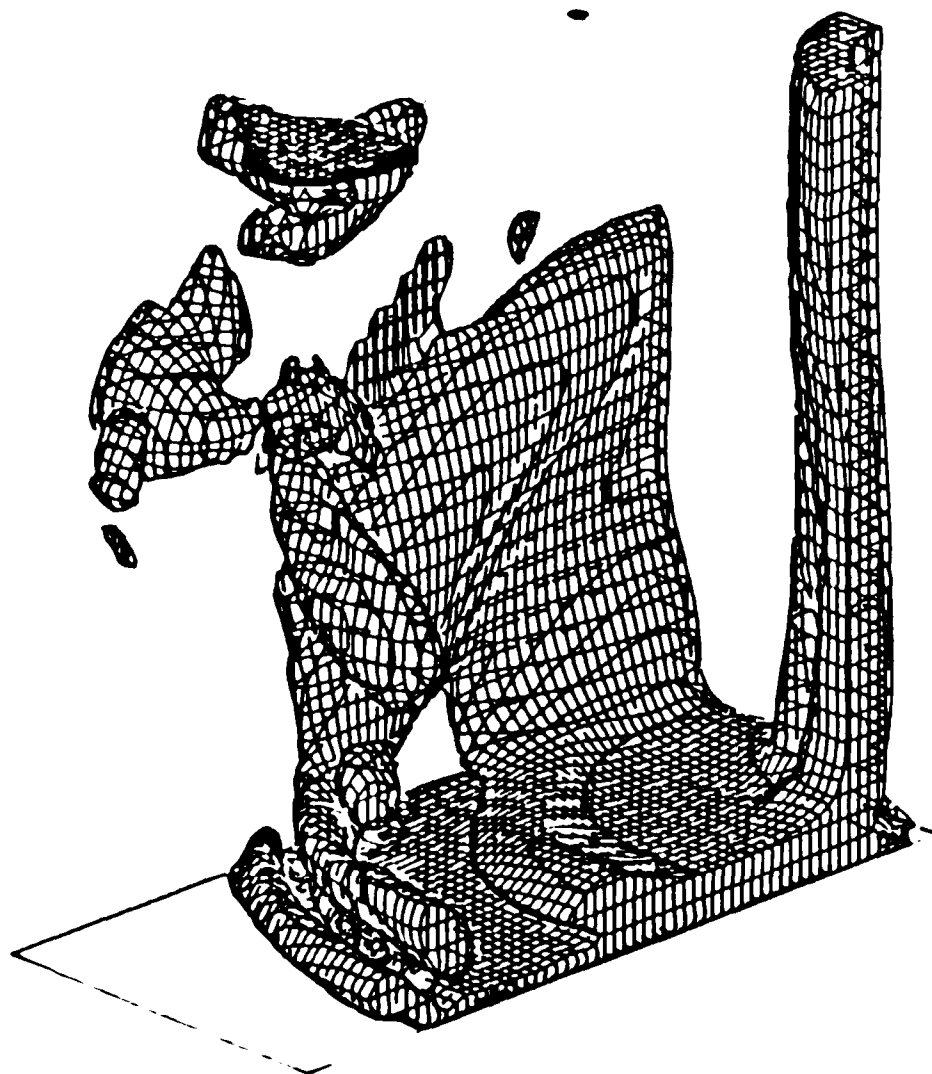
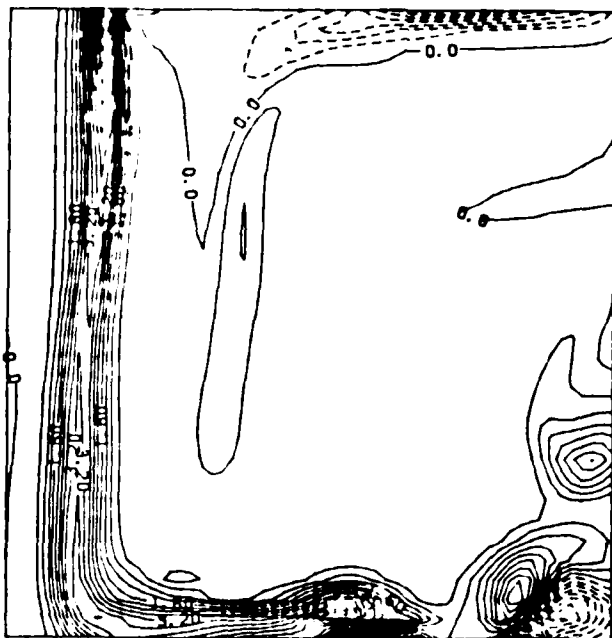


Figure 30. Three-dimensional perspective of the vorticity surface for combined forcing at  $St = 0.235$  and  $0.47$  for  $H = 3D$ . View of the impinging jet and the outflow at  $t = 50.64$ ;  $|\omega| = 1.95$ .

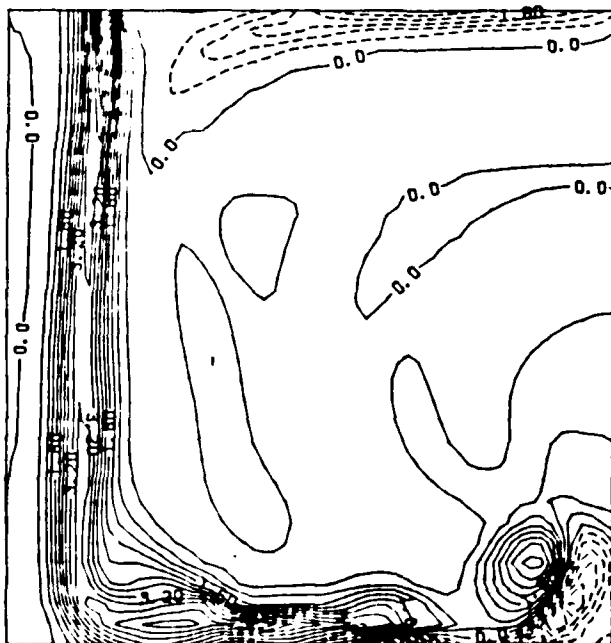




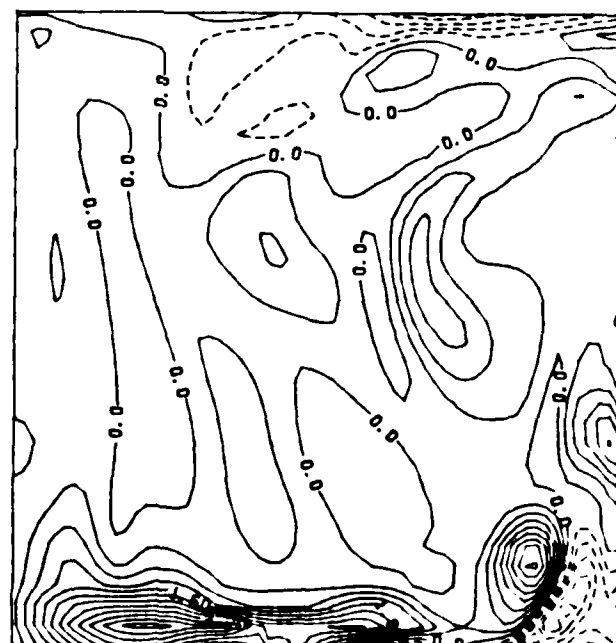
a.  $x = 0$  plane at  $t = 50.64$



b.  $x = 0$  plane at  $t = 52.73$

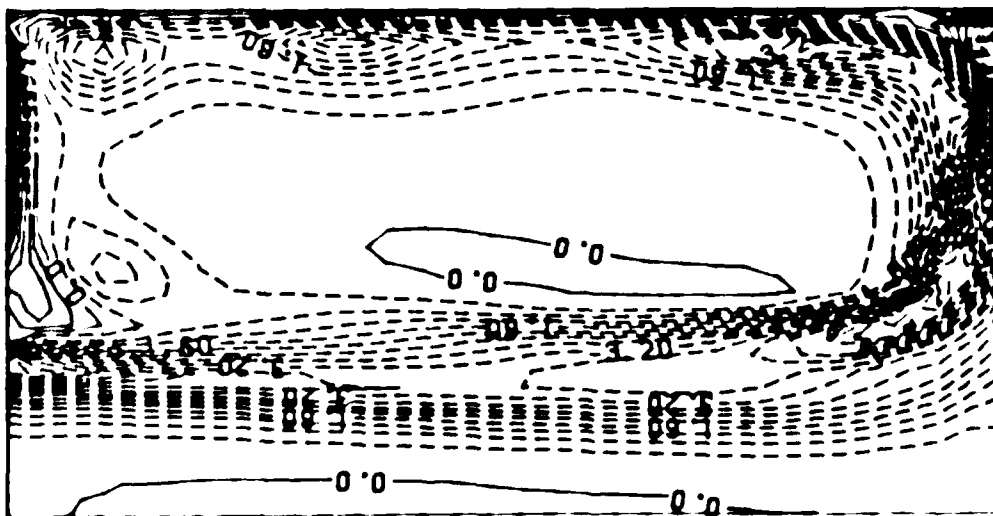


c.  $x = 0$  plane at  $t = 54.84$

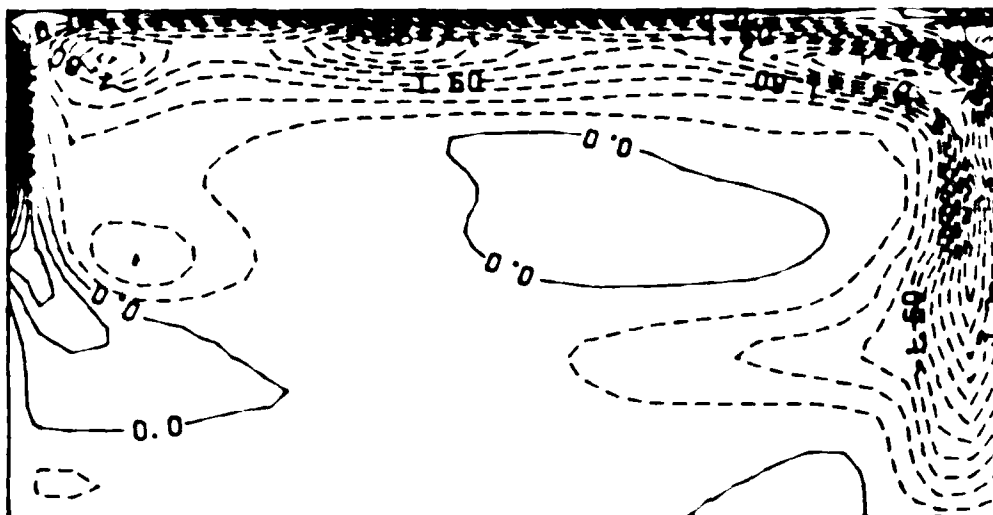


d.  $x = 0.51D$  plane at  $t = 54.84$

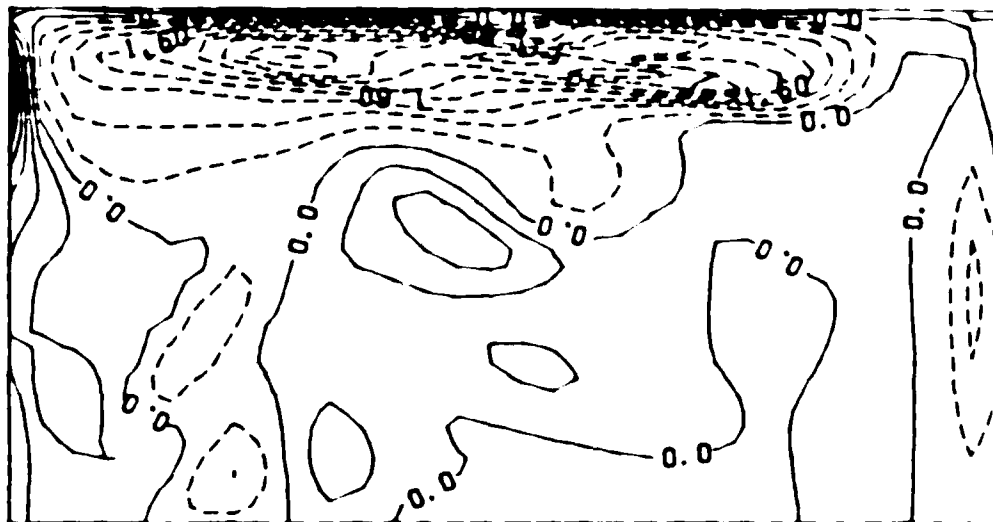
Figure 31. Time sequence of the  $x$ -vorticity in the  $y$ - $z$  plane for forcing at  $St = 0.235$  and  $0.47$  for  $H = 3D$  (contour interval =  $0.4$ ).



a.  $y = 0$  plane at  $t = 54.84$

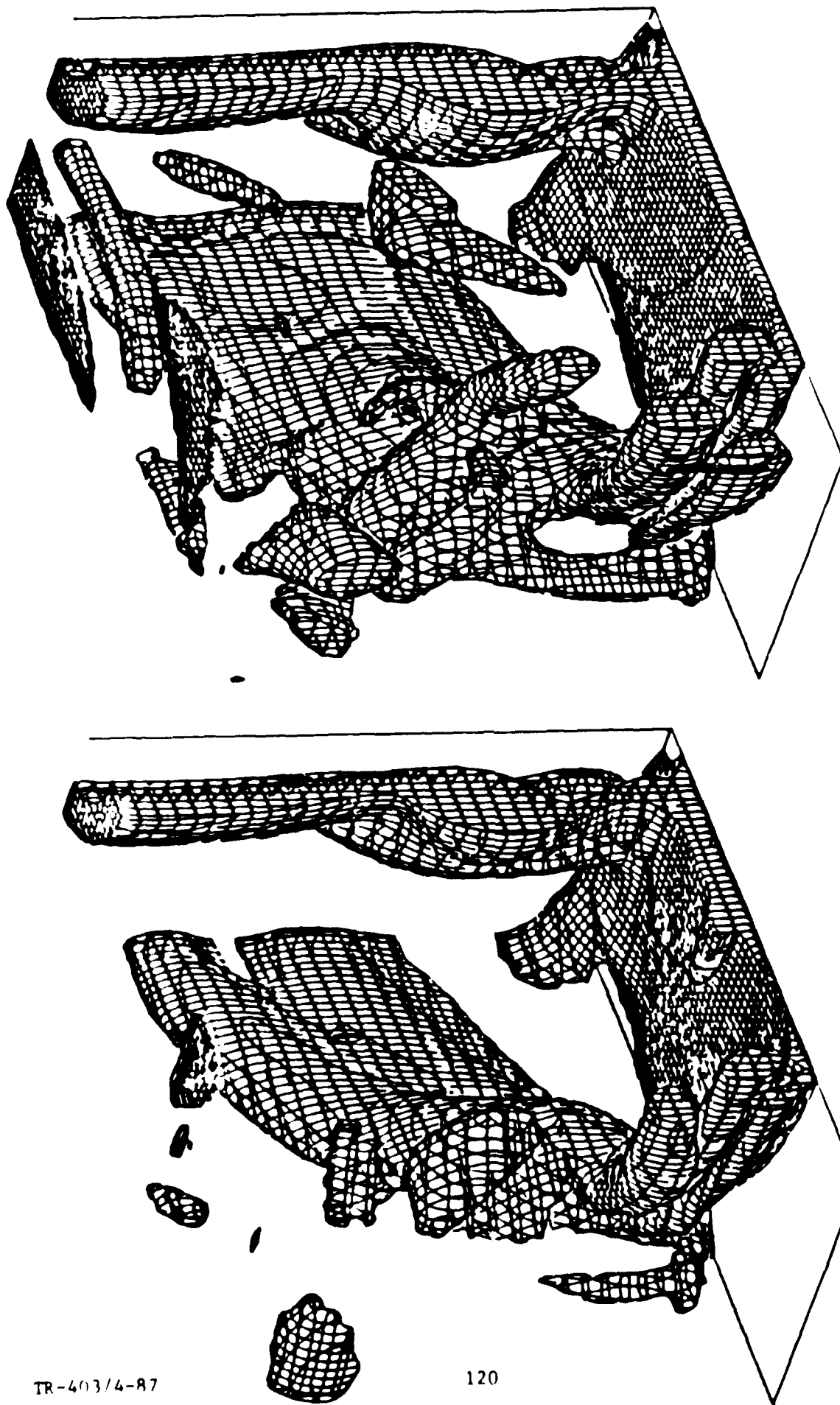


b.  $y = 0.510$  plane at  $t = 54.84$



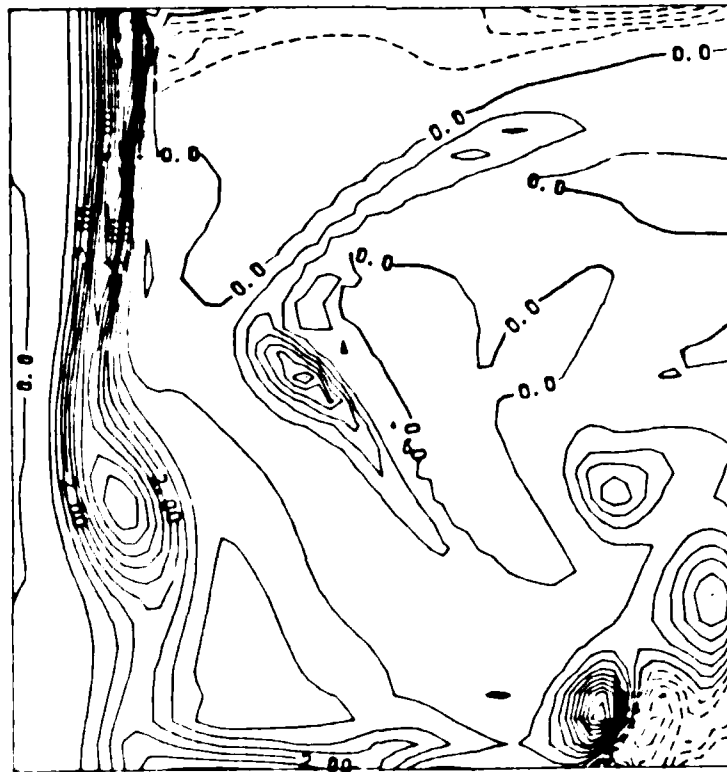
c.  $y = 1.510$  plane at  $t = 54.84$

Figure 32.  $y$ -vorticity contours in the  $x$ - $z$  plane for forcing at  $St = 0.235$  and  $0.47$  for  $H = 3D$  (contour interval =  $0.4$ ).

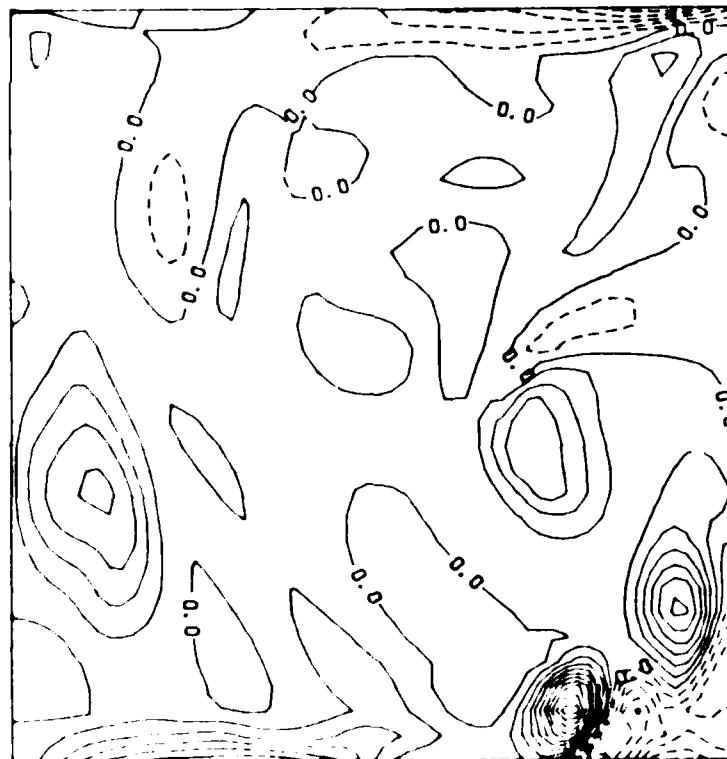


a. view of the impinging jet and the outflow at  $t = 50.64$  and a level  $|\omega| = 1.95$       b. view of the impinging jet and the outflow at  $t = 59.06$  and a level  $|\omega| = 1.5$

Figure 33. Three-dimensional perspective of the vorticity surface for combined forcing at  $St = 0.235$  and  $0.47$ . The forcing level is  $0.2U$ .

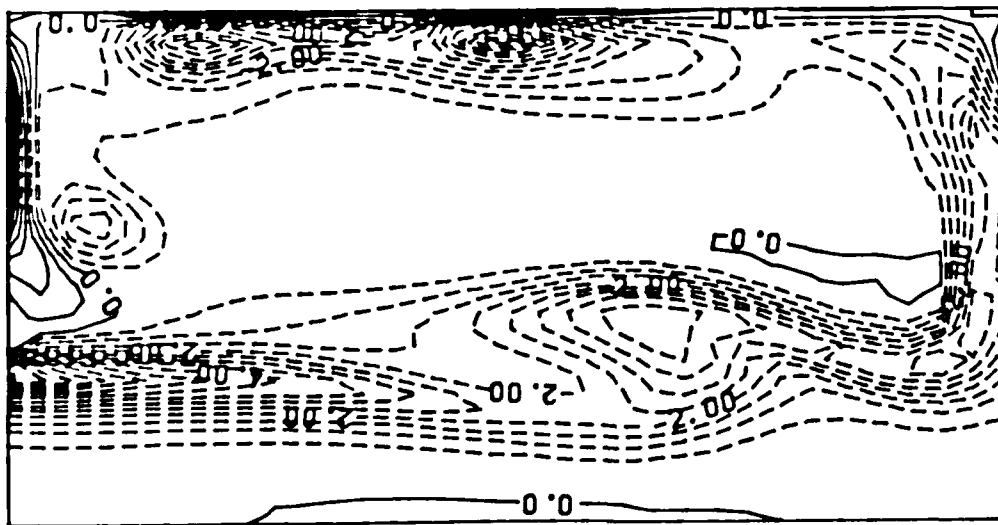


a.  $x = 0$  plane at  $t = 59.06$

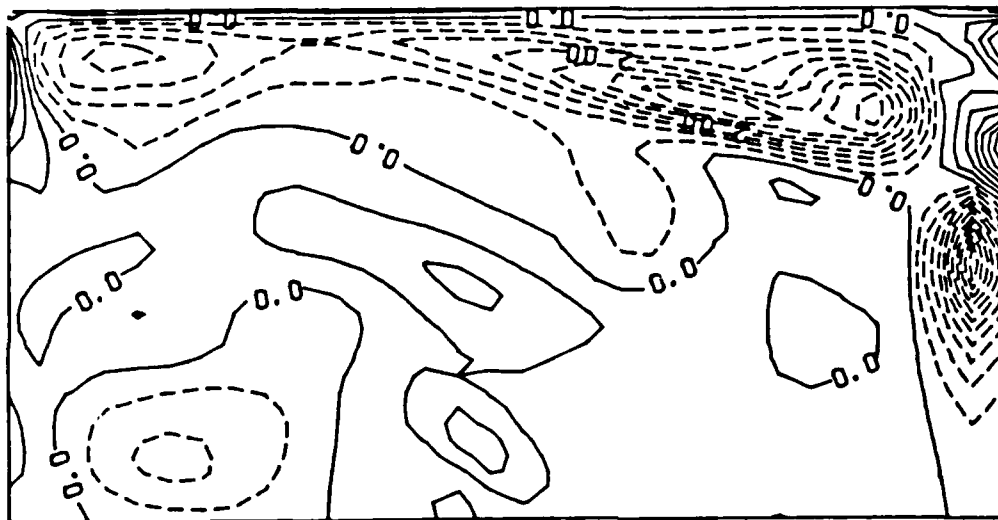


b.  $x = 0.51D$  plane at  $t = 59.06$

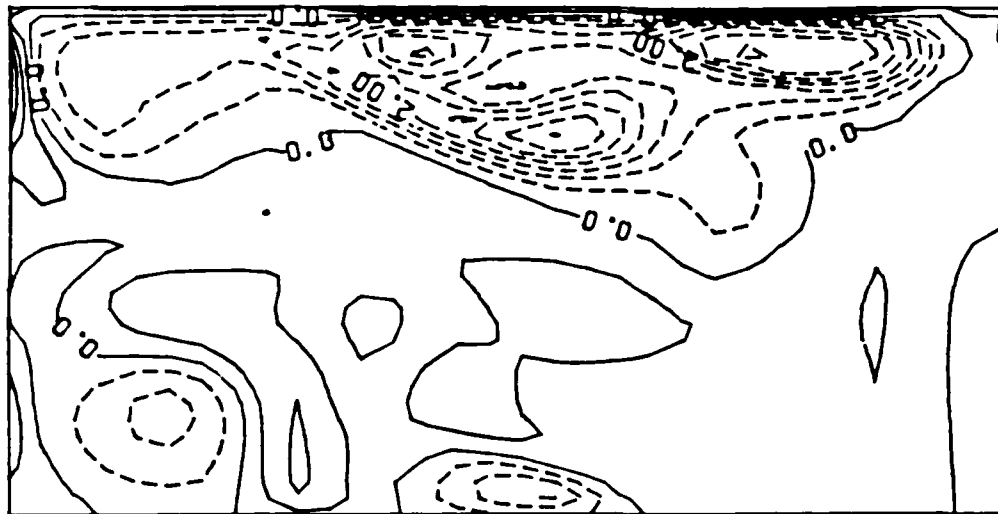
Figure 34.  $x$ -vorticity contours in the  $y$ - $z$  plane for combined forcing at  $St = 0.235$  and  $0.47$  (contour interval =  $0.5$ ).



a.  $y = 0$  plane at  $t = 59.06$

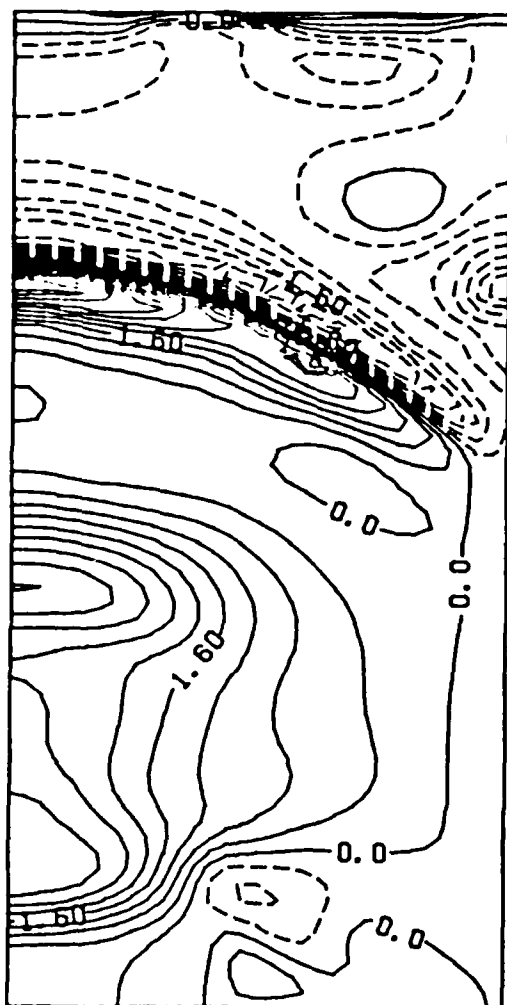


b.  $y = 1.5D$  plane at  $t = 56.95$

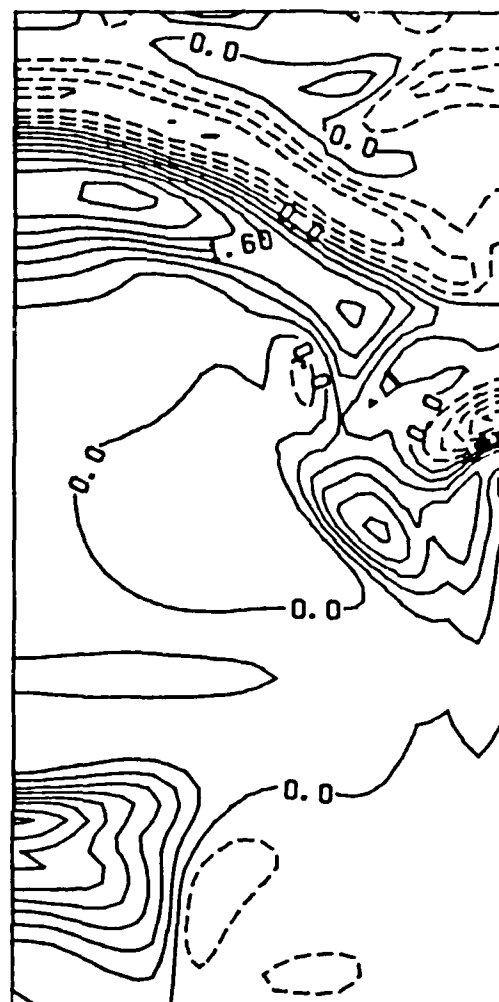


c.  $y = 1.5D$  plane at  $t = 59.06$

Figure 35.  $y$ -vorticity contours in the  $x$ - $z$  plane for combined forcing at  $St = 0.235$  and  $0.47$  (contour interval =  $0.5$ ).

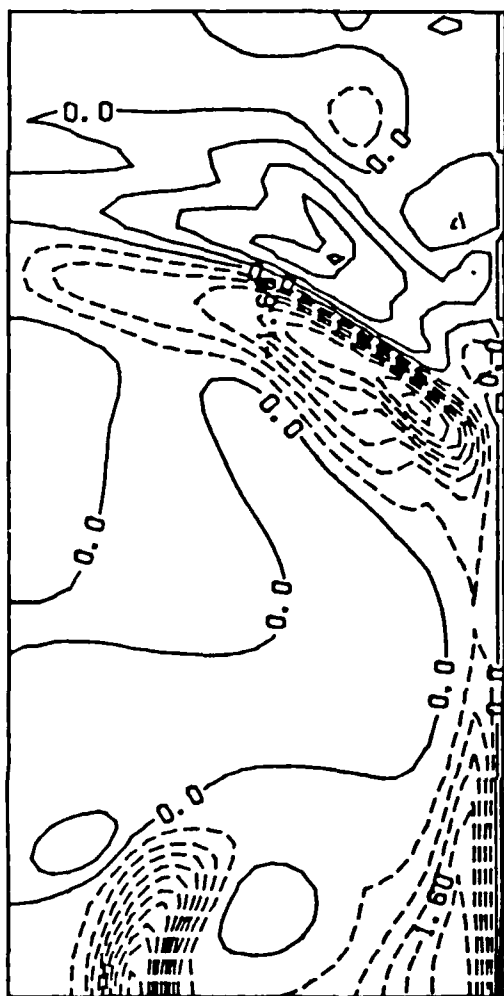


a.  $z = 0.14D$  plane at  $t = 50.64$

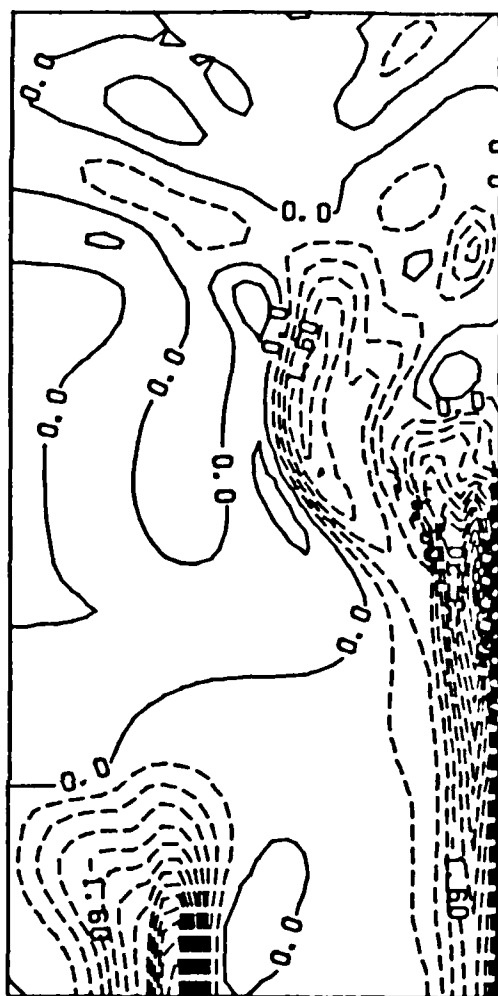


b.  $z = 0.8D$  plane at  $t = 50.64$

Figure 36. Variation of the x-vorticity contours in the x-y plane for combined forcing at  $St = 0.235$  and  $0.47$  (contour interval =  $0.4$ ).

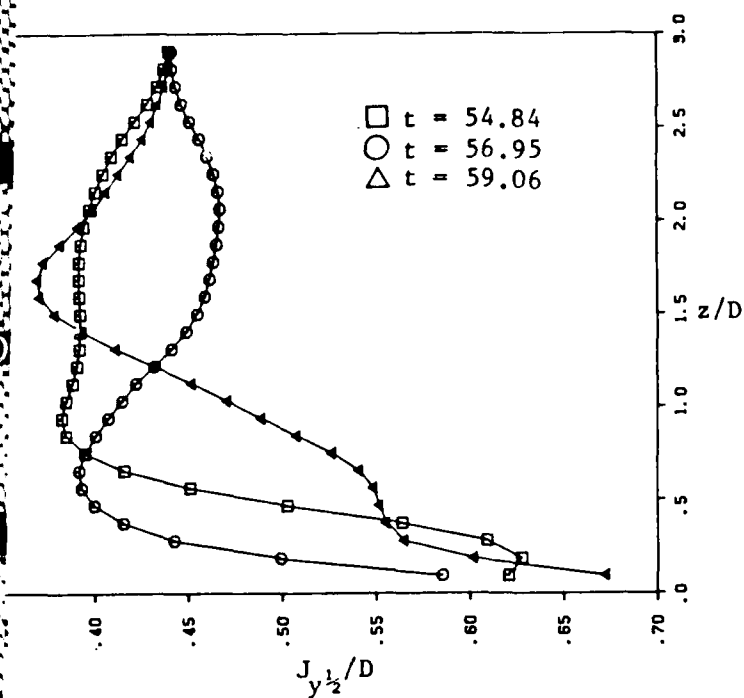


a.  $z = 0.14D$  plane at  $t = 50.64$

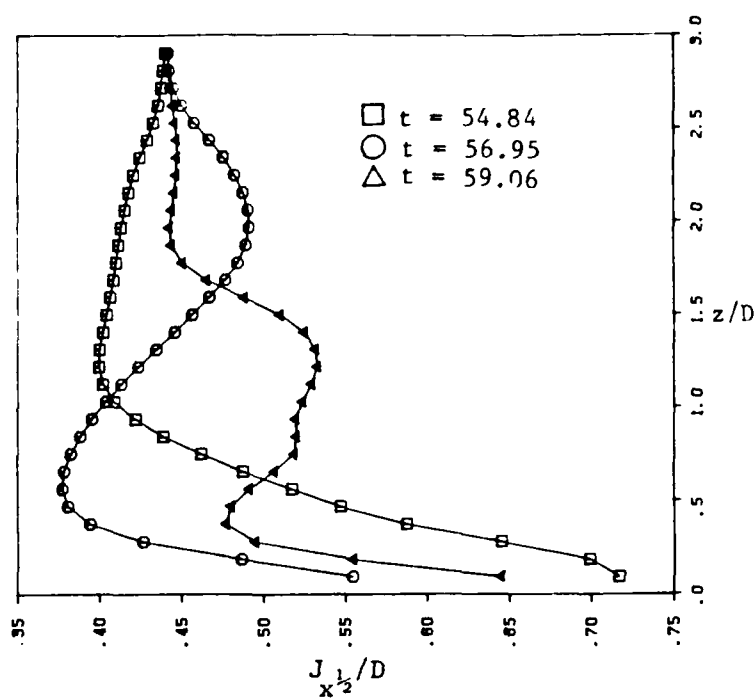


b.  $z = 0.8D$  plane at  $t = 50.64$

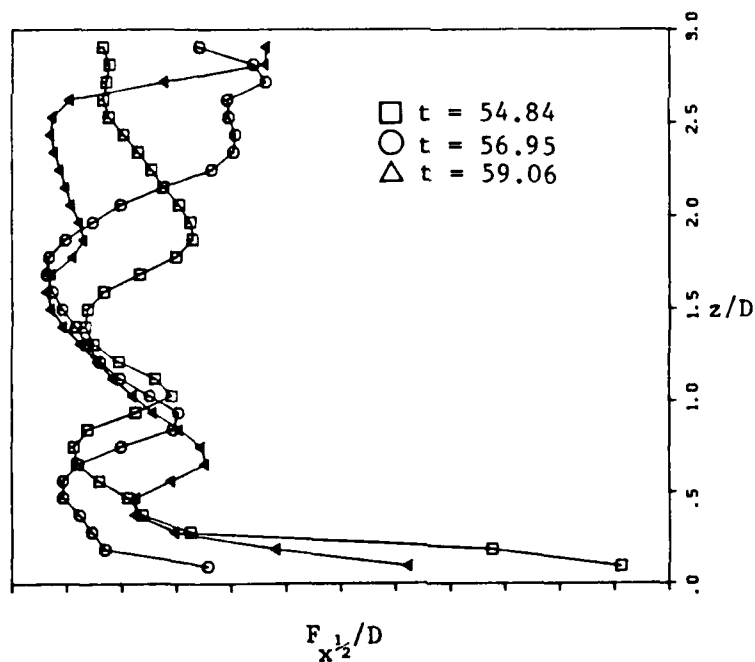
Figure 37. Variation of the  $y$ -vorticity contours in the  $x$ - $y$  plane for combined forcing at  $St = 0.235$  and  $0.47$  (contour interval =  $0.4$ ).



a. jet half-velocity width as a function of  $z$  in the  $y$ - $z$  plane at  $x = 0$



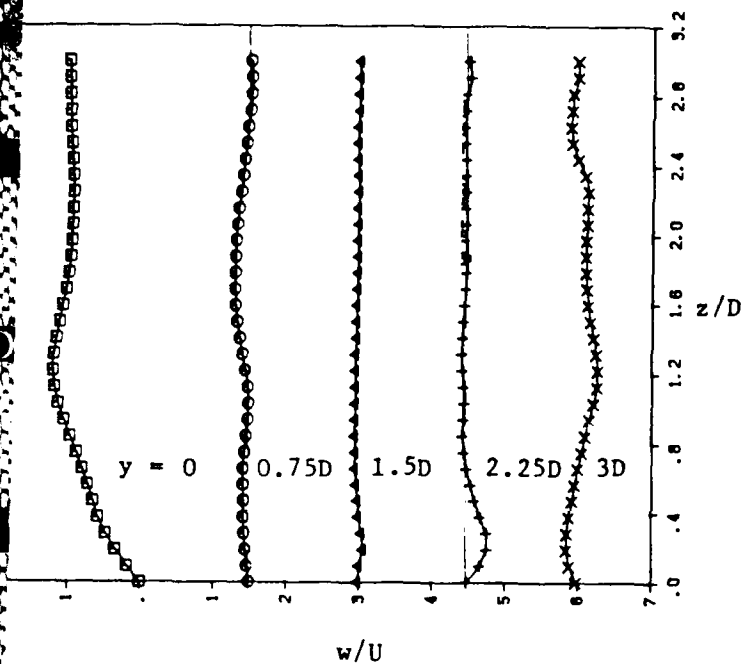
b. jet half-velocity width as a function of  $z$  in the  $x$ - $z$  plane at  $y = 0$



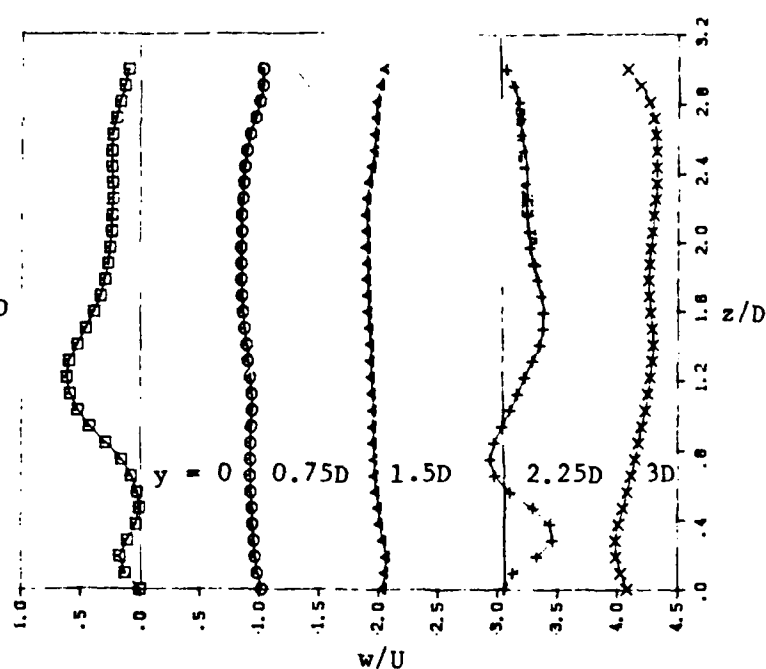
c. fountain half-velocity width as a function of  $z$  in the  $x$ - $z$  plane at  $y = 0$

**Figure 38.** Spreading of the impinging jet and the fountain for combined forcing at  $St = 0.235$  and  $0.47$ .

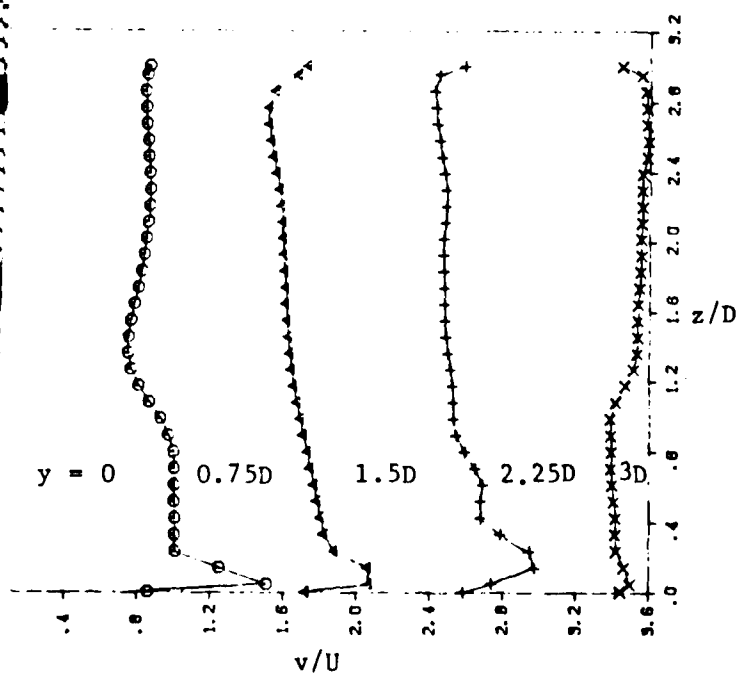




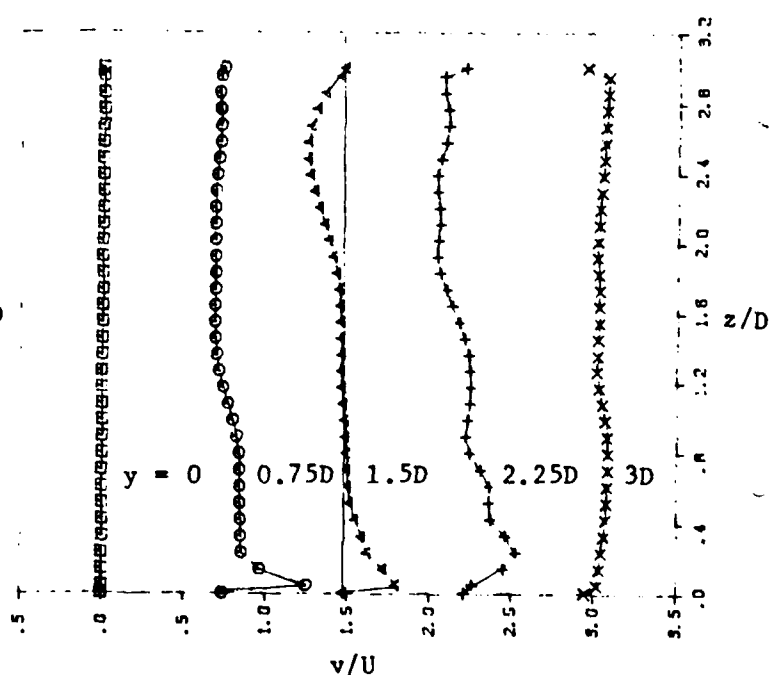
a. w-velocity profiles at  $x = 0$



b. w-velocity profiles at  $x = 0.5D$

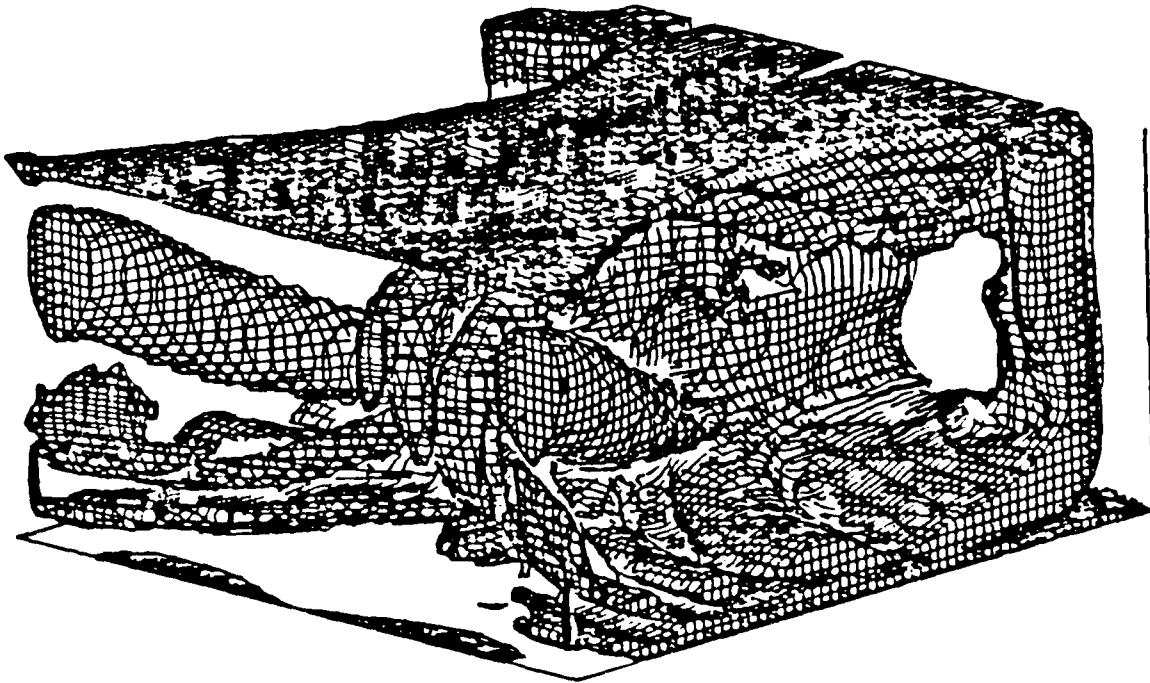


c. v-velocity profiles at  $x = 0$

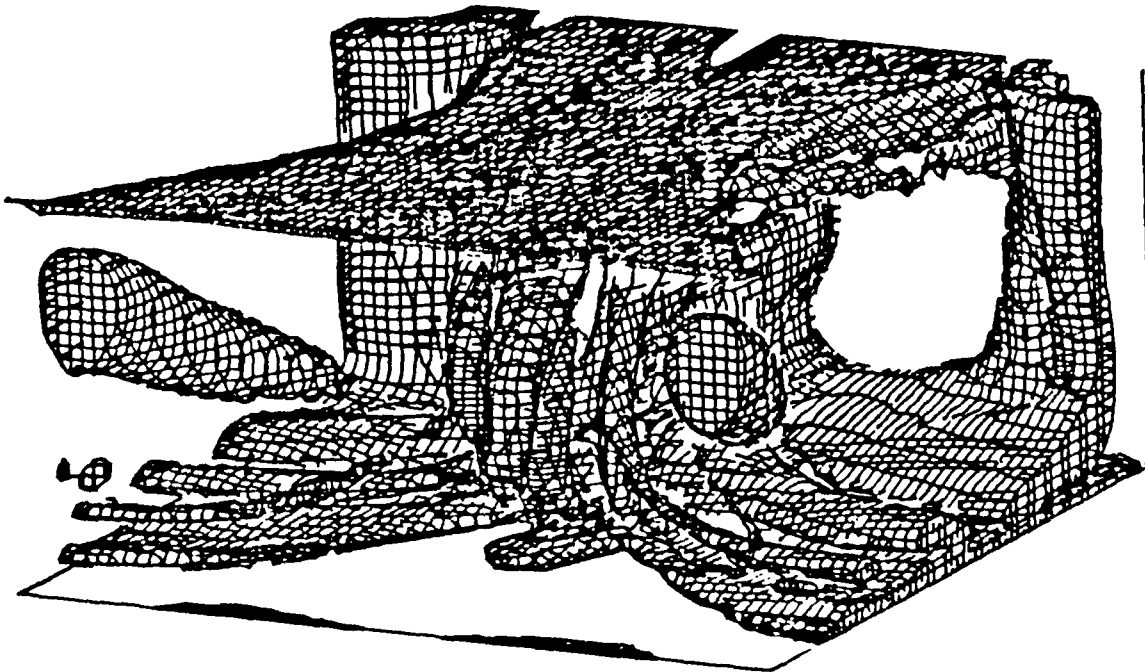


d. v-velocity profiles at  $x = 0.5D$

Figure 39. Velocity profiles in the  $y$ - $z$  plane as a function of  $z$  at  $t = 50.64$  for combined forcing at  $St = 0.235$  and  $0.47$ .

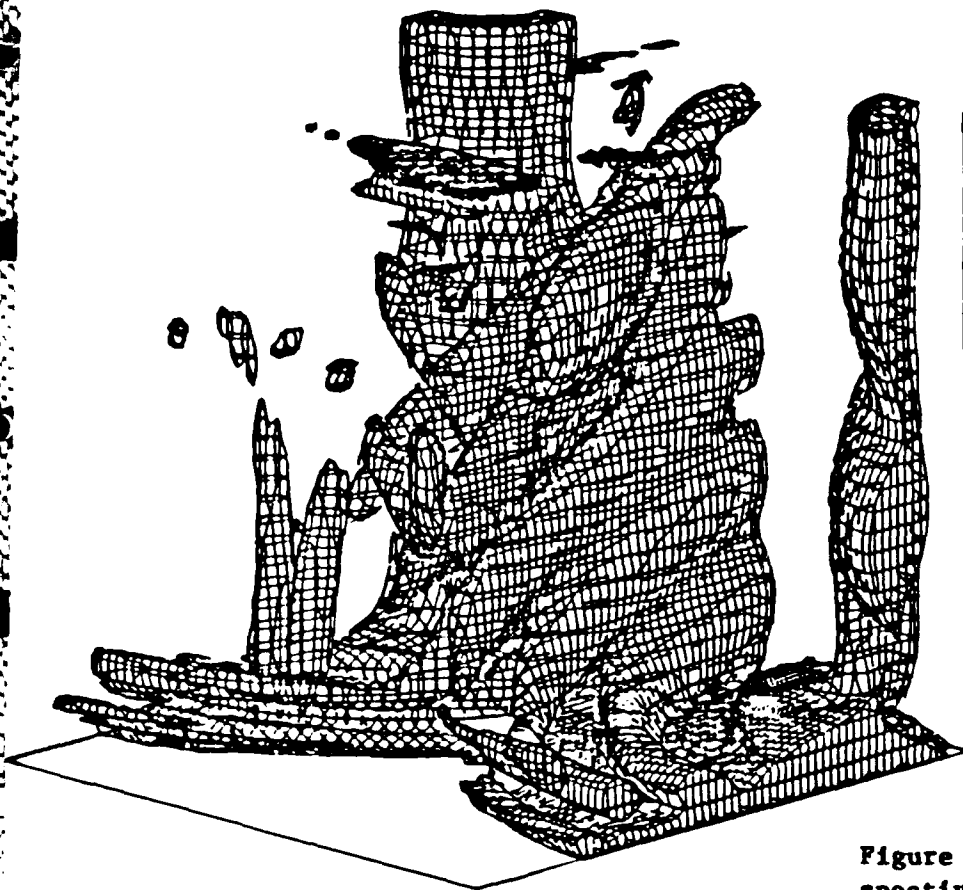


a. vorticity level is  $|\omega| = 1.95$



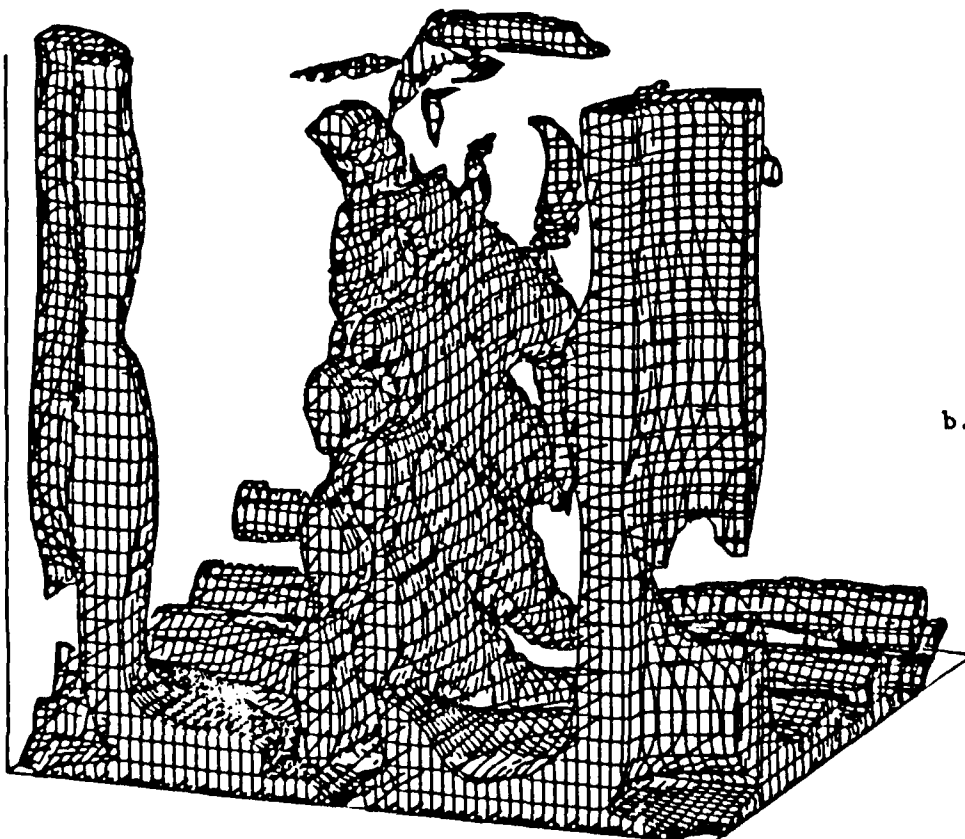
b. vorticity level is  $|\omega| = 2.50$

Figure 40. Three-dimensional perspective of the vorticity surface at  $t = 22.5$  for two jets forced axisymmetrically at  $St = 0.47$  with a phase difference of  $\pi$  for  $H = 1.5D$ .

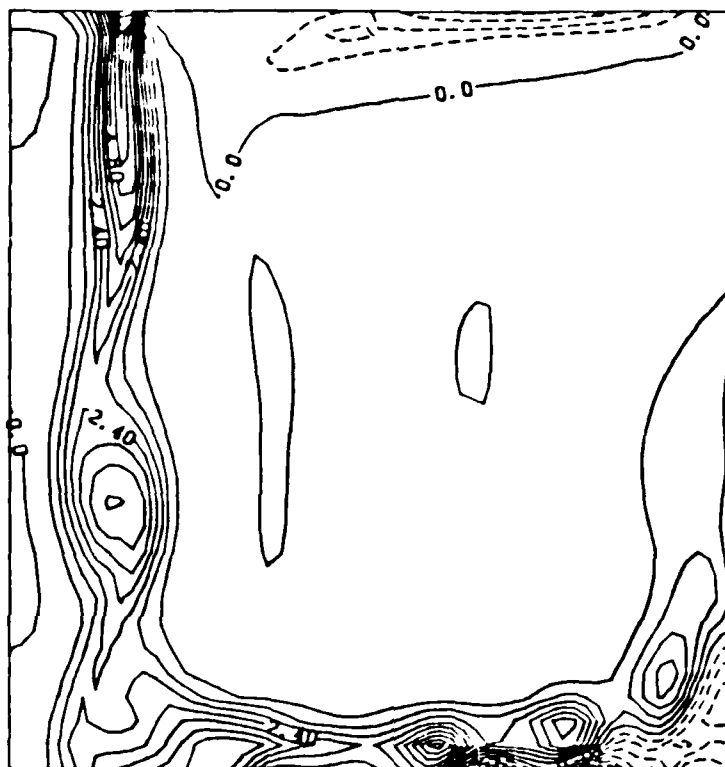


a. view of the impinging jets and the outflow at a level  $|\omega| = 1.95$

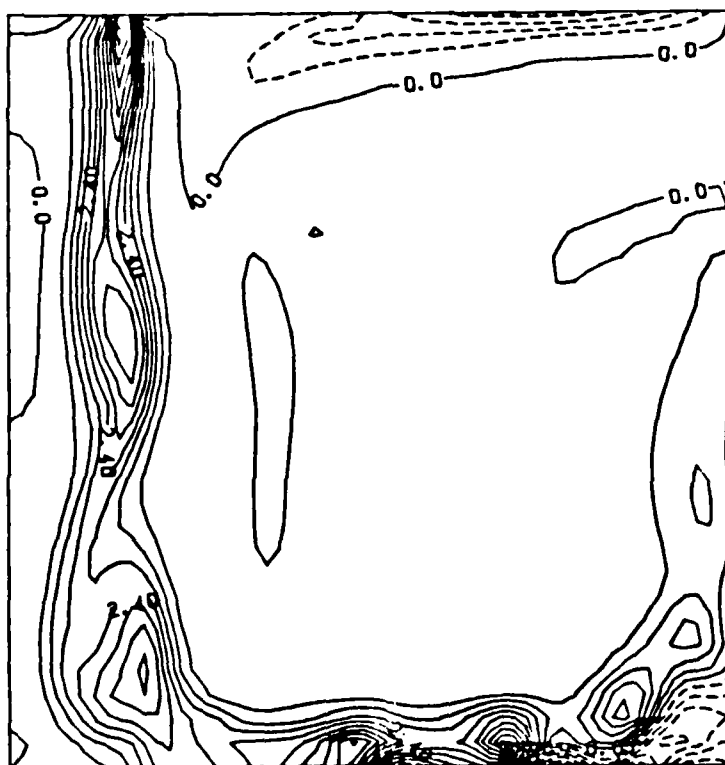
Figure 41. Three-dimensional perspective of the vorticity surface at  $t = 25.3$  for two jets forced axisymmetrically at  $St = 0.47$  with a phase difference of  $\pi$  for  $H = 3D$ .



b. view of the impinging jets and the fountain at a level  $|\omega| = 1.95$

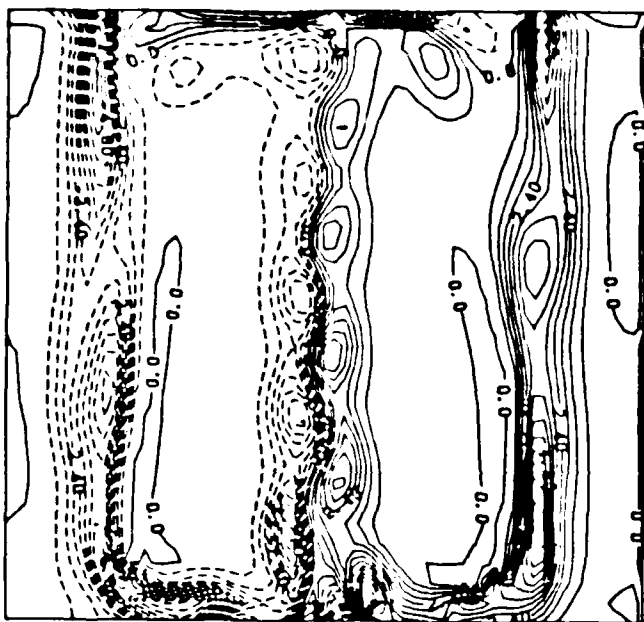


a.  $x = 0$  plane at  $t = 22.3$

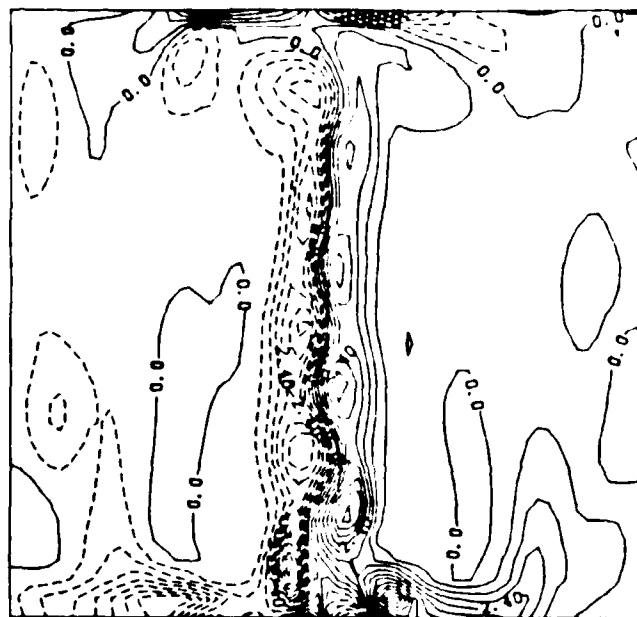
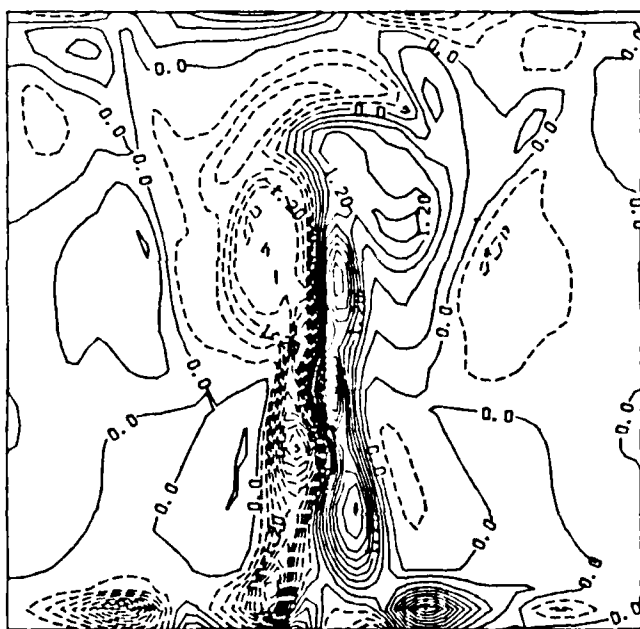


b.  $x = 3D$  plane at  $t = 22.3$

Figure 42.  $x$ -vorticity contours in the  $y$ - $z$  plane for jets forced at  $St = 0.47$  with a phase difference of  $\pi$  for  $H = 3D$  (contour interval = 0.6).

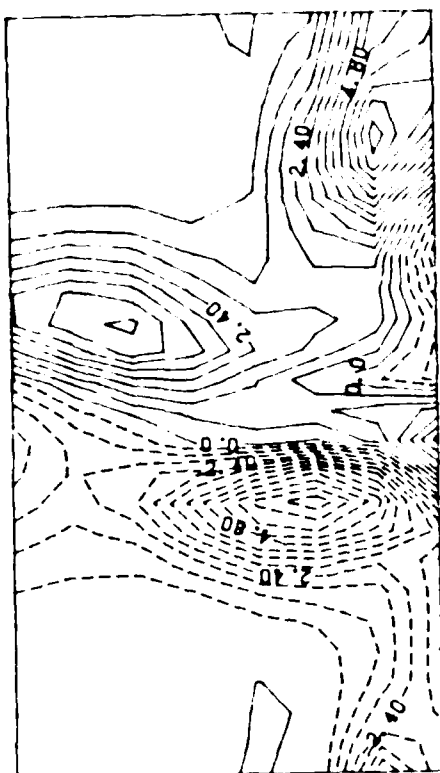


a.  $y = 0$  plane at  $t = 22.3$

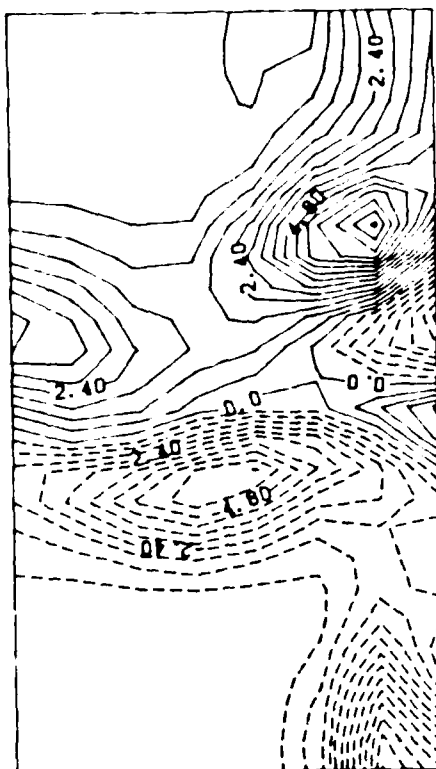
b.  $y = 0.51D$  plane at  $t = 22.3$ 

c.  $y = 1.5D$  plane at  $t = 22.3$ .

Figure 43.  $y$ -vorticity contours in the  $x$ - $z$  plane for jets forced at  $St = 0.47$  with a phase difference of  $\pi$  for  $H = 3D$  (contour interval = 0.6 for a - b; 0.3 for e).

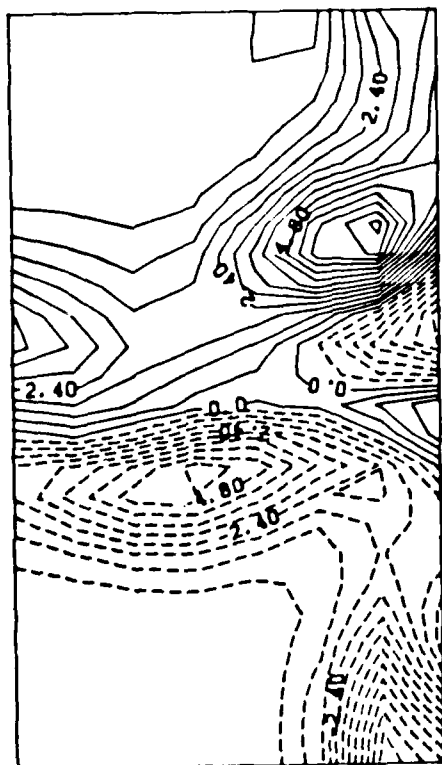


d.  $t = 26.88$

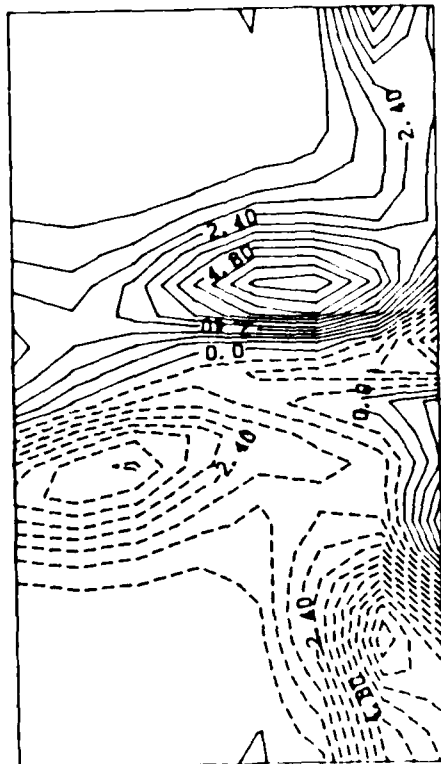


e.  $t = 27.42$

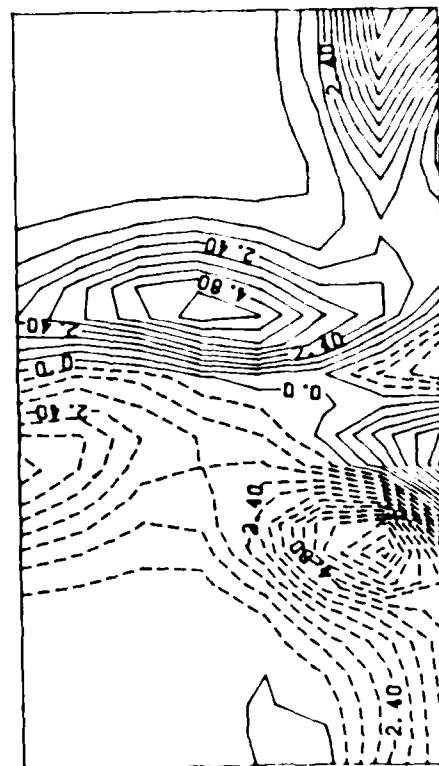
Figure 44. Time sequence of the y-vorticity contours in the x-z plane at  $y = 0$  in the vicinity of the wall jet collision zone for  $H = 3D$ . The jets are forced at  $St = 0.47$  with a phase difference of  $\pi$  (contour interval = 0.6).



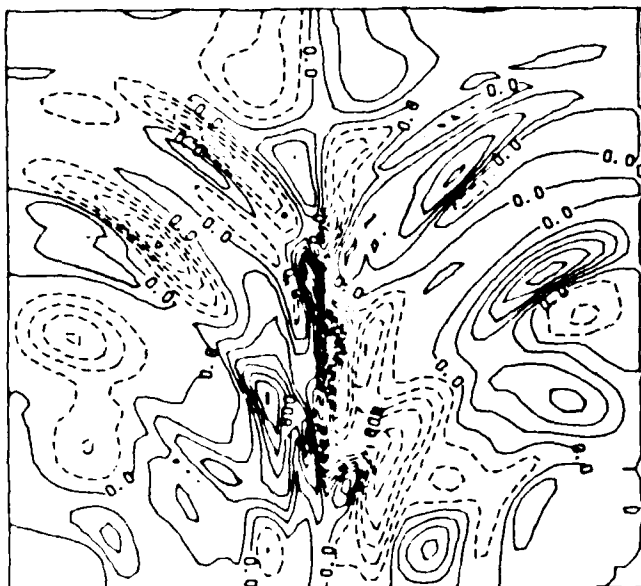
a.  $t = 25.3$



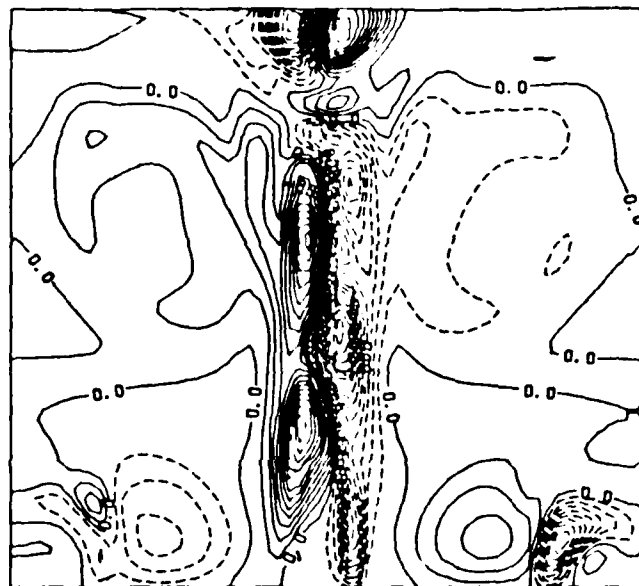
b.  $t = 25.8$



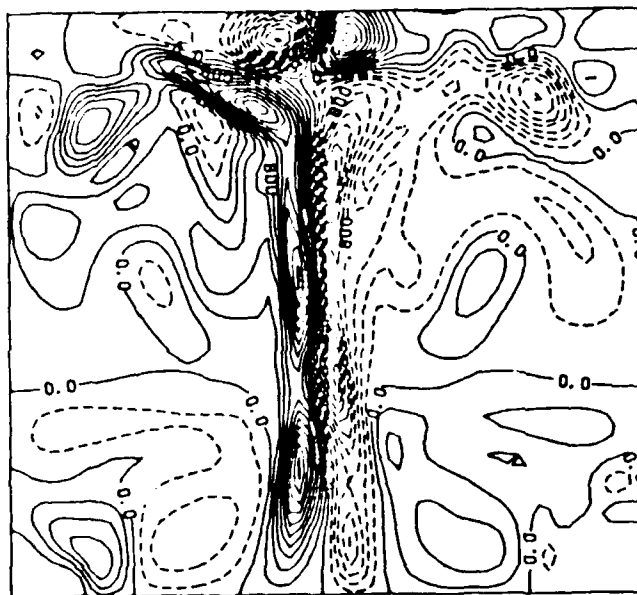
c.  $t = 26.4$



a.  $z = 0.14D$  plane at  $t = 25.3$



b.  $z = 0.8D$  plane at  $t = 25.3$



c.  $z = 1.45D$  plane at  $t = 25.3$

Figure 45.  $z$ -vorticity contours in the  $x$ - $y$  plane for jets forced at  $St = 0.47$  with a phase difference of  $\pi$  for  $H = 3D$  (contour interval = 0.2).

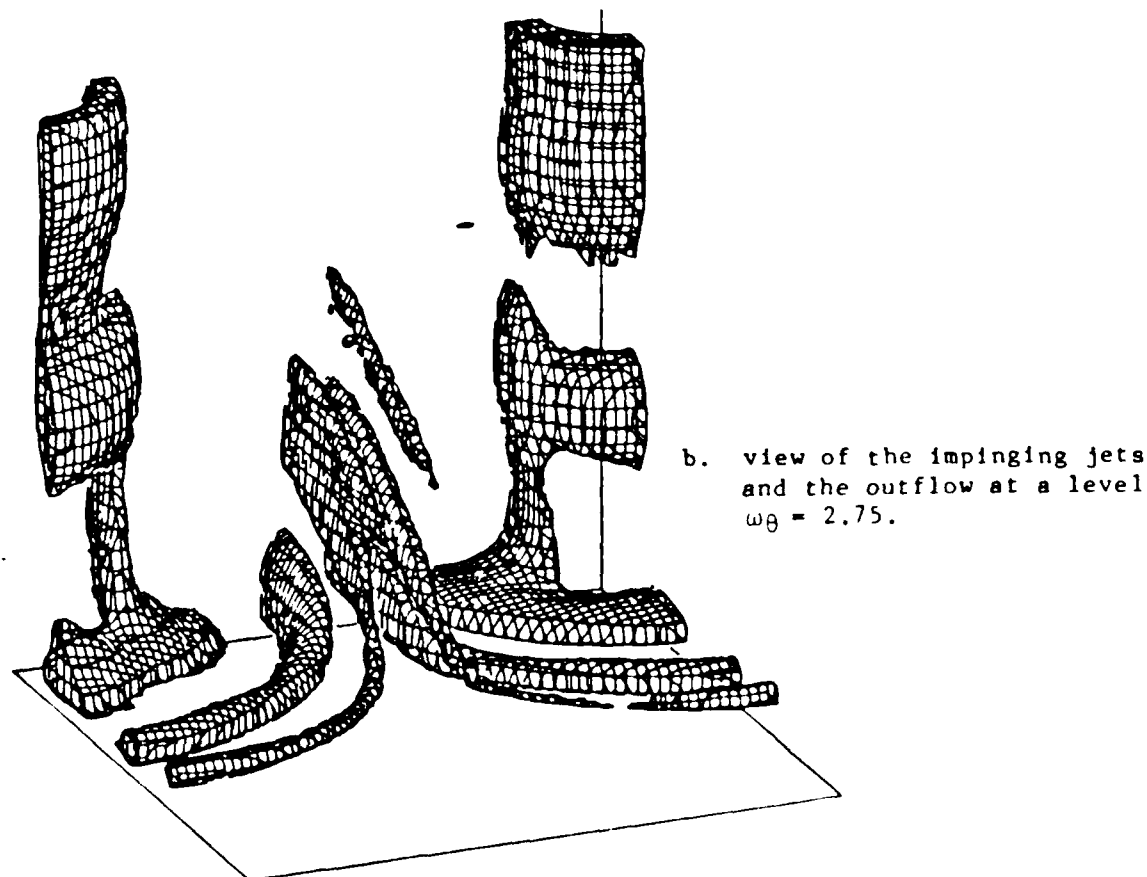
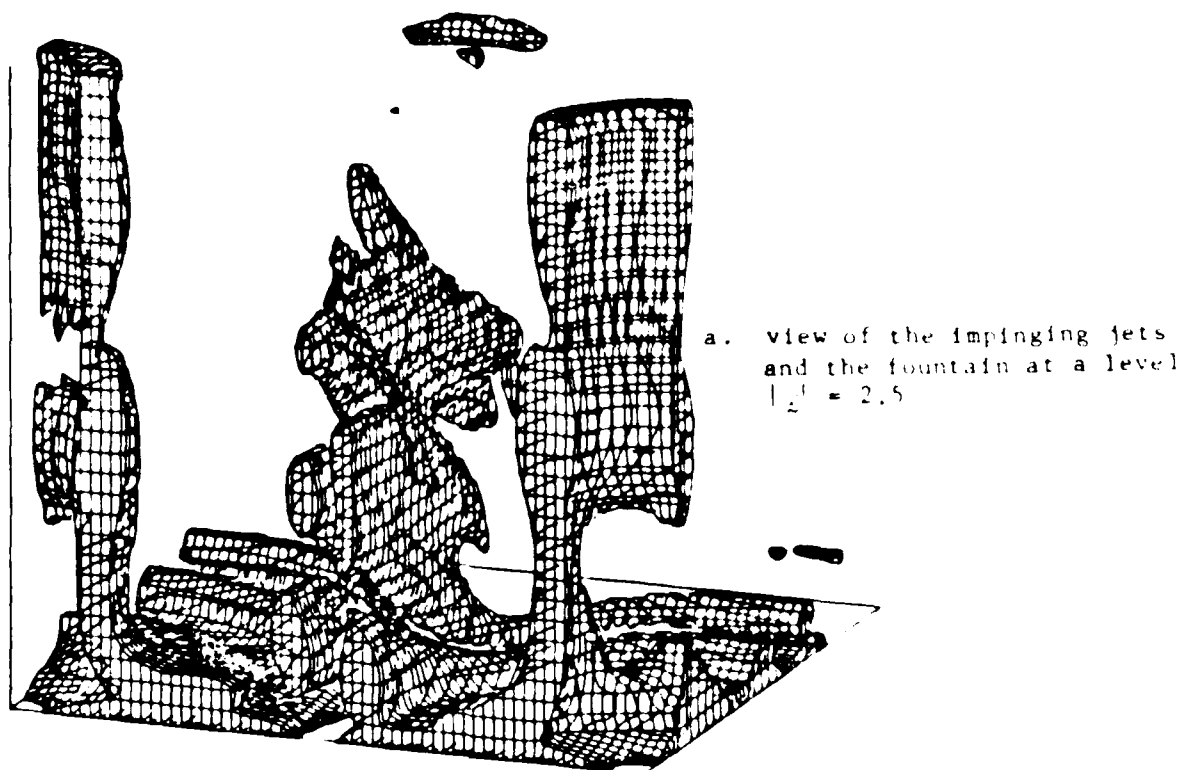
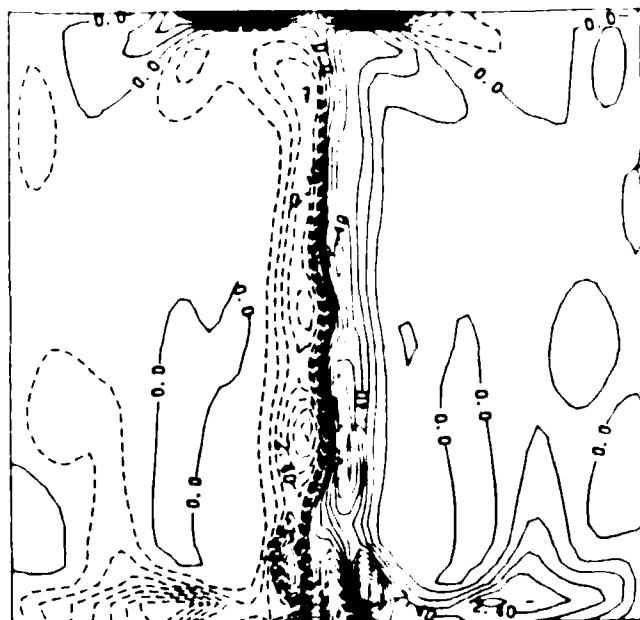


Figure 46. Three-dimensional perspective of the vorticity surface at  $t = 25.3$  for two jets forced axisymmetrically at  $St = 0.47$  with a phase difference of  $\pi/2$ .

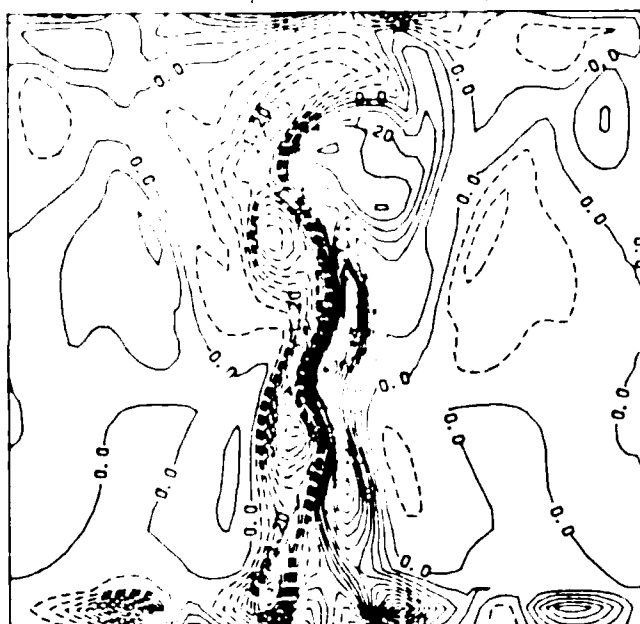




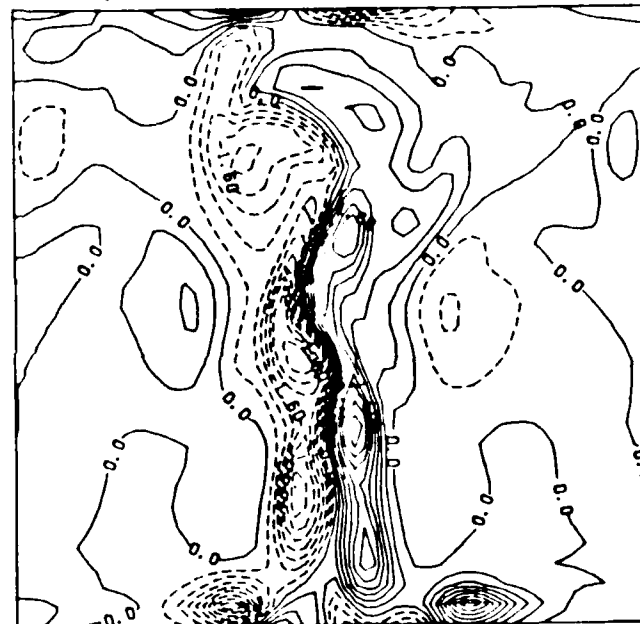
a.  $v = 0$  plane at  $t = 25.3$



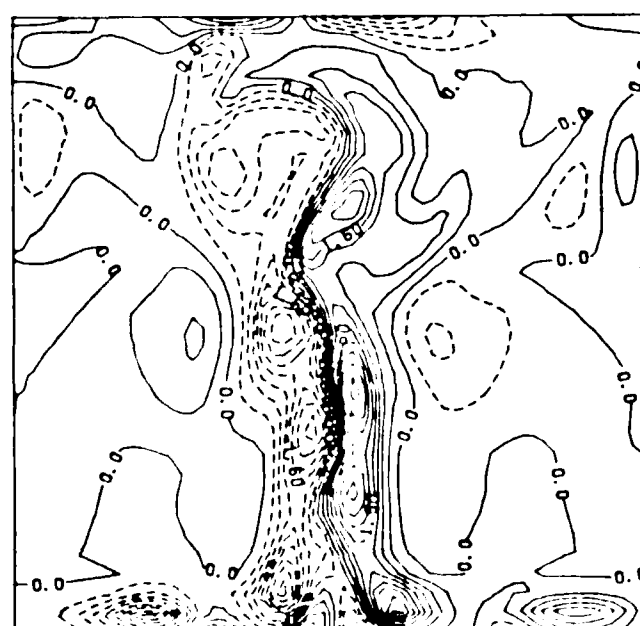
b.  $y = 0.51D$  plane at  $t = 25.3$



c.  $y = 1.5D$  plane at  $t = 25.3$

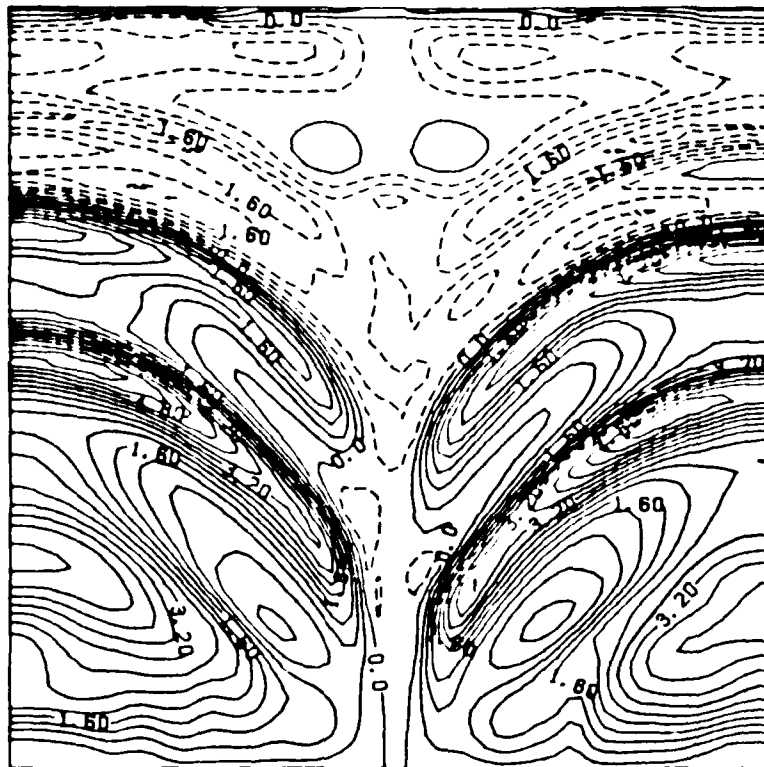


d.  $y = 1.5D$  plane at  $t = 28.47$

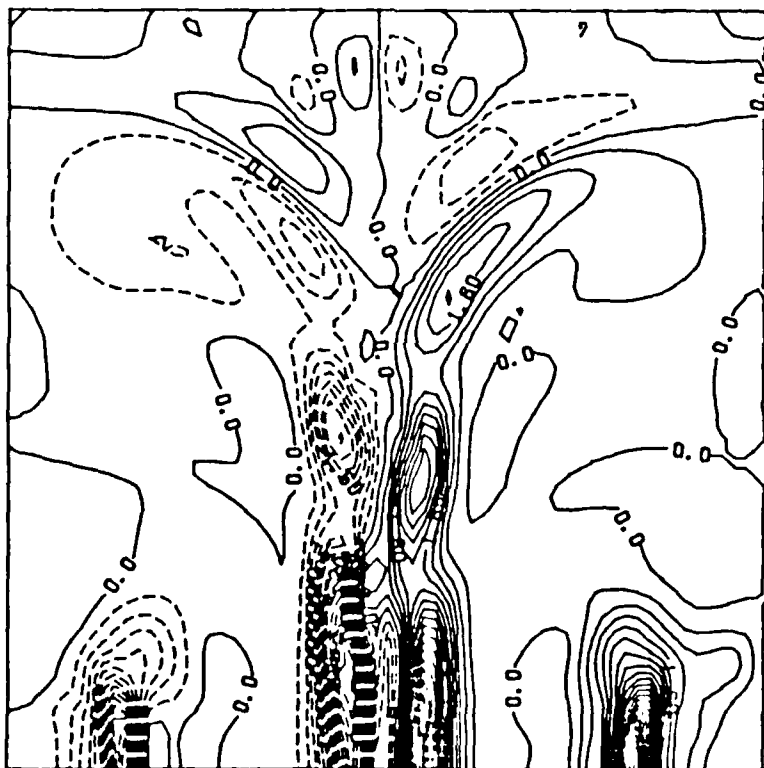


e.  $y = 1.5D$  plane at  $t = 29.53$

Figure 47.  $y$ -vorticity contours in the  $x$ - $z$  plane for jets forced at  $St = 0.47$  with a phase difference of  $\pi/2$  (contour interval = 0.6 for a - b; 0.4 for c - e).



a. x-vorticity contours in the  $z = 0.14D$  plane

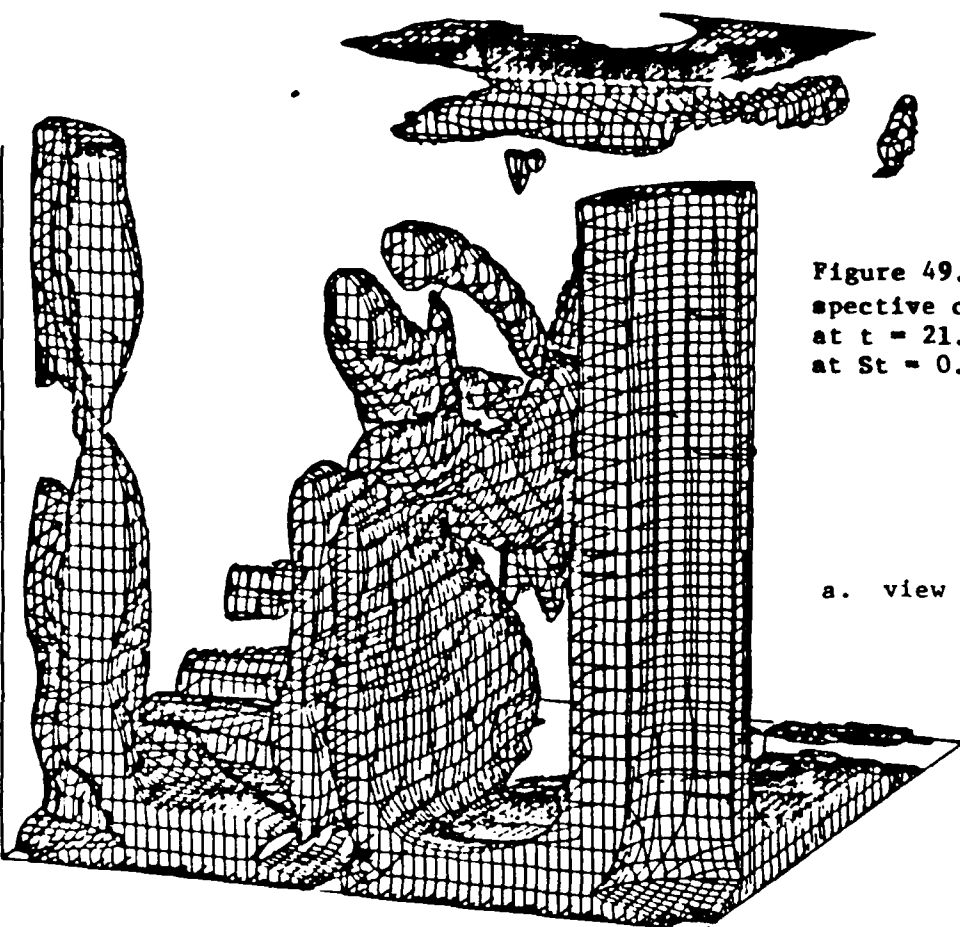


b. y-vorticity contours in the  $z = 0.14D$  plane

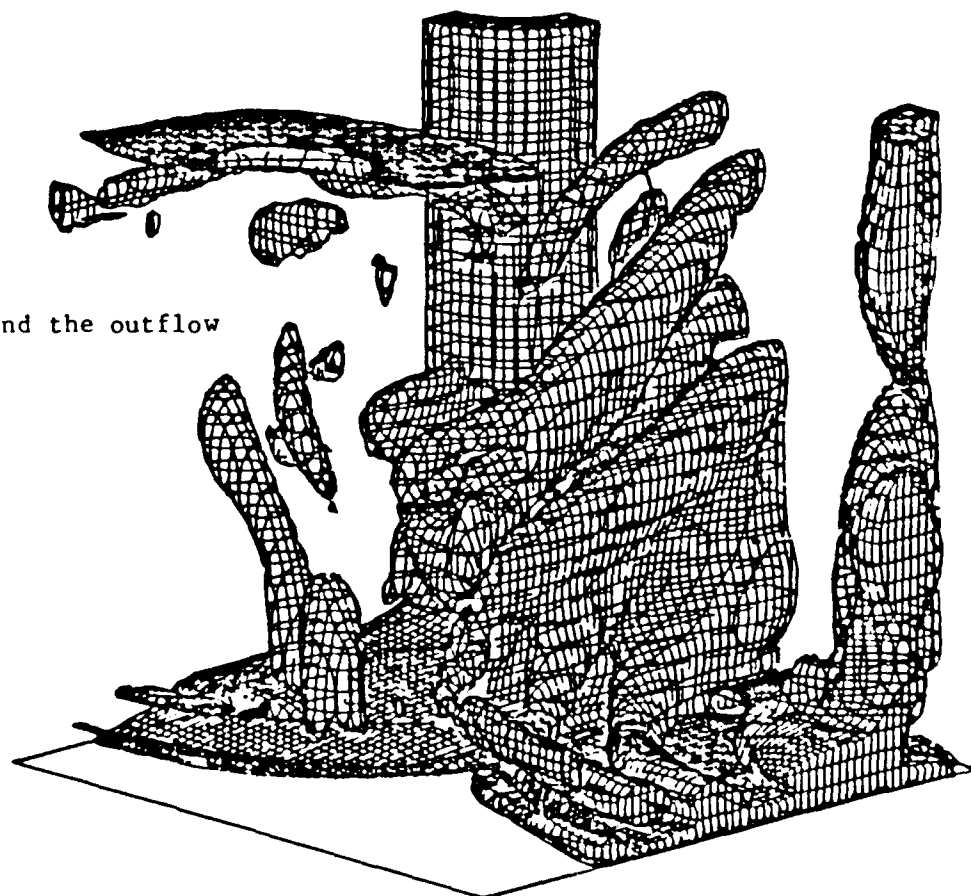
Figure 48. Vorticity contours at  $t = 25.3$  in the  $x$ - $y$  plane for jets forced at  $St = 0.47$  with a phase difference of  $\pi/2$  (contour interval = 0.4).

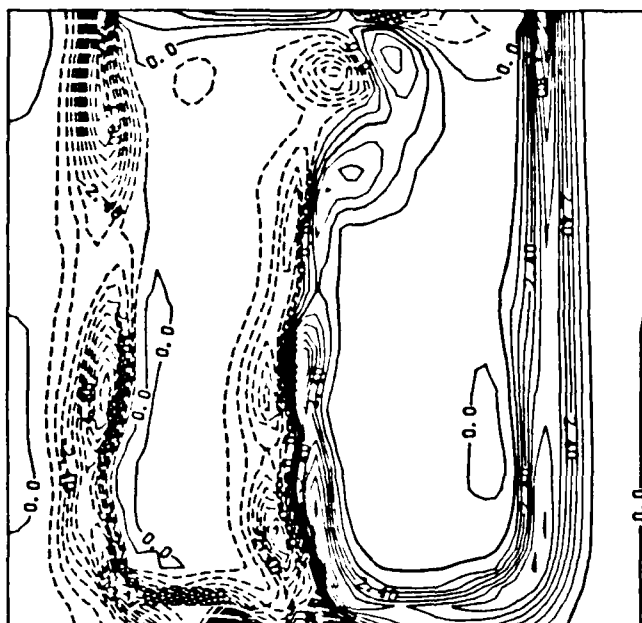
Figure 49. Three-dimensional perspective of the vorticity surface at  $t = 21.1$  for only one jet forced at  $St = 0.47$  at a level  $|\omega| = 1.95$ .

a. view of the jets and the fountain

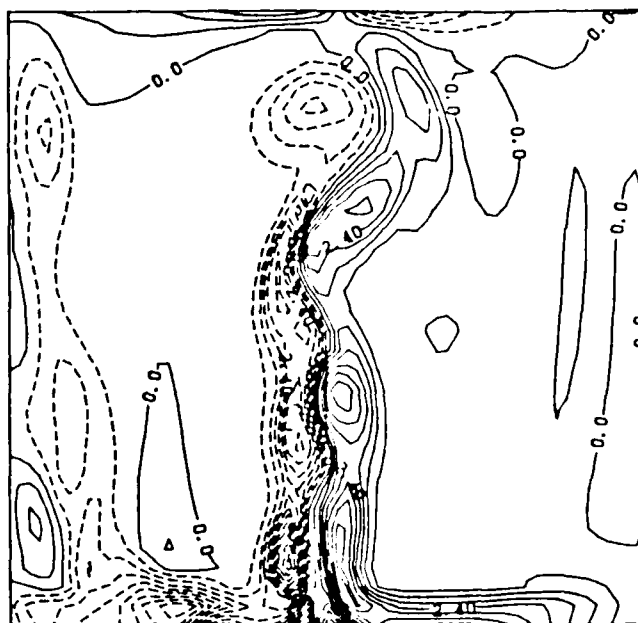


b. view of the jets and the outflow

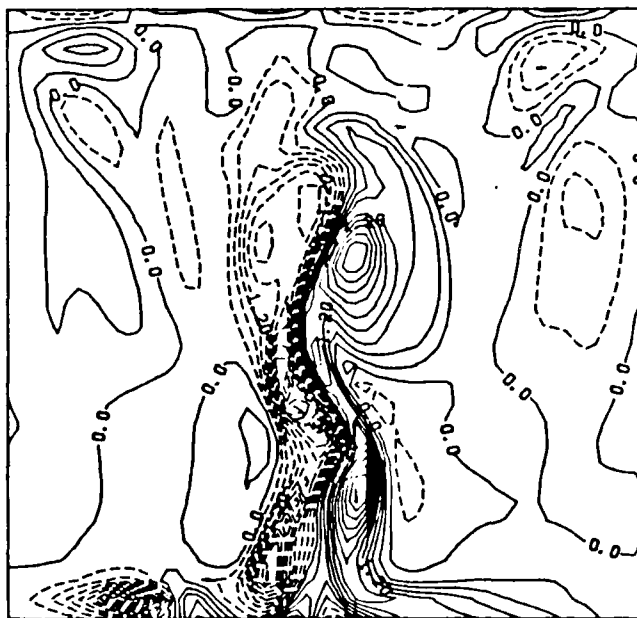




a.  $y = 0$  plane

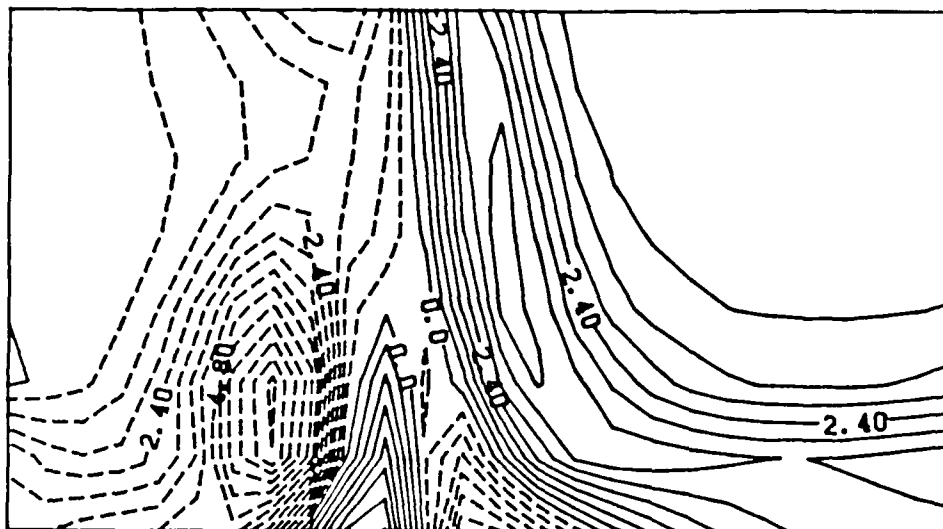


b.  $y = 0.51D$  plane

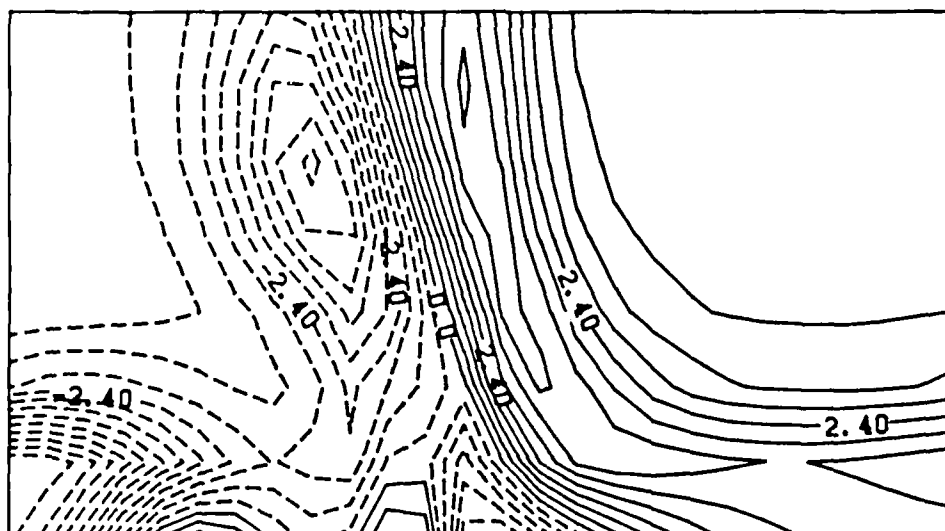


c.  $y = 1.5D$  plane

Figure 50.  $y$ -vorticity contours in the  $x$ - $z$  plane at  $t = 23.2$  for only one jet forced at  $St = 0.47$  (contour interval = 0.6 for a - b; 0.3 for c).

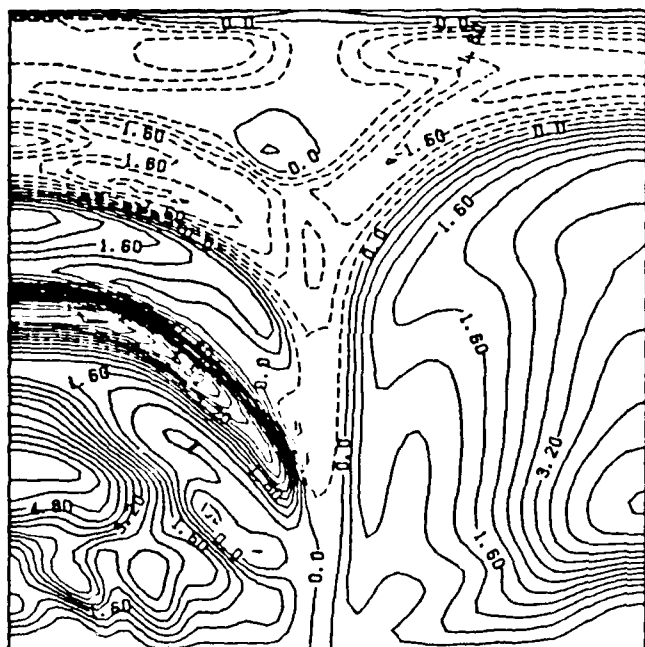


a.  $t = 22.15$

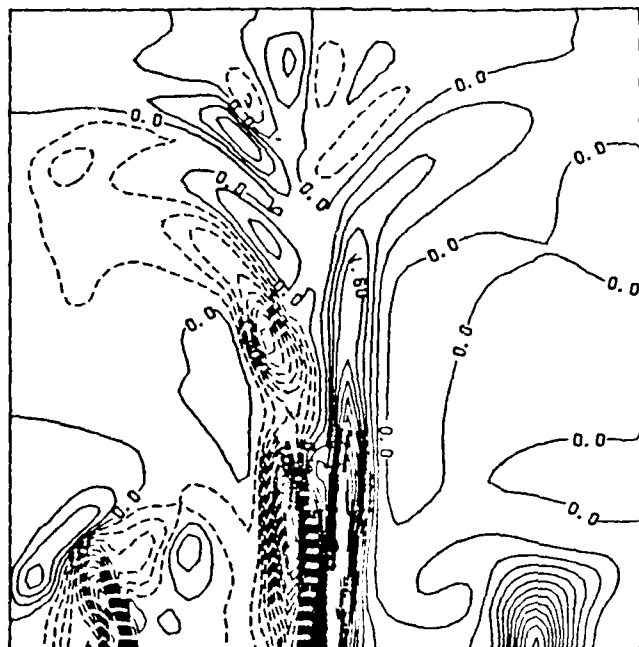


b.  $t = 23.2$

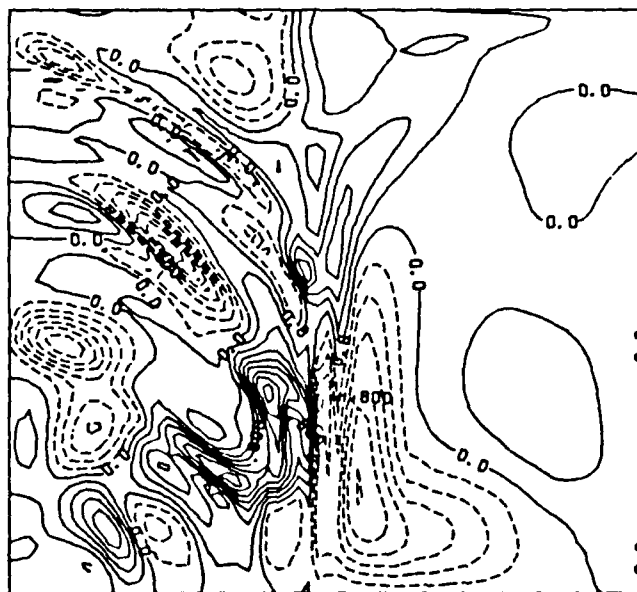
Figure 51.  $y$ -vorticity contours in the  $x$ - $z$  plane at  $y = 0$  in the vicinity of the wall jet collision zone for only one jet forced at  $St = 0.47$ . (contour interval = 0.8).



a. x-vorticity (contour interval = 0.4)

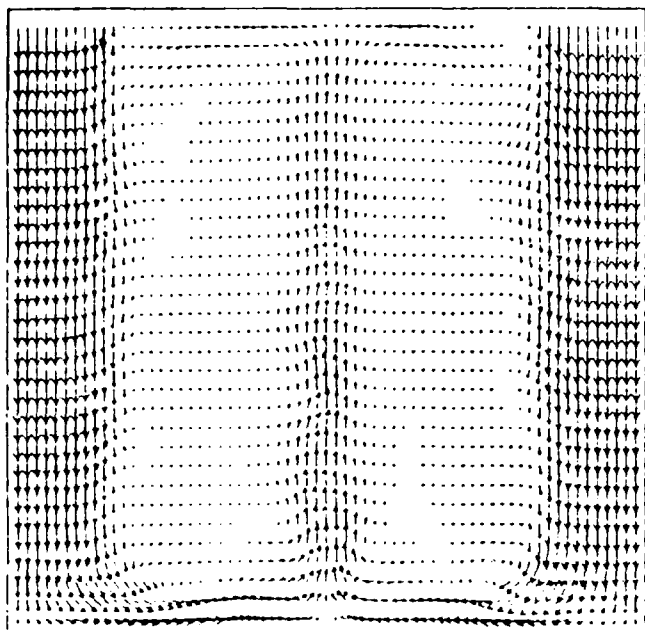


b. y-vorticity (contour interval = 0.4)

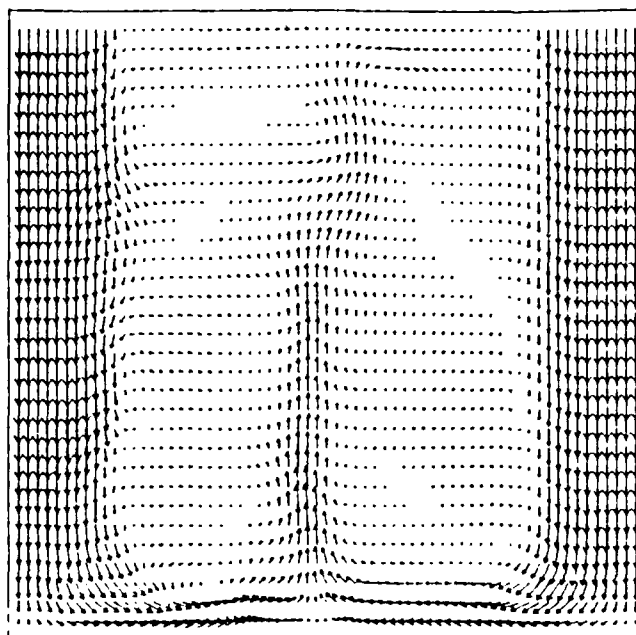


c. z-vorticity (contour interval = 0.2)

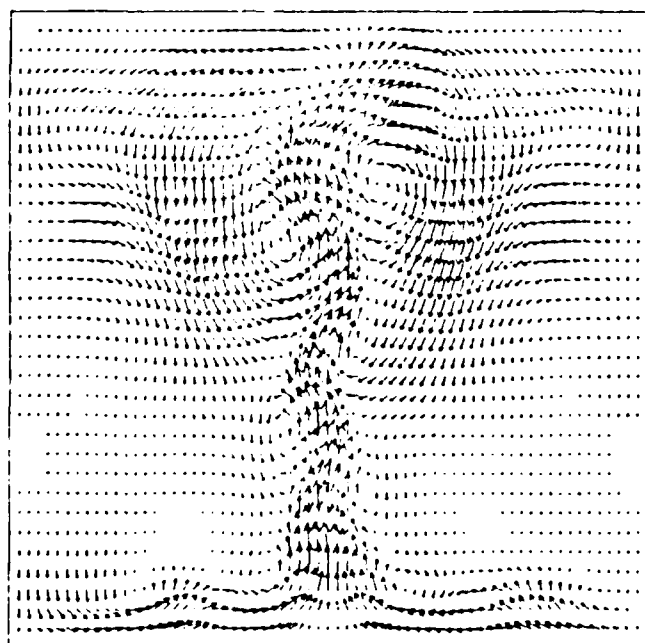
Figure 52. Vorticity contours in the  $x$ - $y$  plane for only one jet forced at  $St = 0.14D$ . View of the  $z = 0.14D$  plane at  $t = 21.1$ .



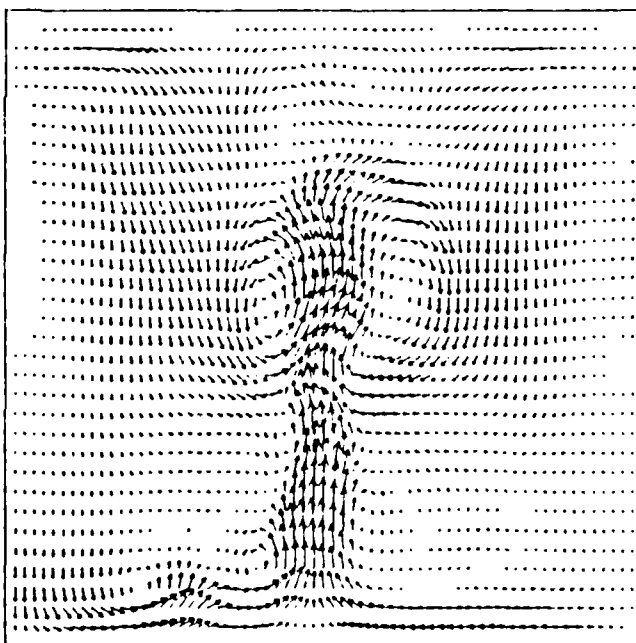
a.  $y = 0$  plane for two jets forced at  $St = 0.47$  with a phase difference of  $\pi/2$



b.  $y = 0$  plane for only one jet forced at  $St = 0.47$



c.  $y = 1.5D$  plane for two jets forced at  $St = 0.47$  with a phase difference of  $\pi/2$



d.  $y = 1.5D$  plane for only one jet forced at  $St = 0.47$

Figure 53. Velocity vector diagram in the x-z plane.

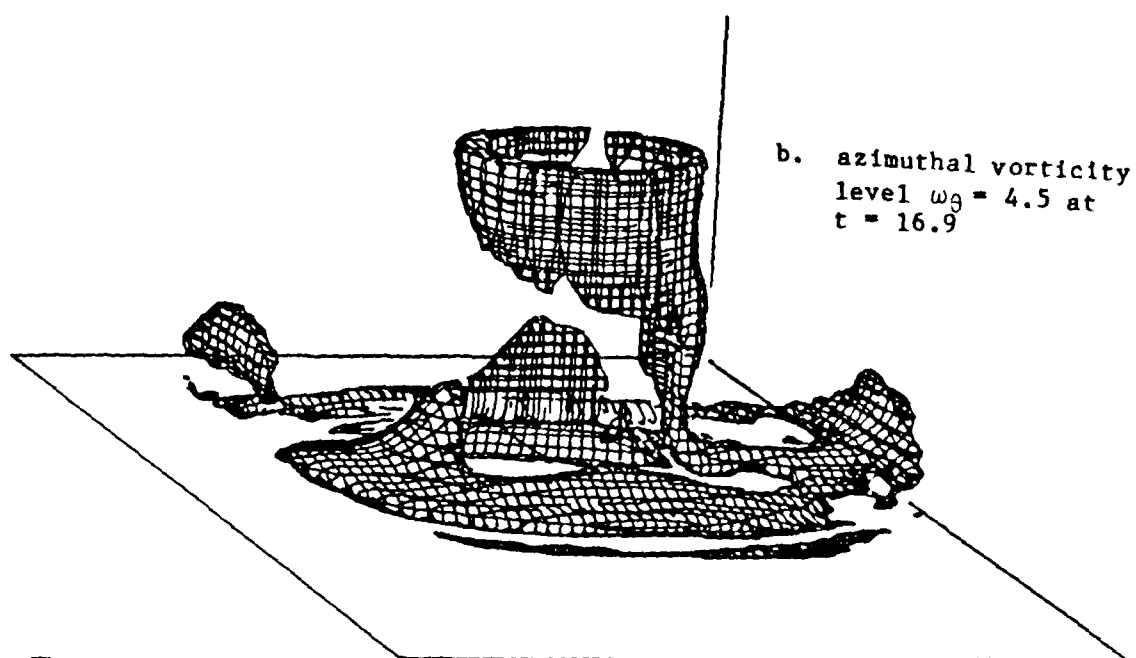
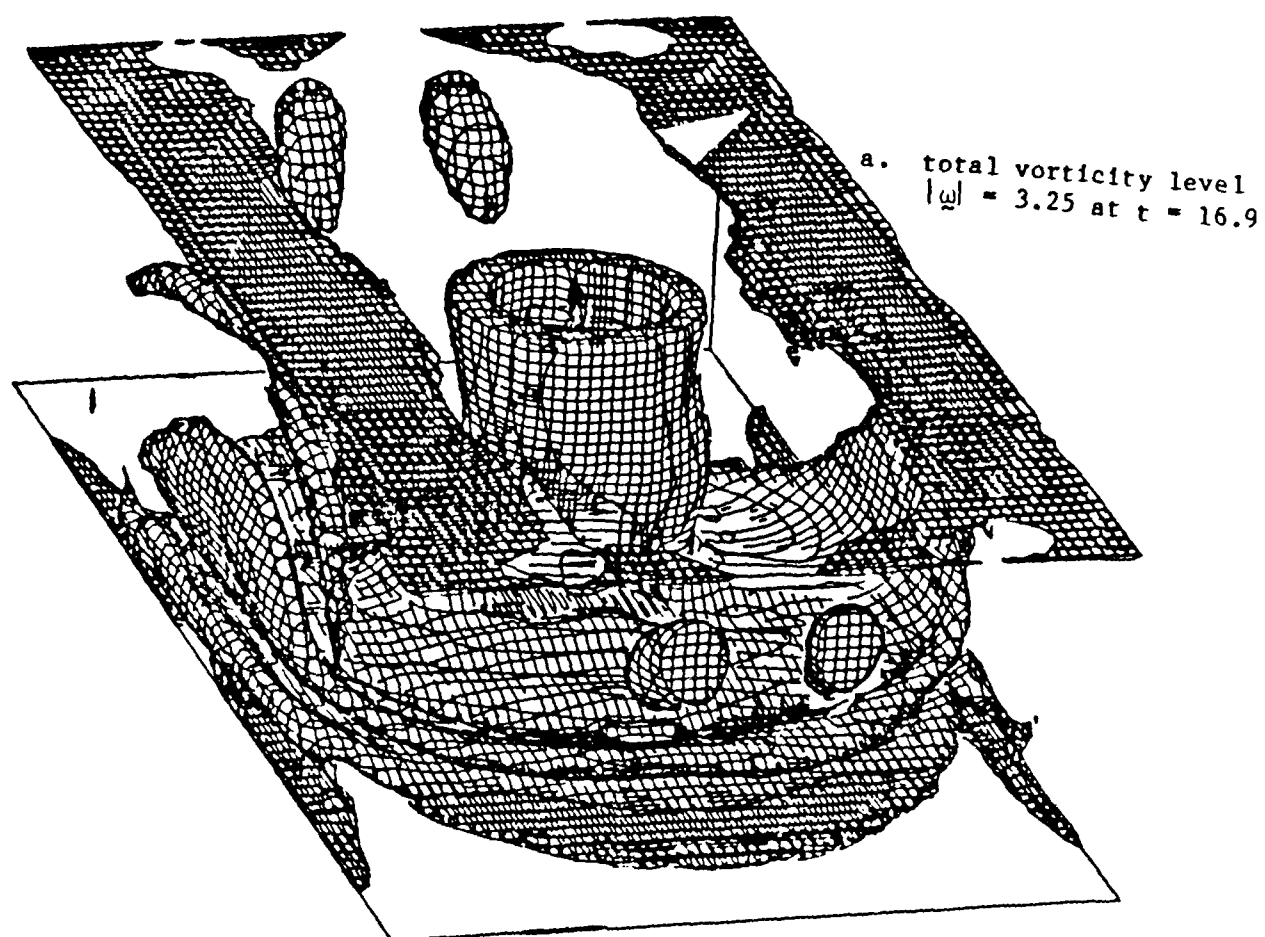
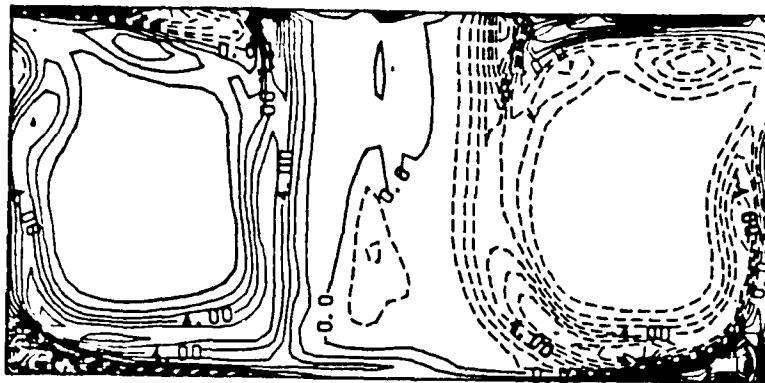
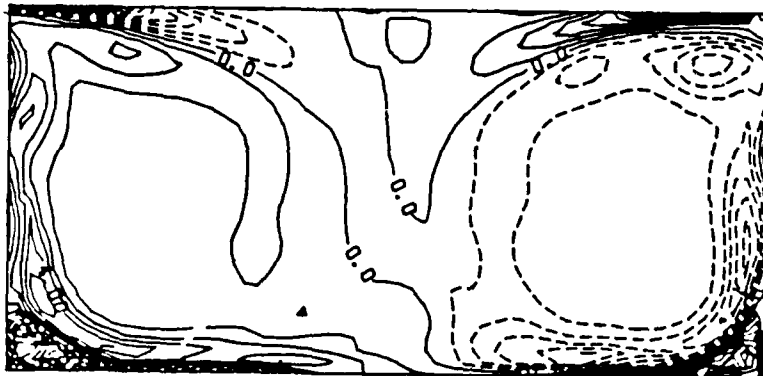


Figure 54. Three-dimensional perspective of the vorticity surface for a jet forced azimuthally at  $St = 0.47$  for  $H = 1.5D$ . The forcing level is  $0.1U$ .

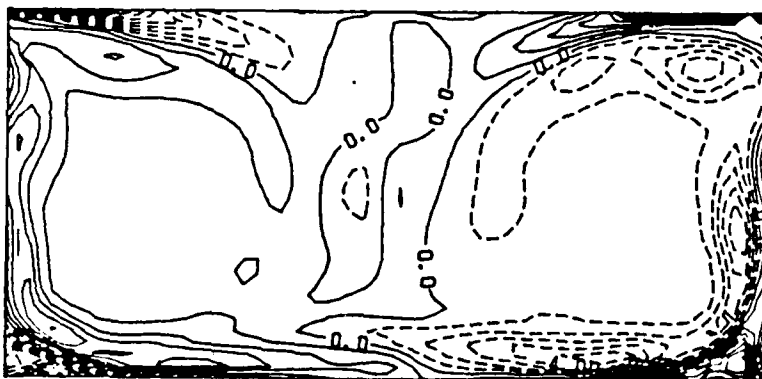




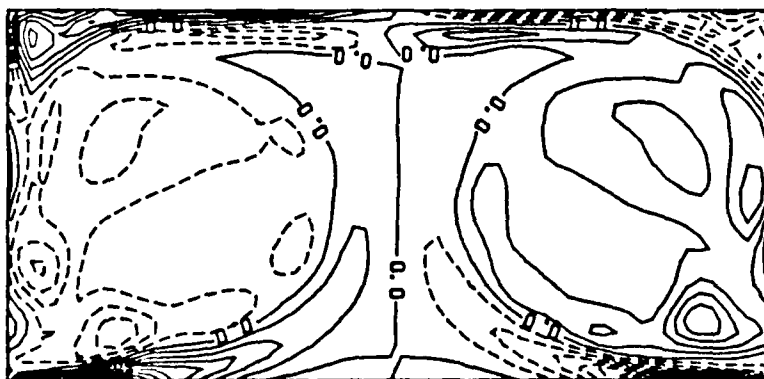
a.  $y = 0$  plane



b.  $y = -0.51D$  plane

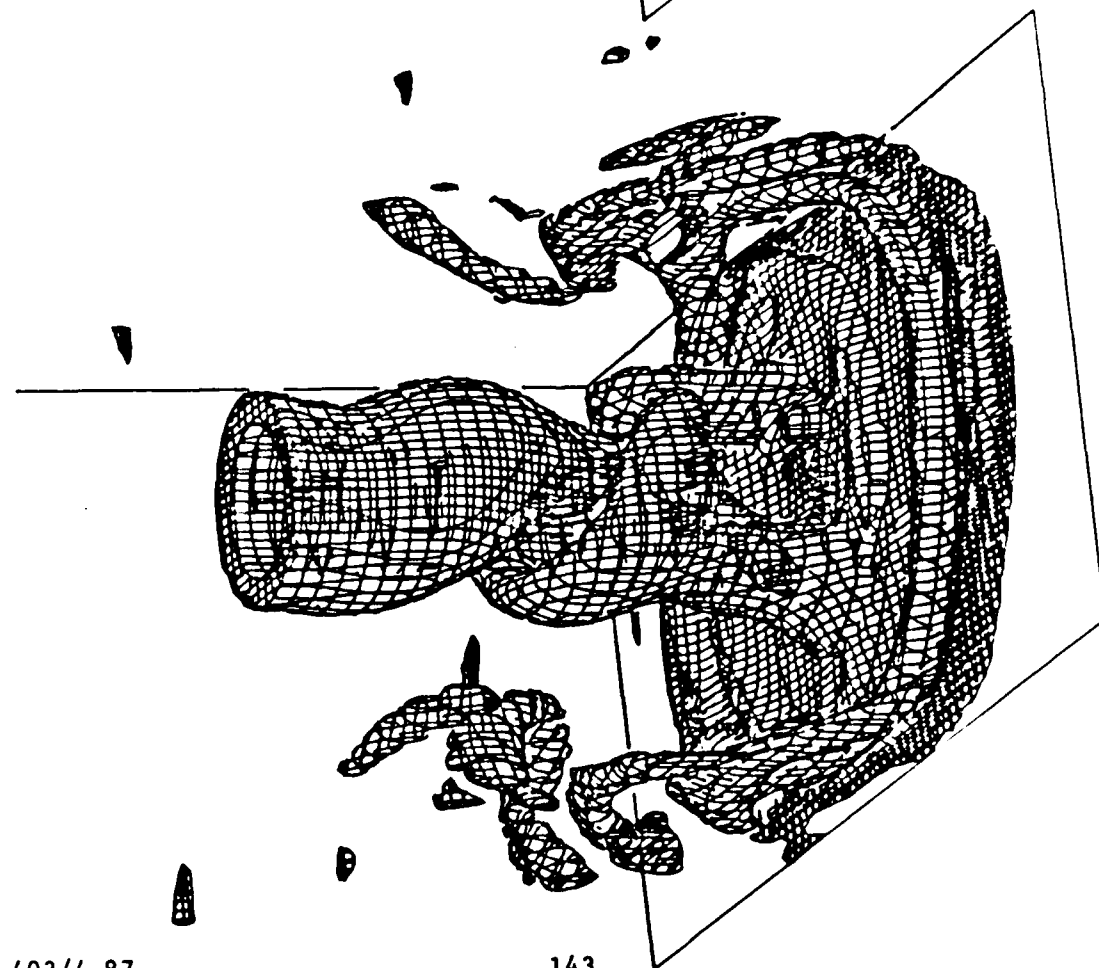


c.  $y = 0.51D$  plane

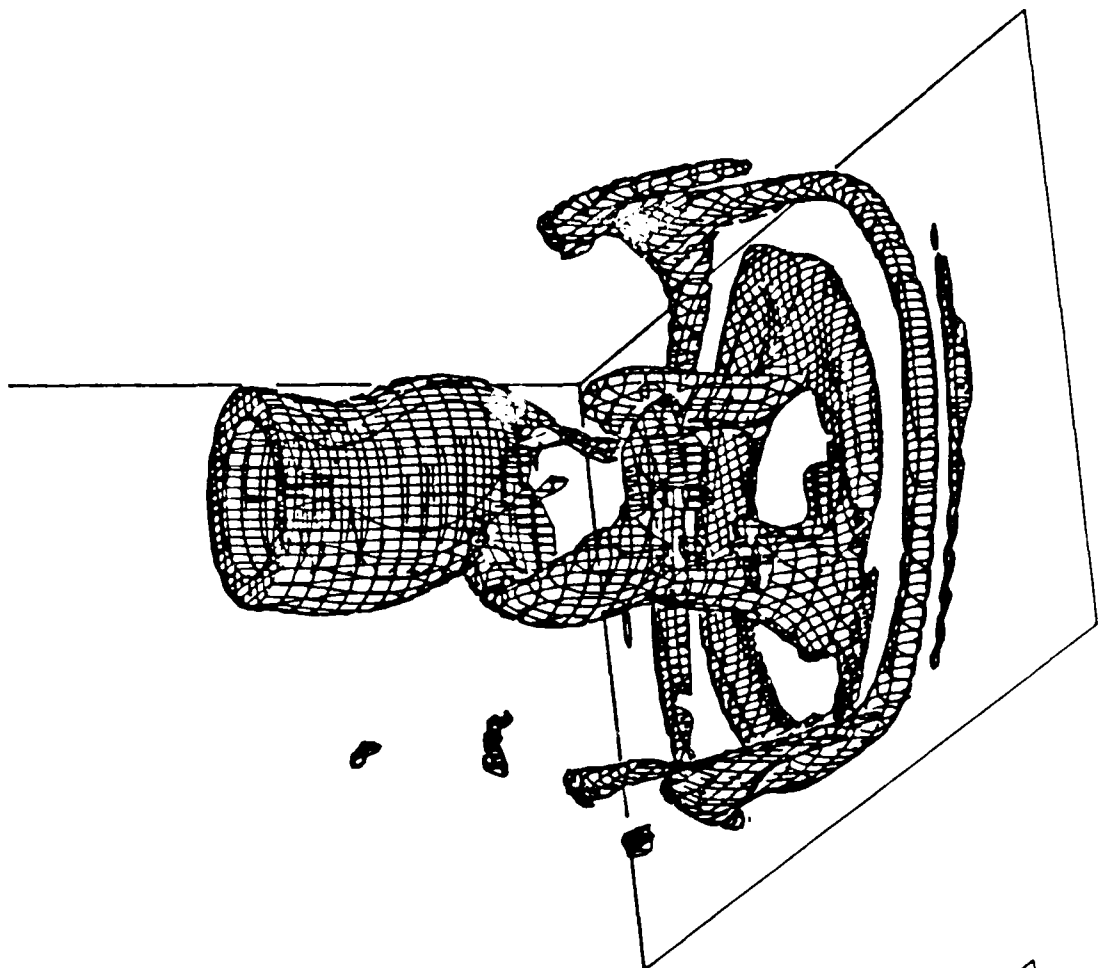


d.  $y = -1.5D$  plane

Figure 55.  $y$ -vorticity contours in the  $x$ - $z$  plane for a jet forced azimuthally at  $St = 0.47$  for  $H = 1.5D$  at  $t = 16.9$  (contour interval = 1.0).

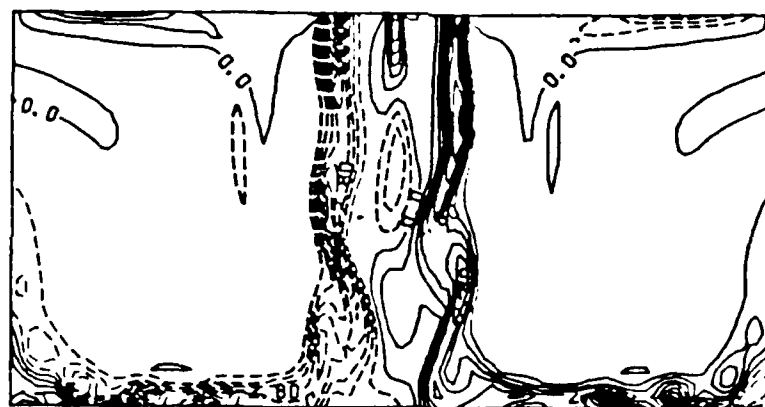


a. total vorticity level  $|\omega| = 3.0$

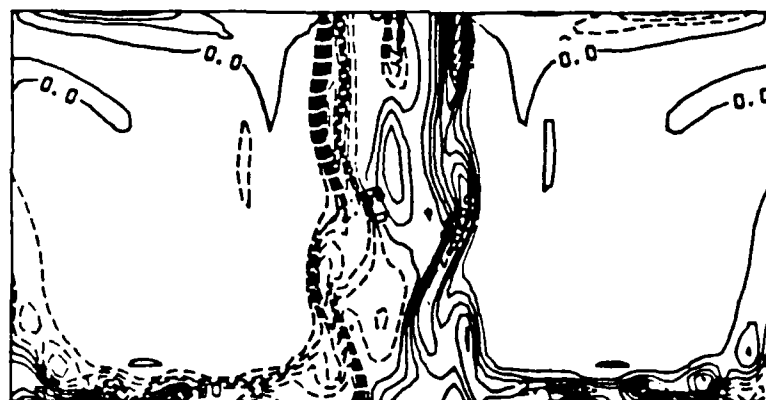


b. azimuthal vorticity level  $\omega_\theta = 3.0$

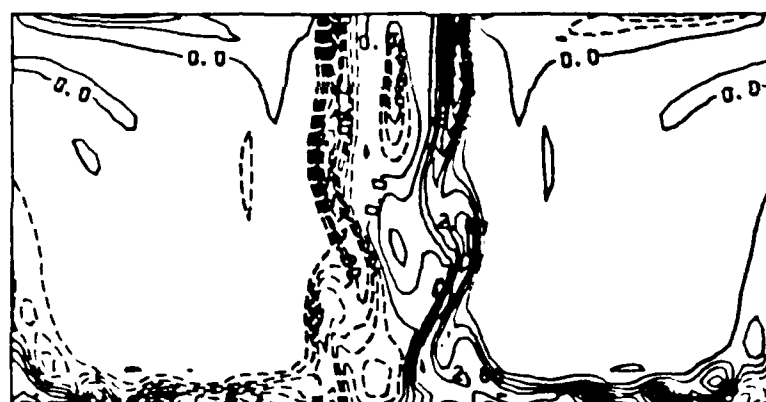
Figure 56. Three-dimensional perspective of the vorticity surface for a jet forced azimuthally at  $St = 0.47$  for  $H = 3D$  at  $t = 23.9$ . The forcing level is  $0.1U$ .



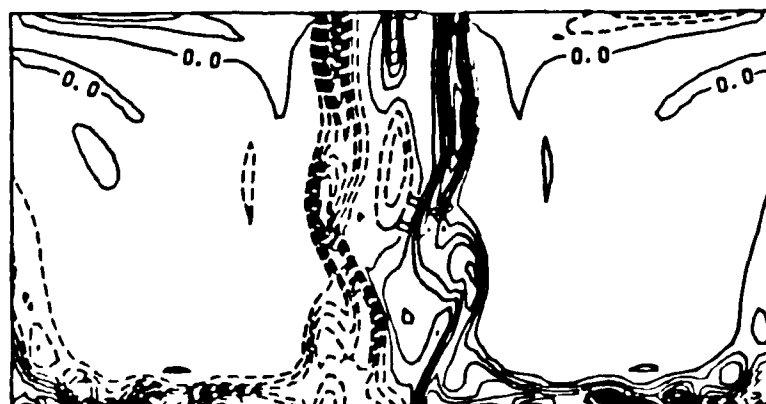
a.  $t = 21.80$



b.  $t = 22.85$

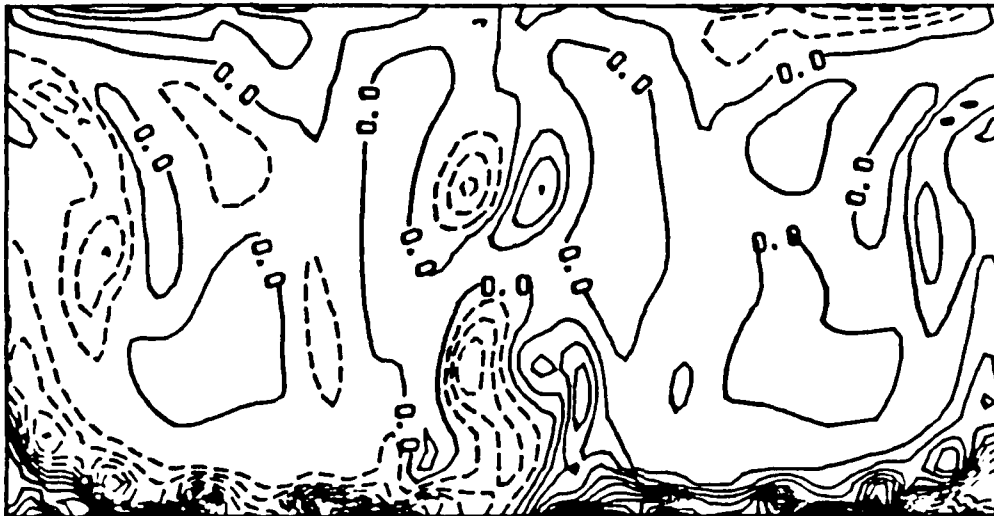


c.  $t = 23.37$

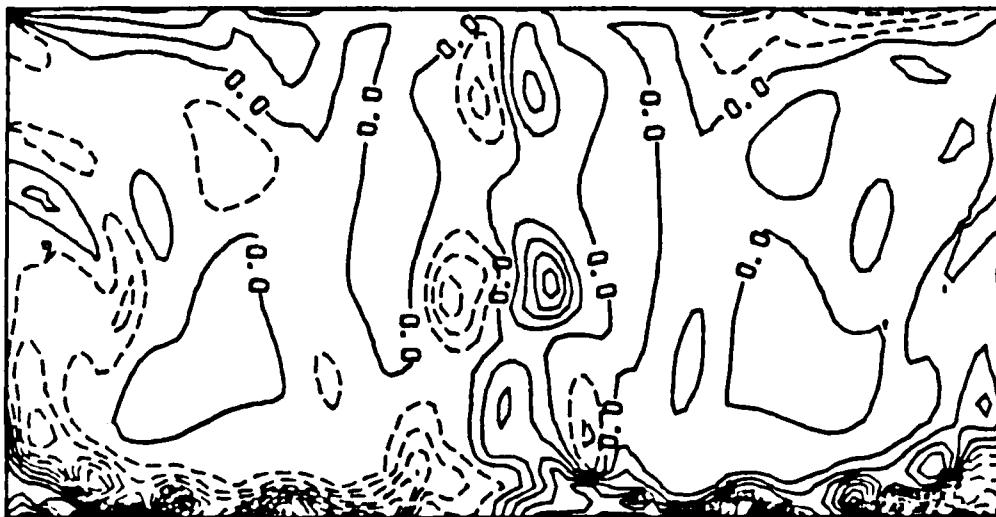


d.  $t = 23.91$

Figure 57. Time sequence of the x-vorticity contours in the y-z plane at  $x = 0$  for azimuthal forcing at  $St = 0.47$  (contour interval = 0.7).



a.  $x = -0.51D$  at  $t = 23.91$

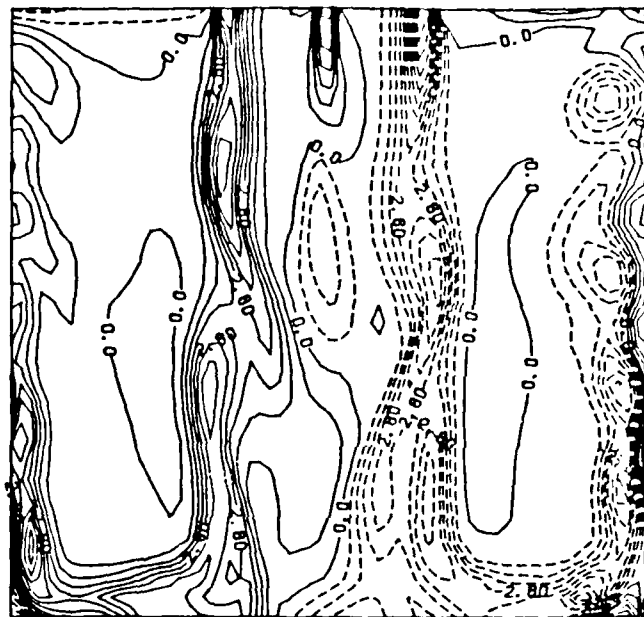


b.  $x = 0.51D$  at  $t = 23.91$

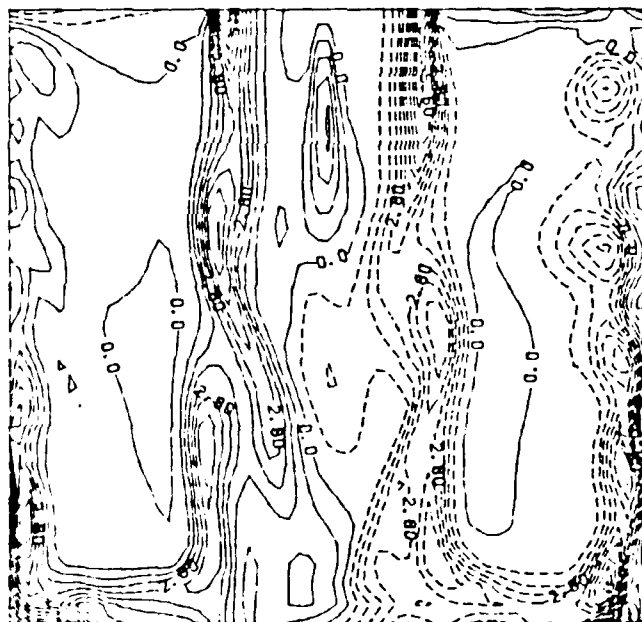
Figure 58.  $x$ -vorticity contours in the  $y$ - $z$  plane for azimuthal forcing at  $St = 0.47$  (contour interval = 0.7).



a.  $t = 22.85$

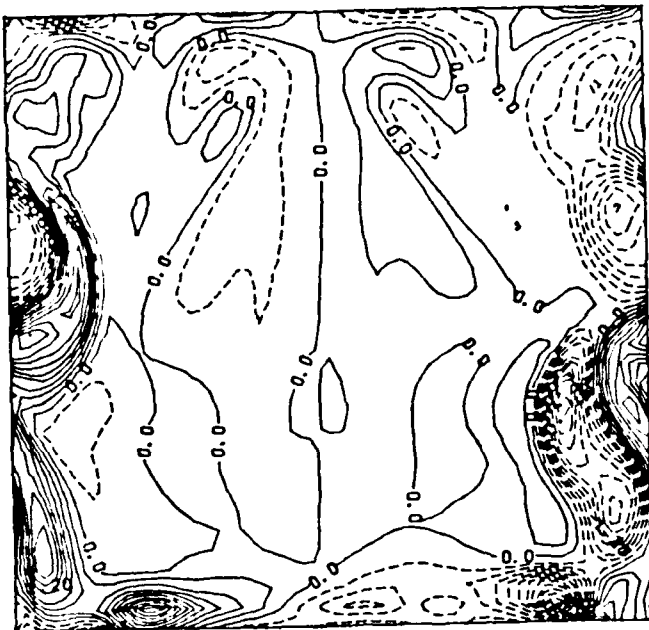


b.  $t = 23.37$

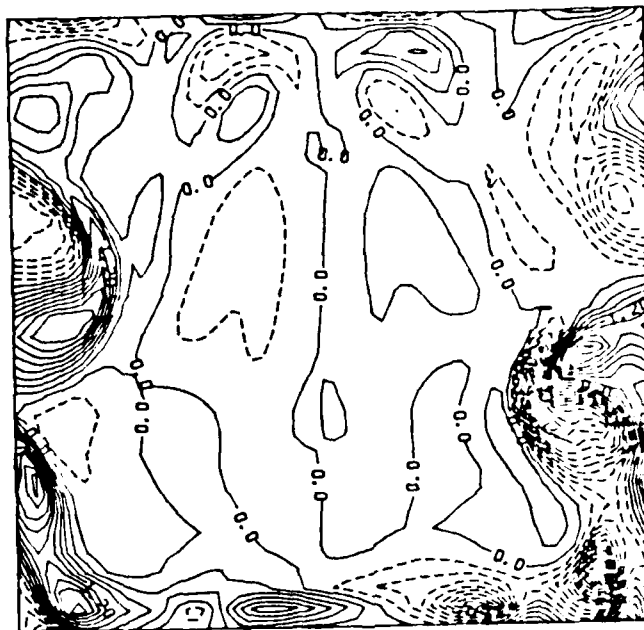


c.  $t = 23.91$

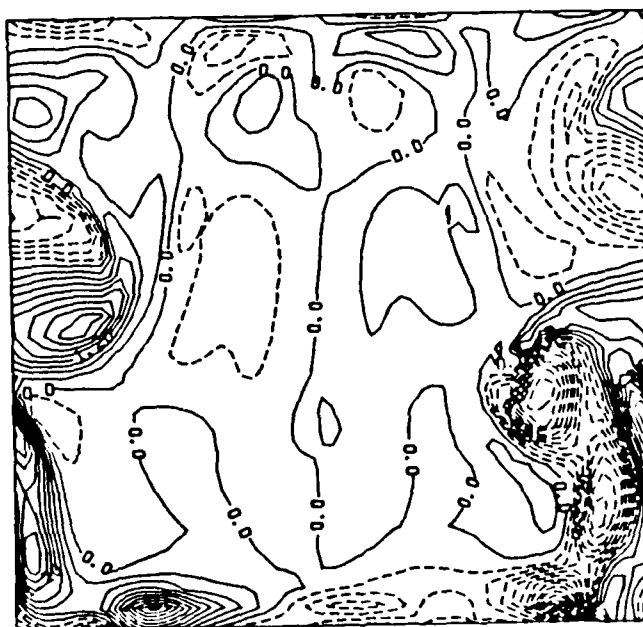
Figure 59. Time sequence of the  $y$ -vorticity contours in the  $x$ - $z$  plane at  $y = 0$  for azimuthal forcing at  $St = 0.47$  (contour interval = 0.7).



a.  $t = 21.80$

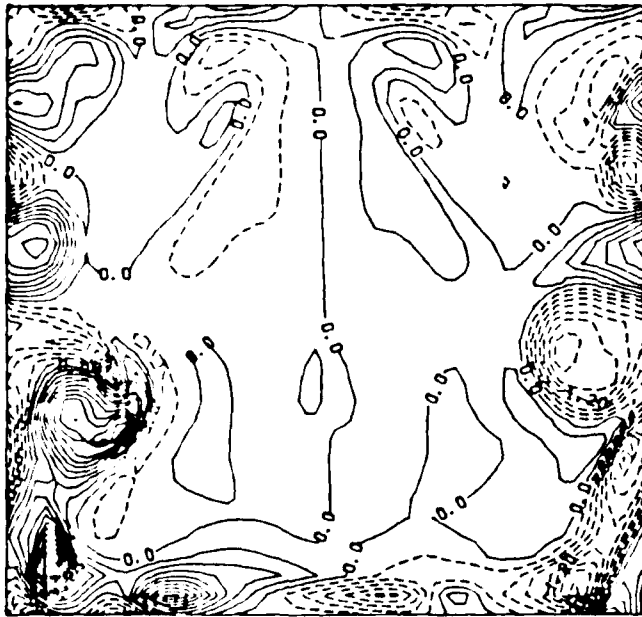


b.  $t = 22.85$

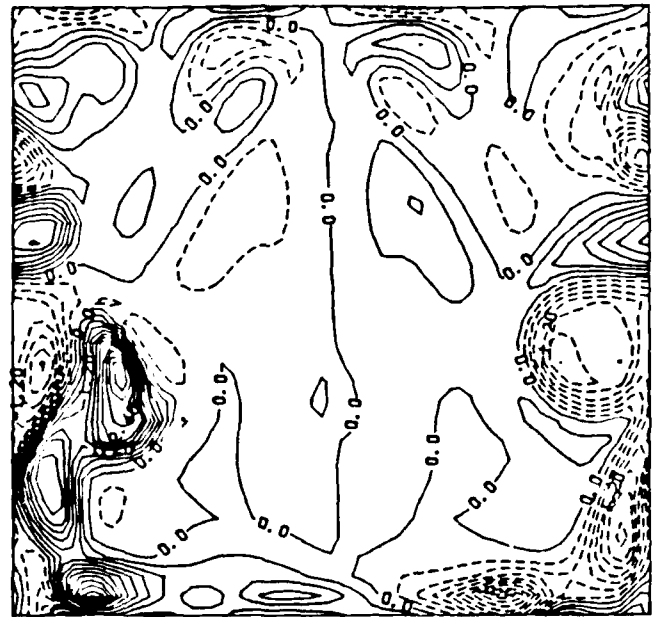


c.  $t = 23.91$

Figure 60. Time sequence of the y-vorticity contours in the x-z plane at  $y = -1.5D$  for azimuthal forcing at  $St = 0.47$  (contour interval = 0.3).



a.  $t = 21.80$

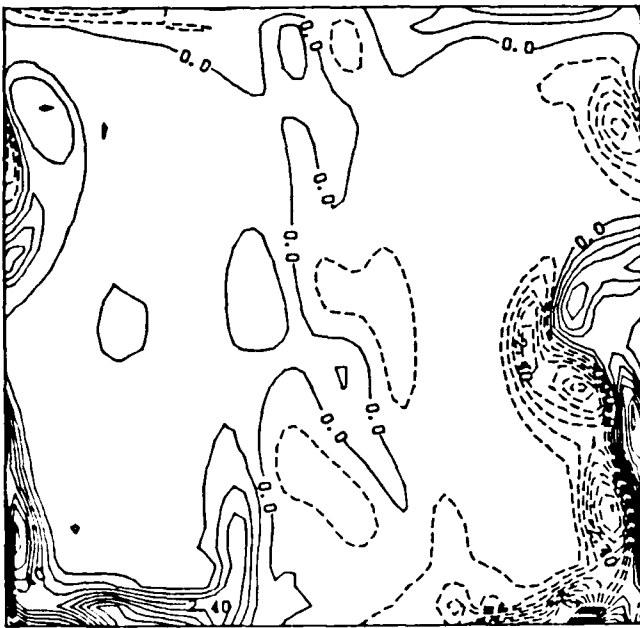


b.  $t = 22.85$

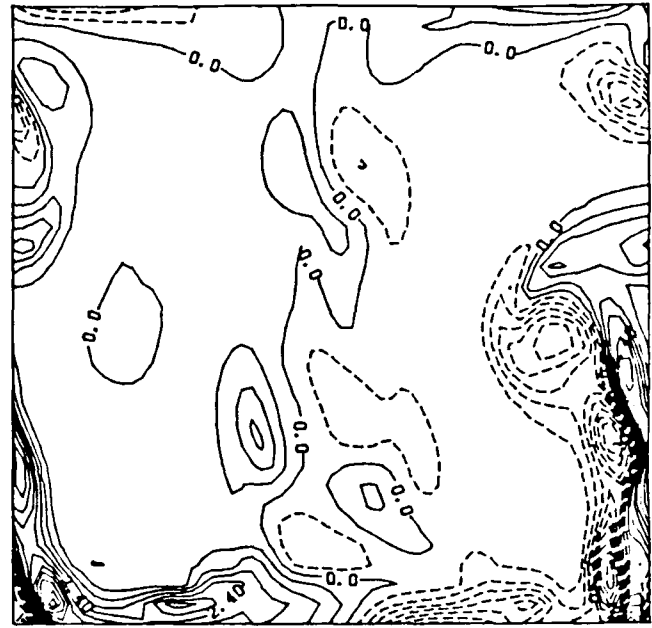


c.  $t = 23.91$

Figure 61. Time sequence of the  $y$ -vorticity contours in the  $x$ - $z$  plane at  $y = 1.5D$  for azimuthal forcing at  $St = 0.47$  (contour interval = 0.3).



a.  $t = 21.80$



b.  $t = 22.85$



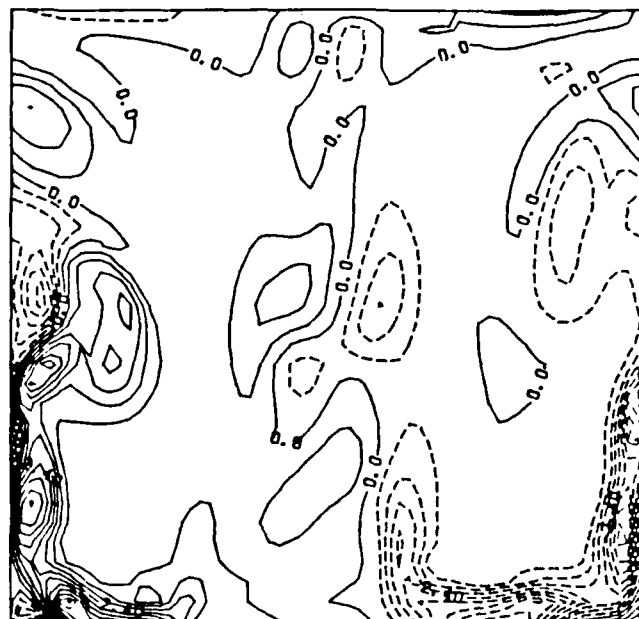
c.  $t = 23.91$

Figure 62. Time sequence of the  $y$ -vorticity contours in the  $x$ - $z$  plane at  $y = -0.51D$  for azimuthal forcing at  $St = 0.47$  (contour interval = 0.6).

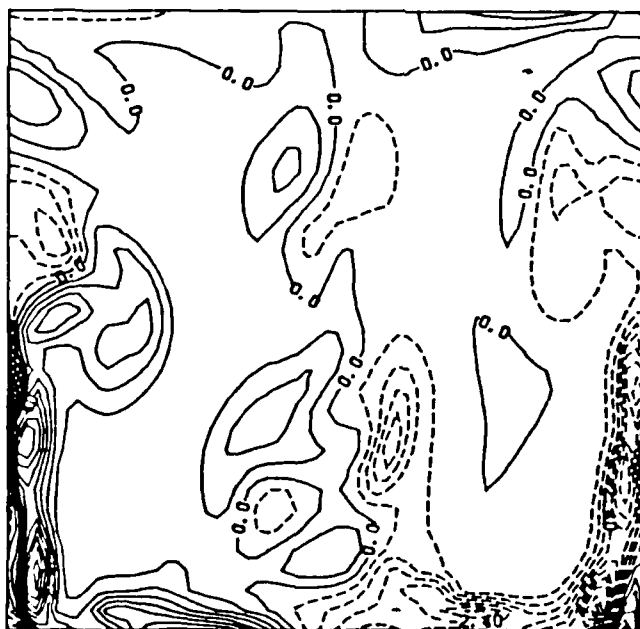




a.  $t = 21.80$



b.  $t = 22.85$



c.  $t = 23.91$

Figure 63. Time sequence of the  $y$ -vorticity contours in the  $x$ - $z$  plane at  $y = 0.5D$  for azimuthal forcing at  $St = 0.47$  (contour interval = 0.6).

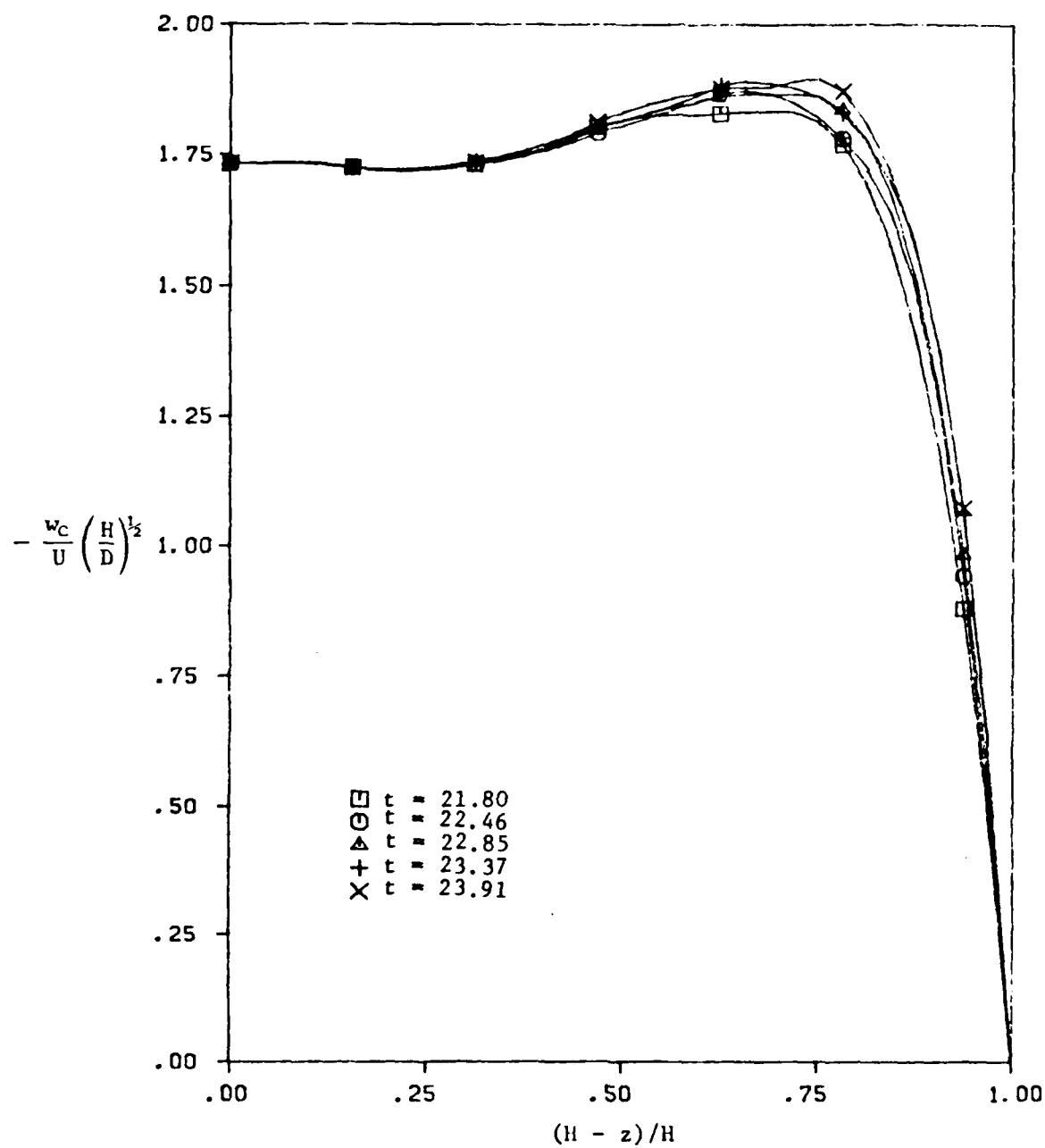
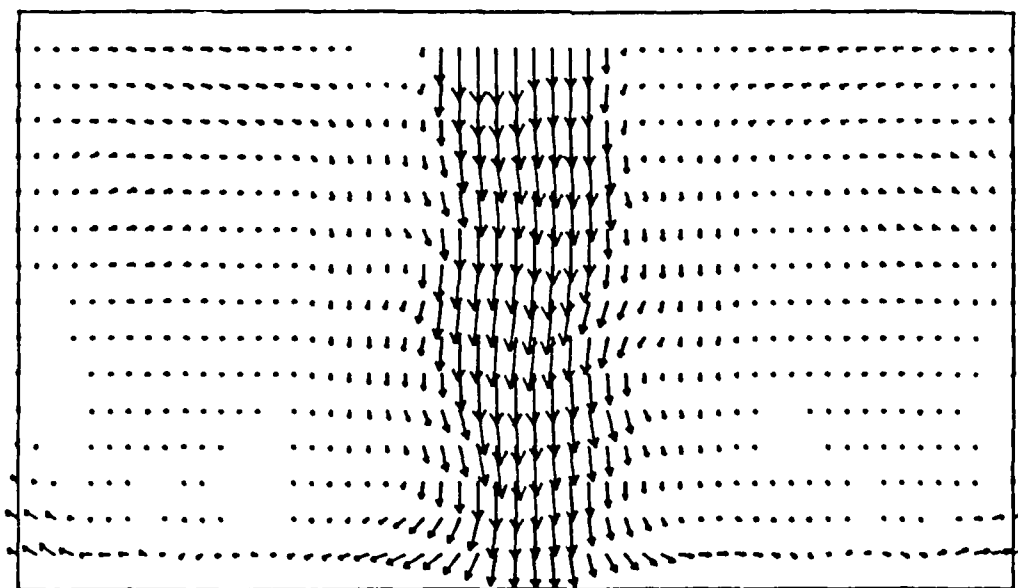
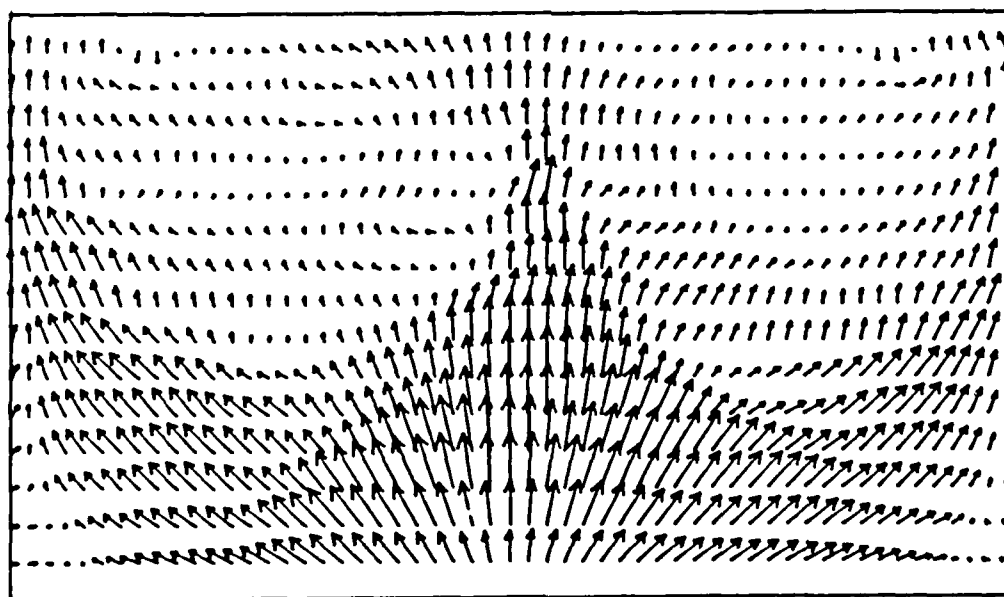


Figure 64. Variation of the centerline velocity as a function of  $z$  for an azimuthally forced cycle at  $St = 0.47$  for  $H = 3D$ .

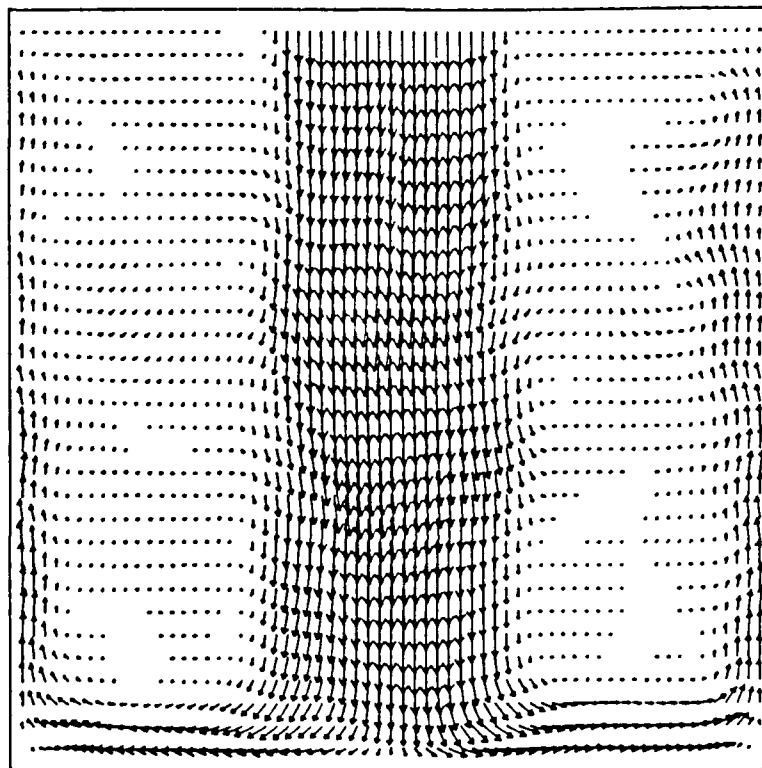


a.  $x = 0$  plane

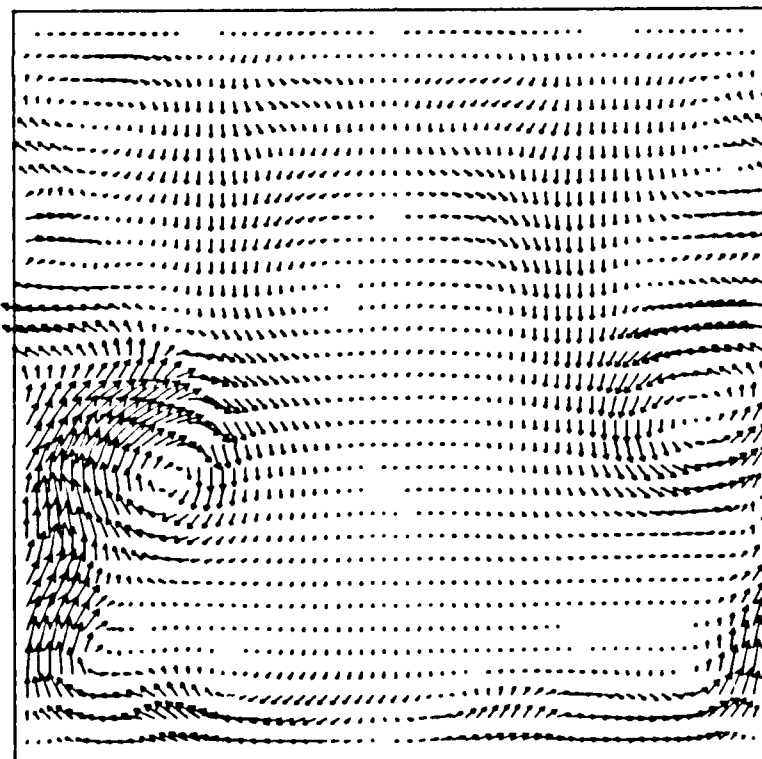


b.  $x = 1.5D$  plane

Figure 65. Velocity vector field in the  $y$ - $z$  plane at  $t = 23.91$  for azimuthal forcing at  $St = 0.47$ .

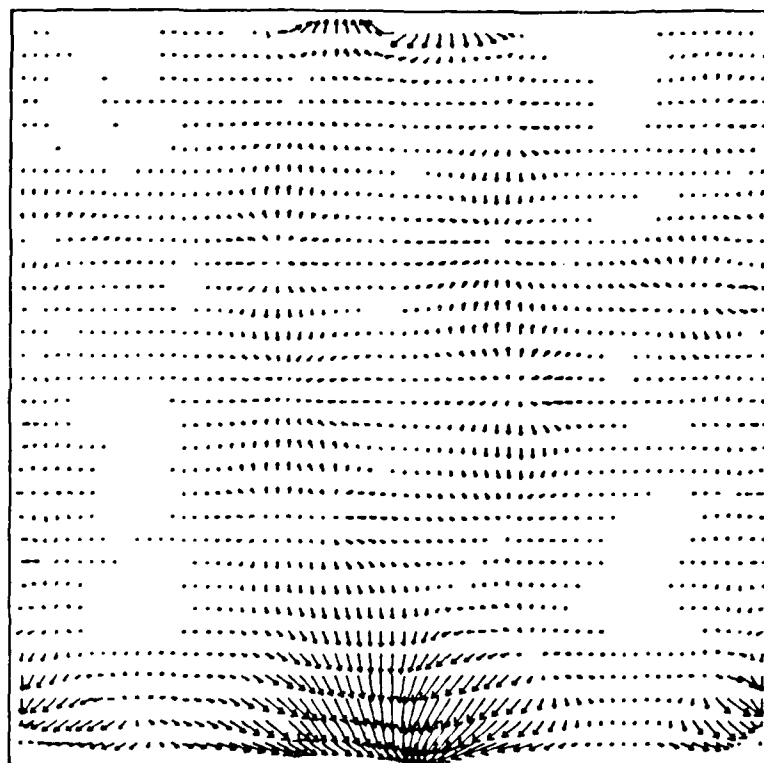


a.  $y = 0$  plane

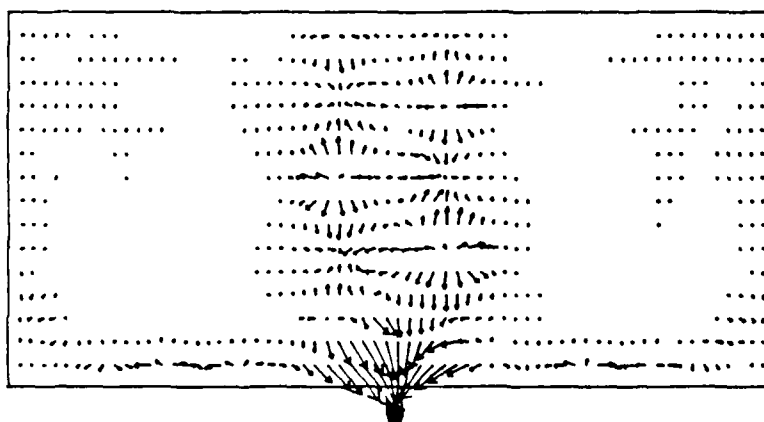


b.  $y = 1.5D$  plane

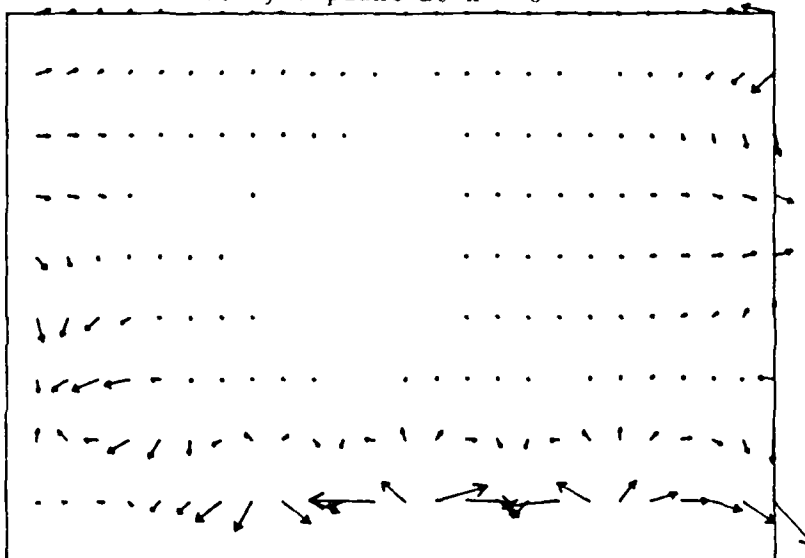
Figure 66. Velocity vector field in the x-z plane at  $t = 23.91$  for azimuthal forcing at  $St = 0.47$ .



a.  $x$ - $z$  plane at  $y = 0$

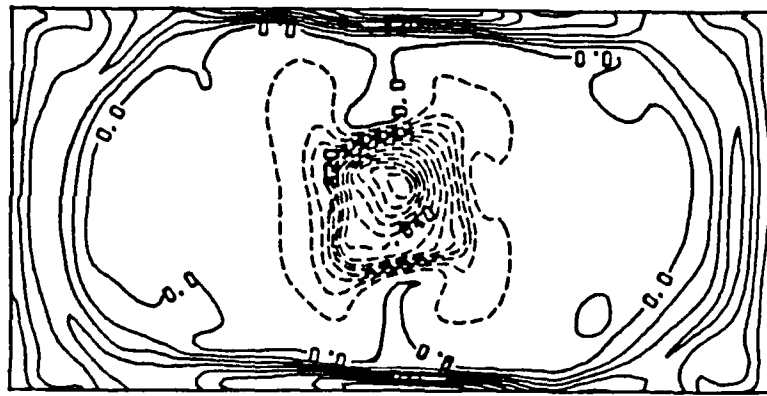


b.  $y$ - $z$  plane at  $x = 0$

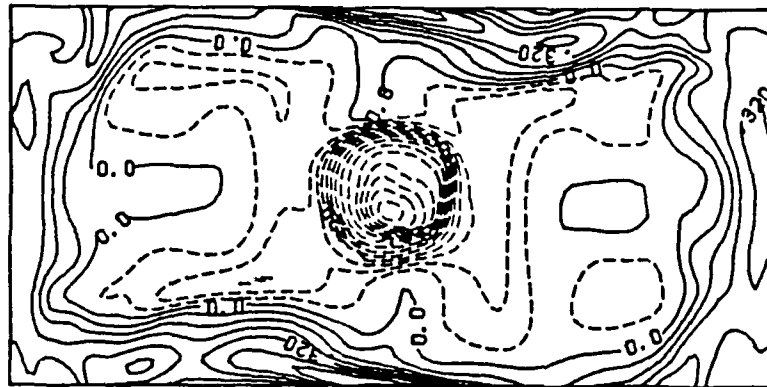


c. wall region in the  $y$ - $z$  plane at  $x = 0$

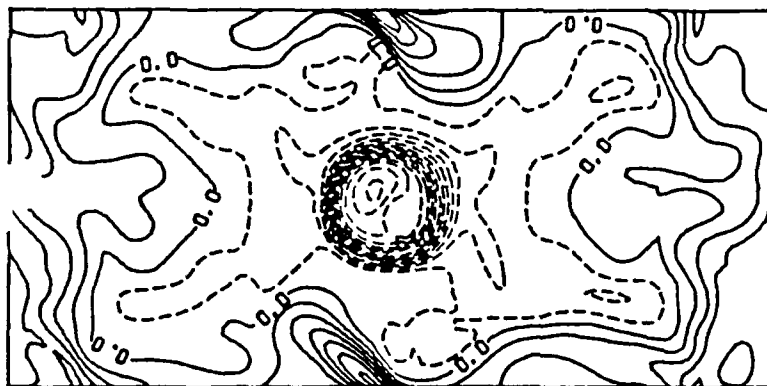
Figure 67. Pressure gradient vector field in the centerline planes at  $t = 32.91$  for azimuthal forcing at  $St = 0.47$ .



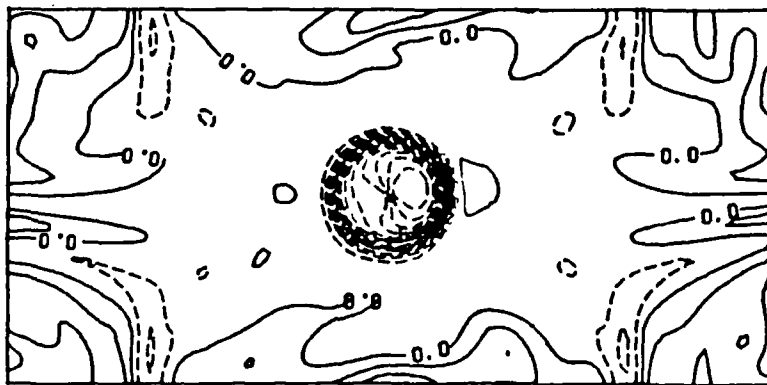
d.  $z = 0.75D$  plane



c.  $z = 1.5D$  plane

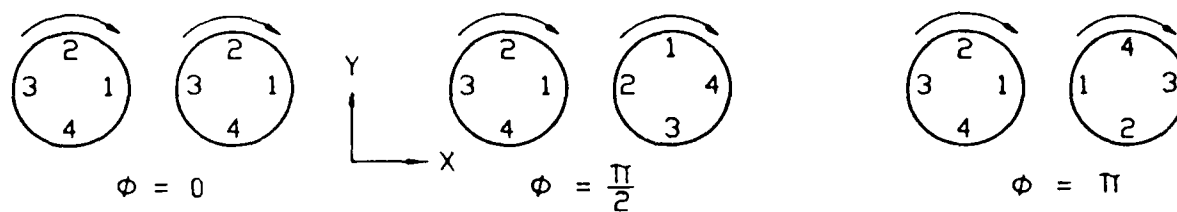


b.  $z = 2.25$  plane

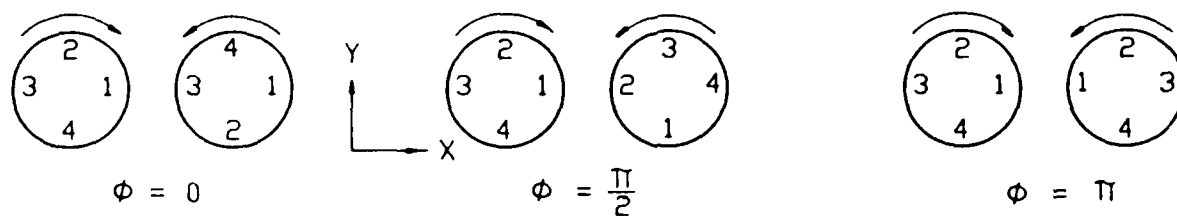


a.  $z = 2.98$  plane

Figure 68. Velocity contours in the x-y plane at  $t = 23.91$  for azimuthal forcing at  $St = 0.47$ .



CLOCK WISE - CLOCK WISE DISTURBANCE



CLOCK WISE - COUNTER CLOCK WISE DISTURBANCE

Figure 69. Azimuthal disturbance at jet exits for the double-jet configuration.

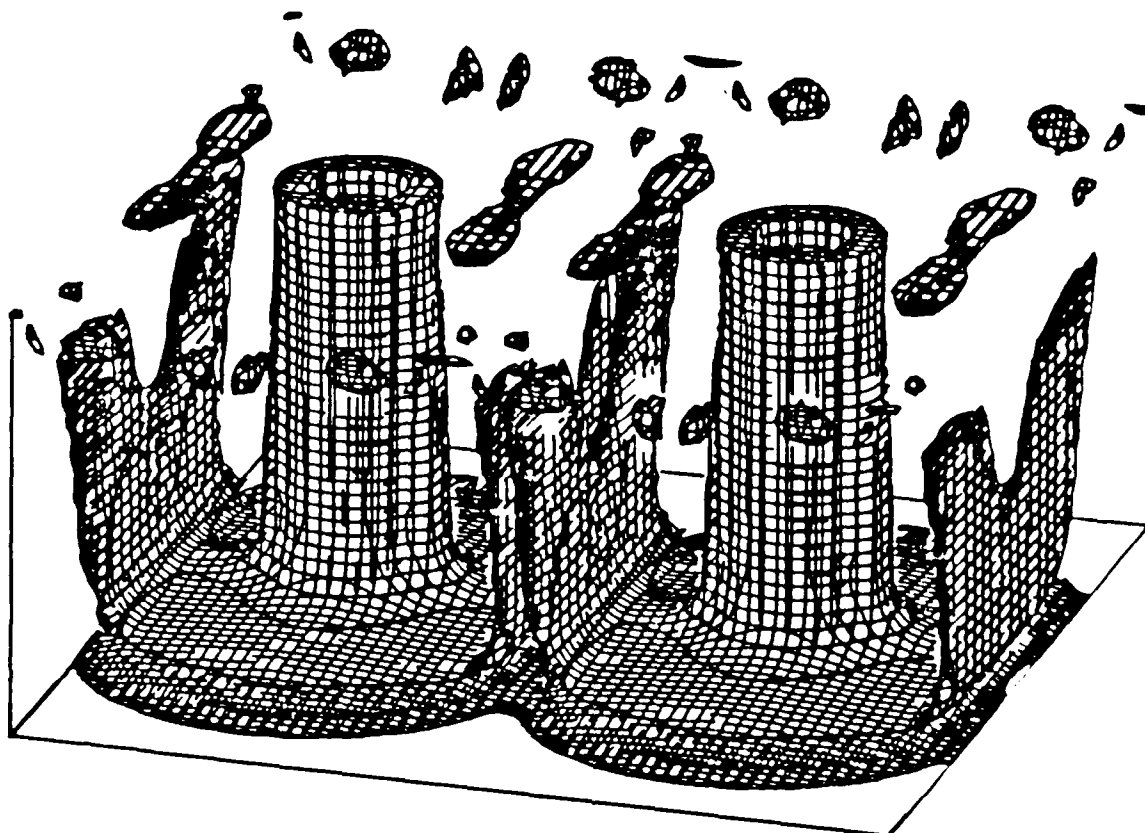
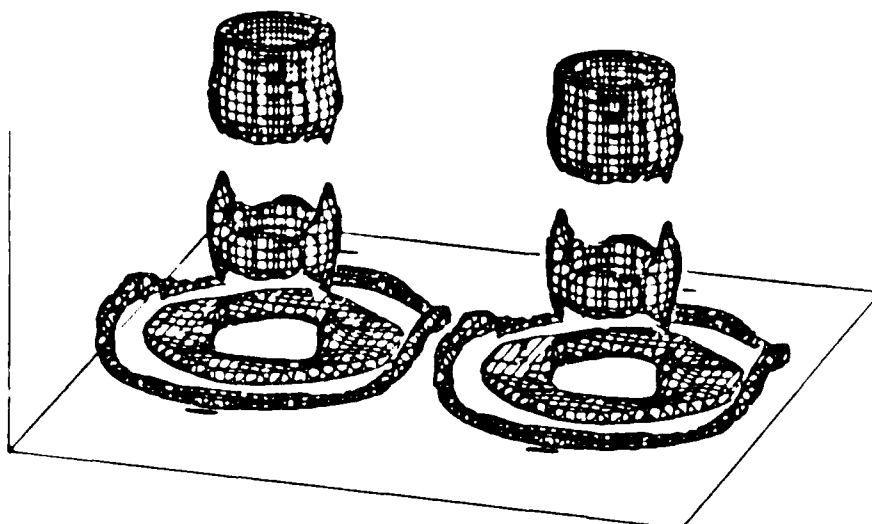
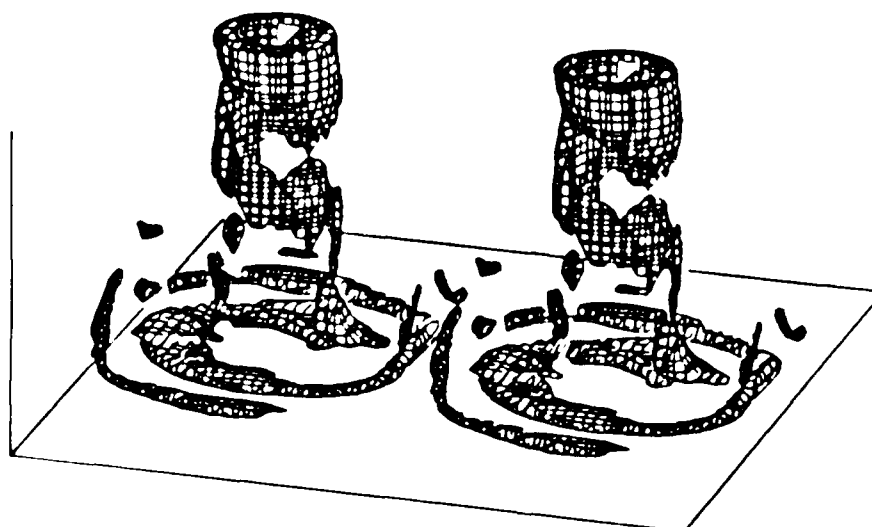


Figure 70. Three-dimensional perspective of the absolute vorticity surface at a level  $|\omega| = 2.1$  for the unperturbed double-jet computation.

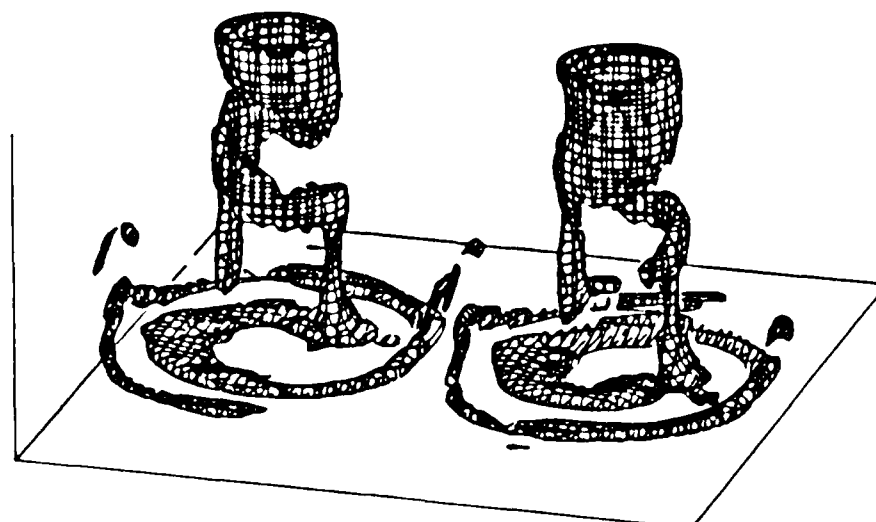




a. axisymmetric forcing

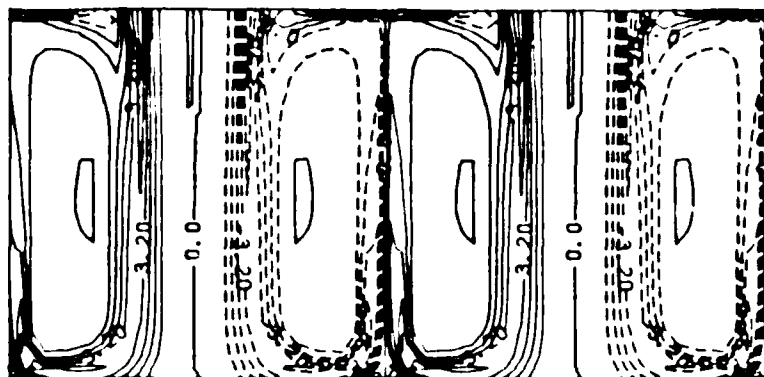


b. CW-CW forcing,  $\phi = 0$

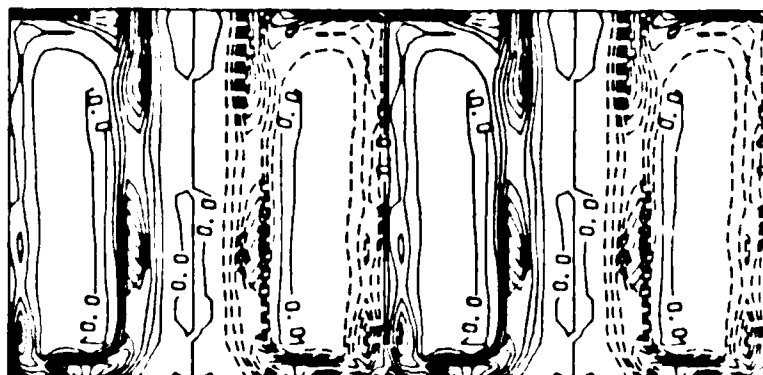


c. CW-CCW forcing,  $\phi = 0$

Figure 71. Three-dimensional perspective of the vorticity surface  $\omega_0 = -3.1$  for forced double-jet computations.



a. unperturbed



b. axisymmetric



c. CW-CW,  $\phi = 0$



d. CW-CCW,  $\phi = 0$

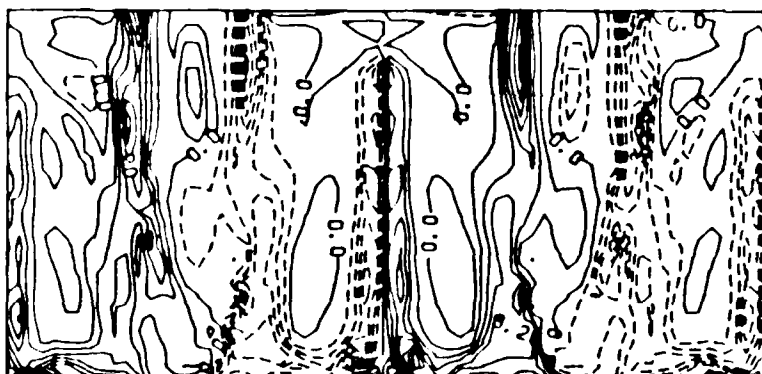
Figure 72. y-vorticity contours in the  $y = 0$  plane for forced double-jet computations (contour interval = 0.8).



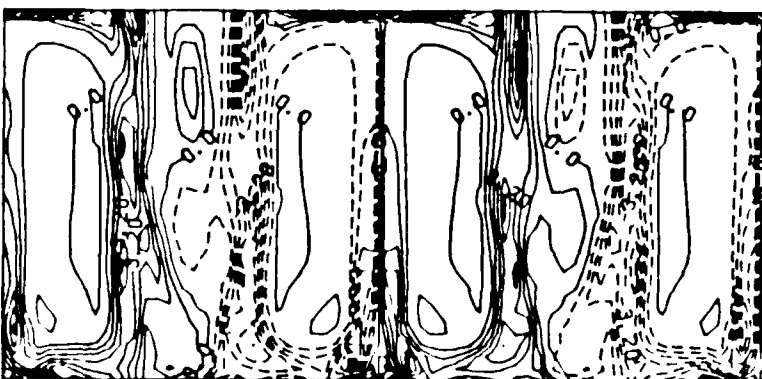
e. CW-CW,  $\phi = \pi/2$



f. CW-CCW,  $\phi = \pi/2$

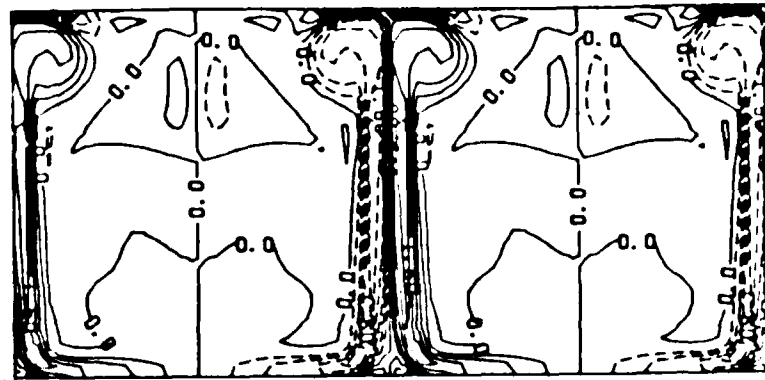


g. CW-CW,  $\phi = \pi$

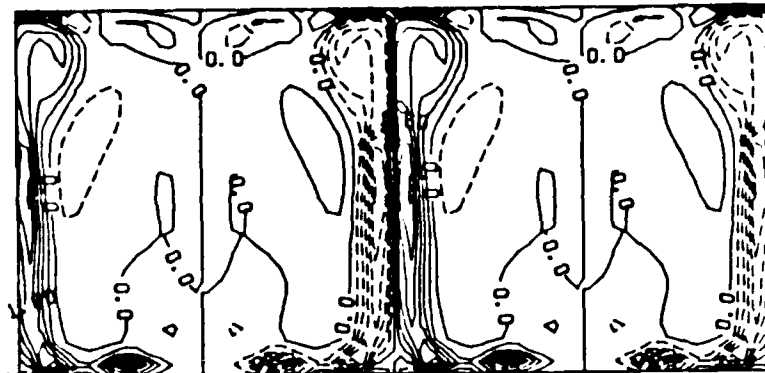


h. CW-CCW,  $\phi = \pi$

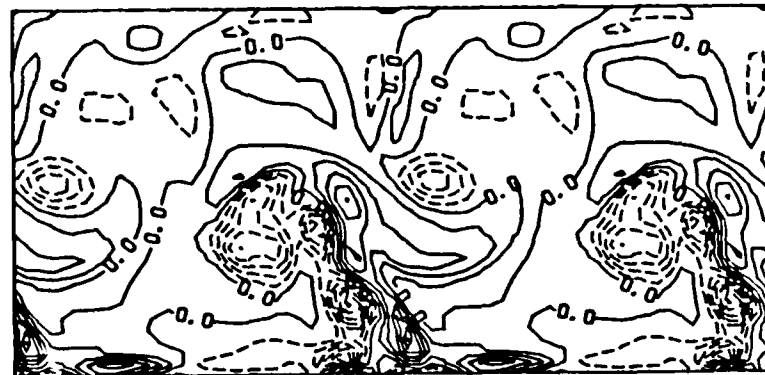
Figure 72.  $y$ -vorticity contours in the  $y = 0$  plane for forced double-jet computations (contour interval = 0.8). (Cont.)



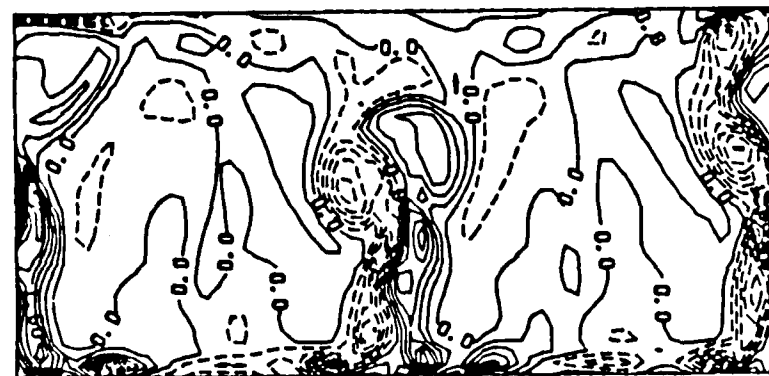
a. unperturbed



b. axisymmetric

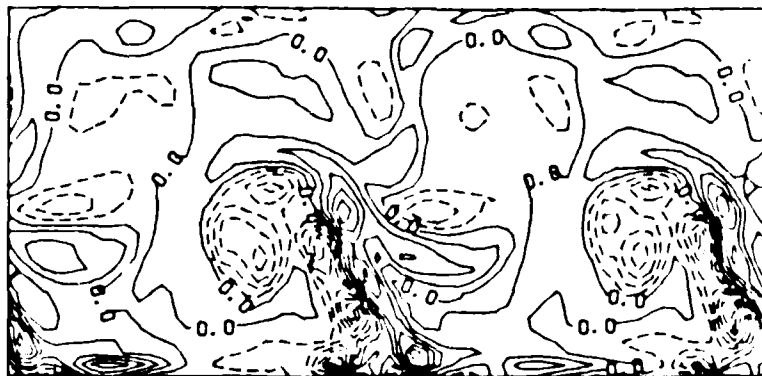


c. CW-CW,  $\phi = 0$

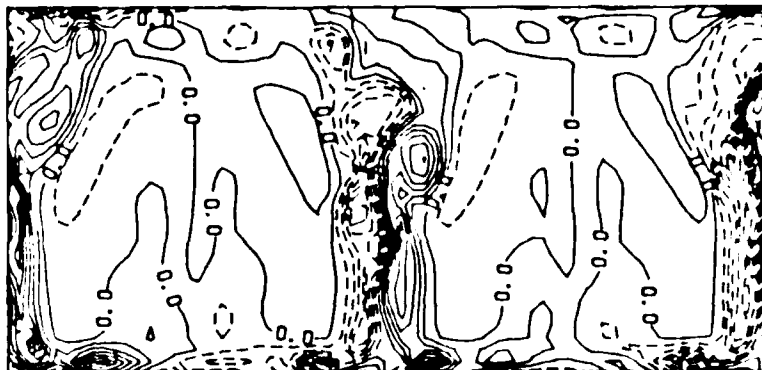


d. CW-CCW,  $\phi = 0$

Figure 73.  $y$ -vorticity contours in the  $y = -1.5D$  plane for forced double-jet computations (contour interval = 0.4).



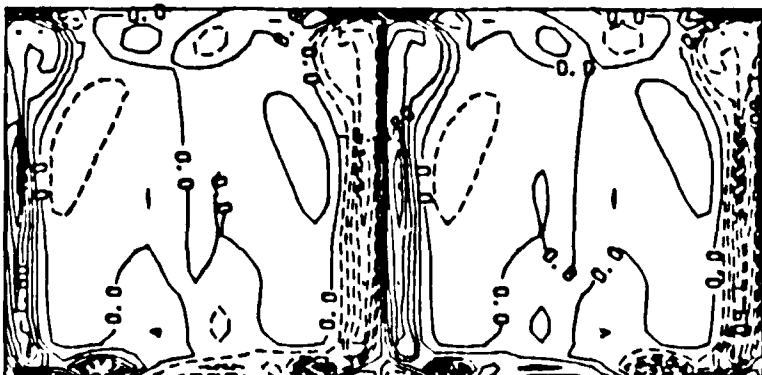
e. CW-CW,  $\phi = \pi/2$



f. CW-CCW,  $\phi = \pi/2$

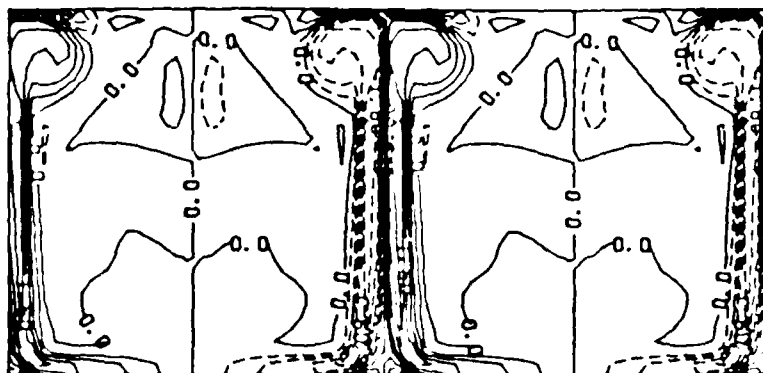


g. CW-CW,  $\phi = \pi$

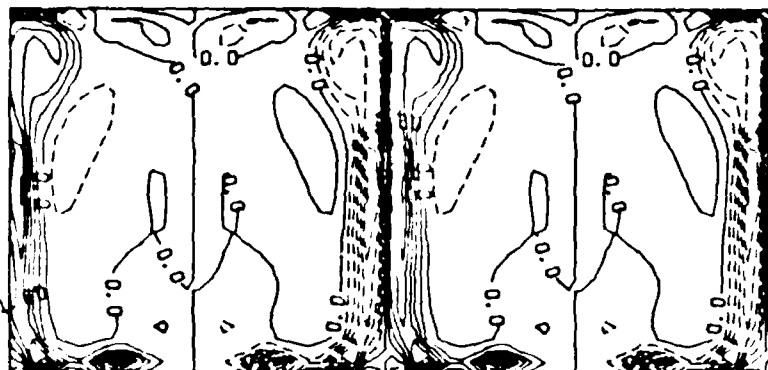


h. CW-CCW,  $\phi = \pi$

Figure 73.  $y$ -vorticity contours in the  $y = -1.5D$  plane for forced double-jet computations (contour interval = 0.4). (Cont.)



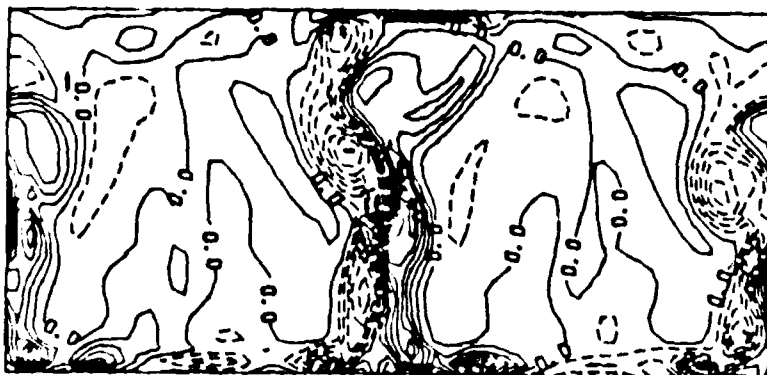
a. unperturbed



b. axisymmetric

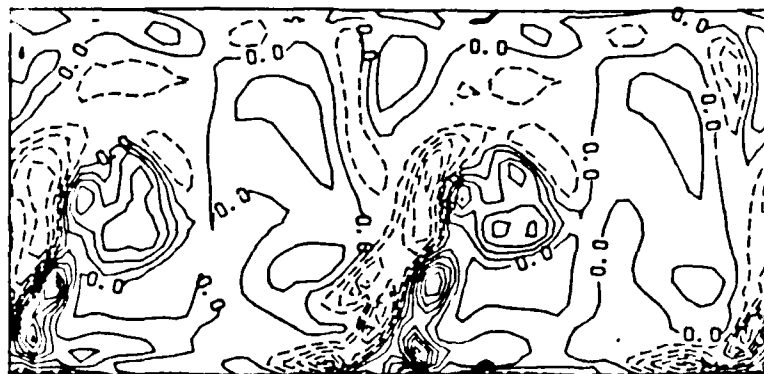


c. CW-CW,  $\phi = 0$

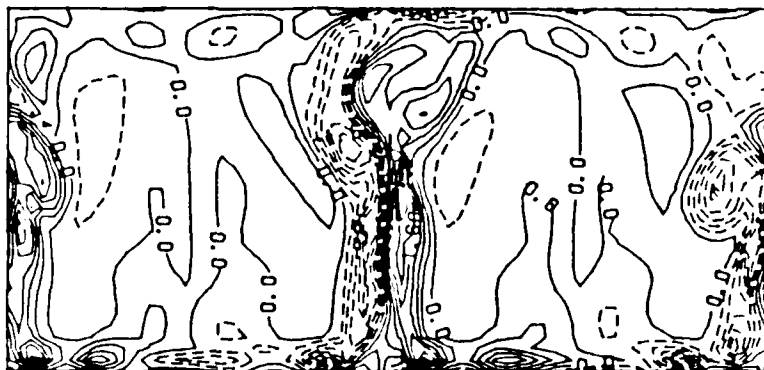


d. CW-CCW,  $\phi = 0$

Figure 74.  $y$ -vorticity contours in the  $y = 1.5D$  plane for forced double-jet computations (contour interval = 0.4).



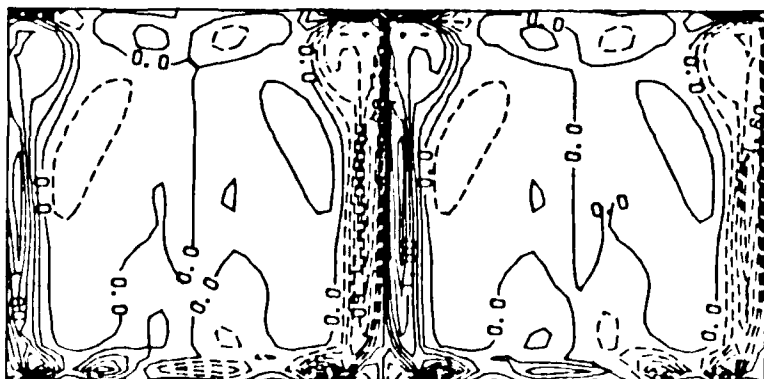
e. CW-CW,  $\phi = \pi/2$



f. CW-CCW,  $\phi = \pi/2$



g. CW-CW,  $\phi = \pi$



h. CW-CCW,  $\phi = \pi$

Figure 74.  $y$ -vorticity contours in the  $y = 1.5D$  plane for forced double-jet computations (contour interval = 0.4). (Cont.)



a.  $\beta = 0$



b.  $\beta = \pi/2$



c.  $\beta = \pi$



d.  $\beta = 3\pi/2$



e.  $\beta = 2\pi$

Figure 75. y-vorticity contours in the  $y = 0$  plane for a complete forcing cycle, CW-CW,  $\phi = 0$  (contour interval = 0.8).





a.  $\beta = 0$



b.  $\beta = \pi/2$



c.  $\beta = \pi$

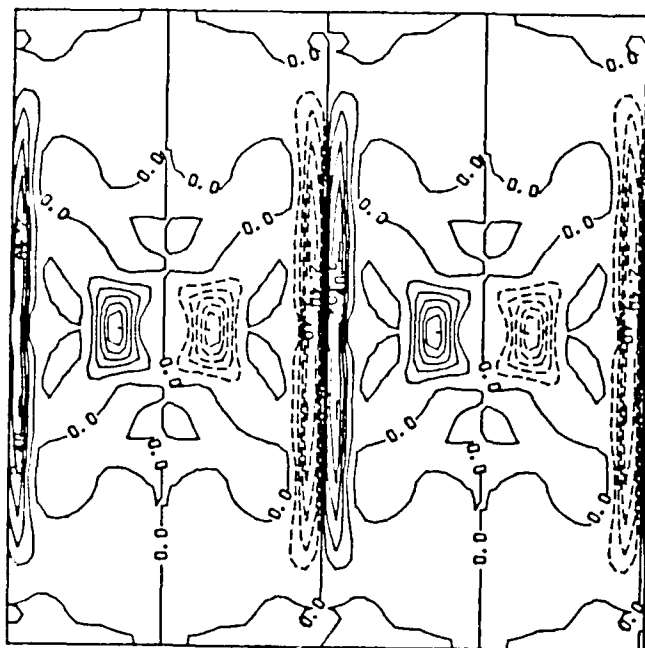


d.  $\beta = 3\pi/2$

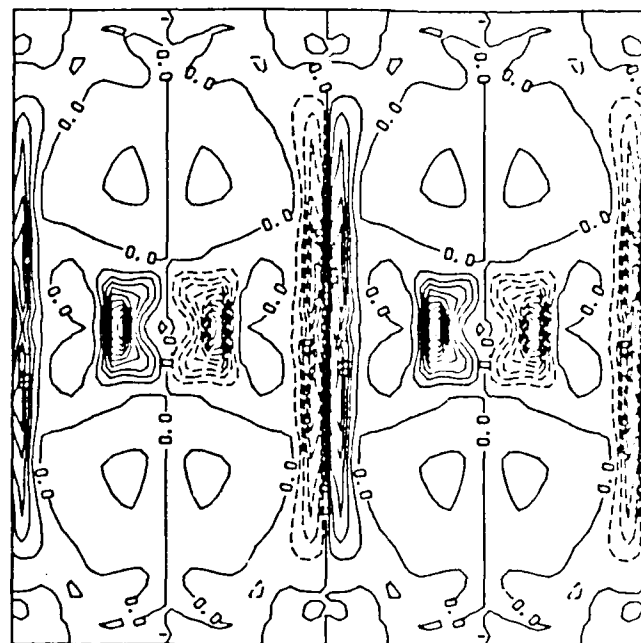


e.  $\beta = 2\pi$

Figure 76.  $y$ -vorticity contours in the  $y = -1.50$  plane for a complete forcing cycle, CW-CW,  $\phi = 0$  (contour interval = 0.4).



a. unperturbed



b. axisymmetric



c. CW-CW,  $\phi = 0$

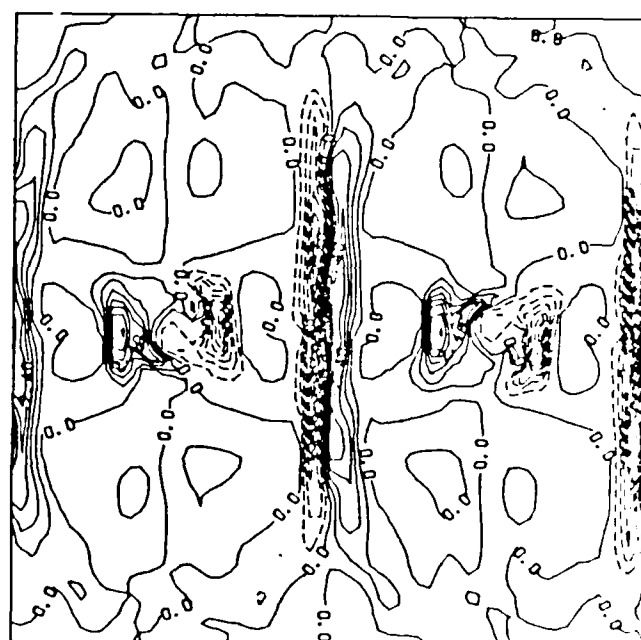
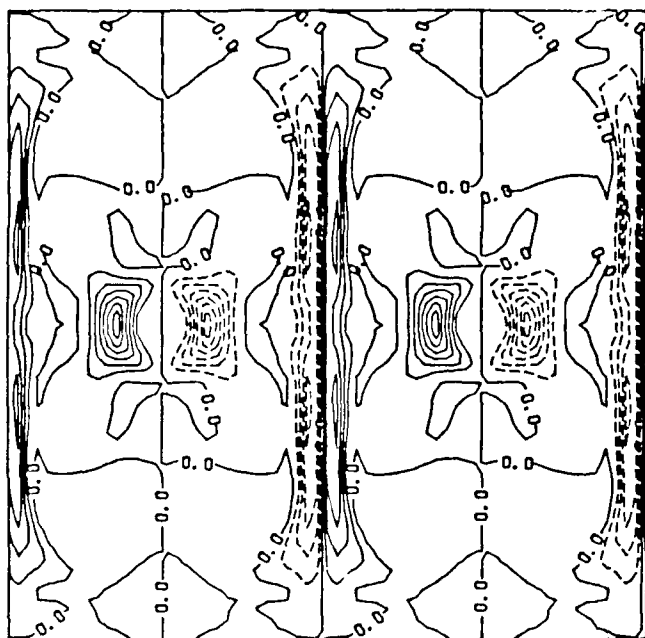
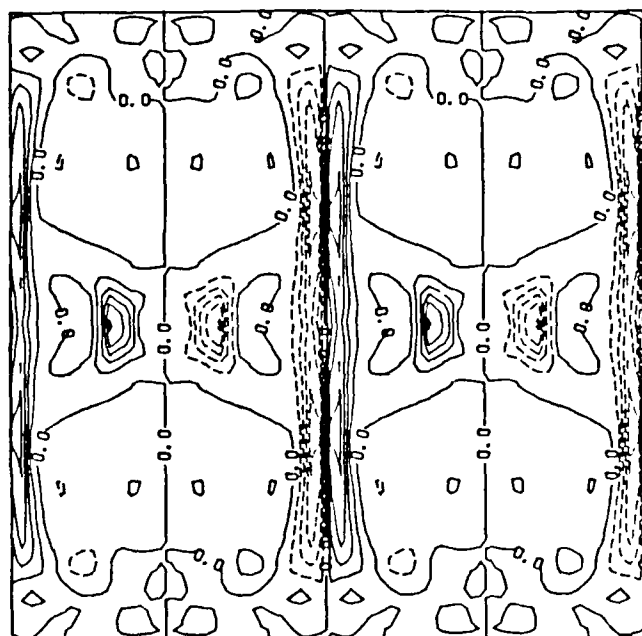


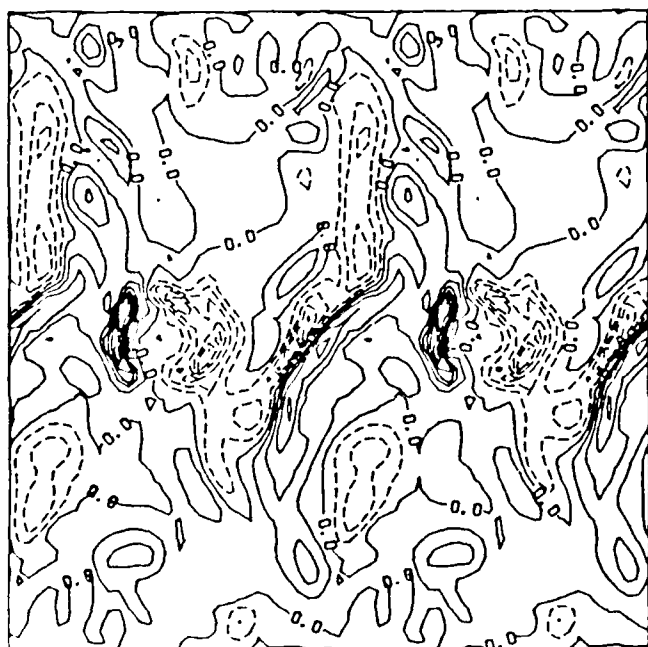
Figure 77. y-vorticity contours in the  $z = 1D$  plane for forced double-jet computations (contour interval = 0.6).



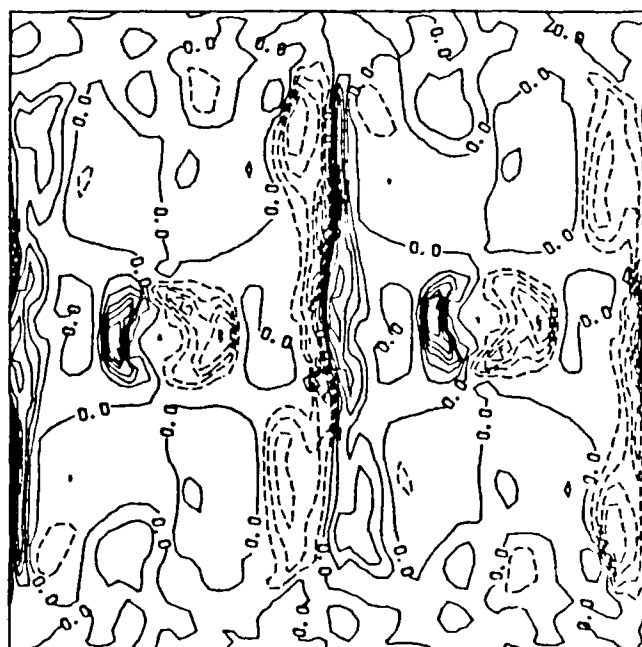
a. unperturbed



b. axisymmetric

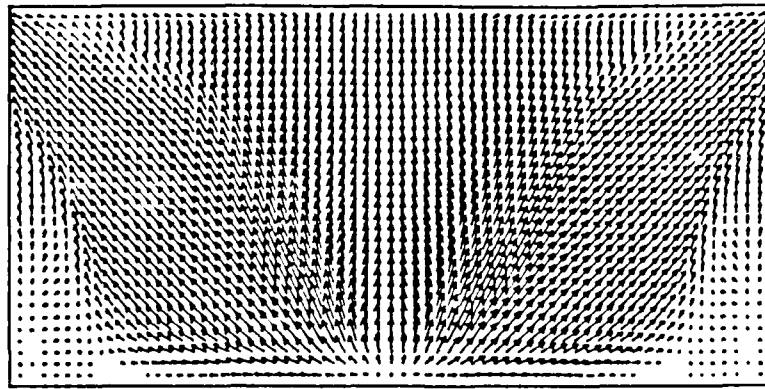


c. CW-CW,  $\phi = 0$

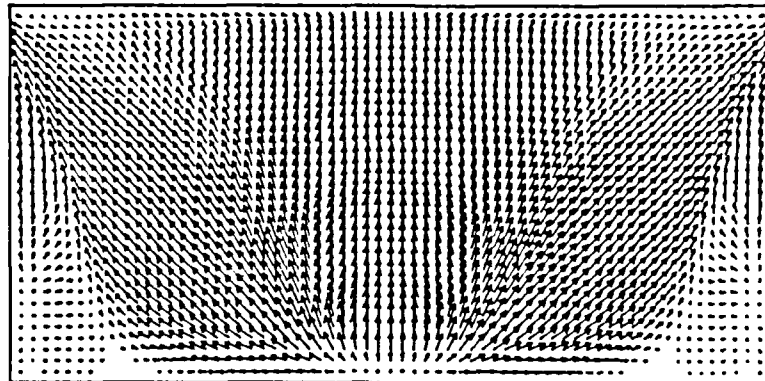


d. CW-CCW,  $\phi = 0$

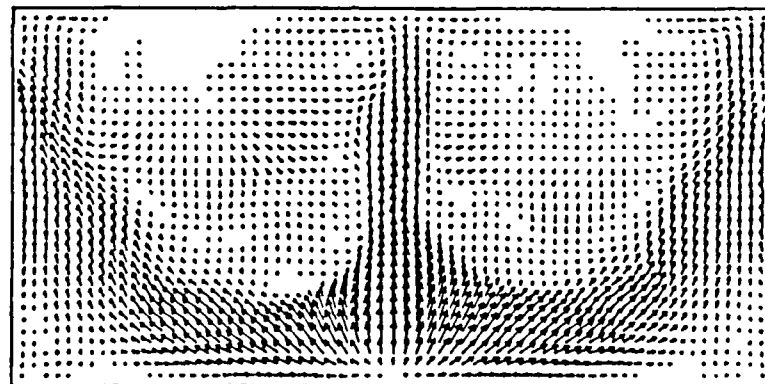
Figure 78.  $y$ -vorticity contours in the  $z = 1.5D$  plane for forced double-jet computations (contour interval = 0.6).



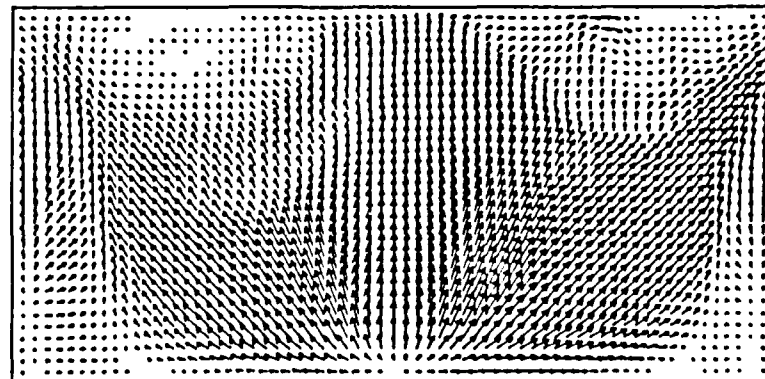
a. unperturbed



b. axisymmetric

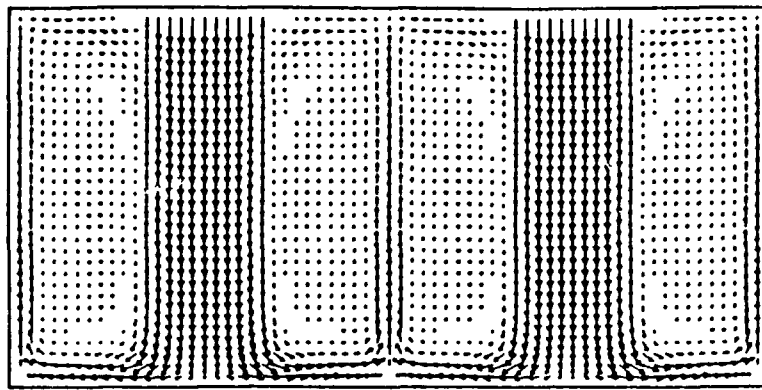


c. CW-CW,  $\phi = 0$

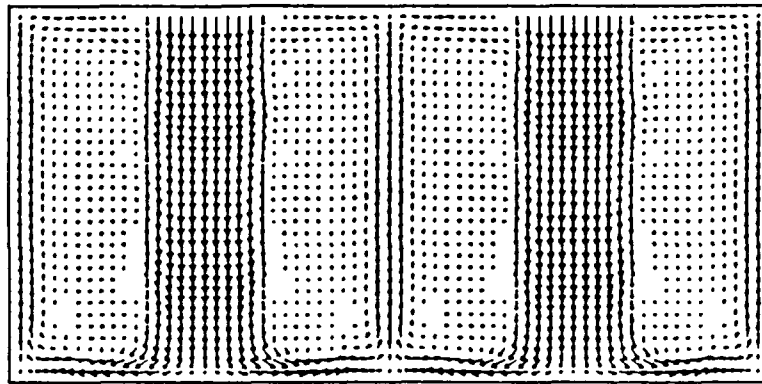


d. CW-CCW,  $\phi = 0$

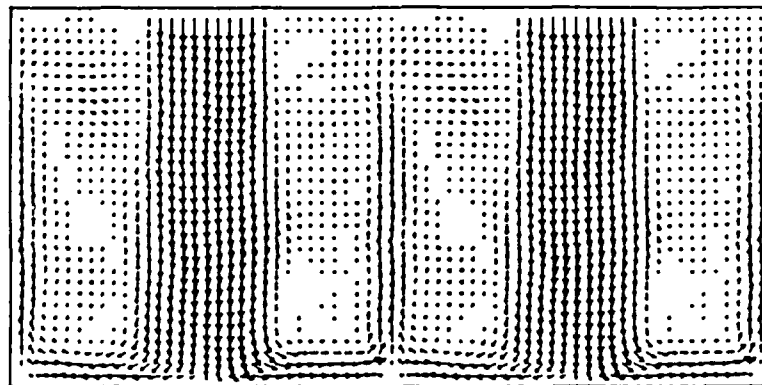
Figure 79. Velocity vector plots in the  $x = x_f$  plane for forced double-jet computations.



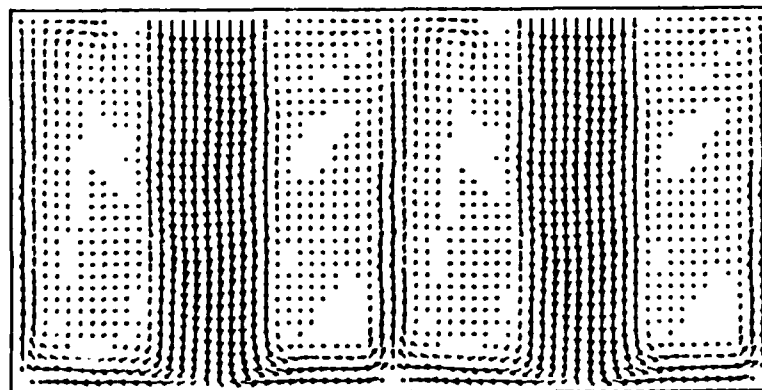
a. unperturbed



b. axisymmetric

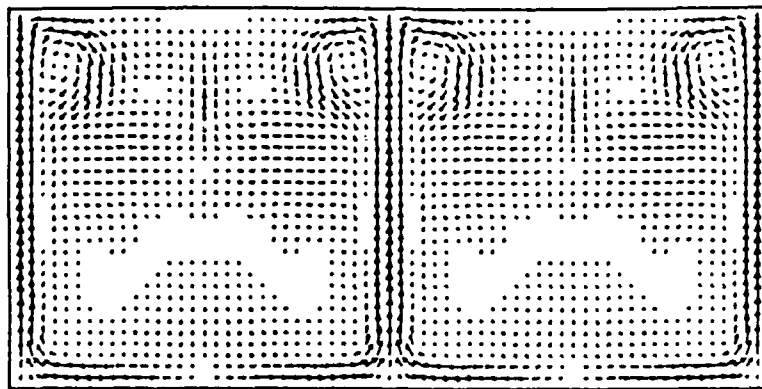


c. CW-CW,  $\phi = 0$

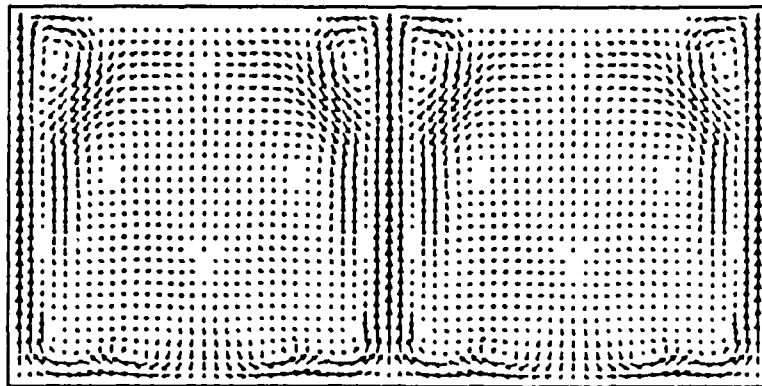


d. CW-CCW,  $\phi = 0$

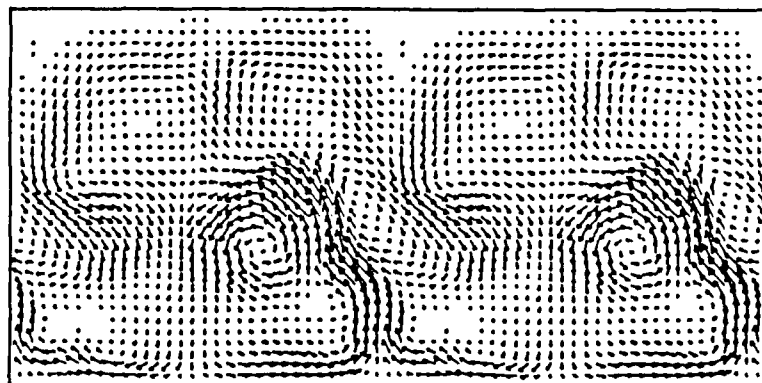
Figure 80. Velocity vector plots in the  $y = 0$  plane for forced double-jet computations.



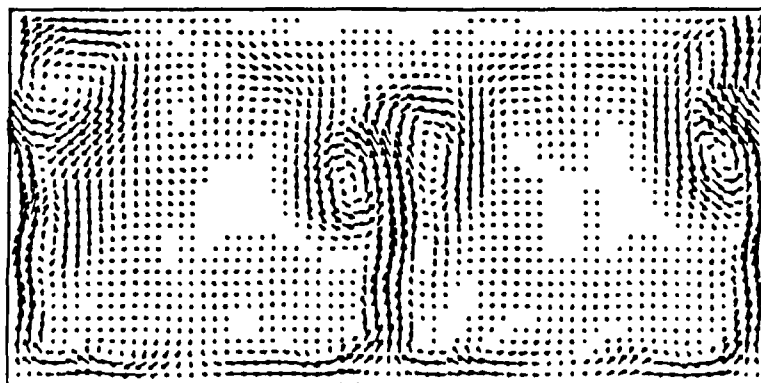
a. unperturbed



b. axisymmetric

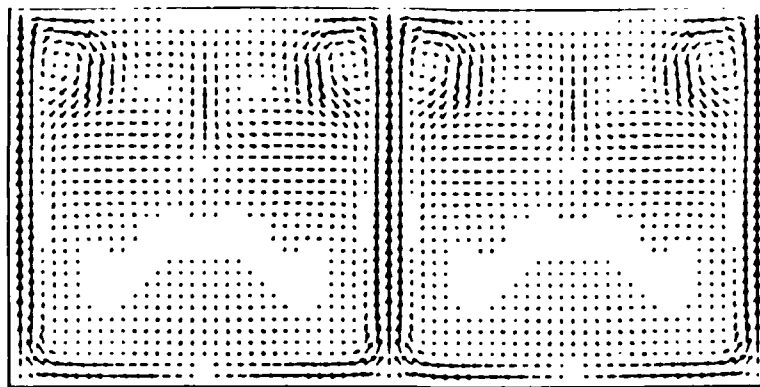


c. CW-CW,  $\phi = 0$

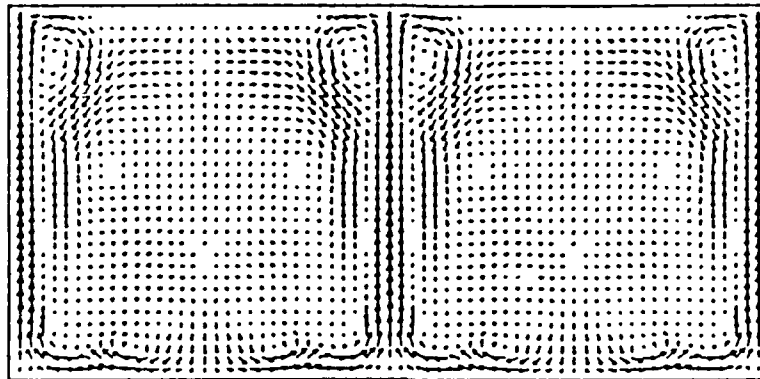


d. CW-CCW,  $\phi = 0$

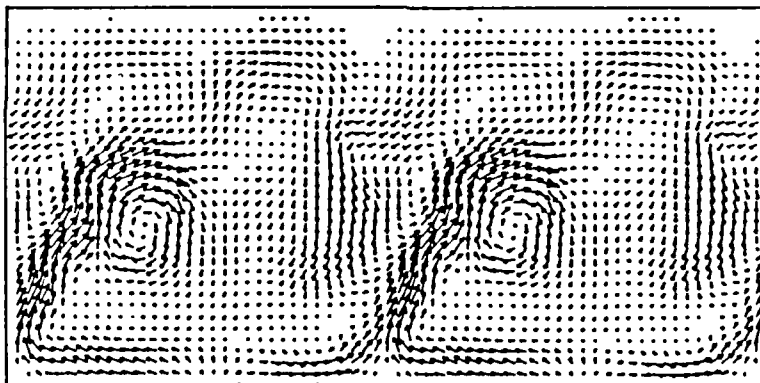
Figure 81. Velocity vector plots in the  $y = -1.5D$  plane for forced double-jet computations.



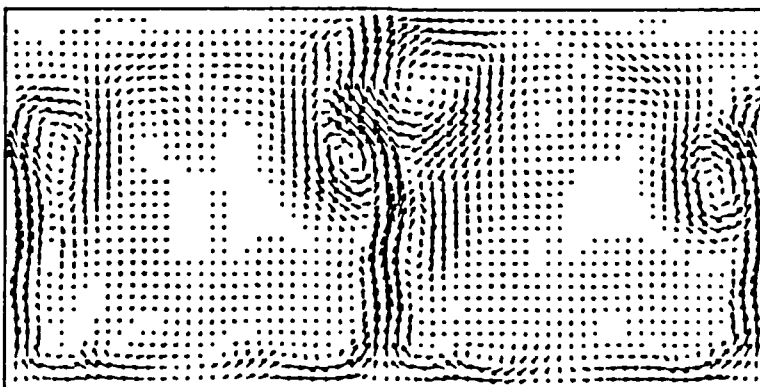
a. unperturbed



b. axisymmetric



c. CW-CW,  $\phi = 0$



d. CW-CCW,  $\phi = 0$

Figure 82. Velocity vector plots in the  $y = 1.5D$  plane for forced double-jet computations.

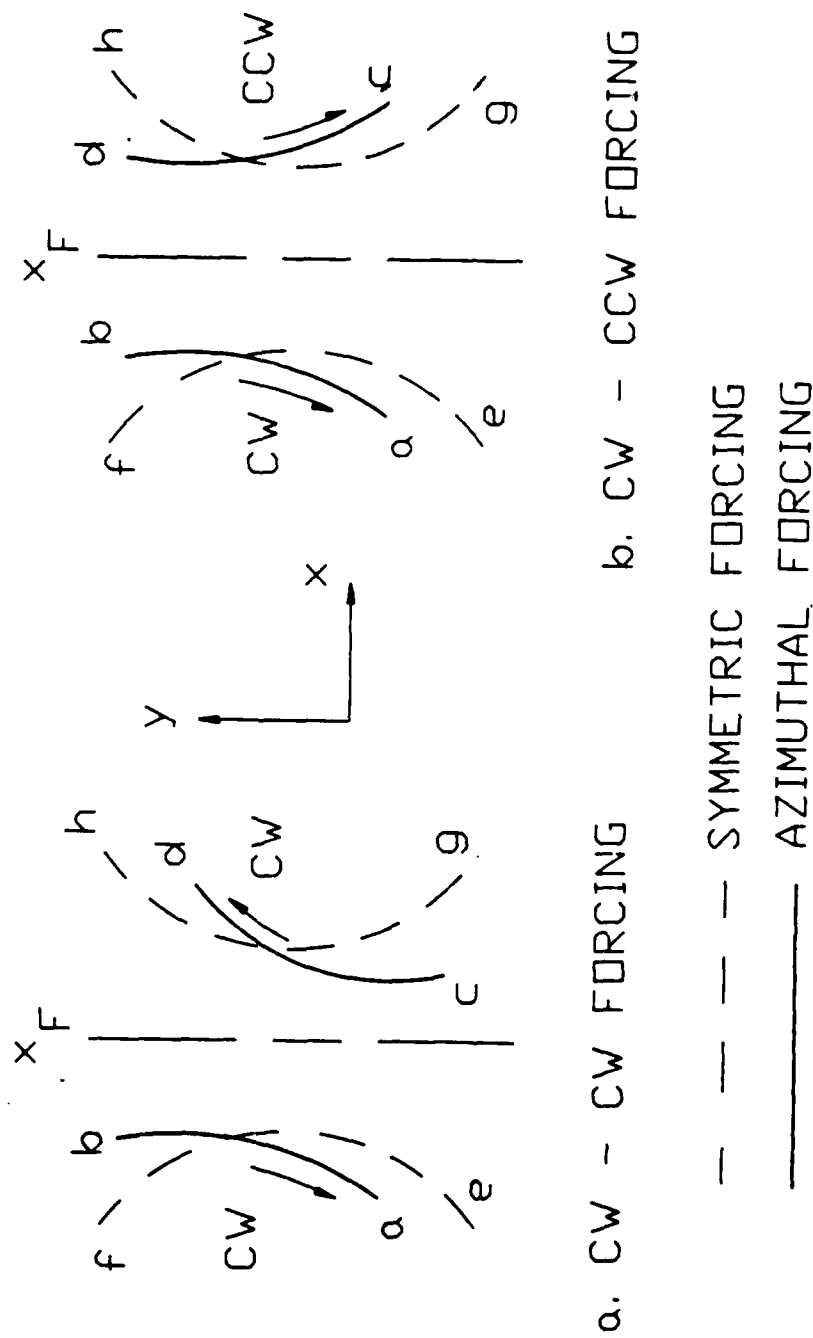
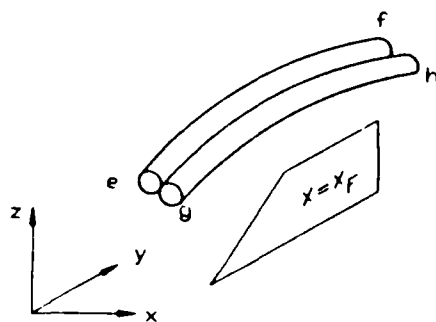
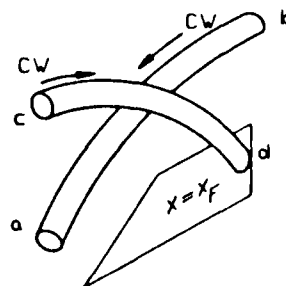


Figure 83. Relative positions of vortex tubes at fountain base.

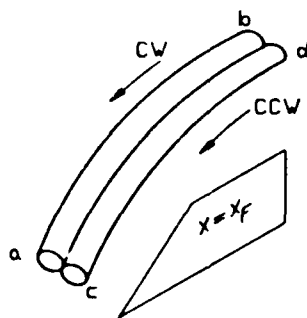




a. AXISYMMETRIC  
FORCING

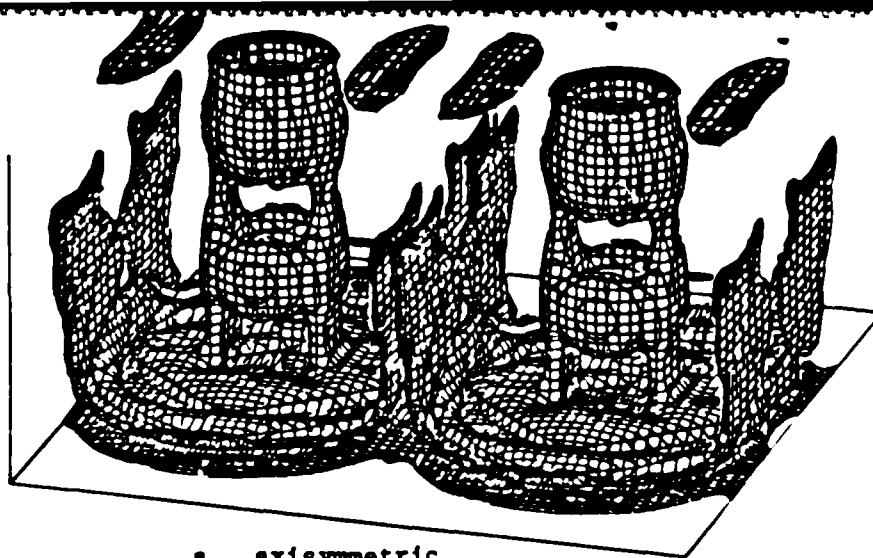


b. CW-CW  
FORCING

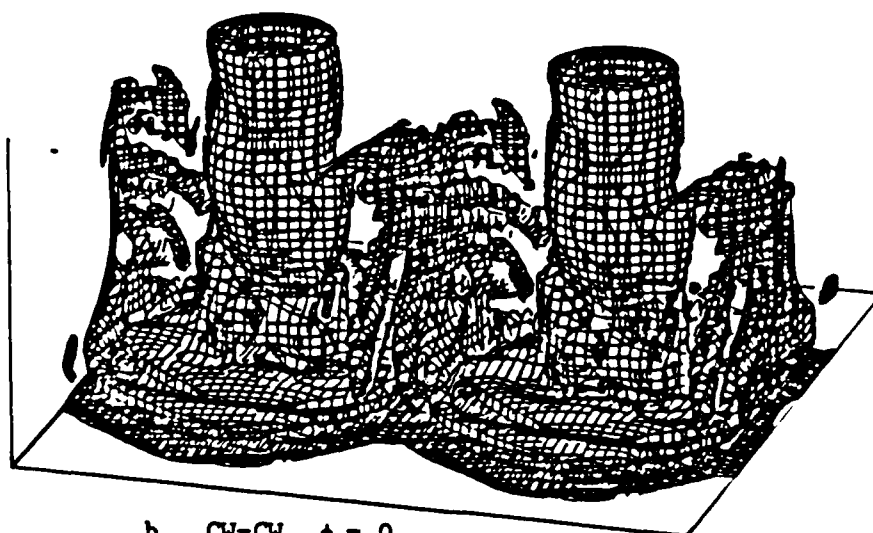


c. CW-CCW  
FORCING

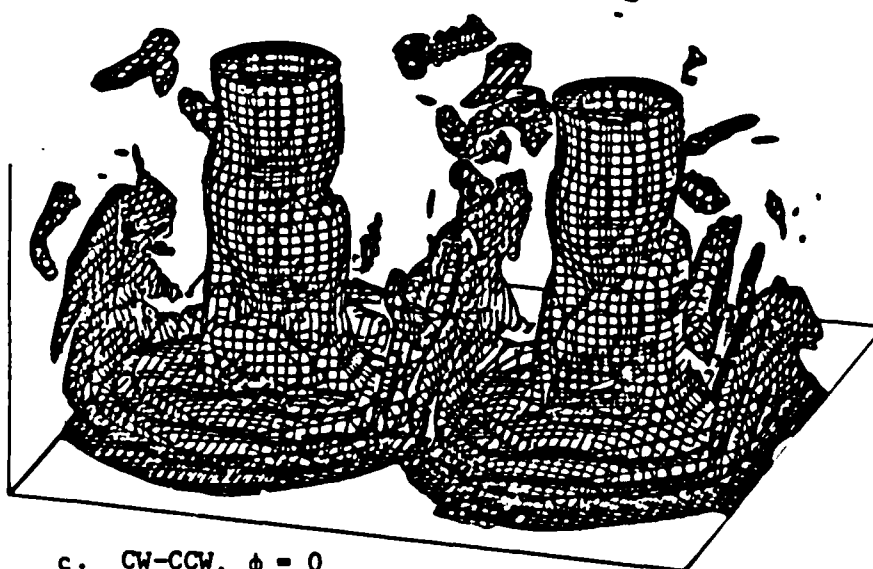
Figure 84. Relative positions of vortex tubes in fountain.



a. axisymmetric

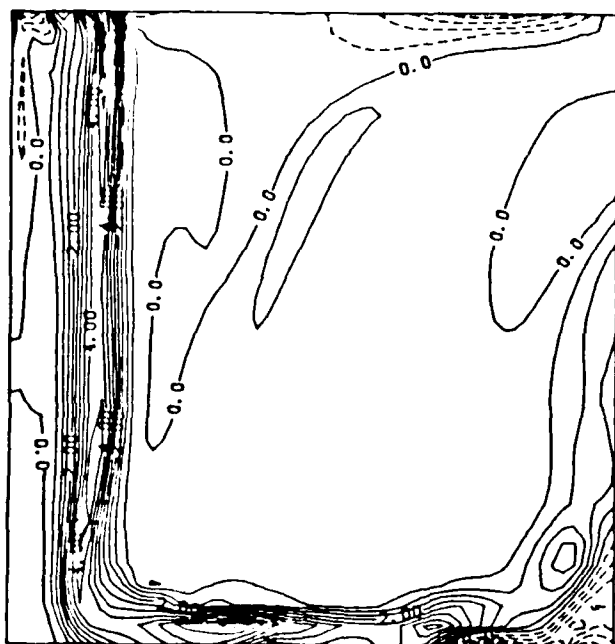


b. CW-CW,  $\phi = 0$

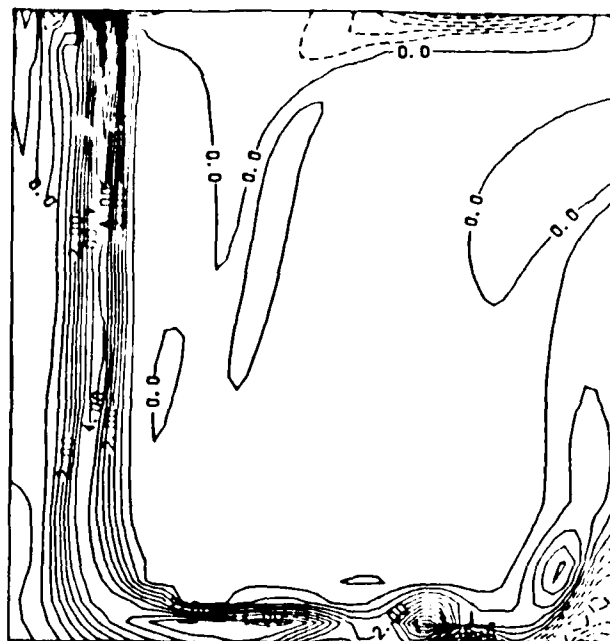


c. CW-CCW,  $\phi = 0$

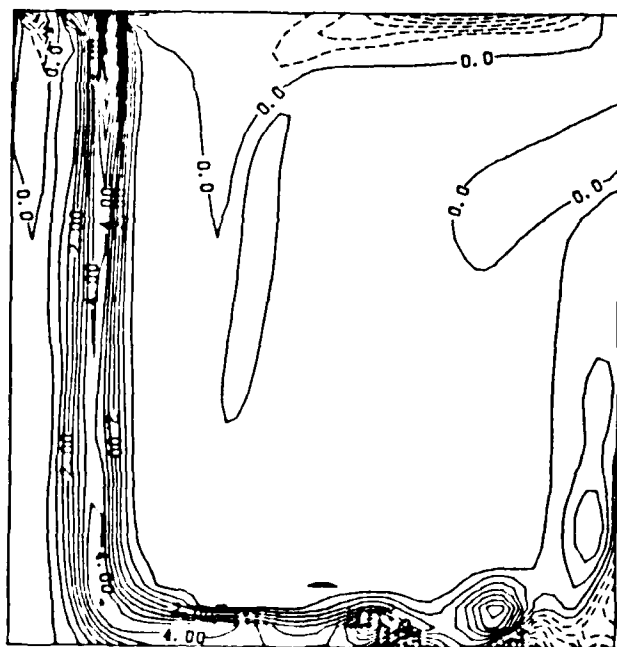
Figure 85. Three-dimensional perspective of the absolute vorticity surface at a level  $|\omega| = 2.1$  for forced double-jet computations.



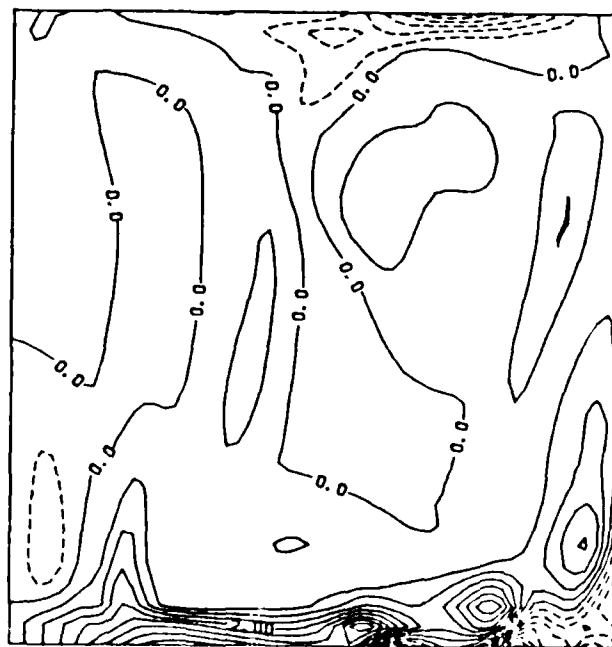
a.  $t = 46.40, x = 0$



b.  $t = 49.22, x = 0$

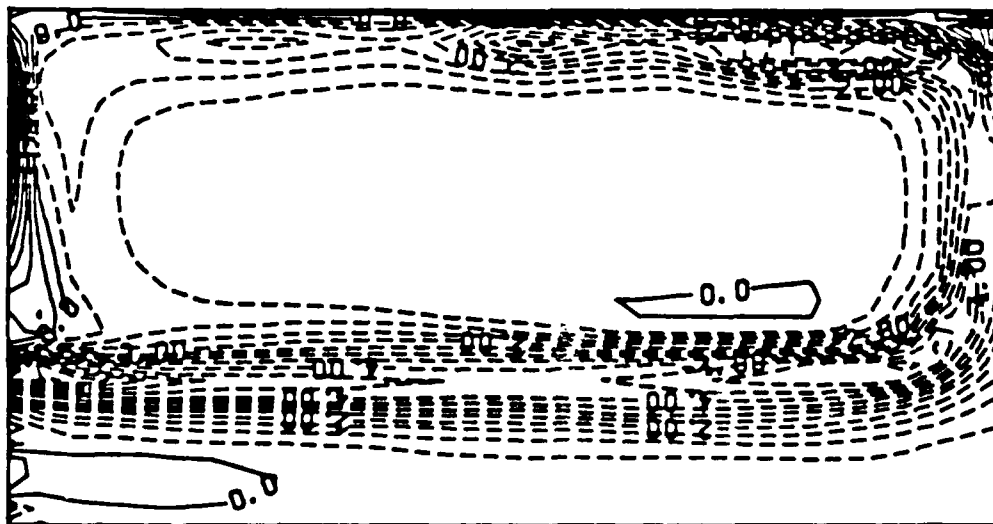


c.  $t = 50.62, x = 0$

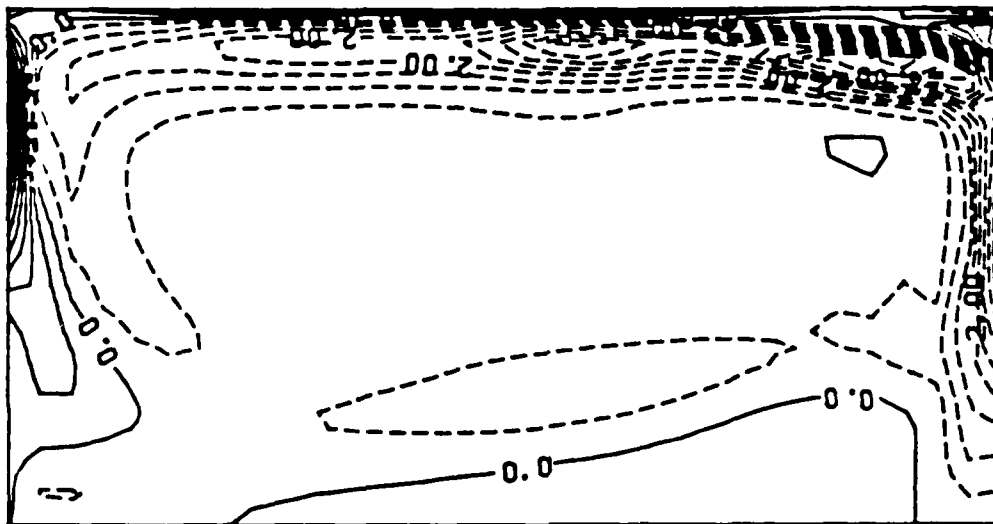


d.  $t = 50.62, x = 0.51D$

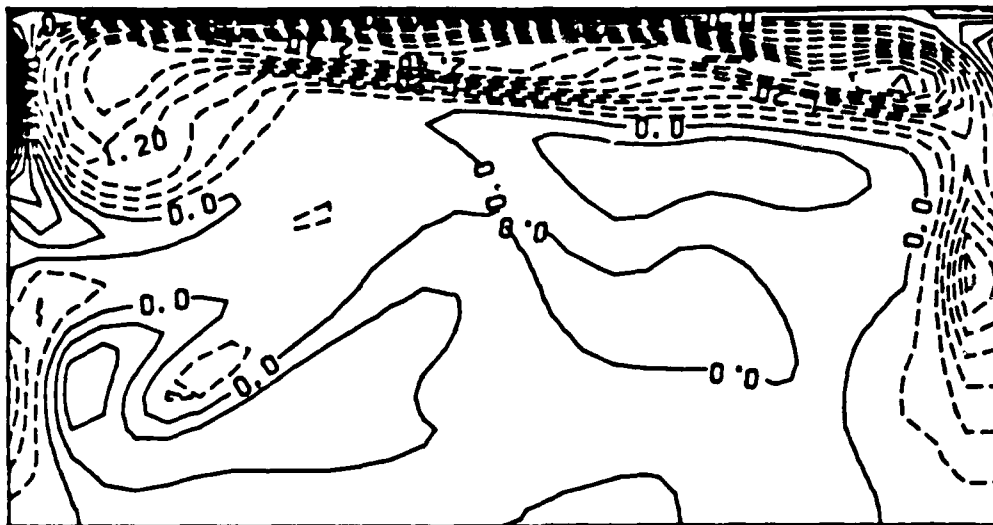
Figure 86.  $\kappa$ -vorticity contours in the  $y$ - $z$  plane due to random excitation for  $H = 3D$ .



a.  $y = 0$  plane

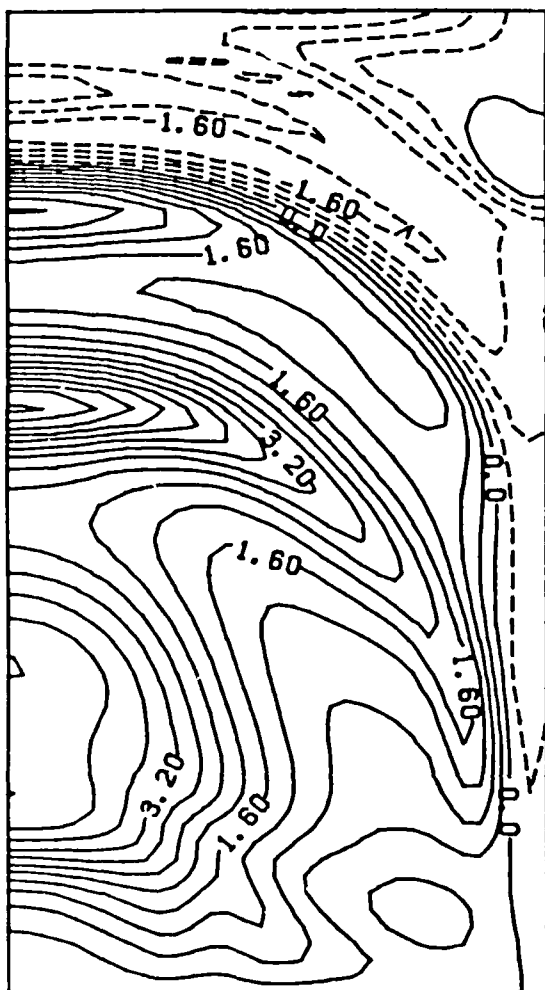


b.  $y = 0.51D$  plane

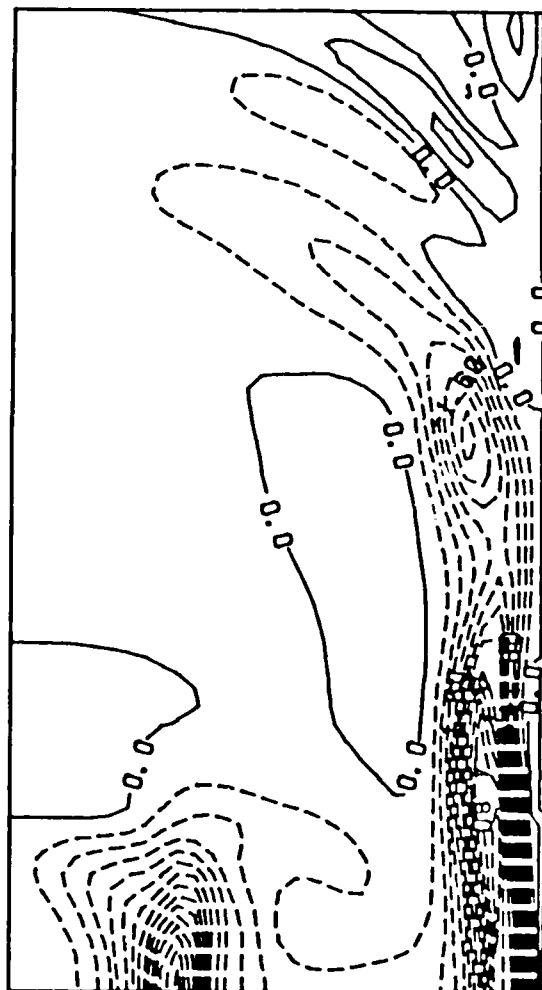


c.  $y = 1.5D$  plane

Figure 87.  $y$ -vorticity contours in the  $x$ - $z$  plane at  $t = 50.62$  due to random excitation for  $H = 3D$ .



a. x-vorticity



b. y-vorticity

Figure 88. Spanwise variation of x- and y-vorticity contours in the  $z = 0$ , x-y plane at  $t = 50.62$  due to random excitation for  $H = 3D$ .

END

FEB.

1988

DTIC